Graphene oxide supported ternary metal sulphides as photocatalyst for the degradation of emerging contaminants

O. C. Olatunde

orcid.org/0000-0002-8245-0763

Thesis accepted in fulfilment of the requirements for the degree *Doctor of Philosophy in Chemistry* at the North-West University

Supervisor:	Prof. D. C. Onwudiwe
Co-supervisor:	Prof. A. T. Kuvarega

Graduation: 2022
Student number: 32587139

Abstract

The development of effective ternary metal sulfides supported graphene oxide composites as catalytic materials have been explored in this thesis. The Single source precursor method employing dithiocarbamate metal complexes were employed as precursor in a heat-up method in the synthesis of the copper-based ternary metal sulphides, which were composited with graphene derivatives through facile techniques.

The suitability of the metal complexes as single source precursors was firstly evaluated by exploring the obtained metal complexes as precursors for the synthesis of their respective binary metal sulphides. Particularly, the ability to obtain different Cu_xS phases, which is important for the selective synthesis of different stoichiometric phases of Cu-M-S was explored. Thermolysis of copper bis dithiocarbamate metal complex in a mixture of oleylamine (OLA) and dodecanethiol (DDT) showed a mixture of phases were obtained at relatively low temperature with pure phase of Cu_5S_9 only obtainable at high temperature. This study showed the significance of solvent property in influencing phase selectivity in the synthesis of $Cu_{2-x}S$.

The thermolysis of bismuth(III) tris (N-methyl-N-phenyl dithiocarbamate) complex was also explore in a solvent mixture oleylamine, dodecanethiol and octadecene. At temperature range of 150 -250 °C Bi_2S_3 nanoparticles with varying microstructural properties was obtained. The microstructural properties of the nanoparticles were explored using the Scherrer equation, Williamson-Hall plot and Rietveld analysis. A close agreement between the models was observed with the particle size ranging between 20.1 – 45.9, 20.9 -26.6 and 23.0-29.7 nm for the Scherrer equation, Williamson-Hall's plot and Rietveld analysis respectively. Similarly, antimony(III) tris (N-methyl-N-phenyl dithiocarbamate) complex was thermolyzed in hexadecylamine solvent and the microstructural property was studied. In addition to the microstructural studies, other crystal properties and empirical parameters such as lattice parameters, cell volume, bulk density, X-ray density, surface area and porosity were evaluated. The particle size for the Sb_2S_3 nanoparticles obtained ranged between 85.1-111.3 nm for the explored models, while all the models affirmed the strain in the strain to be in the lattice to be due to lattice contraction. The empirical analysis showed the presence of Sb vacancies, while the lattice parameters and other cell parameters agreed significantly with values in literature.

After establishing the thermal decomposition products of these complexes, they were co-thermolyzed with other precursor compounds which have comparable decomposition profiles for the synthesis of ternary Cu-M-S. Firstly, the selective synthesis of two phases of copper tin sulphides: petrukite (Cu_3SnS_4) and kuramite (Cu_2SnS_3), was achieved by the solvothermal decomposition of diphenyl tin(II) dithiocarbamate and Cu (II) bis N-methyl-N-phenyl dithiocarbamate complex by the heat-up process in high boiling solvents. Cu2SnS3 was obtained in oleylamine at 220 °C, while Cu_3SnS_4 was obtained in a mixture of oleylamine

and dodecanethiol at 180 °C. The particle size distribution was 13.7 ± 2.4 for Cu_2SnS_3 and 11.3 ± 1.5 nm for Cu_3SnS_4, with the band gap energy being 1.16 and 1.57 for Cu_2SnS_3 and Cu_3SnS_4 respectively. The photoluminescence spectroscopy measurement showed a lower charge carrier recombination in Cu_2SnS_3 compared to Cu_3SnS_4, which account for the 94.0% degradation efficiency towards Tetracycline degradation compare to 73.0% recorded for Cu_3SnS_4. Electrochemical measurements also showed that Cu_2SnS_3 exhibited lower resistance, getter charge transport and conducting properties compare to Cu_3SnS_4.

Subsequently, supported Cu_2SnS_3 and Cu_3SnS_4 nanoparticles were synthesized through facile solvothermal processes. Cu2SnS3 supported by reduced graphene oxide (rGO) were prepared at different rGO ratio 0-20%. The photocatalytic activity of the nanoparticles for tetracycline degradation was influenced by the weight fraction of rGO, with composite with 20% rGO composition showing the maximum degradation efficiency of 93% compared to compared to 64, 65.5 and 68.8% degradation recorded for 0, 5, and 10% rGO composition respectively. rGO was observed to improve the degradation efficiency by enhancing the adsorption capacity of the nanoparticle and also reducing charge carrier recombination. For the Cu3SnS4 phase, the influence of graphene oxide (GO), protonated graphitic carbon nitride (PCN) and composite of GO and PCN (GO/PCN) on the degradation of tetracycline was explored. The study showed that the composite GO/PCN showed the highest degradation efficiency of 96.5% compare to 85.2 and 90.9% recorded for composites with PCN and GO respectively. The enhanced activity of the GO/PCN based composite was found to be due to exciton generation and enhanced adsorption property.

Afterwards, selective synthesis of copper antimony sulphides (CAS) was explored. Three different phases of CAS were obtained: chalcostibite ($CuSbS_2$), famantinite (Cu_3SbS_4) and tetrahedrite ($Cu_{12}Sb_4S_{13}$) using copper(II) dithiocarbamate and antimony(III) dithiocarbamate complexes in a solvothermal heat-up process. The catalytic activity of the three phases for persulfate activation of tetracycline degradation was explored with degradation efficiencies of 26.1, 54.6 and 55.6% achieved by $CuSbS_2$, $Cu_{12}Sb_4S_{13}$ and Cu_3SbS_4 respectively. The study of the influence of pH on the persulfate activation process showed a higher efficiency of 85.5% was achieved under neutral condition. Radical scavenging experiment showed the process was radical based process, with the initiation being a one electron transfer process. the Cu_3SbS_4 phase with tetrahedrite phase exhibiting the highest activity. Further study on improving the activity of $CuSbS_2$ was explored by supporting the nanoparticle on graphene oxide. The supported $CuSbS_2$ was then explored in the degradation of tetracycline in persulfate activation and photocatalytic processes. The percentage degradation was 94 and 74% for the photocatalytic and persulfate activation process respectively. Mechanism study showed that the photocatalytic process proceeded significantly through the activity of photogenerated holes while the persulfate activation process, was a non-radical process.

Finally, the selective synthesis of copper bismuth sulphide (CBS) phase was attempted using Bi(III) bis N-methyl-N-phenyl dithiocarbamate and Cu(III) bis N-methyl-N-phenyl dithiocarbamate as single source precursors. However, only the wittichenite phase (Cu_3BiS_3) was obtained in pure phase. The Cu_3BiS_3

nanoparticles was agglomerated and oval-shaped with a particle size of 60.1 nm. The obtained semiconductor nanoparticle was further supported on reduced graphene oxide and explored as a catalyst in UV-light assisted persulfate activation process and in a photocatalytic process for the degradation of diclofenac. A degradation efficiency of 74% was achieved in the photocatalytic process, while the UV-light assisted persulfate activation process attained 84% degradation efficiency. The composites showed great capacity for degradation for the degradation of a wide variety of pollutant with 100% degradation efficiency achieved for methyl orange, tetracycline and methylene blue, while bisphenol reached 81% efficiency. The study showed that the nanocomposite exhibited a higher activity in the UV-light assisted process, with the process showing lower energy consumption when compared to other reported process.

The results of this study confirm the potential of dithiocarbamate complexes as precursor compounds for achieving phase selectivity synthesis of Cu-M-S semiconductors and also, the potential of these materials as versatile catalysts for advanced oxidation processes. In addition, the study has shown that graphene oxide/reduced graphene oxide is a suitable support material for enhancing the catalytic activity of these semiconductors.

Keywords: Single source precursors; Photocatalyst; Semiconductor; Dithiocarbamate; Thermolysis; Advanced oxidation processes, Persulfate activation.

Acknowledgement

- I would like to thank my supervisor Professor Damian Onwudiwe for his guidance throughout the course of this research work.

- To my wife: Olubukola and my kids: MJ and MIMI, thank you for being there for me and always supporting me through the period of this study.

- To my mother and siblings your emotional support throughout the course of my studies has kept me going.

- My gratitude goes to all the academic and laboratory staff of the Department of Chemistry, North-West University, Mafikeng Campus for all the assistance provided throughout this study.

- To all members of the research group, it has been great working alongside you all and thank you for your encouragement and support.

- To my friends who have contributed in one way or the other to the success of my study, I say a big thank you. Thanks for your support all the way.

List of publications

1. **Olatunde, O.C.** and Onwudiwe, D.C., 2020. Copper-based ternary metal sulphide nanocrystals embedded in graphene oxide as photocatalyst in water treatment. In Nanotechnology in the Beverage Industry (pp. 51-113). Elsevier.
2. **Olatunde, O.C.**, Kuvarega, A.T. and Onwudiwe, D.C., 2020. Photo enhanced degradation of contaminants of emerging concern in waste water. *Emerging Contaminants*, 6, pp.283302.
3. **Olatunde, O.C.** and Onwudiwe, D.C., 2021. Stoichiometric phases and mechanism of crystal phase selectivity of copper-based ternary sulphides. *Materials Science in Semiconductor Processing*, 125, p.105627.
4. Onwudiwe, D.C., **Olatunde, O.C.** and Mathur, S., 2020. Structural studies and morphological properties of antimony sulphide nanorods obtained by solvothermal synthesis. *Physica B: Condensed Matter*, p.412691.
5. **Olatunde, O.C.**, Kuvarega, A.T. and Onwudiwe, D.C., 2020. Photo enhanced degradation of polyfluoroalkyl and perfluoroalkyl substances. *Heliyon*, 6(12), p.e05614.
6. **Olatunde, O.C.** and Onwudiwe, D.C., 2021. Graphene-Based Composites as Catalysts for the Degradation of Pharmaceuticals. *International Journal of Environmental Research and Public Health*, 18(4), p.1529.
7. **Olatunde, O. C.** and Onwudiwe, D.C., 2021. Temperature controlled pure phase evolution of Cu_9S_5 nanoparticles by solvothermal process. *Frontiers in Materials*, 8, p.211. **Olatunde, O.C**. and Onwudiwe, D.C., 2022. A Comparative Study of the Effect of Graphene Oxide, Graphitic Carbon Nitride, and Their Composite on the Photocatalytic Activity of Cu_3SnS_4. Catalysts, 12(1), p.14. https://doi.org/10.3390/catal12010014
8. **Olatunde, O.C**. and Onwudiwe, D.C., 2021. Evaluation of the photocatalytic and persulfate activation properties of GO-$CuSbS_2$ composite. *Journal of Photochemistry and Photobiology*, p.100095. https://doi.org/10.1016/j.jpap.2021.100095
9. **Olatunde, O.C**. and Onwudiwe, D.C., 2021. Graphene-Based Composites as Catalysts for the Degradation of Pharmaceuticals. *International Journal of Environmental Research and Public Health*, *18*(4), p.1529. https://doi.org/10.3390/ijerph18041529
10. **Olatunde, O.C.** and Onwudiwe, D.C., 2021. Selective synthesis of kuramite (Cu_2SnS_3) and petrukite (Cu_3SnS_4) phases of copper tin sulphide, and their electrochemical and photocatalytic properties. *Results in Materials*, p.100249. https://doi.org/10.1016/j.rinma.2021.100249
11. **Olatunde, O.C.** and Onwudiwe, D.C., 2021. Stoichiometric phases and mechanism of crystal phase selectivity of copper-based ternary sulphides. *Materials Science in Semiconductor Processing*, *125*, p.105627. https://doi.org/10.1016/j.mssp.2020.105627

LIST OF ABBREVIATIONS

AOP- Advanced oxidation proces

ASC- Ascorbic acid

CAS- Copper antimony sulphide

CB-Conduction band

CBM- Conduction band minima

CBS- Copper bismuth sulphide

CBTS- Copper-based ternary sulphide

CIGS- copper indium gallium sulphide

CMS-Copper-based metal sulphide

COD- Chemical oxygen demand

CPE- constant phase element

CTS-Copper tin sulphide

CZTSe- Copper zinc tin selenide

DDT- 1-Dedecanethiol

DMF- Dimethylformamide

DWT-Domestic waste treatment

XRD -X-ray density

ECs- Emerging contaminants

EDX-Electron dispersion spectroscopy

EIS- Electrochemical impedance spectroscopy

FRET- Foster resonance energy transfer.

GCN- graphitic carbon nitride

GO- Graphene oxide

GOF- Goodness of fit

LSPR- Localized surface plasmon resonance

MOFs- Metal organic frameworks

NIR- Near infrared

NOM- natural organic matter

NPs- Nanoparticles

NSAIDs- Non-steroidal anti-inflammatory drugs

OLA- Oleylamine

OTC- Oxytetracycline

PCN- Protonated graphitic carbon nitride

PL- Photoluminescence

PMS- Peroxymonosulfate

PS- Persulfate

R_{exp}- Expected residual factor

rGO- reduced graphene oxide

R_p- Residual of least-squares refinement

R_{wp}- Weighted profile R factor

S. A. – Surface area

SEM- Scanning electron microscopy

SSP- Size-strain plot

TBA- Tert buthanol

TC- Tetracycline

TC.HCl-Tetracycline hydrochloride

TEA- Triethanol amine

TEM- Transmission electron microscopy

TOC- Total organic carbon

UDEDM- Uniform deformation energy density model

UDM- Uniform deformation model

USDM- Uniform stress deformation model

UV- Ultraviolet

VB- Valence band

VBM- Valence band maxima

VUV- Vacuum ultraviolet

W-H- Williamson-hall

XRD- X-ray diffraction

WWTP-Wastewater treatment plant

Table of Contents

Preface

This thesis was written using the article format. All experimental works and drafting of initial manuscript were done by Olalekan C. Olatunde, while the research work and proof reading of manuscripts were carried out by Prof. D. C. Onwudiwe. A total of seven (7) published articles and seven (7) submitted manuscripts were combined in compiling the thesis. The list of submitted manuscripts and the reviewing journals are as follows:

1. Bismuth sulphide nanorods from the solvothermal process: effect of reaction temperature on microstructural and optical properties. Submitted to Scientific reports
2. Lattice strain analysis of solvothermally synthesized antimony sulphide. Submitted to Chemphychem
3. Selective synthesis of kuramite (Cu_2SnS_3) and petrukite (Cu_3SnS_4) phases of copper tin sulphide, and their electrochemical and photocatalytic properties. Submitted to Results in Chemistry.
4. Synthesis of reduced graphene oxide/copper tin sulphide (Cu_2SnS_3) composite for the photocatalytic degradation of tetracycline. Submitted to ACS Omega.
5. A comparative study of the effect of graphene oxide, graphitic carbon nitride, and their composite on the photocatalytic activity of Cu_3SnS_4. Submitted to ACS Omega.
6. Evaluation of the photocatalytic and persulfate activation properties of GO-$CuSbS_2$ composite. Submitted to Results in Chemistry.
7. UV-light assisted activation of persulfate by rGO-Cu_3BiS_3 for the degradation of diclofenac. Submitted to Results in Chemistry.

All manuscripts have been included in this thesis with permission from all journal Editors and Co-authours.

List of figures

Chapter Two

Chapter three

Chapter four

Chapter five

Chapter six

Chapter seven

Chapter eight

Chapter nine

Chapter Ten

Chapter Eleven

List of tables

Chapter four

Chapter five

Chapter six

Chapter seven

Chapter eight

Chapter 11

CHAPTER ONE

Introduction

1.0 Problem statement

The lack of safe drinking water is one of the major global challenges facing the world presently. Water supply continues to grapple with the effect of climate change and environmental pollution. Water pollution has been a major concern both because of the huge economic effect and potential adverse effect on the environment. In a recent study by world bank, it was estimated that water pollution could cost some countries up to one-third of their economic growth, while recently, the United States estimated that water pollution costs the nation about $4.3 billion annually. The effects of pollution on the ecosystems may include mortality, as well as inducing physiological, reproductive and bahavioural changes in living organisms. The release of contaminants into water bodies has been a major concern as the drive for industrialization and increase in the production of consumer products continues to rise. This has not only led to an increase in the level of water pollution, but also new compounds, referred to as emerging contaminants have recently been identified in water systems. One of such compounds is pharmaceuticals, whose presence in water has been of major concern in the last two decades. One main strategy that has offered hope for the enhancement of water availability is the reuse/recycling of wastewater. This is driven by the development of suitable techniques for the removal of pollutants/contaminants from wastewater. Several advanced techniques are currently employed in the removal of pollutants in wastewater treatment processes such as adsorption, reverse and forward osmosis, ultrafiltration techniques, membrane technology, ion exchange and advanced oxidation processes. While each of these techniques has shown great efficiency in the removal of pollutants from wastewater, a major concern has been the need to completely remove these contaminants from the environment and prevent their re-introduction into the water system. This has necessitated the incorporation of destructive techniques into the water purification process. This accounts for the immense focus that advanced oxidation processes (AOP) has received among other wastewater treatment techniques (Xia *et al.*, 2020). AOPs comprise a large class of techniques that involves the in-situ generation of reactive radicals such as $^{\bullet}$OH, $O_2^{\bullet -}$ and SO_4^{2-} Among the large class of techniques that fall under the AOPs, the ones that involve the use of light energy and photocatalytic semiconductors have been of particular interest because they are facile, economical and environmentally friendly. Apart from the light source, the property of the semiconductor material plays an important role in the overall effectiveness and efficiency of the photocatalyst-based AOPs. This has led to the continual research to find suitable photocatalytic materials which are economical, non-toxic, and with sufficient stability. Thus, the drive to improve on the efficiency of wastewater treatment processes anchors on the development of new and effective photocatalytic materials that could provide a cost effective and highly efficient process required to improve the quality of water for reuse.

2.0 Motivation and rationale

The need for the development of semiconductor materials with high absorption coefficient and band gap in the 1.0 –1.5 eV range from cheap and earth abundant elements, which are among the main criteria for a semiconductor material, has spurred the interest in the synthesis of ternary copper-based sulphides. In addition, the potential exertion of phase control gives the opportunity to access ternary copper-based metal sulphides that meet this criterion for photon-based applications. Copper-based ternary sulphides have become a subject of great interest because of their numerous unique properties and their non-toxic advantage over lead and cadmium-based semiconductor materials. Copper is an environmentally friendly and relatively abundant metal, with low lying d-orbitals, which consequently result in bandgap lowering, tetrahedral crystal structure adoption and increased stability of copper containing compounds. The compounds are also structurally, compositionally and stoichiometrically versatile, with numerous non-stoichiometric phases identified. Their excellent functional properties such as low thermal conductivity, high carrier concentration, plasmonic properties and direct bandgaps make them potential materials for application as optoelectronic, thermo-electronic and photocatalytic materials. Ternary copper-based sulphides are usually of the form Cu-M-S, where M is either a transition metal (e. g., Fe and Cr) or main-group metals (e.g., Sn, In, Sb and Bi). Among the copper ternary metal sulphides comprising of main-group metals, only compounds of In have shown high promise as semiconductor materials despite the favourable optical properties of these compounds. Also, the study of their photocatalytic activity for wastewater treatment has not been significantly explored. Since the development of suitable semiconductor photocatalysts is important in enhancing the efficiency and effectiveness of wastewater treatment, there is the need to explore routes to enhance the activity of these compounds, which could serve as potential catalysts for the degradation of contaminants in wastewater treatment processes.

3.0 Aim and objectives

The aim of this research is to obtain cost effective and environmentally friendly catalysts for efficient degradation of emerging contaminants.

Objectives

In order to achieve the aim of this research, the following objectives have been set:

1. to synthesize ternary copper-based metal sulphide (CMS) nanoparticles using dithiocarbamate metal complexes as precursors for the synthesis of copper bismuth sulphide (CBS), copper antimony sulphide (CAS) and copper tin sulphide (CTS);

2. to study the phase selectivity of the ternary nanoparticles by varying different reaction parameters including solvent/capping ligand ratio and reaction temperatures;

3. to characterize the prepared ternary metal sulphides using various optical, structural and morphological characterization techniques;

4. to synthesize reduced graphene oxide and characterize it;

5. to decorate the prepared ternary metal sulphides on reduced graphene oxide and characterize them

6. to evaluate the catalytic degradation efficiency of the materials for the degradation of pharmaceuticals (tetracycline and diclofenac) and propose reaction mechanisms for the degradation processes;

7. to optimize the photocatalytic process by varying reaction parameters like pH, dosage of catalyst and concentration of pollutants.

4.0 References

Hamza, F., Merouani, S., Hamdaoui, O. & Pétrier, C. 2016. Persulfate-Enhanced Sonochemical Degradation of Naphthol Blue Black in Water: Evidence of Sulfate Radical Formation. *Ultrasonics Sonochemistry,* 34.

Li, Y., Dong, H., Li, L., Tang, L., Tian, R., Li, R., Chen, J., Xie, Q., Jin, Z., Xiao, J., Xiao, S. & Zeng, G. 2021. Recent advances in waste water treatment through transition metal sulfides-based advanced oxidation processes. *Water Research,* 192**,** 116850.

Lokhande, A. C., Babar, P. T., Karade, V. C., Gang, M. G., Lokhande, V. C., Lokhande, C. D. & Kim, J. H. 2019. The versatility of copper tin sulfide. *Journal of Materials Chemistry A,* 7**,** 17118-17182.

Thakur, K. & Kandasubramanian, B. 2019. Graphene and Graphene Oxide-Based Composites for Removal of Organic Pollutants: A Review. *Journal of Chemical & Engineering Data,* 64**,** 833-867.

Xia, X., Zhu, F., Li, J., Yang, H., Wei, L., Li, Q., Jiang, J., Zhang, G. & Zhao, Q. 2020. A Review Study on Sulfate-Radical-Based Advanced Oxidation Processes for Domestic/Industrial Wastewater Treatment: Degradation, Efficiency, and Mechanism. *Frontiers in Chemistry,* 8.

Xu, Y., Liu, T., Zhang, Y., Ge, F., Steel, R. M. & Sun, L. 2017. Advances in technologies for pharmaceuticals and personal care products removal. *Journal of Materials Chemistry A,* 5**,** 12001-12014.

CHAPTER TWO

Literature review

1.0 Emerging contaminants

According to Sauvé and Desrosiers (2014), emerging contaminants (ECs) or contaminants of emerging concern or could be defined as chemicals or materials that occur naturally or man-made and exist in the environment with persistence or toxicity which have recently been discovered to be capable of altering human body metabolism. These materials constitute a serious danger to the environment and human health, and are yet to be subjected to environmental regulations. These contaminants could be materials that have just recently been discovered in the environment or materials that may have stayed in the environment for a while but recently raised concern. They have reportedly been found in several aquatic environments including rivers, marine waters, lakes, freshwater reservoirs and estuaries (Galindo-Miranda *et al.*, 2019). Their presence in water is at trace levels within the ng - µg per litre of water, which makes them very difficult to detect directly by most analytical tools (Luo *et al.*, 2014).

Contamination by emerging pollutants has raised concern recently in water quality standard due to their increased presence in the environment. This has resulted in the deterioration of water quality, especially in surface water, which could cause serious health issues when consumed (Riva *et al.*, 2018). Also, of concern is the fact that these contaminants usually occur in water as complex mixtures rather than individually, thereby making their identification and assessment very difficult. Part of the challenges associated with the complex mixtures is the undesirable synergy that may also arise between the contaminants (Petrie *et al.*, 2015). Materials classified under this category of pollutants include flame retardants such as per- and poly- fluoroalkyl substances (e.g., perfluorooctanesulfonate), plasticizers, personal care products (e.g., parabens) and pharmaceuticals such as antibiotics, hormones, stimulants, and analgesics (Nilsen *et al.*, 2019). The presence of these pollutants in water bodies has already been reported in the United Kingdom (Rodgers-Gray *et al.*, 2000), Germany (Kuch and Ballschmiter, 2001), Japan (Ying *et al.*, 2002) and South Africa (Chokwe *et al.*, 2019). While a wide range of pharmaceuticals have been detected in water and the number continues to increase on a daily basis, the evaluation of flame retardants, plasticizers and personal care products is relatively new.

Aside the earlier identified challenges with emerging contaminants, the fact that current water treatment systems are not optimized for dealing with these contaminants, results in their incomplete removal. It was recently reported that for almost all tested pharmaceuticals present in the inlet flow of a wastewater treatment plant, above 50% of the initial concentration was retained in the outlet water stream of the treatment plants (Petrovic *et al.*, 2005). In fact, a major source of these pollutants are sludges from wastewater treatment plants that are deposited in landfills or discharged water from waste water treatment plants (Petrie *et al.*, 2015). Thus, there is an urgent need for the incorporation of techniques that will adequately deal with the presence of these contaminants. Techniques such as adsorption, membrane technology, biological treatment and advanced oxidation processes (AOP) have been explored as tertiary methods to deal with the menace of these pollutants. The efficiency of a technique designed for the removal or degradation of ECs is dependent on factors such as physicochemical properties and, biological and chemical persistence of target ECs and condition of operation (Ahmed *et al.*, 2017).

Adsorption technique has shown great promise as an effective process for the removal of ECs due to its high efficiency, low-cost and simple design requirements (Sophia A and Lima, 2018). Some adsorbent materials that have been explored for the removal of ECs include: activated carbon (Torrellas *et al.*, 2016), modified biochar (Xiao and Pignatello, 2015), carbon nanotubes (Babaei *et al.*, 2016), graphene (Zhu *et al.*, 2017) and clay minerals (Putra *et al.*, 2009). Adsorption technology is considered a green route to ECs removal, with low generation of secondary sludge and high compatibility with other treatment systems. However, there is still a great need for development of novel adsorbents with high sorption rate that could be integrated for column use and which could effectively deal with different ECs (Sophia A and Lima, 2018). In addition, the possibility of recontamination is still a major concern with adsorption because the question on adsorbent disposal is still yet to be satisfactorily dealt with. Regeneration of the adsorbent is also another challenge in the current adsorbent systems.

Therefore, a technique that will be generally acceptable for ECs removal must be able to achieve complete destruction of the molecules, which have so far been achieved by biological treatments and AOPs. Technologies based on biological treatments are the most employed techniques explored for ECs degradation. These techniques include: aerobic bioreactor, fungal bioreactor, membrane bioreactor, activated sludge, nitrification, biosorption, tricking filter etc. ECs treatment by biological techniques is achieved via biodegradation, which involves the breaking down of high molecular weight molecules into small molecules by microorganisms like fungi, bacteria and algae (Garcia-Rodríguez *et al.*, 2014). The process of ECs bioremediation usually involves three steps: bioadsorption, bio-uptake and bioremediation. Bioadsorption describes the process by which the ECs are adsorbed to the microorganisms cell wall, while bio-uptake is the transport of the EC into the cell, to be bound by intracellular compounds such as proteins, and the final step is biodegradation via some metabolic catalysis (Sutherland and Ralph, 2019). Biological treatments are most efficient for the degradation of strongly polar substances, most especially pharmaceuticals and their metabolites (Barceló and Petrovic, 2008). However, reports on biological processes have shown that they are most suitable for ECs that are easily biodegradable like caffeine and trimethoprim, while non-biodegradable and low biodegradables like bezafibrate and sulphiride may not be treatable with biological techniques

(Rodriguez-Narvaez *et al.*, 2017). Another major challenge with biological treatment processes is the difficulty in the development of isolation and quantification methodologies for ECs in the by-products of the process. Therefore, for application of biological processes to be more widely employed, there is the need for techniques that can detect ECs in complex matrices (Rodriguez-Narvaez *et al.*, 2017).

2.0 Pharmaceuticals

Pharmaceuticals are compounds produced for the purpose of usage as medicinal drugs. They remain as persistent, biologically active compounds that could be detected in drinking and surface water due to their incomplete removal by conventional processes (Lin *et al.*, 2017). These materials have received much attention recently due to their health and environmental impact (Xu *et al.*, 2017, Magureanu *et al.*, 2015, Wongso *et al.*, 2020). The design of pharmaceuticals is such that when taken even at low concentrations, they can effect physiological changes in humans and animals. These compounds, when excreted either as metabolites or in an unchanged state, remain in the environment for a long time because they are not biologically degraded or reduced (Klavarioti *et al.*, 2009, Bhatia *et al.*, 2017). In aquatic environments, direct discharge of untreated and treated wastewater from treatment plants are the major sources of pharmaceuticals, while terrestrial runoff from agricultural fields, aquaculture facilities and livestock farms are some of the secondary sources as shown in Fig. 1 (Hong *et al.*, 2018, Daughton, 2003). Aquatic channels act as transport routes for pharmaceuticals and their bioaccumulation is mainly due to their lipophilic character; although, other factors such as animal homeostasis, metabolism and inhalation exposure are also important in understanding their accumulation in organisms (Khan *et al.*, 2020, Franzellitti and Fabbri, 2014, Du *et al.*, 2014, Gomez *et al.*, 2011). Compared to other organic contaminants, hydrophobic interactions are not the main influencing parameter on the partitioning dynamics of most pharmaceuticals. Other factors including cation exchange, surface complexation, hydrogen bonding and cation bridging also play vital roles. Thus, modelling approaches that have been created for other organic contaminants such as persistent organic pollutants are inappropriate for assessing the environmental risks of pharmaceuticals (Brooks *et al.*, 2009).

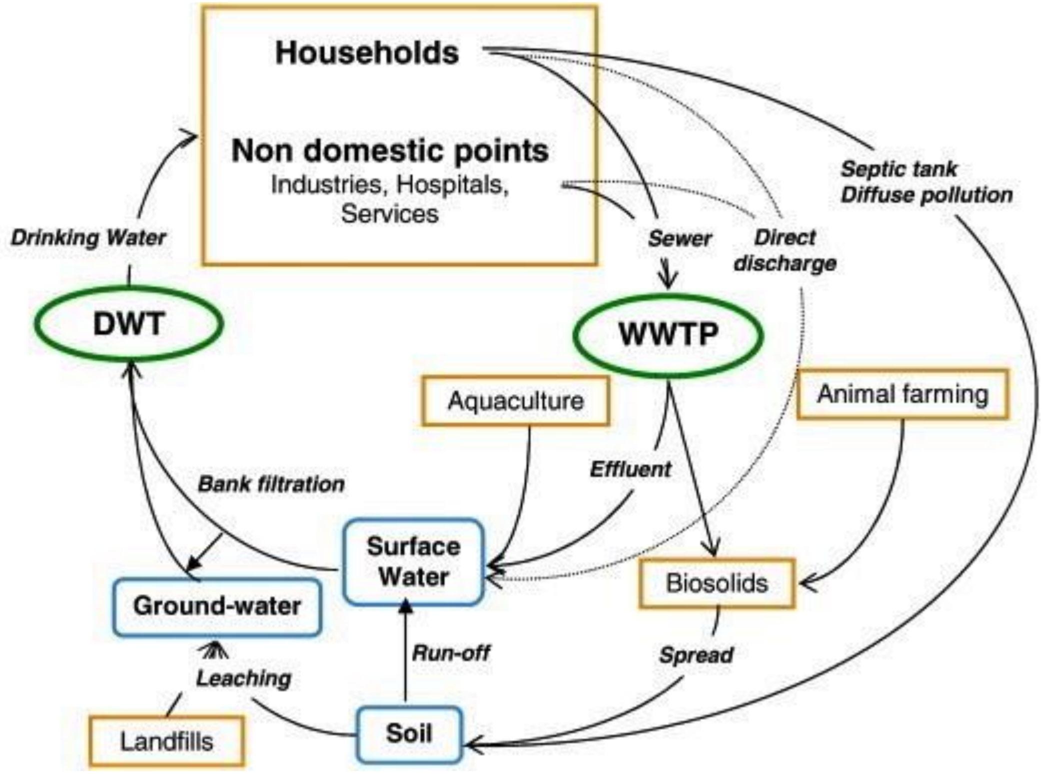

Fig. 1: Origins of pharmaceuticals and their environmental routes. (WWTP = waste water treatment plant; DWT = Domestic waste treatment Reprinted form Sayadi *et al.* (2010)

There is an increasing surge in the global consumption of pharmaceuticals with the global pharmaceutical market worth expected to reach $1170 billion in 2021 from $ 935 billion in 2017. This implies that concerns over the pollution of the environment by the discharge of different types of pharmaceuticals will continue to grow and they have been tagged as part of the emerging anthropogenic hazard pollutants (Ali and Gupta, 2006, Redding *et al.*, 2009). Also, their presence in the environment is due mainly to the inability of treatment plants to completely eliminate them. This, consequently, has led to their detection at concentration range of ng/L to µg/L in surface water, tap water and ground water (Valcarcel *et al.*, 2011, Radjenović *et al.*, 2009, Mompelat *et al.*, 2009). This increase in the concentration of pharmaceuticals in the water system, implies that the reuse of treated water, which has been suggested as the adequate solution for the sustainability of water resource is also under serious treat (Radjenovic *et al.*, 2009).

Pharmaceuticals and their by-products could be classified into 24 therapeutic classes, with non-steroidal anti-inflammatory drugs (NSAIDs) (e.g., ibuprofen, gemfibrozil and diclofenac), antibiotics (e.g., sulfamethoxazole, tetracycline and trimethoprim), anticonvulsants (e.g. carbamazepine) and lipid regulators (propranolol, metoprolol, nadolol) being the four most studied categories. Antibiotics have recently become subject of intense concern as emerging contaminants because of their extensive use in human and veterinary medicine (Scaria *et al.*, 2021). For example, recent projection on the use of tetracycline showed that a 200% increase in its consumption is expected by 2030 (Klein *et al.*, 2018).

Increasing information on the potential chronic or acute effects on the ecosystem and living organisms have begun to emerge recently. For example, Estrogen acts as endocrine modulators or disruptors and can have adverse effects on reproductive and sexual development like feminization of male fishes even at ng/L level (Mompelat *et al.*, 2009, Robinson *et al.*, 2007). Diclofenac has been indicted for its effect on mammalian kidney and the disappearance of the Oriental White backed Vulture in India and Pakistan (Fent *et al.*, 2006). The increased resistance to antimicrobial agents is another risk associated with the presence of pharmaceuticals in the environment (Kümmerer, 2004).

3.0 Advanced oxidation processes

Advanced oxidation processes (AOPs) are a class of treatment technologies based on the generation of reactive radicals for the degradation and mineralization of recalcitrant compounds from wastewater (Moreno-Benito *et al.*, 2013). These technologies have recently been suggested as promising techniques for the degradation of emerging contaminants especially personal care products and pharmaceuticals. The development of AOPs have advanced in the past three decades and employs a variety of methods in generating reactive oxygen species such as hydroxyl radical, superoxide anion radical, singlet oxygen and hydrogen peroxide (Pignatello *et al.*, 2006). The basis for AOPs application in the remediation of organic and inorganic compounds rests on the fundamental reactions of reactive oxygen species (O'Shea and Dionysiou, 2012).

About seventeen (17) AOPs have been identified from literatures as shown in fig. 2. Thus far, each process has shown varying suitability that depends on process conditions such as initial pollutant concentration, pH, chemical oxygen demand (COD), and economic considerations (Marta and Natalia, 2010). The efficiency of any of the processes has been found to depend greatly on rate of free radical generation and the existence of good contact between the generated radicals/oxidants with the molecules of pollutants (Gogate and Pandit, 2004). A major advantage of AOP over other wastewater treatment technologies is that the materials could be used to achieve water detoxification, purification/remediation, and disinfection, leading to water with qualities that fulfill standard regulations for potability (Olatunde and Onwudiwe, 2020).

Contaminants' degradation in AOPs are stimulated either through radiolysis, sonolysis or photolysis. While radiolysis and sonolysis generate radicals in aqueous media without the use of chemical oxidants, photolysis may require the involvement of a catalyst or precursor (Chaplin, 2014, Fernandez *et al.*, 2016, Olatunde *et al.*, 2020). The photon-based processes are preferred to other processes, because they could be carried out at ambient temperature and pressure, and the process could be conducted in very simple reaction systems (Silva *et al.*, 2013, Xu *et al.*, 2020, Li *et al.*, 2020b)

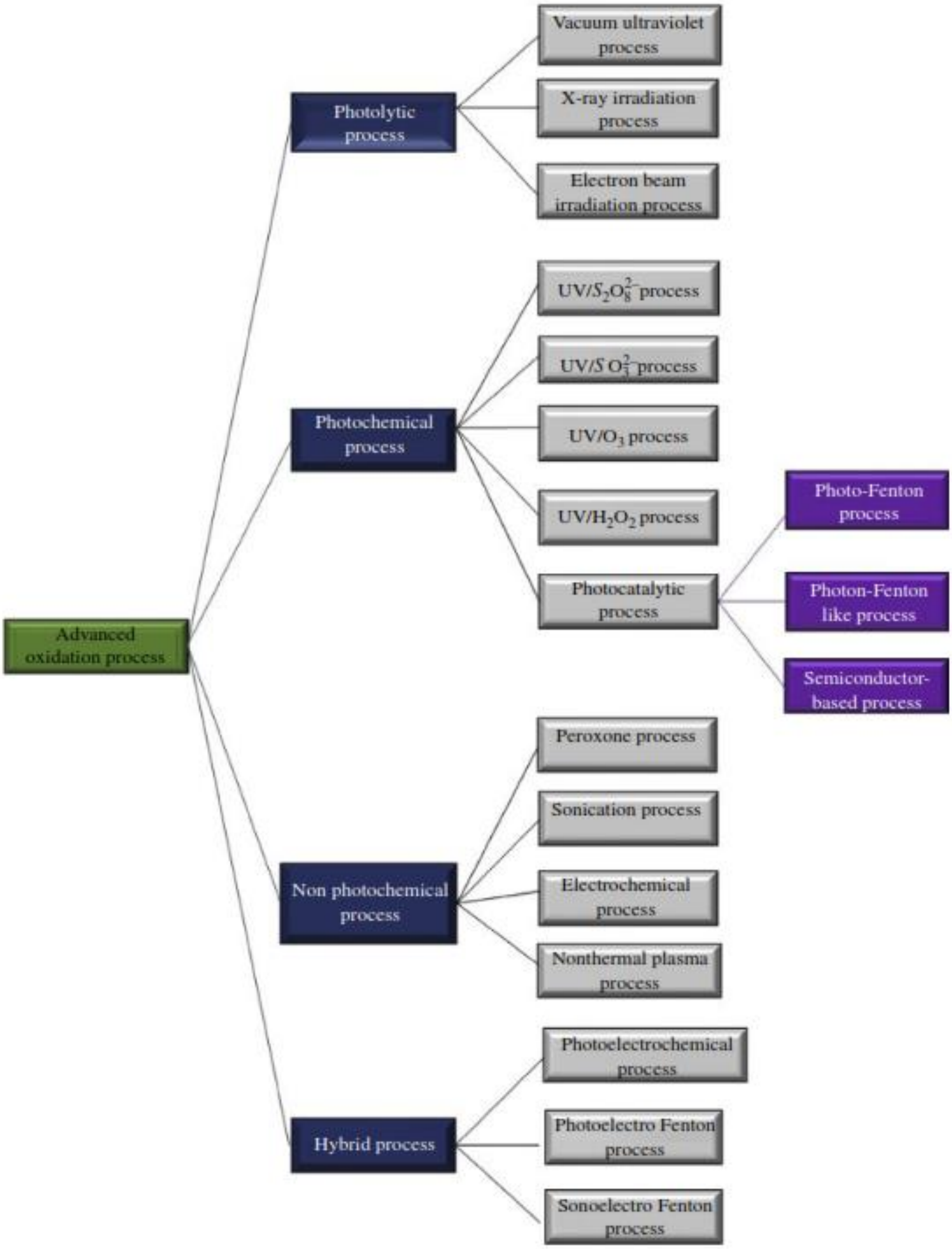

Fig.2: Classification of advanced oxidation processes.

3.1 Photon-based degradation process

Photodegradation processes are based principally on the use of light radiation as energy source. The light source for the process may be ultraviolet lights from mercury or Xenon lamps or solar light from the sun. When photons from light energy sources are absorbed by molecules, both physical and chemical changes take place in the species. The photochemical change can either be by direct or indirect means. In direct processes, the photon energy is absorbed by the target pollutant, which then undergoes homolytic cleavage to produce the degradation products (Chin and Bérubé, 2005). In the indirect photochemical process, the photon energy is absorbed by a photosensitive material, which produces species that interact with the target molecule to effect the degradation of pollutants. Both indirect and direct photochemical processes involve a series of reductive and oxidation reactions and the process can be classified as a redox process.

3.2 Photolysis

Photolysis involves the direct use of photon energy in the degradation of pollutants and is sometimes referred to as chemical-less process because it only involves photon energy in pollutant degradation. Photolysis is only applicable to pollutants with the capacity to absorb photon energy, thus efficiency of degradation is greatly influenced by the absorptivity of the pollutant and the properties of the light source such as wavelength and intensity (Satyro *et al.*, 2017). Generally, three classes of light sources are used in AOP, which include UV (ultraviolet) light, simulated solar lights or natural sunlight. However, for photolysis, UV light is the most probable light source due to the absorption of chemical chromophores within this wavelength region. UV light in AOP applications are usually classified into three UV wavelength ranges: UVA (315- 400 nm), UVB (280-315 nm) and UVC (100-280 nm). UV wavelength lower than 200 nm are often referred to as vacuum UV (VUV) (Matafonova and Batoev, 2018).

In photolysis, molecules are promoted from ground state to the singlet state and then to the triplet state via intersystem crossing. The excited molecules can then undergo heterolysis, homolysis, or photoionization to produce radicals that initiate chain reactions leading to the degradation of pollutants (Litter, 2005). Radicals like $^{\bullet}$OH, H$^{\bullet}$, e_{aq}^{-} , and O_3 (obtained in the presence of O_2) are generated by UV light radiations (Moussavi and Shekoohiyan, 2016)(Eq. 1-4).

$$H_2O + hv \longrightarrow {}^{\bullet}OH + H^{\bullet} \qquad (1)$$

$$H_2O + hv \longrightarrow e_{aq}^{-} + H^{+} + {}^{\bullet}OH \qquad (2)$$

$$O_2 + hv \longrightarrow 2{}^{\bullet}O \qquad (3)$$

$${}^{\bullet}O + O_2 \longrightarrow O_3 \qquad (4)$$

Direct photolysis is mainly suitable for degrading compounds which do not interact with OH or react slowly to it and also possess high molar absorption coefficient (Parsons, 2004). It has been explored in the degradation of pollutants like bromoxynil and trifluralin (Chelme-Ayala *et al.*, 2010), trihalomethanes (Litter, 2005), solophenyl green dye (G. and Faria, 2003), acetaminophen (Moussavi and Shekoohiyan, 2016) and also for inactivation of classes of microorganisms including protozoan cyst, bacteria and viruses (Hijnen *et al.*, 2006). Photolysis of triclocarban under simulated solar light (365.4 nm; 29.8 W/m^2), natural sunlight (365.4 nm; 27.8 W/m^2) and UVC radiation (253.7nm; 3.1 W/m^2), showed that only UVC radiation had sufficient energy for triclocarban degradation, achieving close to 100% degradation (Satyro *et al.*, 2017). Ding *et al.* (2015) reported that the degradation of triclocarban under simulated sunlight followed a pseudo-first order kinetics, with degradation rate that increased with increasing pH and fulvic acid concentration and decreasing initial triclocarban concentration. The degradation was however inhibited by presence of natural organic matter (NOM) like humic acid, nitrate etc. In another study, the degradation of ibuprofen using a UV light source of 15 W and 253.4 nm wavelength only showed about 27.6% total organic carbon (TOC) removal achieved (Tetorou *et al.*, 2019). The degradation of diethyl phthalate by VUV light source (185 nm and photon flux of 1.46×10^{-8} E s^{-1} L^{-1}) was reported by Wu *et al.* (2019), with 85% degradation and pseudo-first order rate constant of 0.1313 min^{-1} achieved. In comparison with UV-C radiation (254 nm and photon flux of 5.03×10^{-7} E s^{-1} L^{-1}) only 30% efficiency was achieved. Despite the promising efficiency of the photolysis process, it is however limited by its low efficiency, inability to degrade compounds with low/or no absorption within the UV range of the electromagnetic spectrum and also, it's inability to deal with multicomponent systems with more than one target molecules (Litter, 2005).

3.3 Photochemical processes

To improve the efficiency of direct photolysis, the process is often coupled with some inorganic oxidants like O_3, $SO_3^{2-}, S_2O_8^{2-}, HSO_5^-$, or H_2O_2 (Khan *et al.*, 2019, Esplugas *et al.*, 2007, Pan *et al.*, 2018, Gu *et al.*, 2017, Khan *et al.*, 2017b). In photochemical AOP, degradation of pollutants can be achieved via three possible routes: (1) photodecomposition, excitation and degradation of pollutant by generated radicals, (2) direct pollutant oxidation by oxidants like H_2O_2 and O_3, and (3) oxidation of pollutants by $^{\bullet}OH$ radicals generated by photocatalysts like TiO_2 and Fe^{3+}. The photodecomposition of some often employed inorganic oxidants is shown in reactions 5 – 10 (Khan *et al.*, 2017a, Mohammed and Fasnabi, 2016, Bustos-Terrones *et al.*, 2016, Khan *et al.*, 2019).

$$H_2O_2 + h\nu \longrightarrow 2^{\bullet}OH \qquad (5)$$

$$S_2O_8^{2-} \longrightarrow 2SO_4^{\bullet -} \qquad (6)$$

$$SO_3^{2-} + h\nu \longrightarrow SO_3^{\bullet -} + e_{aq}^- \qquad (7)$$

$$HSO_3^- + e_{aq}^- + h\nu \longrightarrow SO_3^{2-} + H^{\bullet} \qquad (8)$$

$$HSO_3^- + h\nu \longrightarrow SO_3^{\bullet -} + H^\bullet \qquad (9)$$

$$HSO_5^- + h\nu \longrightarrow SO_4^{\bullet -} + {}^\bullet OH \qquad (10)$$

Among the photochemical AOPs, the UV/H_2O_2 system (Eq. 5) has several advantages, among which are high $^\bullet$OH photogeneration quantum yield (Gligorovski *et al.*, 2015), cost effectiveness due to H_2O_2 low cost (Ganiyu *et al.,* 2015), generation of harmless by-products (O_2 and H_2O) (Wang and Wang, 2016) and the relative ease of H_2O_2 handling (Lanzafame *et al.*, 2017). UV/H_2O_2 has been explored in the degradation of several pharmaceuticals like antibiotics (Keen and Linden, 2013), anticonvulsants (Liu *et al.*, 2018), antiepileptics (Deng *et al.*, 2013); personal care products (Kim *et al.*, 2009), endocrine disrupting compounds (Borikar *et al.*, 2015), perfluoroalkyl and polyfluoroalkyl substances (Merino *et al.*, 2016). There is, however, a major drawback associated with UV/H_2O_2 system, which is the reaction of $^\bullet$OH with natural NOM which is an $^\bullet$OH quencher. The radicals also react with some inorganic anions present in aqueous solution to produce reactive radical species whose reactivity is lesser than that of $^\bullet$OH. The reaction of $^\bullet$OH with carbonates/bicarbonate, chlorides, bromides and nitrite leads to carbonate radical $CO_3^{\cdot -}$,dichloride radical ($Cl_2^{\cdot -}$), dibromide radical ($Br_2^{\cdot -}$) and nitrogen dioxide radical ($NO_2^{\cdot}$) formation respectively (Minero *et al.*, 2008). To circumvent this inherent challenge of the UV/H_2O_2 process, H_2O_2 is being replaced by an analogous peroxide, persulphate $S_2O_8^{2-}$ (UV/PS) and peroxymonosulfate (UV/PMS), which yields $SO_4^{\bullet -}$, a radical with comparable activity with $^\bullet$OH and less interaction with NOM and inorganic ions (Avetta *et al.*, 2015, Matzek and Carter, 2016).

The degradation of methyl 2-aminobenxoate using the UV, UV/H_2O_2 and UV/$S_2O_8^{2-}$ processes was reported by Lanzafame *et al.* (2017). The rate of degradation was observed to increase considerably with concentration of H_2O_2, but a plateau was reached due to the scavenging of $^\bullet$OH by H_2O_2 and absorption saturation of H_2O_2. However, in the presence of chlorine it was observed that no plateau occurred in the in rate of degradation as the rate of degradation increased with increase in H_2O_2 concentration, indicating that the presence of $^\bullet$OH radical as the prevailing radical specie in the system is unlikely. In the presence of carbonate ion, a reduction in the rate of degradation was observed and no further increase in degradation rate was observed beyond H_2O_2 concentration of 5 mM, which was attributed to the formation of the less reactive $CO_3^{\bullet -}$. For the UV/$S_2O_8^{2-}$, a higher increase in degradation rate was observed with increase in the concentration of the persulphate, showing that the reaction between persulphate and $SO_4^{\bullet -}$ did not have much influence on the degradation process compared to the reaction between H_2O_2 and $^\bullet$OH.

Deng *et al.* (2013)investigated the photo-degradation of carbamazepine using UV_{254}/H_2O_2, $UV_{254}/S_2O_8^{2-}$, and UV_{254}/HSO_5^-. After 90 min of reaction, 96.22, 98.91, and 76.2% degradation were achieved by the UV/H_2O_2, UV/PS and UV_{254}/HSO_5^- respectively, compared to 5% degradation achieved with direct photolysis. The efficiency of degradation was found to be influenced by the concentration of oxidants, pH of solution, initial concentration of carbamazepine and the presence of inorganic anions. The maximum degradation of carbamazepine in the processes was observed at pH of 3, 5 and 11 for the UV/H_2O_2, UV/PS and UV$_{254}$/HSO_5^- processes respectively. The degradation efficiency of both UV/H_2O_2, and UV/PS processes was negatively impacted by the presence of Cl^- in the reaction system. This was attributed to the ability of Cl^- to scavenge radicals generated in the system, to form radicals with lower oxidation potential. However, while the degradation efficiency of the UV/H_2O_2 process was inhibited at low concentrations of Cl^-, higher concentrations were required for degradation inhibition in the UV/PS process. While the efficiency of degradation decreases at low Cl^- concentration in the UV/PMS process, a great increase in carbamazepine degradation was observed at Cl^- concentration above 1 mM. This was due to the reaction of PMS with Cl^- to produce highly active chlorine species such as HOCl/Cl_2 which are effective for carbamazepine degradation.

Another photochemical process that has gained much research attention recently is the UV/O_3 process because O_3 absorption is greater than that of H_2O_2. However, its main shortcoming is its low $^{\bullet}OH$ quantum yield at 254 nm, which could be circumvented by using vacuum-UV (VUV) lamp that emits 10% radiation at 185 nm (von Sonntag, 2008). Increased amount of $^{\bullet}OH$ is generated in the process by the photolysis of H_2O by the VUV radiation at 185 nm (Eq. 11), coupled with the generation of $^{\bullet}H$ and hydrated electrons (Eq. 12).

$$H_2O + h\nu_{185nm} \longrightarrow {}^{\bullet}OH + {}^{\bullet}H \qquad (11)$$

$$H_2O + h\nu_{185nm} \longrightarrow {}^{\bullet}OH + H^+ + e_{eq}^- \qquad (12)$$

$$O_3 + H_2O \overset{h\nu}{\rightarrow} 2{}^{\bullet}OH + O_2 \qquad (13)$$

Degradation in the UV/O_3 process involves photolysis by UV radiation, direct oxidation by ozone and oxidation by $^{\bullet}OH$ as shown in Fig 3 (Wang *et al.*, 2004). Irradiation of O_3 with UV generate $^{\bullet}OH$ through Eq.13 (Boczkaj and Fernandes, 2017).

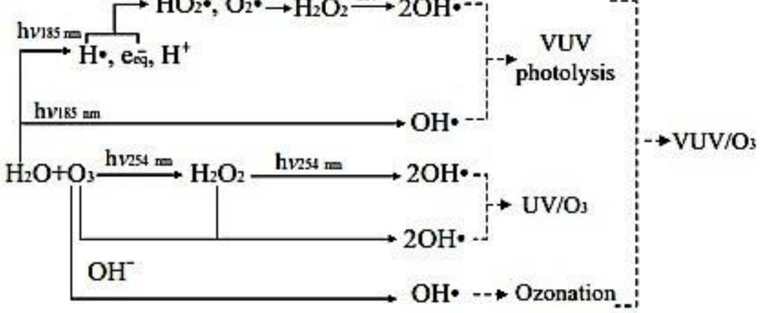

Fig 3: Pathway for the generation of hydroxyl radical in ozonation, photolysis UV/O_3 and VUV/O_3 processes. Reprinted from Fu *et al.* (2016), Copyright (2016), with permission from Elsevier

The efficiency of O_3, O_3/H_2O_2 and UV/O_3 processes for the degradation of 40 pharmaceuticals, detected in wastewater treatment plant, was reported by Kim and Tanaka (2010). The O_3 dosage for the three processes was 6.0 mg/L and the contact time was 10 min. The concentration of H_2O_2 for the O_3/H_2O_2 process was 3.2 mg/L and a low-pressure mercury UV lamp of 254 nm wavelength was employed for the UV/O_3 process. The study showed that while more than 90% removal was achieved for most of the pharmaceuticals in the ozonation process, removal efficiency in the range of 39-89% was recorded for pharmaceuticals like cyclophosphamide, caffeine, chlorotetracycline, diethyltoluamide,and isopropylantipyrine . With the introduction of H_2O_2, higher removal efficiency was achieved for pharmaceuticals with low removal efficiency in the ozonation process and the contact time for the removal of these pharmaceuticals was observed to be shortened by the addition of H_2O_2 to the ozonation process. The UV/O_3 process showed a removal efficiency of more than 90% for most of the pharmaceuticals, with improved degradation of 89 and 99% for cyclophosphamide and clofibric acid, 39 and 43% removal respectively in the ozonation process. Apart from the improved efficiency of the O_3/H_2O_2 and O_3/UV processes, bromate formation in the system was limited due to the reduction of residual concentration of dissolved ozone.

3.4 Photocatalysis

Photocatalysis has recently gained much attention in environmental application due to its high potential in eliminating hazardous contaminants, while upholding the principle of sustainable chemistry. Photocatalysis works on a simple basic principle involving the harnessing of energy from a light source, which is then used in the breaking down of substances (Mueller *et al.*, 2010). Photo-enhanced photocatalytic processes usually involve three components: a light source, a catalyst and an oxidant (Ortiz *et al.,* 2019). The main difference between photochemical AOP and photocatalytic AOP is the presence of the catalyst, which undergoes a cyclic reaction and is regenerated in the process. Depending on the phase of the catalyst relative to the reaction system, catalysis is usually classified as either homogeneous or heterogeneous catalysis. While homogeneous catalysis involves processes in which the catalyst is in the same phase with the reaction system, the catalyst is in a different phase in heterogeneous catalysis. In AOPs, the photo-Fenton process is a homogeneous process employing Fe^{2+} as the catalyst and H_2O_2 as the oxidants. Heterogeneous photocatalytic AOPs usually involve semiconductors like TiO_2, ZnO, ZrO_2 etc as catalysts, with oxygen on the surface of the catalyst acting as the oxidant. Recently heterogeneous Photon-Fenton processes which involve incorporating Fe into a solid matrix have been developed. The photon-Fenton process has been expanded to include the use of alternative transition metals with oxidants in a process often referred to as Fenton-like process (Bandala *et al.*, 2008).

3.4.1 Semiconductor photocatalytic process

Semiconductor photocatalysis is the most explored AOP for the degradation of contaminants of emerging concerns. The process was initially employed for the photo-initiation of water splitting on TiO_2 electrodes before its application was later extended to other redox processes in a wide range of organic and inorganic systems (Calvete *et al.*, 2019). The risk of generation of any secondary pollutant is limited in semiconductor photocatalysis as the process does not require the use of any chemical or gas and the process' oxidation capacity is adequate for the degradation of most recalcitrant pollutants to simpler molecules (Khan *et al.*, 2015b).

Fig 4 shows the basic mechanism of action of a photocatalyst. The general mechanism for the semiconductor photocatalytic process follows Eq. 14-22. It initiates with the absorption of light energy (usually in the UV or visible region of the electromagnetic spectrum) by a photocatalyst, with equal or greater energy than its bandgap leading to the formation of electron (e^-)/hole(h^+) pair, which dissociates into positively charged holes (h^+) and negatively charged electrons (e^-) in the valence band (VB) and conduction band (CB) of the photocatalyst respectively (Eq. 14).

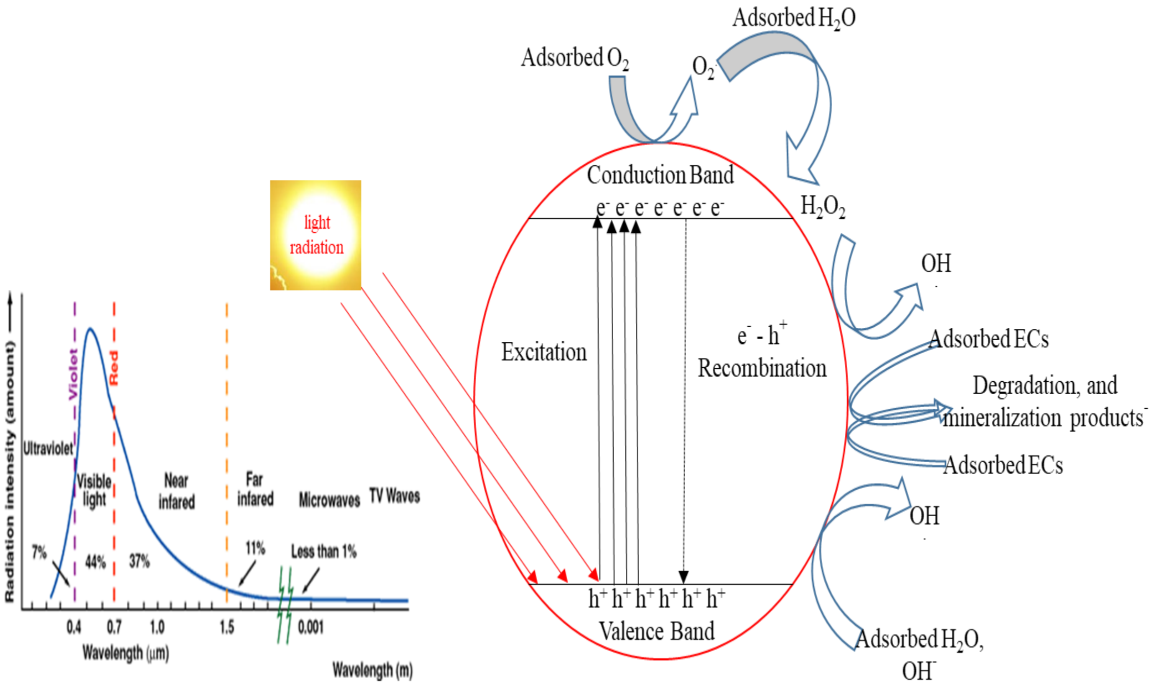

Fig 4: Mechanism of action of a semiconductor photocatalyst.

The generated hole possesses a high oxidation potential and produces hydroxy radicals from adsorbed water or hydroxy ion on the semiconductor surface (Eq. 15-16)). The electrons also contribute to the generation of radical species by reducing dissolved O_2 to produce superoxide radical ion ($O_2^{\cdot-}$), which subsequently reacts with H_2O to produce H_2O_2 (Eq. 17-19). The H_2O_2 generates more $^{\bullet}OH$ by acting as electron acceptor (Eq. 20). The adsorbed contaminants (ECs) are then degraded either by the photogenerated h^+ or by the generated $^{\bullet}OH$ at the surface of the photocatalyst to produce degradation products or the ultimate degradation products which are CO_2 and H_2O (Eq. 21-22)

$$SP \overset{hv}{\rightarrow} SP(e^- + h^+) \tag{14}$$

$$SP_{surf}(h^+) + H_2O_{ads} \longrightarrow SP_{surf} + {}^{\bullet}OH_{ads} + H^+ \tag{15}$$

$$SP_{surf}(h^+) + HO^- \longrightarrow SP_{Surf} + {}^{\bullet}OH_{ads} \tag{16}$$

$$SP(e^-) + O_2 \longrightarrow SP + O_2^{\bullet -} \tag{17}$$

$$O_2^{\bullet -} + H_2O \longrightarrow {}^{\bullet}HO_2 + HO^- \tag{18}$$

$$2{}^{\bullet}HO_2 \longrightarrow H_2O_2 + O_2 \tag{19}$$

$$SP(e^-) + H_2O_2 \longrightarrow SP_{surf} + HO^- + {}^{\bullet}OH \tag{20}$$

$$SP(h^+) + EC_{ads} \longrightarrow SP + EC_{ads}^{+} \tag{21}$$

$${}^{\bullet}OH + EC \longrightarrow degradation\, products\ (CO_2, H_2O\ and\ intermediates) \tag{22}$$

Based on this outlined mechanism of action, it is therefore desirable that electron-hole pair recombination is reduced to the minimum in a photocatalyst and also the complete mineralization of the target pollutant be achieved. High catalytic activity at ambient temperature, ultra-bandgap energy, reaction initiation by oxygen, ease of compositing into heterostructures, economic viability, stability and environmental friendliness are also an important factor being considered in the development of photocatalysts (Ahmed and Haider, 2018).

According to Anwer *et al.* (2019) three generations of photocatalysts have been identified (Fig. 5). The first generation of photocatalysts are the single component catalytic materials like ZnO, TiO_2 and CdS, while multi-component photocatalyst like C_3N_4/Ag_3VO_4, $WO_3/NiWO_4$ and $BiOI/ZnTiO_3$ belong to the second generation of photocatalysts. The third generation of photocatalysts are the supported catalysts like Glass/P-TiO_2 and FTO/WO_3-ZnO. The first generation of catalysts are large bandgap semiconductors, with single conduction and valence band. Thus, UV radiation is needed for electron-hole generation and the probability of recombination of the generated charge carriers is very high, which limits the quantity of ROS generated for pollutant degradation (Tahir and Amin, 2015). In the second generation of photocatalysts, charge carrier recombination is suppressed due to the large spatial separation between the conduction and the valence bands, achieved by the localization of the electron in one component, while the holes are localized in the other component (Etacheri *et al.*, 2013, Yan *et al.*, 2016). The second generation photocatalysts also possess lower bandgaps compared to the first generation, with absorbance most often within the visible range of the electromagnetic spectrum. The low band gap allows for the potential use of direct radiation from the sun. The third generation of photocatalysts were developed to address the additional cost incurred due to difficulty associated with separation of the catalyst from suspension and need for increased stability to enhance greater recycling/reuse of the photocatalyst. These drawbacks are circumvented by immobilising first and second generation on support materials such as graphene, glass, graphene oxide and polymers. The immobilisation can be achieved either through a binder or binder-less route (Robert *et al.*, 2013).

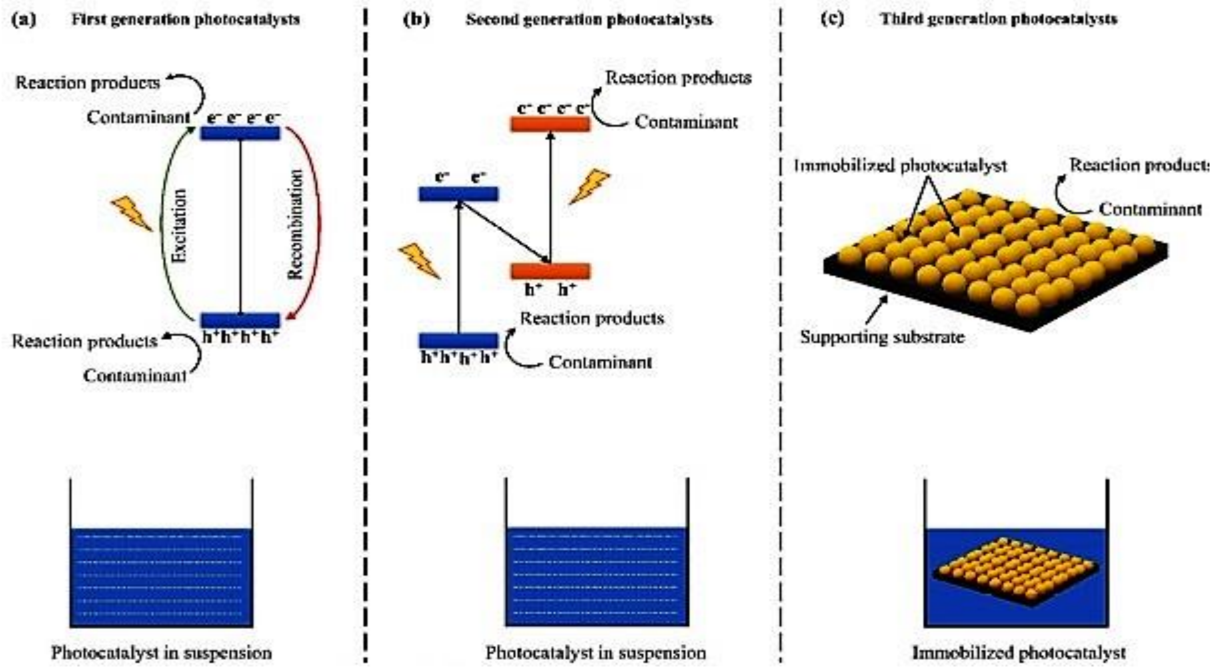

Fig 5: Schematic representation of the three generations of photocatalysts. Reprinted by permission from Springer Nature (Anwer *et al.*, 2019)

The development of photocatalytic materials has been greatly spurred and also advanced by the field of nanotechnology. The development of nanomaterials has given access to numerous synthetic materials with optical properties that were previously the monopoly of few naturally existing elements such as germanium and silicon. Numerous materials such as metals, metal sulphides (Regulacio and Han, 2016), metal oxides, metal nitrides, carbon-based structures (Mestre and Carvalho, 2019), metal-organic frameworks (MOFs) (Salimi *et al.*, 2019), dendrimers and heterostructures (Zhao *et al.*, 2019) have been explored as photocatalysts for degradation of emerging contaminants. The effectiveness of a novel Co_3O_4/WO_3 nanocomposite photocatalyst for the degradation of ethylparaben was studied and the effect of process parameters and radical scavengers also evaluated (Ngigi *et al.*, 2019). The composite showed a higher activity than the individual components, with efficiencies of 88, 70 and 60% reported for

Co_3O_4/WO_3, WO_3 and Co_3WO_4 respectively achieved after 15 min. In the presence of humic acid, the activity of the catalyst was significantly reduced due to reduction in light penetration and competition of humic acid for the catalysts active site. The presence of NO_3^-, however, enhanced the photocatalytic activity of the nanocomposite. The effect of radical scavengers on the process confirmed that $^{\bullet}OH$ was the most significant radical in the process followed by O_2^-, and h^+ was the least active specie in the process.

A solar light driven photocatalyst for the degradation of cefixime was prepared by decorating the metal organic framework MIL-125 (Ti)-mixed linker with g-C_3N_4 (Salimi *et al.*, 2019). The study showed that a degradation efficiency of 98% was achieved for the process at optimum conditions despite the reduction in the surface area of the MIL-125(Ti) MOF after the incorporation of g-C_3N_4. Photoluminescence and photoelectrochemical analysis confirmed a higher charge separation efficiency and also increased photocurrent response by the composite than the pure MOF and g-C_3N_4. Also, Bisphenol A (BPA) was successfully degraded under visible light radiation by a novel bismuth oxychloride nanosheet catalyst ($Bi_{12}O_{15}Cl_6$) (Wang *et al.*, 2016). The photocatalytic activity of the nanosheet was closely related to its band structure. The bandgap of the nanosheet was estimated from the UV-Vis spectroscopy to be 2.36 eV, a relatively lower value compared to the bandgap energy of 3.37 eV reported for BiOCl, a more common bismuth oxychloride. The degradation study showed that while almost complete degradation was achieved after 6 h with $Bi_{12}O_{15}Cl_6$, only 10% and 20% degradation was reported for BiOCl and TiO_2 catalyst. Kinetics studies showed that the rate constant for degradation activity of $Bi_{12}O_{15}Cl_6$ was 0.368 h^{-1} with a surface area normalized activity of 0.0497 g h^{-1} m^{-2} compared to 0.0046 and 0.0001 g $h^{-1}m^{-2}$ reported for BiOCl and TiO_2 respectively. The photocatalytic activity of another bismuth-based nanocomposite g-$C_3N_4/Bi_2O_2CO_3$ with varied amount of g-C_3N_4 was reported by Zhao *et al.* (2019) using tetracycline (TC), oxytetracycline (OTC) and tetracycline hydrochloride (TC.HC) as test pollutants. The photocatalytic activity of the prepared nanocomposites was found to depend greatly on the weight composition of g-C_3N_4, with the optimum weight composition achieved at 10 w%. At lower weight percent composition, the activity of the nanocomposite was not as much as that of the bare $Bi_2O_2CO_3$, but increased with increase in the weight percent of g-C_3N_4 until a plateau was reached. This was attributed to the inability of the g-C_3N_4 to facilitate charge separation at lower concentration at the interface between the two compounds. Above the optimum 10% composition, a reduction in photoactivity was recorded, which was ascribed to limitation in H_2O diffusion to the $Bi_2O_2CO_3$ surface at high g-C_3N_4 composition resulting in low generation of $^{\bullet}OH$.

4.0 Copper-based ternary sulphide semiconductors (CBTS)

Ternary metal sulphides nanomaterials have become subject of great interest for researchers in the field of nanotechnology and material science. This is due to their unique structural, chemical and physical characteristics, which have made them potential materials in numerous optoelectronic devices including sensors, biomarkers, superconductors, solar cells and also as photocatalysts and sensitizers. They are formed by substituting the metal in the binary system with two metals while still maintaining equal total charge (Matthews *et al.*, 2017a). Compared to binary compounds, the addition of a third element makes ternary sulphides more interesting due to increased stoichiometric variation, access to inaccessible band gaps and synergistic effect (Gao *et al.*, 2018). For instance the performance of $CuFeS_2$ nanosheet was reported to be much higher than those of FeS_2 and CuS in the hydrogen evolution reaction (Li *et al.*, 2017). A wide variety of ternary metal sulphides have been identified; however, CBTS have gained more attention because of its abundance and low toxicity.

4.1 Earth abundant copper-based ternary sulphides (CBTS)

CBTS compounds are obtained by incorporating transition metals (Ga, Zn, Cr, Fe) or main-group metals (In, Sn, Bi, Sb) into binary CuS system, resulting in wide variety of stoichiometries. Although diamond-like structure is the main crystal structure in Cu ternary chalcogenides, the lower enthalpy of formation of defects pairs like $2Cu_{In}^{2-}$ + In_{Cu}^{2+} and $2V_{Cu}^{-}$ + In_{Cu}^{2+} accounts for the occurrence of ordered non-stoichiometric compounds like $CuIn_3S_5$, $CuIn_5S_8$, and $CuIn_7S_{11}$ (Coughlan *et al.*, 2017). CBTS can be classified on the basis of the position of the second metal in the periodic table. Identified classes include: group I-III-VI_2, group I-IV-VI, and group I-V-VI. The main advantage of these materials is that their morphology, crystal structure, size, stoichiometry and thus applications can be controlled through synthesis conditions like precursor type and ratio, temperature, capping agent/solvent and the time of reaction. Numerous ternary copper-based metal sulphide (CMS) semiconductors incorporating different metals have been synthesized such as shown in Fig 6 (Chiang *et al.*, 2018, Liu *et al.*, 2016b). However, interests are more on ternary copper-based metal sulphides of earth-abundant elements as semiconductor materials as they are the most probable economic alternatives for current materials which are often composed of costly and sometimes toxic elements. This has aroused the interests in Cu-M-S of tin, bismuth and antimony and their numerous phases. Due to the variable oxidation states of Cu (I or II) and M (Sb/Bi: III or V; Sn: II or IV) and the different possible coordination environments of Cu and M (CuS_n and MS_n, n = 3, 4), Cu-M-S semiconductors is comprised of a large group of crystalline structural phase (Wang *et al.*, 2018)

.

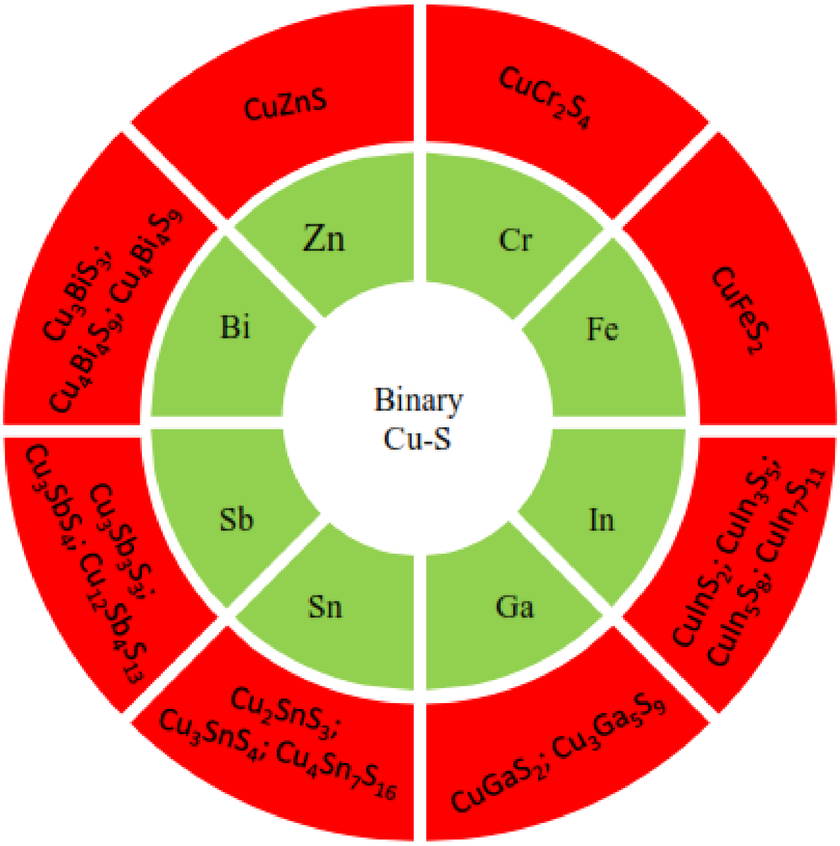

Fig 6: Copper-based ternary metal sulphides and their different stoichiometric phases.

Ternary copper-based sulphides of main-group metals have recently become subject of intense research as semiconductor materials for numerous applications. One advantage of this class of materials is that it allows for the incorporation of two earth-abundant and non-toxic element into the composition of these materials. This makes Cu-M-S of tin (CTS), antimony (CAS) and bismuth (CBS) most sort after semiconductor materials. Apart from this advantage, the ability of these materials to exist in different stoichiometric phases with unique optical and electronic properties has further fuelled the interest in developing synthetic routes to obtain the different phases and explore their application in numerous fields. The need for the development of semiconductor materials with high absorption coefficient and band gap in the 1.0-1.5 eV range from cheap and earthly abundant elements, which are among the main criteria for a semiconductor material has spurred the interest in the synthesis of copper-based ternary sulphides and the potential exertion of phase control gives the opportunity to access ternary semiconductors that meet this criteria for photovoltaic applications (Matthews *et al.*, 2017b). These materials are synthesized using different synthetic methods which include solvothermal synthesis (Manimozhi *et al.*, 2018), hydrothermal synthesis (Hu *et al.*, 2003), chemical vapour deposition (Deshmukh *et al.*, 2018), microwave-assisted synthesis (Aup-Ngoen *et al.*, 2011), co-evaporation (Kanai *et al.*, 2015), thermal decomposition (Deng *et al.*, 2014), electrodeposition, and spray pyrolysis (Liu *et al.*, 2015).

4.1.1 Copper antimony sulphide (CAS)

Copper antimony sulphide (CAS) is the most studied group of the earth abundant copper-based ternary metal sulphides and the variety of stoichiometries is not large compare to other groups. They are all p-type materials with high absorption coefficients higher than 10^5 cm^{-1} and band gaps within the range of 1.1-1.8 eV (Xu *et al.*, 2013, Qiu *et al.*, 2013, Yang *et al.*, 2014). Theoretical studies have shown that the shallow defect of copper vacancy (V_{cu}), which has the lowest formation energy compared to other acceptor defects like Cu_{Sb} (Cu on Sb antisite) and donor defects like Sb_{Cu} and Cu_i (copper interstitial) is responsible for the p-type conductivity of CAS, because the influence of other defects is minimized by their higher formation energy (Yang *et al.*, 2014, Krishnan *et al.*, 2015). The presence of deep donor level of sulphur vacancy (Vs) in Sb-rich, S-poor and Cu-rich structures have also been observed, but its influence on conductivity is minimized because it cannot generate free electron carriers due to its ionization level being far from the conduction band. However, because V_{Cu} is a shallow acceptor, it can ionize easily at room temperature to generate free hole carries. This accounts for why CAS structures are p-type semiconductors either under S-poor or S-rich conditions (Krishnan *et al.*, 2015, Yang *et al.*, 2014). Four stoichiometries have been identified, which are $CuSbS_2$ (chalcostibite), Cu_3SbS_3 (skinnerite), $CuSbS_4$ (famatinite) and $Cu_{12}Sb_4S_{13}$ (tetrahedrite). According to the ionic mode, ternary Cu-M-S compounds of the form Cu-V-VI can be classified as either high valence (Cu-V^{5+}-VI) or low-valence (Cu-V^{3+}-VI) base on the oxidation state of the V-group atom. While Cu_3SbS_4 is in the high-valence group, the other stoichiometric phases are classified in the low-valence group. A major difference between the low valence and the high valence compounds is that the s(V) orbitals of the group V atom, contribute largely to the conduction band state than the valence band states but for low-valence compounds the p(V) orbitals contribute largely (Shi *et al.*, 2013, Yu *et al.*, 2013). Fig. 7 shows the crystal structure of Cu_3SbS_4, $CuSbS_2$, Cu_3SbS_3 and $Cu_{12}Sb_4S_{13}$.

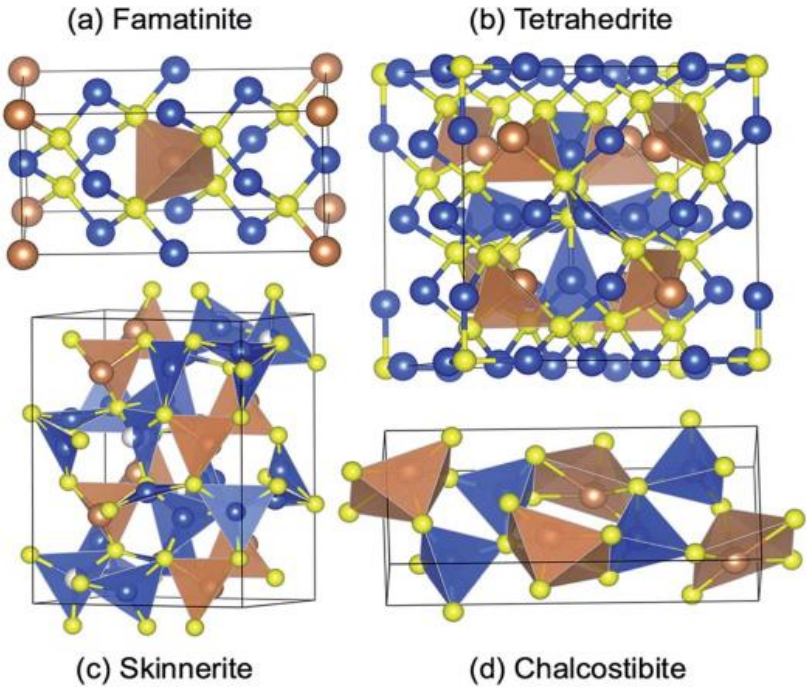

Fig 7: Crystal structure of (a) famentinite (b) tetrahedrite (c) skinnerite and (d) chalcostibite. Sulphur is represented by the small yellow ball, Cu by the medium size blue balls and antimony is represented by the large brown balls. Adapted with permission from Royal Society of Chemistry (Du *et al.*, 2017)

$CuSbS_2$ exhibits an orthorhombic layered crystal structure, with a unit cell comprising of 4 Cu, 4 Sb and 8 S atoms to make a total of 16 atoms per unit cell. The Sb and Cu cation shows a coordination number of four and five respectively in relation to neighbouring S anions (Kumar and Persson, 2013b). The crystal lattice parameters are a = 6.045 Å, b = 3.807 Å and c = 14.545 Å with space group *Pnma* (no 62). Its layered structure accounts for its high structural stability, enhanced characteristic charge transport and good interfacial property compare to other CAS stoichiometries (Krishnan *et al.*, 2015). Analysis of the electronic properties of $CuSbS_2$ showed that its valence band is composed mainly of Cu-3d and S-3p, closely related to what is obtainable in many Cu-S based materials like copper indium gallium sulphide (CIGS) and copper zinc tin selenide (CZTSe), while the conduction band is composed of Sb-p states (Persson, 2010, Kumar and Persson, 2013b). The strong localization of the p-like state of trivalent cations is responsible for the higher sharpness of the top of the conduction band of $CuSbS_2$ compared to those of other Cu-S based compounds which have more broadened conduction band. This accounts for its strong absorption coefficient.

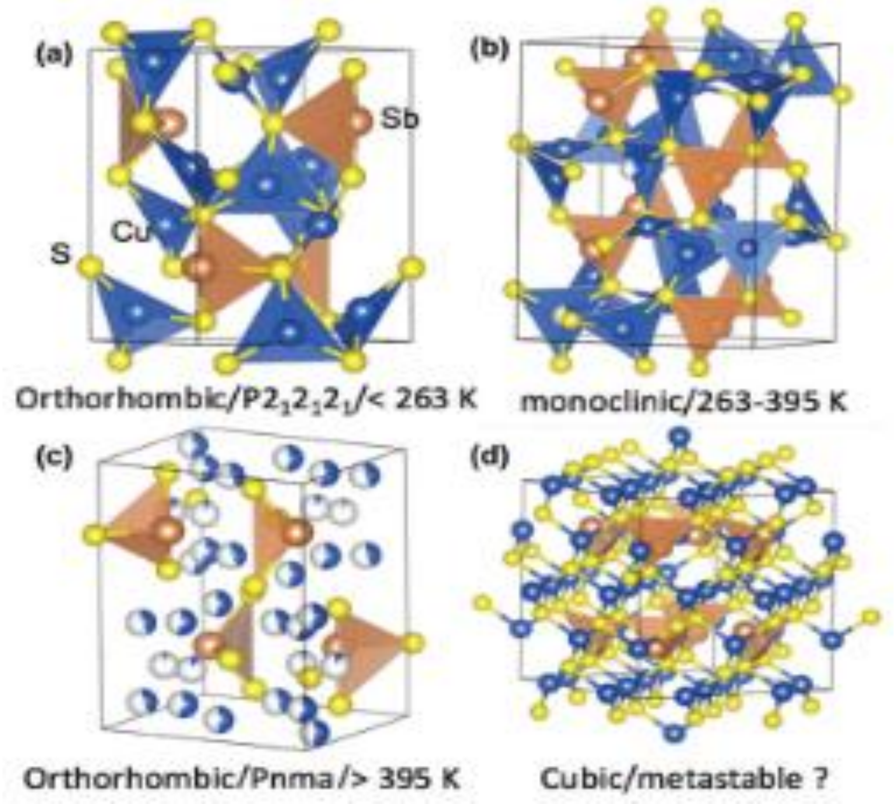

Fig 8: Temperature dependent crystal structures of Cu_3SbS_3 (a)Wittichenite (b) skinnerite (c) orthorhombic and (d) cubic. Sulphur is represented by small balls, Copper by medium sized balls and antimony is represented by large balls (Du *et al.*, 2019)

Cu_3SbS_3 is the least studied member of CAS group despite its high potential as a thermoelectric material due to its high vibrational anharmonicity. However, its temperature dependent crystal structure means that it undergoes phase transitions within some working temperature range. Fig.8 shows the temperature dependent polymorphs of Cu_3SbS_3. The wittichenite-type orthorhombic crystal structure has a space group $P2_12_12_1$ with lattice parameter a =7.884 Å, b = 10.221Å, c = 6.624Å; and is only stable at temperatures below 263 K. In this structure the Sb exhibits three-fold coordination with three S atoms forming a SbS_3 pyramidal unit, while Cu coordination is in a distorted trigonal plane comprising of three S atoms. At temperatures above 395 K, Cu_3SbS_3 crystallizes in an orthorhombic structure, with *Pnma* space group and lattice parameters a= 7.808 Å, b = 10.252 Å and c = 6.587. Between 263 and 395 K, a slight distortion of the CuS_3 trigonal plane, results in the monoclinic skinnerite structure with $P2_1/c$ space group and lattice parameters a= 7.808 Å, b = 10.233 Å, c = 13.268 Å and β = 90.31˚ (Du *et al.*, 2019, Kehoe *et al.*, 2013). The cubic crystal structure with space group $1\bar{4}3m$ has also been suggested as a probable phase for Cu_3SbS_3 (Jiasong *et al.*, 2010). The phase is similar to the tetrahedrite phase, but lacks the central S atom in the unit cell. The stable temperature range for this phase is yet to be identified (Du *et al.*, 2019). The absence of a central S atom in the cubic structure of Cu_3SbS_3 makes it unstable and an attempt to stabilize the structure has been made by incorporating group IIIA elements or trivalent transition metals of group VIII as substitutional dopants. This alters the bonding environments in the compound as the substituted sites form sp^3 hybridization due to difference in valence number between the dopant and Sb (Du *et al.*, 2019). Evaluation of the electronic properties of Cu_3SbS_3 revealed that the valence band is composed mainly of Cu-d, Sb-p and S-p states, while the conduction band comprises mainly of Sb-p and S-p states. Small amount of Sb-s states is present at the bottom of the valence band but cannot interact with the Sb-p states because of their low energy. However, the Sb-s states can mix with the Sb-p states by forming filled antibonding states at the top of the VB when mixed with the S-p states. This generates lone pair states on the Sb ion, which accounts for the anisotropic charge distribution surrounding the Sb atoms (Kehoe *et al.*, 2013).

Cu_3SbS_4 (famatinite) has a simple crystal structure compared to other members of the CAS family as shown in Fig 9(a). It crystallizes in the ordered zinc-blende superstructure with space group $1\bar{4}2m$ (no.121) and lattice parameters a = b =5.39 Å and c = 10.764 Å (Pfitzner and Reiser, 2002). In the crystal lattice two non-equivalent Cu atoms Cu (1) and Cu (2) and Sb forms CuS_4 and SbS_4 tetrahedrons by coordinating with four nearest S atoms as shown in Fig 9(b), thus no lone pair electron is present in Cu_3SbS_4 since all the outer shell electrons of Sb are involved in bonding (Crespo, 2016). This accounts for its high thermal conductivity and impacts on its applicability in processes requiring low intrinsic thermal conductivity. The electronic structure of Cu_3SbS_4, shows a VB that is comprised of mainly Cu-d states and a lower S-p state while the CB states are obtained mainly from Sb-s and S-p states (Crespo, 2016).

$Cu_{12}Sb_4S_{12}$ (tetrahedrite) possess a body centred cubic crystal lattice with space group $1\bar{4}3m$ and lattice parameter a = 10.33 Å. $Cu_{12}Sb_4S_{13}$ can somewhat be described as a S-rich crystal of stoichiometric Cu_3SbS_3 and its molecular formula is sometimes written as $Cu_3SbS_{3.25}$. Tetrahedrite comprises of two non-equivalent copper atoms Cu (1) and Cu (2) and two non-equivalent S atoms S (1) and S (2). While Cu (1) is tetrahedrally coordinated to S atoms, Cu (2) is triangularly coordinated. The S (1) trigonally coordinates to 3 Cu and 1 Sb atoms while S (2) coordinates octahedrally to 1 Cu atom. The Sb atoms coordinates trigonally to S (1).

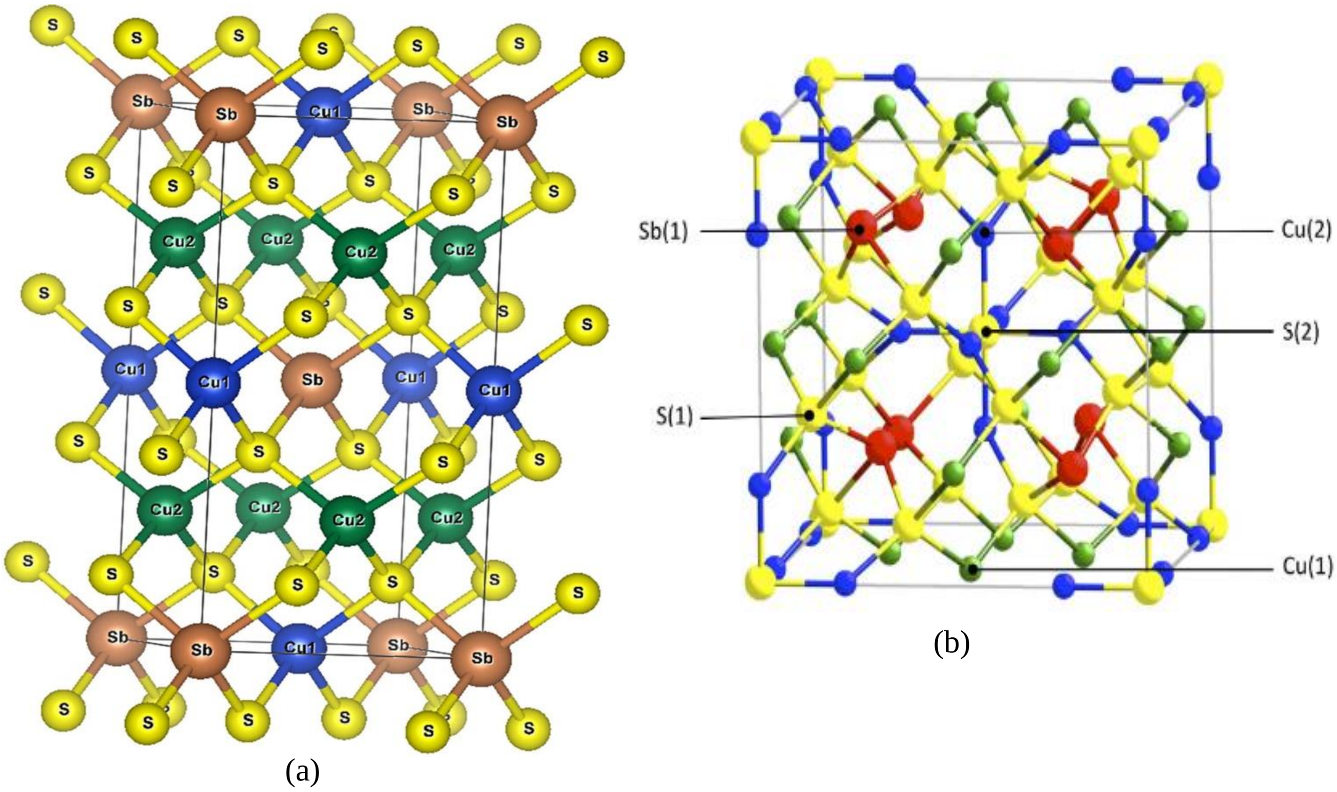

(a)

(b)

Fig 9: (a) Crystal structure of Cu_3SbS_4 showing the non-equivalent Cu atoms Cu(1) and Cu (2) and Sb tetrahedrally bonded to four S atoms. Reproduced with permission from (Crespo, 2016) (b)The crystal structure of tetrahedrite unit cell showing the Cu (1) triangularly coordinated to S (1); Cu (2) tetrahedrally coordinated to S (2) and Sb trigonally coordinated to S (1). Adapted with permission from van Embden *et al.* (2013)

4.1.2 Copper bismuth sulphide (CBS)

Ternary copper bismuth sulphides are an interesting class of materials as solar absorbers in photovoltaic devices, though it has not received much attention as other earth abundant copper-based ternary sulphides. Numerous stoichiometries with unique properties have been identified, however the most studied compounds in the class are- $CuBiS_2$ (emplectite), Cu_3BiS_3 (wittichenite) and $Cu_4Bi_4S_9$. These compounds are p-type semiconductors; crystallize in an orthorhombic crystal structure and show high absorption coefficients in the range of $10^4 – 10^5$ cm^{-1} (Miller and Bernechea, 2018).

$CuBiS_2$ and $CuSbS_2$ are isostructural compounds and thus share a lot of similarity structurally. It crystallizes in the orthorhombic crystal phase, space group *pnma* and lattice parameters a = 6.134, b = 3.9111 and c = 14.548 Å. Like $CuSbS_2$, the crystal comprises of square pyramids of BiS_5 and nearly regular tetrahedral CuS_4. However, the bond length in the $CuBiS_2$ square pyramid is usually longer than those of $CuSbS_2$, because of the bigger size of Bi atom compared to Sb atom. The larger lattice parameters of $CuBiS_2$ is also due to the influence of the longer bond length in the BiS_5 square pyramida and the larger Cu-S_2-Cu bond angles (Kyono and Kimata, 2005). The electronic band structure of both analogues are also similar with the main difference being the position of the VB maxima and CB minima (Kumar and Persson, 2013b). The VB is composed mainly of Cu-3*d* and S-3*p* states while the CB is composed mainly of Bi-*p* states.

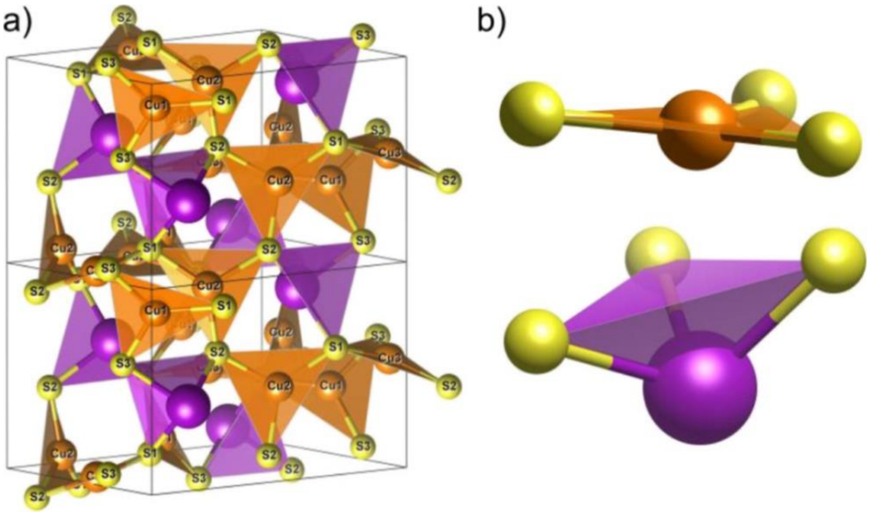

Fig 10: (a) Crystal structure of Cu_3BiS_3. Orange, purple and yellow balls represent Cu, Bi and S atoms respectively. Inequivalent Cu and S sites are denoted by numbers (b) The BiS_3 and CuS_3 structural units.

Cu_3BiS_3 is the bismuth analogue of Cu_3SbS_3. It crystallizes in the orthorhombic crystal phase with space group $P2_12_12_1$ (no 19) shown in fig.10(a). The structural unit of the crystal lattice of Cu_3BiS_3 is composed of Bi atoms with threefold coordination to S atom to form distorted tetrahedral BiS_3 units, with Bi positioned at one of the tetrahedron's vortex, in a manner similar to the single coordination environment observed in Bi_2S_3 (Caracas and Gonze, 2005). The Cu atom also possesses a threefold coordination to S, but forms a highly irregular tetrahedra, near-planer distorted trigonal CuS_3, similar to those in low chalcocite Cu_2S (Whittles *et al.*, 2019). Despite the occupation of three different lattice sites by both Cu and S, there is only a slight variation in the bond length and bond angle, but the coordination number remain unchanged. The unit cell of Cu_3BiS_3 is made up of 12 Cu atoms, 4 Bi atoms and 12 S atoms, to give a total of 28 atoms per unit cell (Kumar and Persson, 2013a). The VB of Cu_3BiS_3 consist mainly of Cu-3*d* and S-3*p* alongside a negligible contribution from Bi-6*p*, while the CB comprises mainly of Bi-6*p*, though Bi-6*p*/S-3*p* hybridized state may also be present. Cu_3BiS_3 possesses a large absorption coefficient due to the formation of a flat energy band by the localized Bi-

6*p* states in the CB, which results in increased absorption coefficient of photons in the low energy region (Kumar and Persson, 2013a).

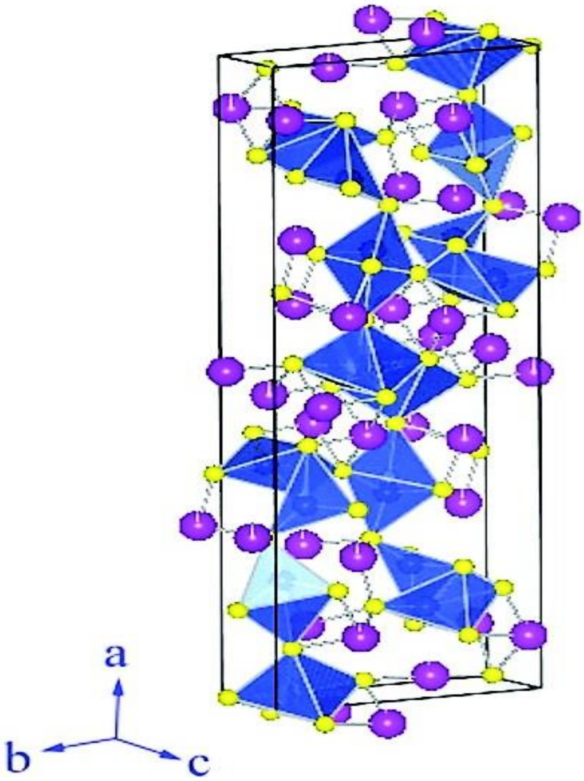

Fig 11: Unit cell structure of $Cu_4Bi_4S_9$. Big purple ball represents Bi, blue medium balls represent Cu and small yellow balls represent S. Reprinted with permission from Li *et al.* (2011).

$Cu_4Bi_4S_9$ is a phase of CBS that has only received limited research attention. It crystallizes in the orthorhombic crystal structure as shown in Fig. 11, with space group *pbnm* and cell parameters a = 31.528 Å, b = 11.622 Å, c = 3.95 (Li *et al.*, 2011). The large unit cells and relatively complex crystal structure of $Cu_4Bi_4S_9$ makes them compounds of interest for technologies requiring intrinsically low thermal conductivity like rewriteable data storage and thermal barrier coatings (Hobbis *et al.*, 2020, Cho *et al.*, 2013). X-ray photoelectron spectroscopic study of $Cu_4Bi_4S_9$ showed that Cu and Bi atoms in the lattice were in the +1 and +3 oxidation states respectively (Li *et al.*, 2014a). Pressure-induced phase transition study of Cu_4Bi4S_9 single crystal shows that the compound undergoes lattice compression within pressure range of 0.03-9.17 GPa, while at 14.5 GPa a change of phase was observed. At 25.6 GPa a pressure-induced reversible amorphization of the crystal was observed (Hu *et al.*, 2013).

4.1.3 Copper tin sulphides (CTS)

CTS belongs to the I-IV-VI group of Cu-M-S compounds and are considered as low-cost, earth-abundant and potential photovoltaic absorbers due to their excellent optoelectronic properties. Copper tin sulphides (CTS) are p-type semiconductors, with electronic structure comprising of Cu 3d and S 3*p* components in the valence band maximum (VBM) and Sn 5*s* and S 3*p* components in the conduction band minimum (CBM) (Xi *et al.*, 2012). The p-type conductivity arises from defects which can be due to vacancies, cation-cation disorders, cation-anion disorders or intrinsic defects (Lokhande *et al.*, 2019). Based on the Cu/Sn ratio, the structure of CTS formed can be influenced to give Cu rich compositions like Cu_3SnS_4, Cu_2SnS_3 and Cu_4SnS_4 phases or Cu deficient compositions like $Cu_4Sn_7S_{16}$. Of the reported CTS stoichiometries, Cu_2SnS_3 is the most explored because of its phase dependent band gap range of 0.95 - 1.5 eV, which lies within the maximum radiation range of the solar spectrum (Zhai *et al.*, 2011). As shown in Fig. 12 bulk Cu_2SnS_3 can crystallize at low temperature (below 780 ˚C) in the monoclinic (*Cc*), tetragonal (*1-42m*) and triclinic (*P1*) phase while at temperatures above 780 ˚C it can crystallize in the wurtzite (or metastable zincblende phase) (Chen *et al.*, 2003, Onoda *et al.*, 2000). For nanoscale Cu_2SnS_3, the wurtzite and zincblende crystal structures are also accessible even at low temperatures (Liu *et al.*, 2011). The band gap for each structure also varies slightly with the monoclinic, triclinic, cubic and tetragonal structures showing band gaps of 0.93, 0.95, 0.98-1.15 and 1.35 eV respectively (Zhai *et al.*, 2011, Berg *et al.*, 2012).

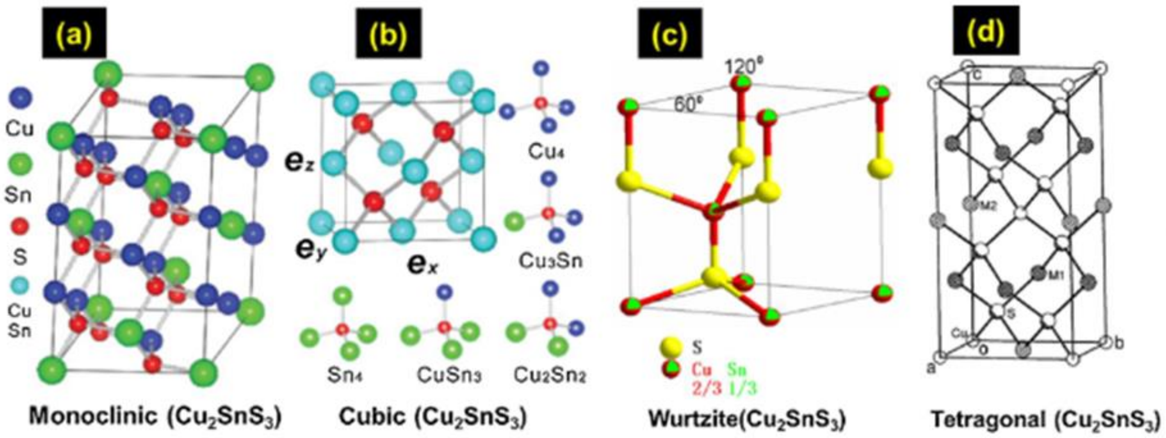

Fig 12: Crystal structures of Cu_2SnS_3. Reprinted with permission from Pejjai *et al.* (2018)

In Cu_2SnS_3 crystal structures the S atom is tetrahedrally coordinated to four cations and atomic layers are connected by perpendicular bonds. In general, the basic structure of all the stable phases of Cu_2SnS_3 are superstructures of the zinc-blende phase with S atoms surrounded by cation clusters of Cu_3Sn and Cu_2Sn_2 which occupies the fcc sublattice of the zinc-blende structure (Zhai *et al.*, 2011). These cation clusters possess low and closely degenerate energies, which results in partial and long-range disordering of Cu and Sn atoms in the cation sublattice.

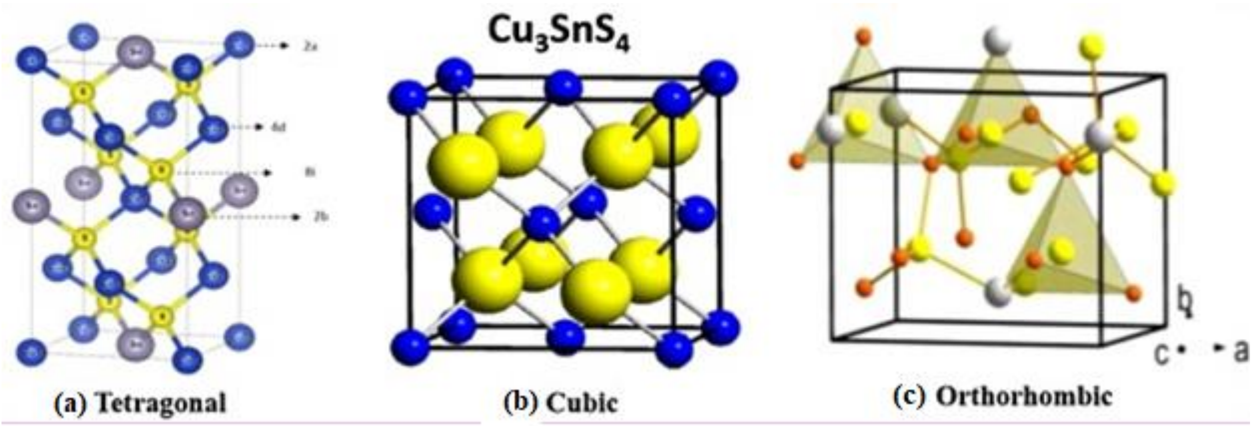

(a) Tetragonal (b) Cubic (c) Orthorhombic

Fig 13: Polymorphs of Cu_3SnS_4. Adapted with permission from Minnam Reddy *et al.* (2019)

The Cu_3SnS_4 phase of CTS also exists in different polymorphs which are the tetragonal, cubic and orthorhombic structures as shown in Fig. 13 with space group of $1 - 42m$, $F - \bar{4}3m$ and pmn2_i respectively. In the tetragonal structure, there is full ordering of the cations and all atoms are tetrahedrally coordinated. Cu_3SnS_4 exhibits metallic properties with or without surface S vacancies, which accounts for its high conductivity and application in catalysis, quantum dot sensitized solar cells and lithium batteries (Chen *et al.*, 2017).

4.2 Synthesis of earth-abundant copper-based ternary sulphides

Several physical and chemical methods have been explored for the synthesis of 1D nanostructures. Some of these methods include vapor-liquid-solid processes, solution-liquid-solid processes, template-assisted synthesis, solvothermal/hydrothermal synthesis and single-source precursor thermolysis in ligating solvents. The solvothermal method is a powerful, low temperature route for controlled synthesis of 1D semiconductors. In this method, organic-ligand molecules such as alkylamines, alkyl thiols and fatty acids are used as high boiling solvents, reducing agents and surface capping agents to synthesize nanoscale inorganic semiconductors (Vykoukal *et al.*, 2019). The organic-ligand molecules possess both metal coordinating and solvophillic groups, via which they can selectively attach to crystallographic faces and impact dynamic control on the nanoscopic morphologies of the obtained product (Li *et al.*, 2011).

Solvothermal/hydrothermal synthesis may be considered as a special type of chemical transport reaction, which final product can be influenced by a variety of experimental factors (Sheldrick and Wachhold, 1997). The kinetics of the reaction is significantly impacted by the choice of reagents such as precursors, redox agents, surfactants and solvents and their concentration. The temperature profile also exerts significant influence, since the final products differ under varying reaction condition, the time and temperature of reactant addition to the reaction system is also of great importance (Wang *et al.*, 2018). In the solvothermal synthesis of earth-abundant copper-based ternary sulphides, two main precursor types have been explored: (i) combination of metal salt and sulphur precursors (ii) single molecular sources, which hold the metal source and sulphur source in a molecule.

Two synthetic approaches have been identified in the solvothermal synthesis of semiconductors, which could be either through the hot-injection or heat-up method. The hot-injection method involves the injection of organometallic precursors into hot organic solvents at temperatures usually above 150 ℃. Hot-injection method results in isolated crystalline nanoparticles and narrow particle size distribution which is important for energy level control, since optical and electronic properties are both size dependent. The hot-injection method also allows for better size control via injected precursor concentration and reaction temperature (Šutka *et al.*, 2018). This method is the most widely explored synthetic route for ternary copper-based metal sulphides. However, system conditions such as local concentration of precursors at the point of injection significantly affect ligand coordination which may influence reaction kinetics due to mixing dynamics (Deshmukh *et al.*, 2019). The alternative method to the hot-injection approach is the one pot heat-up method, which is a more scalable technique when compared to the hot-injection method (van Embden *et al.*, 2015). While the hot-injection method involves the rapid exposure of precursor to high temperature, the heat-up method employs a gradual exposure of the precursor to increasing temperature over an extended period of time. Though there is a similarity in the particle formation mechanism in both heat-up and hot-injection methods, there is the need for a proper understanding of the chemistry of both ligands and precursors in heat-up process in order for a rapid nucleation leading to the generation of large quantities of nuclei within a short time to be achieved. In addition, reduction in polydispersity by appropriately separating the nucleation stage from the growth stage is very important (van Embden *et al.*, 2015).

5.0 Graphene/Graphene derivatives

Graphene is regarded as the strongest, thinnest and lightest compound known till date. These properties are related to its structural features such as interlayer crosslinks arising either from covalent bonding between side atoms of different sheets or Van der Waals forces arising from interactions between carbon atoms of different layers of the graphene sheet. Also, intralayer forces, such as the sp^2 carbon-carbon covalent bonds and crosslinks occurring at the graphene sheet edges contribute to the unique properties of graphene and its derivatives. Graphene-based materials are therefore outstanding materials for catalyst support in catalysis as they improve the stability and surface area of the catalyst, which are important in bringing the pollutants closer to the catalyst surface where catalytic activities occur.

Perfect graphene has a zero bandgap, and this makes pristine graphene a perfect conductor with high conductivity. The zero band gap of graphene is due to the anti-bonding π^* orbitals and bonding π degenerate orbital that meets at the Brillouin zone corners (Putri *et al.*, 2015). Doping of graphene leads to the formation of band gap between the π^* and π orbital, thereby converting graphene into a semiconductor and creating more active sites for reactions. Large bandgaps could be achieved by high dopant concentration, thus improving the electrical property of graphene (Koe *et al.*, 2020, Rani and Jindal, 2013).

The electron arrangement in the graphene lattice is dominated by the s and p orbitals. However, low dispersibility, difficult recovery and ease of restacking are major drawbacks to its application. This informed the development of many strategies to modify it by incorporating several functional groups such as halogens, chalcogens, boron, nitrogen and phosphorus (Sturala *et al.*, 2018). Complex functional groups such as aryl and alkyl hydrocarbons have also been reportedly incorporated (Wang *et al.*, 2012). The methods of incorporating functional groups into graphene are shown in Fig. 14. The most studied functionalized graphene derivatives are graphene oxide (GO) and reduced graphene oxides (rGO), which are derivatives with poorly defined composition, that is strongly influenced by the synthesis method (Sturala *et al.*, 2018). The abundant amount of oxygen functionalities on the GO surface, coupled with other properties such as structural defects, and irregularity of heteroatoms makes them potential materials for specific applications. In graphene oxide, the electronic properties are strongly determined by its chemical structure (Kumar *et al.*, 2014). Compared to graphene, GO is hydrophilic and also an insulator by nature because of the presence of numerous surface hydroxyl (-OH), keto (C=O), epoxy (C-O-C) and carboxy (-COOH) groups (Zhang *et al.*, 2020). The formation of C-O bond significantly induces the local distortion of graphene, therefore altering the bonding character from planar sp^2 to partial sp^3 hybridization. By reducing GO, partial restoration of the intrinsic structural and electronic properties of graphene can be restored to produce rGO. However, the removal of oxygen-containing functionalities can lead to the rapid re-aggregation of rGO nanosheets into graphite (Han *et al.*, 2016). Considering an arrangement of epoxy functional groups in fully oxidized graphene sheet and the effect of epoxy arrangement on electronic properties, a significant induction of bandgap of 0.529 eV has been recorded (Ye *et al.*, 2001).

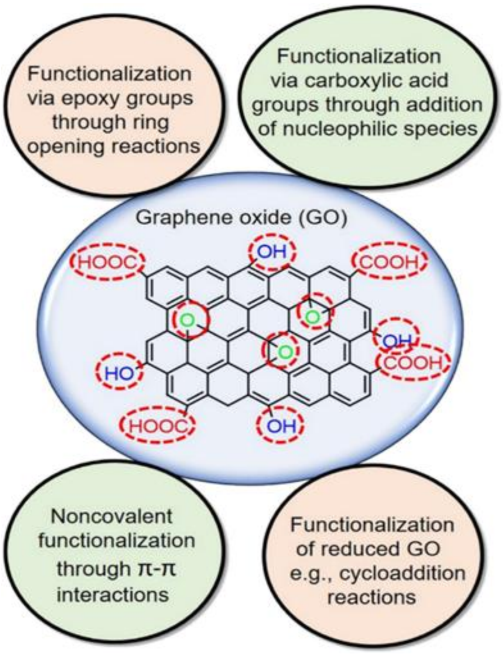

Fig 14: Different routes to graphene/graphene derivatives functionalization. Reproduced from Bilal *et al.* (2020). Copyright (2020) Elsevier.

5.1 Synthesis of graphene oxide and reduced graphene oxide

GO is widely employed in several applications because it is easy to synthesize, process and functionalize chemically. GO is generally prepared either by the Brodie, Staudenmaier, Hummers, Tours or by modified forms of any of these methods. All the methods involve the oxidation of graphite to varying levels. The wet-chemical oxidative process used to convert graphite into GO involves four steps: (i) intercalation of graphite, (ii) oxidation, (iii) oxidized sheets exfoliation, and (iv) impurity removal (Chen *et al.*, 2015, Dong *et al.*, 2017, Liu *et al.*, 2014, Morimoto *et al.*, 2016, Peng *et al.*, 2015, Pendolino *et al.*, 2015). The intercalation step involves the insertion of small molecules within the graphite layers. Alkali compounds such as $NaNO_3$ and $KClO_3$ are usually intercalated into the graphite layers, which is then subsequently oxidized by acids such as HNO_3, HCl and H_2SO_4. The properties of the final product are influenced by several factors such as graphite's nature and source, nature and concentration of hydrogen peroxide, oxidant, water and sulfuric acid and other parameters such as reaction time and temperature. The first reliable method for GO synthesis from graphite was reported in 1855 (Brodie, 1855). It involves the treatment of graphite with fuming HNO_3 and $KClO_3$. This method was improved on by using H_2SO_4 as additive and also the use of excess HNO_3 (Staudenmaier, 1898). This gave highly oxidized GO compared to the Brodie method within a shorter period of time. The widely used Hummer's method involves the treatment of graphite with $NaNO_3$, $KMnO_4$ and H_2SO_4.

Recently, the Tour's method as described by Marcano *et al.* (2010) introduced the use of H_3PO_4 as co-acids with H_2SO_4 and six equivalents of $KMnO_4$ as oxidant.

Electrochemical stripping of graphite is another well explored technique for GO synthesis. This method is a safe, pollution-free, and efficient technique involving no chemical oxidant and achievable within hours or sometimes minutes. It also offers ease of manipulating GO properties such as defect density and degree of oxidation by tuning the electrical process (Pei *et al.*, 2018, Muthoosamy and Manickam, 2017). The technique explores the conductivity of graphite to intercalate anions/molecules in the electrolyte under bias current or voltage. The GO is then obtained by ultrasonication of the graphite oxide formed through the oxidation of the graphite intercalation compound by oxygenated species produced by the electrolysis of water (Li *et al.*, 2020a). The mechanism of formation of graphene oxide via the electrochemical stripping process is shown in Fig. 15. The mechanism could either be anodic or cathodic based on the applied potential. In anodic process, electrons are withdrawn from the graphite electrode leading to the creation of positive charge, allowing for the intercalation of negative ions like sulfate anions. In cathodic process, negative charges created at the graphite electrode attract positively charge ions. Incorporation of these ions increases the interlayer spacing between the graphene sheets and enhances its exfoliation (Yu *et al.*, 2015).

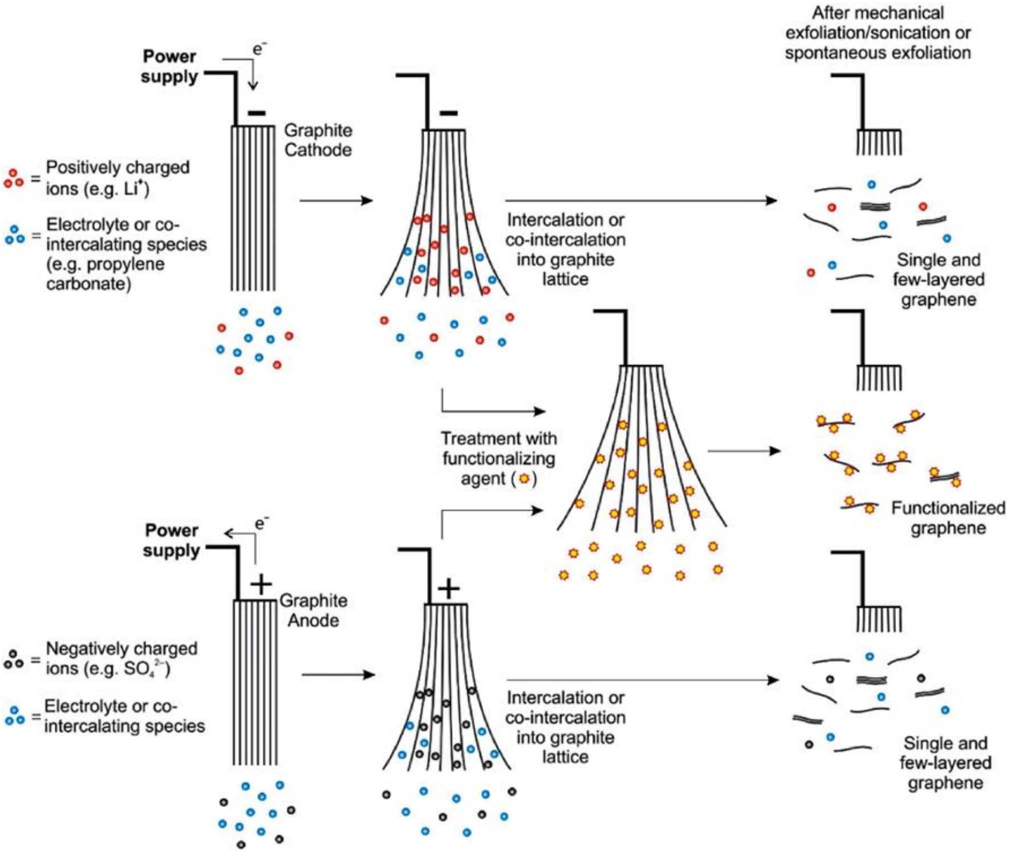

Fig. 15: A schematic overview of mechanism of cathodic and anodic exfoliation. Functionalization of graphene may be achieved either during exfoliation by introducing functionalizing agent or after exfoliation. Reprinted with permission from Yu *et al.* (2015). Copyright (2015) Elsevier.

The removal of oxygen functional groups from GO is a subject of continued research, with different methods such as thermal, photochemical, biological and chemical methods of some already established routes as depicted in Fig 16 (De Silva *et al.*, 2017). Each method produces rGO of varying properties such as morphology, dispersibility, conductivity and mechanical strength. The choice of reduction method is influenced by factors such as C/O ratio of end product, selectivity in removal of either -OH, -COOH or C-O-C functionalities, choice of reducing agent, surface defect reduction and improvement in chemical and physical properties (Smith *et al.*, 2019). The chemical method is the most explored routes to rGO. It involves treating GO suspension with reducing agents such as hydrazine (Gholampour *et al.*, 2017, Venkanna and Chakraborty, 2014, Minitha and Rajendrakumar, 2013), ascorbic acid (Habte and Ayele, 2019, Andrijanto *et al.*, 2016, De Silva *et al.*, 2018, Qu *et al.*, 2010), sodium borohydride (Yang *et al.*, 2015, Chua and Pumera, 2013, Shin *et al.*, 2009, Berzina *et al.*, 2015) and sodium hypophosphite monohydrate (Wang *et al.*, 2013, Liu *et al.*, 2016a). In a report by Luo *et al.* (2011), the reduction of GO by $N_2H_4{\bullet}H_2O$, $NaBH_4$, NaOH, solvothermal, high-temperature, and a two-step method combining $NaBH_4$ and high temperature was comparatively studied using four criteria: degree of reduction, level of defect repair, dispersibility, and electrical conductivity. The study showed that by combining two reduction processes, the properties of rGO could be greatly enhanced.

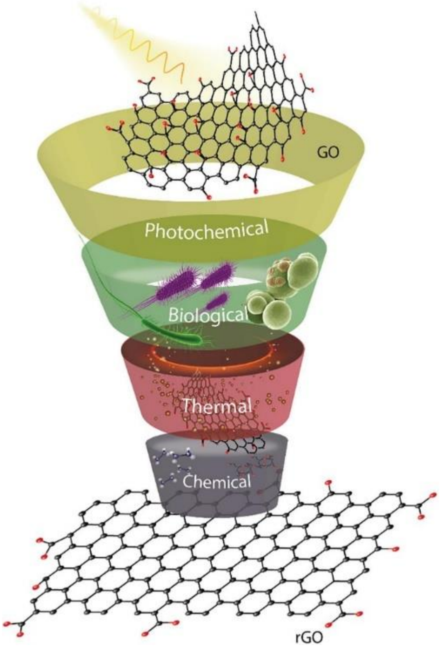

Fig 16: Routes to reduction of graphene oxide. Reprinted with permission from Agarwal and Zetterlund (2021). Copyright (2021) Elsevier.

Recently, the use of plant extracts as green reductants for rGO synthesis has been explored. The method involves the use of extracts from different plant parts such as seeds, roots, flowers and fruits. The reduction could be initiated by polyphenols (such as catechol and pyrogallol) or flavonoids (glucoside, diosmetin and apigenin) in the plant extracts. According to the mechanism proposed by Bhattacharya *et al.* (2017), shown in Fig. 17, the carboxylic groups in GO reacts with reduced species in plant extracts to form esters by condensation reaction , which is further reduced by ring opening reaction. The hydroxyl groups first undergo a condensation reaction, which is also followed by ring cleavage. The epoxy group reacts with polyhydroxy groups in extracts to form an intermediate which undergoes subsequent ring formation and cleavage.

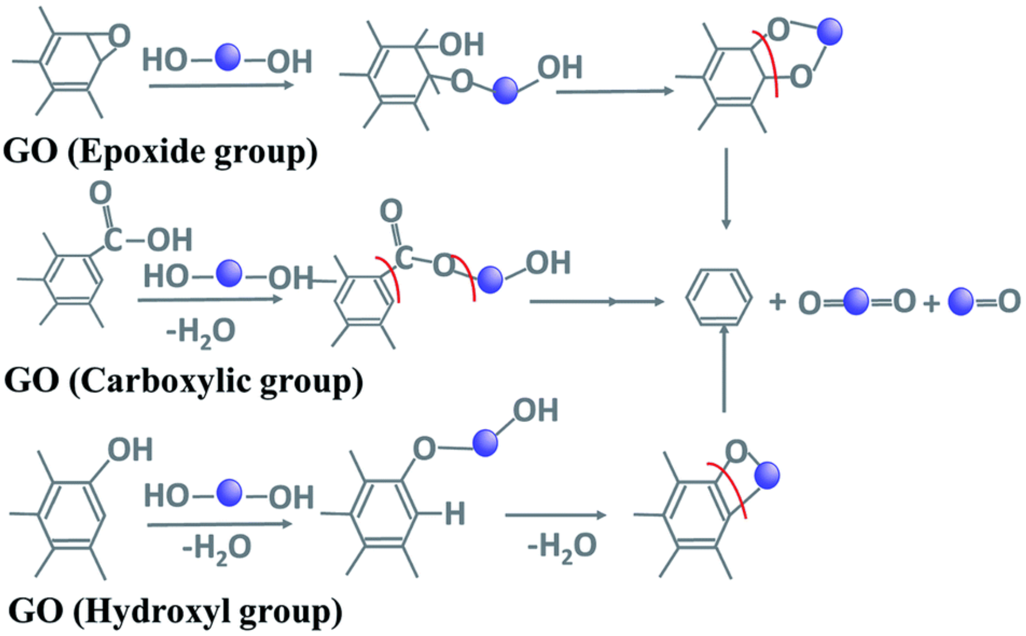

Fig 17: Reduction of oxygen functionality in GO by plant extracts. Adapted with permission from Bhattacharya *et al.* (2017) under Creative Commons Attribution 4.0 International.

5.2 Composites of graphene/graphene derivatives

Increased utilization of graphene and its derivatives have motivated the exploration of different functionalization routes. Compositing of graphene with other nanomaterials take advantage of its superior properties to enhance catalytic activities. Graphene possesses a two-dimensional carbon network with sp^2 hybridization and exhibits unique properties including high specific surface area, high intrinsic electron mobility and high thermal conductivity (Liang *et al.*, 2010). High degradation of pollutants could be achieved by hybridizing graphene with catalysts due to its effective electron conductivity and effective minimization of charge carrier's recombination via its acceptance of photogenerated electrons.

The improvement of catalytic activity by graphene and its derivatives is mainly due to their ability to extend light absorption range, absorptivity enhancement, enhance surface area and improve charge separation and transport (Williams *et al.*, 2008). The compositing of a photocatalyst results in decreased

h^+/e^- recombination and enhances the electron transfer rate, while also enhancing chemical species adsorption via π-π interactions (Pan *et al.*, 2014). Generally, in graphene-based composites, graphene can either act as a support (Khan *et al.*, 2015a), dopant or a coating (Kamegawa *et al.*, 2010, Sun *et al.*, 2020). The three classes of composite could be prepared either via "*ex situ*" or "*in situ*" compositing as shown in Fig 18.

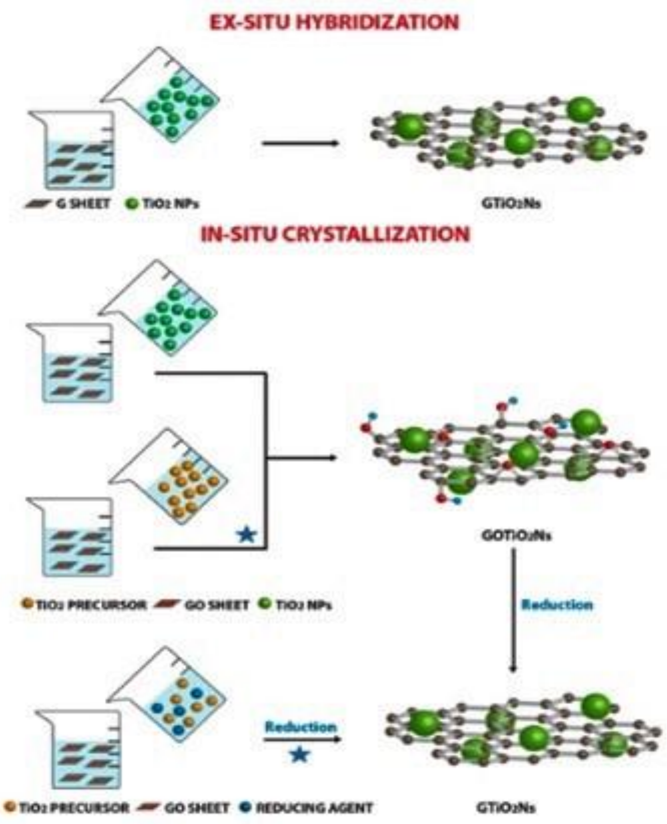

Fig 18: *In-situ* and *Ex-situ* compositing of metal salt with graphene and graphene derivatives. Reproduced with permission from Giovannetti *et al.* (2017) under Creative Commons Attribution 4.0 International.

Ex situ compositing process involves the mixing of nanoparticles with graphene dispersions. To enhance the process, the graphene sheets may be functionalized through covalent C-C coupling or non-covalent π-π stacking reactions (He *et al.*, 2010). *Ex situ* compositing may sometimes result in low density and non-uniform distribution of the nanoparticles on the graphene. Several synthetic routes have been developed based on the *ex situ* process. AbdelDayem *et al.* (2020) reported the *ex situ* compositing of alumina with graphene oxide by mixing pre-prepared alumina with GO solution and refluxing the mixture at 80℃ for 8 h. A two-phase method to the compositing of GO and CdS was reported by Gao *et al.* (2013). In this method, synthesized GO and CdS were dispersed in water and toluene respectively. The two solutions were then mixed together and stirred continuously for 24 h, followed by washing and drying. The interaction between the GO functional groups and CdS led to the distribution of the CdS on the GO surface and the aggregation of the CdS particles was minimized by the process. The synthesis of TiO_2@rGO through mechanochemical synthesis involving the grinding of TiO_2 nanoparticles and rGO was also reported by Deng *et al.* (2020).

The *in-situ* method is the most explored for graphene/nanoparticle composites and it involves direct reaction of GO/rGO sheets and nanoparticles' precursors in solution. The growth of nanoparticles on the surface of GO/rGO have been explored widely through solvothermal and/or hydrothermal techniques. It has been explored frequently in the synthesis of GO/rGO-metal oxide/sulphide nanocomposites. In the *in-situ* method, nanoparticle's nucleation and growth occurs on the GO/rGO surface under high-temperature and pressure, with the hydroxyl and carboxyl functional groups acting as nucleation sites for nanoparticles growth via metal-O-C bond formation (Wang and Dai, 2013, Li *et al.*, 2014b, Liang *et al.*, 2013). A microwave assisted reduction synthetic method via a mixture of $PdCl_2$, $RuCl_3$ and GO, was employed for the synthesis of bimetallic-graphene composite. Reduction of the metal salts to metallic state was achieved with $NaBH_4$, which was enhanced by holding the mixture in a microwave oven (Acidereli *et al.*, 2020). A method involving the mixture of GO/rGO precursor and nanoparticle precursors was described by Anand *et al.* (2020) for the synthesis of rGO/$Bi_2Al_4O_9$. In the synthesis [$Bi(NO_3)•5H_2O$] and $AlNO_3•9H_2O$ were dissolved into the graphene oxide synthesis set-up. The mixture was then stirred for 30 min and further sonicated for 5 min. The process of stirring and sonicating was repeated for 4 h and the reaction was quenched afterwards. GO reduction to rGO was achieved by adding 10% ascorbic acid solution to the reaction system and heating at 95 ºC for 1 h. Cao *et al.* (2020) reported the combination of precursor mixing and annealing for the *in-situ* synthesis of ZnO/rGO. In this synthesis route, ZnO powder was firstly mixed with GO solution and the mixture stirred vigorously for 3 h. The mixture was further kept at room temperature for 3 h and the product collected by centrifugation was dried at 60 ºC for 12 h. The product was then annealed for 2 h at 350 ºC at a heating rate of 2ºC/min to obtain the ZnO/rGO.

Electrochemical exfoliation method is another simple and one-step *ex-situ* technique used in preparing GO/rGO-composite. Ansari and Payami (2020) reported the synthesis of magnetic graphene-Fe_2O_3 nanocomposite using this method. The electrolytic cell was made with graphite foil anode and iron plate as cathode, and applying a voltage of 10 V DC for 3 h. In a study to evaluate the effect of synthesis method on the properties of GO/rGO-composite, Aquino *et al.* (2020) reported the synthesis of GO/WO_3NW/PANI through chemical and electrochemical routes. It was reported that the electrochemical process resulted in a composite with disorganized structure, which however, increased the doping level in the polymer chain, enhanced porosity and also permitted higher synergistic effect among the components of the composites, when compared to the nanocomposites prepared via the chemical route.

The growth of nanoparticles on GO/rGO sheets is influenced by the amount of functional group present on the sheet (Wang *et al.*, 2010). So, compared to rGO, GO can facilitate the growth of nanoparticles leading to higher density and smaller nanoparticle size (Huang *et al.*, 2011). Therefore, to overcome low particle loading and poor solubility of rGO, surfactant molecules or polymers are employed in composite synthesis. The synthesis of Pd-CuO/rGO and Au-CuO/rGO via an ionic liquid-assisted approach was reported by Alhumaimess *et al.* (2020). The addition of little amount of the ionic liquid 1-butyl-3methyl imidazolium tetrafluoroborate resulted in uniformly dispersed nanoparticles, with simultaneous reduction of GO.

Graphene doped with heteroatoms such as nitrogen (N), sulphur (S), boron (B) have also been explored in synthesis of composites with semiconductors. *Ex-situ* synthesis of doped-GO/rGO-composite such as N-graphene, and B-graphene have also been reported. Liu *et al.* (2020) reported the solvothermal synthesis of NG/TiO_2 by mixing N-graphene oxide and TiO_2 in a Teflon-lined reactor. The synthesis of Co_3Sn_2@Co-NG was also reported by Mahmood *et al.* (2013) via the *in-situ* approach.

6.0 GO/rGO supported copper-based ternary sulphides

Despite the excellent optical properties of copper-based ternary metal sulphides reports have shown that the compounds display very low quantum efficiency when explored as absorber. This has been attributed to the short lifetime and mobility of charge carrier, which leads to limited diffusion and photo-generated charge carrier separation. Several techniques have, thus, been explored to improve their photovoltaic efficiency such as post-annealing treatment (Zhang *et al.*, 2019), chemical etching (Wang *et al.*, 2020) and thermochemical treatment (de Souza Lucas *et al.*, 2016). So far, compositing of these materials with suitable support material to enhance their optical efficiency has not been given much focus, though there are a few reports.

RGO/Cu_2SnS_3 flowers nanocomposite prepared via a biomolecule-assisted solvothermal one-step method was reported by Vadivel *et al.* (2016). The weight percent of GO in the composite was at 3%. While the introduction of the GO did not affect the crystal phase of the Cu_2SnS_3, the UV-vis diffuse reflectance spectra of both the pure Cu_2SnS_3 and the GO/Cu_2SnS_3 composite showed that the composite material showed a higher absorption of visible light compare to the single semiconductor, this was attributed to the strong electronic interaction between GO and Cu_2SnS_3. Study of the internal charge transfer process through photocurrent studies showed that the value of the photocurrent of the composite is higher compare to Cu_2SnS_3, confirming the reduction in charge carrier recombination in the composite due to GO addition. EIS analysis of the materials showed that the composite exhibited a better charge transport, lower resistance and good conductivity compared to pure Cu_2SnS_3. Evaluation of the photocatalytic activity of Cu_2SnS_3 and GO/Cu_2SnS_3 composite towards Eosin dye degradation, confirmed the improved photoactivity of the composite. Studying the effect of the percentage composition of the GO on the activity of the composite, it was observed that in the concentration range of 0.5 – 3.0% an increase in photocatalytic activity with increase in GO concentration was observed. while, above this value a reduction in the photoactivity of the composite was observed. This was attributed to the shielding effect of GO on the catalyst, which led to a decrease in the light intensity passing through the reaction medium. The stability of the composite was also affirmed as only a slight reduction in activity was observed after three re-use cycle. In another study, GO/Cu_2SnS_3 and rGO/Cu_2SnS_3 photocatalyst prepared via the ball milling method with percentage GO and rGO varied between 1-5% was explored as photocatalyst for methylene blue degradation under visible light irradiation. Surface area and pore size distribution analysis of the CTS and the composites showed an increase in the specific surface area and pore size distribution with increase in the percentage of the incorporated GO and rGO. Though no smooth correlation existed between the percentage composition of GO and rGO on the band gap of the prepared composites, GO/CTS composite showed a relatively lower band gap compare to the pristine CTS, while the band gaps of rGO/CTS composite were similar to that of the pristine CTS. The photocatalytic studies showed that optimum activity was obtained with 1% GO and 2% rGO. Beyond these percentages, a decrease in photocatalytic activity was observed(Akash, 2019).

7.0 References

AbdelDayem, H. M., Salib, B. G. & El-Hosiny, F. I. 2020. Facile synthesis of hydrothermal stable hierarchically macro-mesoporous hollow microspheres gamma-Al_2O_3-graphene oxide composite: As a new efficient acid-base catalyst for transesterification reaction for biodiesel production. *Fuel,* 277.

Acidereli, H., Cellat, K., Calimli, M. H. & Sen, F. 2020. Palladium/ruthenium supported on graphene oxide (PdRu@GO) as an efficient, stable and rapid catalyst for hydrogen production from DMAB under room conditions. *Renewable Energy,* 161**,** 200-206.

Agarwal, V. & Zetterlund, P. B. 2021. Strategies for reduction of graphene oxide – A comprehensive review. *Chemical Engineering Journal,* 405.

Ahmed, M. B., Zhou, J. L., Ngo, H. H., Guo, W., Thomaidis, N. S. & Xu, J. 2017. Progress in the biological and chemical treatment technologies for emerging contaminant removal from wastewater: A critical review. *Journal of Hazardous Materials,* 323 274-298.

Ahmed, S. N. & Haider, W. 2018. Heterogeneous photocatalysis and its potential applications in water and wastewater treatment: a review. *Nanotechnology,* 29**,** 342001.

Akash, S. 2019. Enhanced electrocatalytic and photocatalytic activity of ball milled copper tin sulphide by incorporating GO and rGO. *Applied Surface Science,* 484**,** 265-275.

Alhumaimess, M. S., Alsohaimi, I. H., Alshammari, H. M., Aldosari, O. F. & Hassan, H. M. A. 2020. Synthesis of gold and palladium nanoparticles supported on CuO/rGO using imidazolium ionic liquid for CO oxidation. *Research on Chemical Intermediates*.

Ali, I. & Gupta, V. K. 2006. Advances in water treatment by adsorption technology. *J Nature protocols,* 1**,** 2661.

Anand, A., Meena, D. & Bhatnagar, M. C. 2020. Synthesis and characterization of flexible PVDF/$Bi_2Al_4O_9$/RGO based piezoelectric materials for nanogenerator application. *Journal of Alloys and Compounds,* 843.

Andrijanto, E., Shoelarta, S., Subiyanto, G. & Rifki, S. 2016. Facile synthesis of graphene from graphite using ascorbic acid as reducing agent. *AIP Conference Proceedings,* 1725.

Ansari, N. & Payami, Z. 2020. Synthesis of Magnetic Graphene-Fe_3O_4 Nanocomposite by Electrochemical Exfoliation Method. *Journal of Nanostructures,* 10**,** 39-43.

Anwer, H., Mahmood, A., Lee, J., Kim, K.-H., Park, J.-W. & Yip, A. C. K. 2019. Photocatalysts for degradation of dyes in industrial effluents: Opportunities and challenges. *Nano Research,* 12**,** 955-972.

Aquino, C. B., Nagaoka, D. A., Machado, M. M., Candido, E. G., da Silva, A. G. M., Camargo, P. H. C. & Domingues, S. H. 2020. Chemical versus electrochemical: What is the best synthesis method to ternary GO/WO_3NW/PAni nanocomposites to improve performance as supercapacitor? *Electrochimica Acta,* 356.

Aup-Ngoen, K., Thongtem, S. & Thongtem, T. 2011. Cyclic microwave-assisted synthesis of Cu_3BiS_3 dendrites using l-cysteine as a sulfur source and complexing agent. *Materials Letters,* 65**,** 442-445.

Avetta, P., Pensato, A., Minella, M., Malandrino, M., Maurino, V., Minero, C., Hanna, K. & Vione, D. 2015. Activation of persulfate by irradiated magnetite: Implications for the degradation of phenol under heterogeneous photo-Fenton-like conditions. *Environ. Sci. Technol.,* 49**,** 1043-1050.

Babaei, A. A., Lima, E. C., Takdastan, A., Alavi, N., Goudarzi, G., Vosoughi, M., Hassani, G. & Shirmardi, M. 2016. Removal of tetracycline antibiotic from contaminated water media by multi-walled carbon nanotubes: operational variables, kinetics, and equilibrium studies. *Water Sci. Technol,* 74**,** 1202-1216.

Bandala, E. R., Pelaez, M. A., Salgado, M. J. & Torres, L. 2008. Degradation of sodium dodecyl sulphate in water using solar driven Fenton-like advanced oxidation processes. *J Hazard Mater,* 151**,** 578-84.

Barceló, D. & Petrovic, M. 2008. Conclusions and future research needs. *In:* BARCELÓ, D. & PETROVIC, M. (eds.) *Emerging Contaminants from Industrial and Municipal Waste.* Springer.

Berg, D. M., Djemour, R., Gütay, L., Zoppi, G., Siebentritt, S. & Dale, P. J. 2012. Thin film solar cells based on the ternary compound Cu_2SnS_3. *Thin Solid Films,* 520**,** 6291-6294.

Berzina, A., Tupureina, V., Orlovs, R., Saharovs, D., Bitenieks, J. & Knite, M. 2015. Increase of Electrical Conductivity due to Chemical Reduction of Pre-Exfoliated Graphene Oxide by Sodium Borohydride. *Advanced Materials Research,* 1117**,** 187-190.

Bhatia, V., Malekshoar, G., Dhir, A. & Ray, A. K. 2017. Enhanced photocatalytic degradation of atenolol using graphene TiO_2 composite. *Journal of Photochemistry and Photobiology a-Chemistry,* 332**,** 182-187.

Bhattacharya, G., Sas, S., Wadhwa, S., Mathur, A., McLaughlin, J. & Roy, S. S. 2017. Aloe vera assisted facile green synthesis of reduced graphene oxide for electrochemical and dye removal applications. *RSC Advances,* 7**,** 26680-26688.

Bilal, M., Rasheed, T., Mehmood, S., Tang, H., Ferreira, L. F. R., Bharagava, R. N. & Iqbal, H. M. N. 2020. Mitigation of environmentally-related hazardous pollutants from water matrices using nanostructured materials - A review. *Chemosphere,* 253**,** 126770.

Boczkaj, G. & Fernandes, A. 2017. Wastewater treatment by means of advanced oxidation processes at basic pH conditions: A review. *Chemical Engineering Journal,* 320**,** 608-633.

Borikar, D., Mohseni, M. & Jasim, S. 2015. Evaluations of conventional, ozone and UV/$H_2O_2$for removal of emerging contaminants and THM-FPs. *Water Quality Research Journal of Canada,* 50**,** 140-151.

Brodie, B. 1855. Note sur un nouveau procédé pour la purification et la désagrégation du graphite. *J. Ann. Chim. Phys.,* 45**,** 351-353.

Brooks, B. W., Huggett, D. B., Boxall, A. B. J. E. T. & Chemistry 2009. Pharmaceuticals and personal care products: research needs for the next decade. 28**,** 2469.

Bustos-Terrones, Y., Rangel-Peraza, J. G., Sanhouse, A., Bandala, E. R. & Torres, L. G. 2016. Degradation of organic matter from wastewater using advanced primary treatment by O_3 and O_3/UV in a pilot plant. *Phys. Chem. Earth,* 91 61-67.

Calvete, M. J. F., Piccirillo, G., Vinagreiro, C. S. & Pereira, M. M. 2019. Hybrid materials for heterogeneous photocatalytic degradation of antibiotics. *Coordination Chemistry Reviews,* 395**,** 63-85.

Cao, P. J., Cai, Y. Z., Pawar, D., Navale, S. T., Rao, C. N., Han, S., Xu, W. Y., Fang, M., Liu, X. K., Zeng, Y. X., Liu, W. J., Zhu, D. L. & Lu, Y. M. 2020. Down to ppb level NO_2 detection by ZnO/rGO heterojunction based chemiresistive sensors. *Chemical Engineering Journal,* 401.

Caracas, R. & Gonze, X. 2005. First-principles study of the electronic properties of A_2B_3 minerals, with A=Bi,Sb and B=S,Se. *Physics and Chemistry of Minerals,* 32**,** 295-300.

Chaplin, B. P. 2014. Critical review of electrochemical advanced oxidation processes for water treatment applications. *Environmental Science: Processes & Impacts,* 16**,** 1182-1203.

Chelme-Ayala, P., El-Din, M. G. & Smith, D. W. 2010. Degradation of bromoxynil and trifluralin in natural water by direct photolysis and UV plus H_2O_2 advanced oxidation process. *Water Res,* 44**,** 2221-2228.

Chen, J., Li, Y., Huang, L., Li, C. & Shi, G. 2015. High-yield preparation of graphene oxide from small graphite flakes via an improved Hummers method with a simple purification process. *Carbon,* 81**,** 826-834.

Chen, S.-L., Tao, J., Shu, H.-B., Tao, H.-J., Tang, Y.-X., Shen, Y.-Z., Wang, T. & Pan, L. 2017. Efficient electron transfer kuramite Cu_3SnS_4 nanosheet thin film towards platinum-free cathode in dye-sensitized solar cells. *Journal of Power Sources,* 341**,** 60-67.

Chen, X., Wang, X., An, C., Liu, J. & Qian, Y. 2003. Preparation and characterization of ternary Cu–Sn–E (E=S, Se) semiconductor nanocrystallites via a solvothermal element reaction route. *Journal of Crystal Growth,* 256**,** 368-376.

Chiang, Y.-H., Lin, K.-Y., Chen, Y.-H., Waki, K., Abate, M. A., Jiang, J.-C. & Chang, J.-Y. 2018. Aqueous solution-processed off-stoichiometric Cu–In–S QDs and their application in quantum dot-sensitized solar cells. *Journal of Materials Chemistry A,* 6**,** 9629-9641.

Chin, A. & Bérubé, P. R. 2005. Removal of disinfection by-product precursors with ozone-UV advanced oxidation process. *Water Research,* 39**,** 2136-2144.

Cho, J. Y., Mun, H., Ryu, B., Kim, S. I., Hwang, S., Roh, J. W., Yang, D. J., Shin, W. H., Lee, S. M., Choi, S.-M., Kang, D. J., Kim, S. W. & Lee, K. H. 2013. Cu–Bi–Se-based pavonite homologue: a promising thermoelectric material with low lattice thermal conductivity. *Journal of Materials Chemistry A,* 1**,** 9768-9774.

Chokwe, T. B., Magubane, M. N., Abafe, O. A., Okonkwo, J. O. & Sibiya, I. V. 2019. Levels, distributions, and ecological risk assessments of polybrominated diphenyl ethers and alternative flame retardants in river sediments from Vaal River, South Africa. *Environmental Science and Pollution Research,* 26**,** 7156-7163.

Chua, C. K. & Pumera, M. 2013. Reduction of graphene oxide with substituted borohydrides. *Journal of Materials Chemistry A,* 1**,** 1892-1898.

Coughlan, C., Ibanez, M., Dobrozhan, O., Singh, A., Cabot, A. & Ryan, K. M. 2017. Compound Copper Chalcogenide Nanocrystals. *Chem Rev,* 117**,** 5865-6109.

Crespo, C. T. 2016. Microscopic Optical Absorption, Analysis, and Applications of Famatinite Cu_3SbS_4. *The Journal of Physical Chemistry C,* 120**,** 7959-7965.

Daughton, C. G. 2003. Cradle-to-cradle stewardship of drugs for minimizing their environmental disposition while promoting human health. I. Rationale for and avenues toward a green pharmacy. *Environmental health perspectives,* 111**,** 757-774.

De Silva, K. K. H., Huang, H.-H. & Yoshimura, M. 2018. Progress of reduction of graphene oxide by ascorbic acid. *Applied Surface Science,* 447**,** 338-346.

De Silva, K. K. H., Huang, H. H., Joshi, R. K. & Yoshimura, M. 2017. Chemical reduction of graphene oxide using green reductants. *Carbon,* 119**,** 190-199.

de Souza Lucas, F. W., Welch, A. W., Baranowski, L. L., Dippo, P. C., Hempel, H., Unold, T., Eichberger, R., Blank, B., Rau, U., Mascaro, L. H. & Zakutayev, A. 2016. Effects of Thermochemical Treatment on $CuSbS_2$ Photovoltaic Absorber Quality and Solar Cell Reproducibility. *The Journal of Physical Chemistry C,* 120**,** 18377-18385.

Deng, D. R., Cui, X. Y., Wu, Q. H., Zheng, M. S. & Dong, Q. F. 2020. In-situ synthesis TiO_2 nanosheets@rGO for ultrafast sodium ion storage at both room and low temperatures. *Journal of Alloys and Compounds,* 835.

Deng, J., Shao, Y., Gao, N., Xia, S., Tan, C., Zhou, S. & Hu, X. 2013. Degradation of the antiepileptic drug carbamazepine upon different UV-based advanced oxidation processes in water. *Chemical Engineering Journal,* 222**,** 150-158.

Deng, M., Shen, S., Zhang, Y., Xu, H. & Wang, Q. 2014. A generalized strategy for controlled synthesis of ternary metal sulfide nanocrystals. *New J. Chem.,* 38**,** 77-83.

Deshmukh, S. D., Ellis, R. G., Sutandar, D. S., Rokke, D. J. & Agrawal, R. 2019. Versatile Colloidal Syntheses of Metal Chalcogenide Nanoparticles from Elemental Precursors Using Amine-Thiol Chemistry. *Chemistry of Materials,* 31**,** 9087-9097.

Deshmukh, S. G., Kheraj, V. & Panchal, A. K. 2018. Effect of annealing on the properties of Cu_3BiS_3 thin films deposited via chemical bath deposition. *Materials Today: Proceedings,* 5**,** 10712-10716.

Ding, S.-L., Wang, X.-K., Jiang, W.-Q., Zhao, R.-S., Shen, T.-T., Wang, C. & Wang, X. 2015. Influence of pH, inorganic anions, and dissolved organic matter on the photolysis of antimicrobial triclocarban in aqueous systems under simulated sunlight irradiation. *Environmental Science and Pollution Research,* 22**,** 5204-5211.

Dong, L., Chen, Z., Lin, S., Wang, K., Ma, C. & Lu, H. 2017. Reactivity-Controlled Preparation of Ultralarge Graphene Oxide by Chemical Expansion of Graphite. *Chemistry of Materials,* 29**,** 564-572.

Du, B., Haddad, S. P., Luek, A., Scott, W. C., Saari, G. N., Kristofco, L. A., Connors, K. A., Rash, C., Rasmussen, J. B., Chambliss, C. K. & Brooks, B. W. 2014. Bioaccumulation and trophic dilution of human pharmaceuticals across trophic positions of an effluent-dependent wadeable stream. *Philosophical Transactions of the Royal Society B: Biological Sciences,* 369**,** 20140058.

Du, B., Zhang, R., Chen, K., Mahajan, A. & Reece, M. J. 2017. The impact of lone-pair electrons on the lattice thermal conductivity of the thermoelectric compound $CuSbS_2$. *Journal of Materials Chemistry A,* 5**,** 3249-3259.

Du, B., Zhang, R., Liu, M., Chen, K., Zhang, H. & Reece, M. J. 2019. Crystal structure and improved thermoelectric performance of iron stabilized cubic Cu_3SbS_3 compound. *Journal of Materials Chemistry C,* 7**,** 394-404.

Esplugas, S., Bila, D. M., Krause, L. G. T. & Dezotti, M. 2007. Ozonation and advanced oxidation technologies to remove endocrine disrupting chemicals (EDCs) and pharmaceuticals and personal care products (PPCPs) in water effluents. *Journal of Hazardous Materials,* 149**,** 631-642.

Etacheri, V., Michlits, G., Seery, M. K., Hinder, S. J. & Pillai, S. C. 2013. A highly efficient $TiO_{2-x}C$ nano-heterojunction photocatalyst for visible light induced antibacterial applications. *ACS Appl. Mater. Interfaces,* 5**,** 1663–1672.

Fent, K., Weston, A. A. & Caminada, D. 2006. Ecotoxicology of human pharmaceuticals. *Aquatic Toxicology,* 76**,** 122-159.

Fernandez, N. A., Rodriguez-Freire, L., Keswani, M. & Sierra-Alvarez, R. 2016. Effect of chemical structure on the sonochemical degradation of perfluoroalkyl and polyfluoroalkyl substances (PFASs). *Environmental Science: Water Research & Technology,* 2**,** 975-983.

Franzellitti, S. & Fabbri, E. 2014. Response to Commentary on “Are some invertebrates exquisitely sensitive to the human pharmaceutical fluoxetine?”. *Aquatic Toxicology,* 146**,** 264-265.

Fu, P., Feng, J., Yang, H. & Yang, T. 2016. Degradation of sodium n-butyl xanthate by vacuum UV-ozone (VUV/O_3) in comparison with ozone and VUV photolysis. *Process Safety and Environmental Protection,* 102**,** 64-70.

G., d. S. C. & Faria, J. L. 2003. Photochemical and photocatalytica degradation of an azo dye in aqueous solution by UV irradiation. *J Photochem Photobiol A: Chem,* 155**,** 133.

Galindo-Miranda, J. M., Guízar-González, C., Becerril-Bravo, E. J., Moeller-Chávez, G., León-Becerril, E. & Vallejo-Rodríguez, R. 2019. Occurrence of emerging contaminants in environmental surface waters and their analytical methodology – a review. *Water Supply***,** 1-14.

Ganiyu, S. O., van Hullebusch, E. D., Cretin, M., Esposito, G. & Oturan, M. A. 2015. Coupling of membrane filtration and advanced oxidation processes for removal of pharmaceutical residues: A critical review. *Separation and Purification Technology,* 156**,** 891-914.

Gao, P., Liu, J., Sun, D. D. & Ng, W. 2013. Graphene oxide-CdS composite with high photocatalytic degradation and disinfection activities under visible light irradiation. *J Hazard Mater,* 250-251**,** 412-20.

Gao, T., Zhang, Q., Li, L., Zhou, X., Li, L., Li, H. & Zhai, T. 2018. 2D Ternary Chalcogenides. *Advanced Optical Materials,* 6**,** 1800058.

Garcia-Rodríguez, A., Matamoros, V., Fontàs, C. & Salvadó, V. 2014. The ability of biologically based wastewater treatment systems to remove emerging organic contaminants-a review. *Environ. Sci. Pollut. Res. ,* 21**,** 11708-11728.

Gholampour, A., Valizadeh Kiamahalleh, M., Tran, D. N. H., Ozbakkaloglu, T. & Losic, D. 2017. From Graphene Oxide to Reduced Graphene Oxide: Impact on the Physiochemical and Mechanical Properties of Graphene–Cement Composites. *ACS Applied Materials & Interfaces,* 9**,** 43275-43286.

Giovannetti, R., Rommozzi, E., Zannotti, M. & D'Amato, C. 2017. Recent Advances in Graphene Based TiO_2 Nanocomposites ($GTiO_2Ns$) for Photocatalytic Degradation of Synthetic Dyes. *Catalysts,* 7**,** 305.

Gligorovski, S., Strekowski, R., Barbati, S. & Vione, D. 2015. Environmental Implications of Hydroxyl Radicals ($^{\cdot}OH$). *Chem Rev,* 115**,** 13051-92.

Gogate, P. R. & Pandit, A. B. 2004. A review of imperative technologies for wastewater treatment I: oxidation technologies at ambient conditions. *Advances in Environmental Research,* 8**,** 501-551.

Gomez, C. F., Constantine, L., Moen, M., Vaz, A., Wang, W. & Huggett, D. B. 2011. Ibuprofen Metabolism in the Liver and Gill of Rainbow Trout, Oncorhynchus mykiss. *Bulletin of Environmental Contamination and Toxicology,* 86**,** 247-251.

Gu, Y., Liu, T., Zhang, Q. & Dong, W. 2017. Efficient decomposition of perfluorooctanoic acid by a high photon flux UV/sulfite process: Kinetics and associated toxicity. *Chemical Engineering Journal,* 326**,** 1125-1133.

Habte, A. T. & Ayele, D. W. 2019. Synthesis and Characterization of Reduced Graphene Oxide (rGO) Started from Graphene Oxide (GO) Using the Tour Method with Different Parameters. *Advances in Materials Science and Engineering,* 2019**,** 5058163.

Han, C., Zhang, N. & Xu, Y.-J. 2016. Structural diversity of graphene materials and their multifarious roles in heterogeneous photocatalysis. *Nano Today,* 11**,** 351-372.

He, F., Fan, J., Ma, D., Zhang, L., Leung, C. & Chan, H. L. 2010. The attachment of Fe_3O_4 nanoparticles to graphene oxide by covalent bonding. *Carbon,* 48**,** 3139-3144.

Hijnen, W., Beerendonk, E. & Medema, G. J. 2006. Inactivation credit of UV radiation for viruses, bacteria and protozoan (oo) cysts in water: a review. *Water Res.,* 40**,** 3-22.

Hobbis, D., Wang, H., Martin, J. & Nolas, G. S. 2020. Thermal Properties of the Very Low Thermal Conductivity Ternary Chalcogenide $Cu_4Bi_4M_9$ (M = S, Se). *physica status solidi (RRL) – Rapid Research Letters,* 14.

Hong, B., Lin, Q., Yu, S., Chen, Y., Chen, Y. & Chiang, P. 2018. Urbanization gradient of selected pharmaceuticals in surface water at a watershed scale. *Science of The Total Environment,* 634**,** 448-458.

Hu, J.-Y., Li, J., Zhang, S.-J., Zhao, H.-F., Zhang, Q.-H., Yao, Y., Zhao, Q., Shi, L.-J., Zou, B.-S., Li, Y.-C., Li, X.-D., Liu, J., Zhu, K., Liu, Y.-L., Jin, C.-Q. & Yu, R.-C. 2013. Pressure-induced phase transitions in single-crystalline $Cu_4Bi_4S_9$ nanoribbons. *Chinese Physics B,* 22**,** 116201.

Hu, J., Deng, B., Wang, C., Tang, K. & Qian, Y. 2003. Convenient hydrothermal decomposition process for preparation of nanocrystalline mineral Cu_3BiS_3 and $Pb_{1-x}Bi_{2x/3}S$. *Materials Chemistry and Physics,* 78**,** 650-654.

Huang, X., Boey, F. & Zhang, H. U. A. 2011. A Brief Review on Graphene-Nanoparticle Composites. *Cosmos,* 06**,** 159-166.

Jiasong, Z., Weidong, X., Huaidong, J., Wen, C., Lijun, L., Xinyu, Y., Xiaojuan, L. & Haitao, L. 2010. A simple L-cystine-assisted solvothermal approach to Cu_3SbS_3 nanorods. *Materials Letters,* 64**,** 1499-1502.

Kamegawa, T., Yamahana, D. & Yamashita, H. 2010. Graphene Coating of TiO_2 Nanoparticles Loaded on Mesoporous Silica for Enhancement of Photocatalytic Activity. *The Journal of Physical Chemistry C,* 114**,** 15049-15053.

Kanai, A., Toyonaga, K., Chino, K., Katagiri, H. & Araki, H. 2015. Fabrication of Cu_2SnS_3 thin-film solar cells with power conversion efficiency of over 4%. *Japanese Journal of Applied Physics,* 54.

Keen, O. S. & Linden, K. G. 2013. Degradation of antibiotic activity during UV/H_2O_2 advanced oxidation and photolysis in wastewater effluent. *Environ Sci Technol,* 47**,** 13020-30.

Kehoe, A. B., Temple, D. J., Watson, G. W. & Scanlon, D. O. 2013. Cu_3MCh_3 (M = Sb, Bi; Ch = S, Se) as candidate solar cell absorbers: insights from theory. *Phys Chem Chem Phys,* 15**,** 15477-84.

Khan, H. K., Rehman, M. Y. A. & Malik, R. N. 2020. Fate and toxicity of pharmaceuticals in water environment: An insight on their occurrence in South Asia. *Journal of Environmental Management,* 271.

Khan, M., Tahir, M. N., Adil, S. F., Khan, H. U., Siddiqui, M. R. H., Al-warthan, A. A. & Tremel, W. 2015a. Graphene based metal and metal oxide nanocomposites: synthesis, properties and their applications. *Journal of Materials Chemistry A,* 3**,** 18753-18808.

Khan, M. M., Adil, S. F. & Al-Mayouf, A. 2015b. Metal oxides as photocatalysts. *J. Saudi Chem. Soc.,* 19**,** 462–464.

Khan, S., He, X., Khan, J. A., Khan, H. M., Boccelli, D. L. & Dionysiou, D. D. 2017a. Kinetics and mechanism of sulfate radical- and hydroxyl radical-induced degradation of highly chlorinated pesticide lindane in UV/peroxymonosulfate system. *Chem. Eng. J. ,* 318**,** 135-142.

Khan, S., He, X., Khan, J. A., Khan, H. M., Boccelli, D. L. & Dionysiou, D. D. 2017b. Kinetics and mechanism of sulfate radical- and hydroxyl radical-induced degradation of highly chlorinated pesticide lindane in UV/peroxymonosulfate system. *Chemical Engineering Journal,* 318**,** 135-142.

Khan, S., Sayed, M., Sohail, M., Ali Shah, L. & Ali Raj, M. 2019. Advanced Oxidation and Reduction Processes. *Advances in Water Purification Technique.* Elsevier.

Kim, I. & Tanaka, H. 2010. Use of ozone-based processes for the removal of pharmaceuticals detected in a wastewater treatment plant. *Water Environ Res,* 82**,** 294-301.

Kim, I., Yamashita, N. & Tanaka, H. 2009. Photodegradation of pharmaceuticals and personal care products during UV and UV/H_2O_2 treatments. *Chemosphere,* 77**,** 518-25.

Klavarioti, M., Mantzavinos, D. & Kassinos, D. 2009. Removal of residual pharmaceuticals from aqueous systems by advanced oxidation processes. *Environ Int,* 35**,** 402-17.

Klein, E. Y., Van Boeckel, T. P., Martinez, E. M., Pant, S., Gandra, S., Levin, S. A., Goossens, H. & Laxminarayan, R. 2018. Global increase and geographic convergence in antibiotic consumption between 2000 and 2015. *Proceedings of the National Academy of Sciences,* 115**,** E3463.

Koe, W. S., Lee, J. W., Chong, W. C., Pang, Y. L. & Sim, L. C. 2020. An overview of photocatalytic degradation: photocatalysts, mechanisms, and development of photocatalytic membrane. *Environ Sci Pollut Res Int,* 27**,** 2522-2565.

Krishnan, B., Shaji, S. & Ernesto Ornelas, R. 2015. Progress in development of copper antimony sulfide thin films as an alternative material for solar energy harvesting. *Journal of Materials Science: Materials in Electronics,* 26**,** 4770-4781.

Kuch, H. M. & Ballschmiter, K. 2001. Determination of endocrine disrupting phenolic compounds and estrogens in surface and drinking water by HRGC- (NCI)-MS in the pictogram per liter range. *Environ. Sci. Technol.,* 35**,** 3201-3206.

Kumar, M. & Persson, C. 2013a. Cu_3BiS_3 as a potential photovoltaic absorber with high optical efficiency. *Applied Physics Letters,* 102.

Kumar, M. & Persson, C. 2013b. $CuSbS_2$ and $CuBiS_2$ as potential absorber materials for thin-film solar cells. *Journal of Renewable and Sustainable Energy,* 5.

Kumar, P. V., Bardhan, N. M., Tongay, S., Wu, J., Belcher, A. M. & Grossman, J. C. 2014. Scalable enhancement of graphene oxide properties by thermally driven phase transformation. *Nature Chemistry,* 6**,** 151-158.

Kümmerer, K. 2004. Pharmaceuticals in the Environment — Scope of the Book and Introduction. *In:* KÜMMERER, K. (ed.) *Pharmaceuticals in the Environment: Sources, Fate, Effects and Risks.* Berlin, Heidelberg: Springer Berlin Heidelberg.

Kyono, A. & Kimata, M. 2005. Crystal structures of chalcostibite ($CuSbS_2$) and emplectite ($CuBiS_2$): Structural relationship of stereochemical activity between chalcostibite and emplectite. *American Mineralogist,* 90**,** 162-165.

Lanzafame, G., Sarakha, M., Fabbri, D. & Vione, D. 2017. Degradation of Methyl 2-Aminobenzoate (Methyl Anthranilate) by H_2O_2/UV: Effect of Inorganic Anions and Derived Radicals. *Molecules,* 22**,** 619.

Li, H., Zhang, Q., Pan, A., Wang, Y., Zou, B. & Fan, H. J. 2011. Single-Crystalline $Cu_4Bi_4S_9$ Nanoribbons: Facile Synthesis, Growth Mechanism, and Surface Photovoltaic Properties. *Chemistry of Materials,* 23**,** 1299-1305.

Li, J., wang, X., Liu, R., shi, L., Kamran, M. A., Zhong, H. & Zou, B. 2014a. The length controllable synthesis and near-infrared photoluminescence of one-dimensional ternary Cu4Bi4S9 semiconductor nanobelts. *Materials Research Bulletin,* 49**,** 180-186.

Li, L., Zhang, D., Deng, J., Kang, Q., Liu, Z., Fang, J. & Gou, Y. 2020a. Review—Progress of Research on the Preparation of Graphene Oxide via Electrochemical Approaches. *Journal of The Electrochemical Society,* 167.

Li, Q., Mahmood, N., Zhu, J., Hou, Y. & Sun, S. 2014b. Graphene and its composites with nanoparticles for electrochemical energy applications. *Nano Today,* 9**,** 668-683.

Li, T., Wang, C., Wang, T. & Zhu, L. 2020b. Highly efficient photocatalytic degradation toward perfluorooctanoic acid by bromine doped BiOI with high exposure of (001) facet. *Applied Catalysis B: Environmental,* 268**,** 118442.

Li, Y. X., Wang, Y., Pattengale, B., Yin, J., An, L., Cheng, F. Y., Li, Y. F., Huang, J. E. & Xi, P. X., , . 2017. High-index faceted $CuFeS_2$ nanosheets with enhanced behaviour for boosting hydrogen evolution reaction. *Nanoscale* 9**,** 9230.

Liang, Y., Li, Y., Wang, H. & Dai, H. 2013. Strongly Coupled Inorganic/Nanocarbon Hybrid Materials for Advanced Electrocatalysis. *Journal of the American Chemical Society,* 135**,** 2013-2036.

Liang, Y. Y., Wang, H. L., Casalongue, H. S., Chen, Z. & Dai, H. J. 2010. TiO_2 Nanocrystals Grown on Graphene as Advanced Photocatalytic Hybrid Materials. *Nano Research,* 3**,** 701-705.

Lin, L., Wang, H. & Xu, P. 2017. Immobilized TiO_2-reduced graphene oxide nanocomposites on optical fibers as high performance photocatalysts for degradation of pharmaceuticals. *Chemical Engineering Journal,* 310**,** 389-398.

Litter, M. I. 2005. Introduction to Photochemical Advanced Oxidation Processes for Water Treatment. *In:* BOULE, P., BAHNEMANN, D. W. & ROBERTSON, P. K. J. (eds.) *Environmental Photochemistry Part II.* Berlin, Heidelberg: Springer.

Liu, C., Han, G., Chang, Y., Xiao, Y., Li, Y., Li, M. & Zhou, H. 2016a. Capacitive Performances of Reduced Graphene Oxide Hydrogel Prepared by Using Sodium Hypophosphite as Reducer. *Chinese Journal of Chemistry,* 34**,** 89-97.

Liu, J., Chen, K.-Y., Wang, J., Du, M., Gao, Z.-Y. & Song, C.-X. 2020. Preparation and Photocatalytic Properties of N-Doped Graphene/TiO_2 Composites. *Journal of Chemistry,* 2020**,** 1-10.

Liu, Q., Zhao, Z., Lin, Y., Guo, P., Li, S., Pan, D. & Ji, X. 2011. Alloyed $(ZnS)_x(Cu_2SnS_3)_{(1-x)}$ and $(CuInS_2)_{(x)}(Cu_2SnS_3)_{(1-x)}$ nanocrystals with arbitrary composition and broad tunable band gaps. *Chem Commun (Camb),* 47**,** 964-6.

Liu, S., Wang, X., Nie, L., Chen, L. & Yuan, R. 2015. Spray pyrolysis deposition of Cu_3BiS_3 thin films. *Thin Solid Films,* 585**,** 72-75.

Liu, T., Yin, K., Liu, C., Luo, J., Crittenden, J., Zhang, W., Luo, S., He, Q., Deng, Y., Liu, H. & Zhang, D. 2018. The role of reactive oxygen species and carbonate radical in oxcarbazepine degradation via UV, UV/H_2O_2: Kinetics, mechanisms and toxicity evaluation. *Water Res,* 147**,** 204-213.

Liu, Z., Duan, X., Zhou, X., Qian, G., Zhou, J. & Yuan, W. 2014. Controlling and formation mechanism of oxygen-containing groups on graphite oxide. *Industrial and Engineering Chemistry Research,* 53**,** 253-258.

Liu, Z., Tian, C., Lu, L. & Su, X. 2016b. A novel aptamer-mediated $CuInS_2$ quantum dots@graphene oxide nanocomposites-based fluorescence “turn off–on” nanosensor for highly sensitive and selective detection of kanamycin. *RSC Advances,* 6**,** 10205-10214.

Lokhande, A. C., Babar, P. T., Karade, V. C., Gang, M. G., Lokhande, V. C., Lokhande, C. D. & Kim, J. H. 2019. The versatility of copper tin sulfide. *Journal of Materials Chemistry A,* 7**,** 17118-17182.

Luo, D., Zhang, G., Liu, J. & Sun, X. 2011. Evaluation Criteria for Reduced Graphene Oxide. *The Journal of Physical Chemistry C,* 115**,** 11327-11335.

Luo, Y., Guo, W., Ngo, H., Nghiem, L., Hai, F., Zhang, J., Liang, S. & Wang, X. 2014. A review on the occurrence of micropollutants in the aquatic environment and their fate and removal during wastewater treatment. *Science of the Total Environment* 473-474**,** 619-641.

Magureanu, M., Mandache, N. B. & Parvulescu, V. I. 2015. Degradation of pharmaceutical compounds in water by non-thermal plasma treatment. *Water Res,* 81**,** 124-36.

Mahmood, N., Zhang, C., Liu, F., Zhu, J. & Hou, Y. 2013. Hybrid of Co_3Sn_2@Co Nanoparticles and Nitrogen-Doped Graphene as a Lithium Ion Battery Anode. *ACS Nano,* 7**,** 10307-10318.

Manimozhi, T., Archana, J. & Ramamurthi, K. 2018. Shape controlled synthesis of Cu_3BiS_3 nano- and microstructures by PEG assisted solvothermal method and functional properties. *Ceramics International,* 44**,** 15385-15392.

Marcano, D. C., Kosynkin, D. V., Berlin, J. M., Sinitskii, A., Sun, Z., Slesarev, A., Alemany, L. B., Lu, W. & Tour, J. M. 2010. Improved Synthesis of Graphene Oxide. *ACS Nano,* 4**,** 4806-4814.

Marta, I. L. & Natalia, Q. 2010. Photochemical Advanced Oxidation Processes for Water and Wastewater Treatment. *Recent Patents on Engineering,* 4**,** 217-241.

Matafonova, G. & Batoev, V. 2018. Recent advances in application of UV light-emitting diodes for degrading organic pollutants in water through advanced oxidation processes: A review. *Water Research,* 132**,** 177-189.

Matthews, P. D., McNaughter, P. D., Lewis, D. J. & O'Brien, P. 2017a. Shining a light on transition metal chalcogenides for sustainable photovoltaics. *Chemical Science,* 8**,** 4177-4187.

Matthews, P. D., McNaughter, P. D., Lewis, D. J. & O'Brien, P. 2017b. Shining a light on transition metal chalcogenides for sustainable photovoltaics. *Chem Sci,* 8**,** 4177-4187.

Matzek, L. W. & Carter, K. E. 2016. Activated persulfate for organic chemical degradation: A review. *Chemosphere,* 151**,** 178-188.

Merino, N., Qu, Y., Deeb, R. A., Hawley, E. L., Hoffmann, M. R. & Mahendra, S. 2016. Degradation and Removal Methods for Perfluoroalkyl and Polyfluoroalkyl Substances in Water. *ENVIRONMENTAL ENGINEERING SCIENCE,* 33**,** 615-649.

Mestre, A. S. & Carvalho, A. P. 2019. Photocatalytic Degradation of Pharmaceuticals Carbamazepine, Diclofenac, and Sulfamethoxazole by Semiconductor and Carbon Materials: A Review. *Molecules,* 24.

Miller, N. C. & Bernechea, M. 2018. Research Update: Bismuth based materials for photovoltaics. *APL Materials,* 6.

Minero, C., Pellizzari, P., Maurino, V., Pelizzetti, E. & Vione, D. 2008. Enhancement of dye sonochemical degradation by some inorganic anions present in natural waters. *Appl. Catal. B Environ.,* 77**,** 308-316.

Minitha, C. R. & Rajendrakumar, R. T. 2013. Synthesis and Characterization of Reduced Graphene Oxide. *Advanced Materials Research,* 678**,** 56-60.

Minnam Reddy, V. R., Pallavolu, M. R., Guddeti, P. R., Gedi, S., Yarragudi Bathal Reddy, K. K., Pejjai, B., Kim, W. K., Kotte, T. R. R. & Park, C. 2019. Review on Cu_2SnS_3, Cu_3SnS_4, and Cu_4SnS_4 thin films and their photovoltaic performance. *Journal of Industrial and Engineering Chemistry,* 76**,** 39-74.

Mohammed, S. & Fasnabi, P. 2016. Removal of dicofol from waste-water using advanced oxidation process. *Procedia Technol.,* 24**,** 645-653.

Mompelat, S., Le Bot, B. & Thomas, O. 2009. Occurrence and fate of pharmaceutical products and by-products, from resource to drinking water. *Environ Int,* 35**,** 803-14.

Moreno-Benito, M., Yamal-Turbay, E., Espuña, A., Pérez-Moya, M. & Graells, M. 2013. Optimal recipe design for Paracetamol degradation by advanced oxidation processes (AOPs) in a pilot plant. *In:* KRASLAWSKI, A. & TURUNEN, I. (eds.) *Computer Aided Chemical Engineering.* Elsevier.

Morimoto, N., Kubo, T. & Nishina, Y. 2016. Tailoring the oxygen content of graphite and reduced graphene oxide for specific applications. *Scientific reports,* 6**,** 21715.

Moussavi, G. & Shekoohiyan, S. 2016. Simultaneous nitrate reduction and acetaminophen oxidation using the continuous-flow chemical-less VUV process as an integrated advanced oxidation and reduction process. *J Hazard Mater,* 318**,** 329-338.

Mueller, N., Nowack, B., Oy, S. & Saari, J. 2010. Environment: Photocatalysis for water treatment. *ObservatoryNano***,** 1-4.

Muthoosamy, K. & Manickam, S. 2017. State of the art and recent advances in the ultrasound-assisted synthesis, exfoliation and functionalization of graphene derivatives. *Ultrasonics Sonochemistry,* 39**,** 478-493.

Ngigi, E. M., Nomngongo, P. N. & Ngila, J. C. 2019. Novel Z-scheme Co_3O_4/WO_3 nanocomposite performance in adsorption and photocatalytic degradation of ethylparaben and methylene blue in water. *Advances in Natural Sciences: Nanoscience and Nanotechnology,* 10.

Nilsen, E., Smalling, K. L., Ahrens, L., Gros, M., Miglioranza, K. S. B., Pico, Y. & Schoenfuss, H. L. 2019. Critical Review: Grand Challenges in Assessing the Adverse Effects of Contaminants of Emerging Concern on Aquatic Food Webs. *Environmental Toxicology and Chemistry,* 38**,** 46-60.

O'Shea, K. E. & Dionysiou, D. D. 2012. Advanced Oxidation Processes for Water Treatment. *The Journal of Physical Chemistry Letters,* 3**,** 2112-2113.

Olatunde, O. C., Kuvarega, A. T. & Onwudiwe, D. C. 2020. Photo enhanced degradation of contaminants of emerging concern in waste water. *Emerging Contaminants,* 6**,** 283-302.

Olatunde, O. C. & Onwudiwe, D. C. 2020. Chapter 3 - Copper-based ternary metal sulfide nanocrystals embedded in graphene oxide as photocatalyst in water treatment. *In:* AMRANE, A., RAJENDRAN, S., NGUYEN, T. A., ASSADI, A. A. & SHAROBA, A. M. (eds.) *Nanotechnology in the Beverage Industry.* Elsevier.

Onoda, M., Chen, X.-a., Sato, A. & Wada, H. 2000. Crystal structure and twinning of monoclinic Cu_2SnS_3. *Materials Research Bulletin,* 35**,** 1563-1570.

Ortiz, I., Rivero, M. J. & Margallo, M. 2019. Advanced oxidative and catalytic processes. 161-201.

Pan, X., Yan, L., Qu, R. & Wang, Z. 2018. Degradation of the UV-filter benzophenone-3 in aqueous solution using persulfate activated by heat, metal ions and light. *Chemosphere,* 196**,** 95-104.

Pan, X., Yang, M.-Q., Tang, Z.-R. & Xu, Y.-J. 2014. Noncovalently Functionalized Graphene-Directed Synthesis of Ultralarge Graphene-Based TiO2 Nanosheet Composites: Tunable Morphology and Photocatalytic Applications. *The Journal of Physical Chemistry C,* 118**,** 27325-27335.

Parsons, S. 2004. *Advanced Oxidation Processes for Water and Wastewater Treatment,* London, UK, IWA Publishing.

Pei, S., Wei, Q., Huang, K., Cheng, H.-M. & Ren, W. 2018. Green synthesis of graphene oxide by seconds timescale water electrolytic oxidation. *Nature Communications,* 9**,** 145.

Pejjai, B., Minnam Reddy, V. R., Gedi, S. & Park, C. 2018. Review on earth-abundant and environmentally benign Cu–Sn–X(X = S, Se) nanoparticles by chemical synthesis for sustainable solar energy conversion. *Journal of Industrial and Engineering Chemistry,* 60**,** 19-52.

Pendolino, F., Armata, N., Masullo, T. & Cuttitta, A. 2015. Temperature influence on the synthesis of pristine graphene oxide and graphite oxide. *Materials Chemistry and Physics,* 164**,** 71-77.

Peng, L., Xu, Z., Liu, Z., Wei, Y., Sun, H., Li, Z., Zhao, X. & Gao, C. 2015. An iron-based green approach to 1-h production of single-layer graphene oxide. *Nature communications,* 6**,** 1-9.

Persson, C. 2010. Electronic and optical properties of Cu_2ZnSnS_4 and $Cu_2ZnSnSe_4$. *Journal of Applied Physics,* 107**,** 053710.

Petrie, B., Barden, R. & Kasprzyk-Hordern, B. 2015. A review on emerging contaminants in wastewaters and the environment: Current knowledge, understudied areas and recommendations for future monitoring. *Water Research*, 72**,** 3-27.

Petrovic, M., Hernando, M. D., Díaz-Cruz, M. S. & Barceló, D. 2005. Liquid chromatography-tandem mass spectrometry for the analysis of pharmaceutical residues in environmental samples: a review. *J. Chromatogr. A*, 1067**,** 1-14.

Pfitzner, A. & Reiser, S. 2002. Refinement of the crystal structures of Cu_3PS_4 and Cu_3SbS_4 and a comment on normal tetrahedral structures. *Zeitschrift für Kristallographie - Crystalline Materials,* 217**,** 51 - 54.

Pignatello, J. J., Oliveros, E. & MacKay, A. 2006. Advanced Oxidation Processes for Organic Contaminant Destruction Based on the Fenton Reaction and Related Chemistry. *Critical Reviews in Environmental Science and Technology,* 36**,** 1-84.

Putra, E. K., Pranowo, R., Sunarso, J., Indraswati, N. & Ismadji, S. 2009. Performance of activated carbon and bentonite for adsorption of amoxicillin from wastewater: mechanisms, isotherms and kinetics. *Water Res.,* 43**,** 2419-2430.

Putri, L. K., Ong, W.-J., Chang, W. S. & Chai, S.-P. 2015. Heteroatom doped graphene in photocatalysis: A review. *Applied Surface Science,* 358**,** 2-14.

Qiu, X., Ji, S., Chen, C., Liu, G. & Ye, C. 2013. Synthesis, characterization, and surface-enhanced Raman scattering of near infrared absorbing Cu_3SbS_3 nanocrystals. *CrystEngComm,* 15.

Qu, Y., Zhang, C., Li, F., Chen, J. & Zhou, Q. 2010. Photo-reductive defluorination of perfluorooctanoic acid in water. *Water Res.,* 44**,** 2939–2947.

Radjenovic, J., Petrovic, M. & Barcelo, D. 2009. Fate and distribution of pharmaceuticals in wastewater and sewage sludge of the conventional activated sludge (CAS) and advanced membrane bioreactor (MBR) treatment. *Water Res,* 43**,** 831-41.

Radjenović, J., Petrović, M. & Barceló, D. 2009. Fate and distribution of pharmaceuticals in wastewater and sewage sludge of the conventional activated sludge (CAS) and advanced membrane bioreactor (MBR) treatment. *Water Research,* 43**,** 831-841.

Rani, P. & Jindal, V. K. 2013. Designing band gap of graphene by B and N dopant atoms. *RSC Advances,* 3**,** 802-812.

Redding, A. M., Cannon, F. S., Snyder, S. A. & Vanderford, B. J. J. W. r. 2009. A QSAR-like analysis of the adsorption of endocrine disrupting compounds, pharmaceuticals, and personal care products on modified activated carbons. 43**,** 3849-3861.

Regulacio, M. D. & Han, M. Y. 2016. Multinary I-III-VI_2 and I_2-II-IV-VI_4 Semiconductor Nanostructures for Photocatalytic Applications. *Acc Chem Res,* 49**,** 511-9.

Riva, F., Castiglioni, S., Fattore, E., Manenti, A., Davoli, E. & Zuccato, E. 2018. Monitoring emerging contaminants in the drinking water of Milan and assessment of the human risk. *International Journal of Hygiene and Environmental Health,* 221**,** 451-457.

Robert, D., Keller, V. & Keller, N. 2013. Immobilization of a semiconductor photocatalyst on solid supports: Methods, materials, and applications. *In:* PICHAT, P. (ed.) *Photocatalysis and Water Purification: From Fundamentals to Recent Applications.* Weinheim, Germany: Wiley-VCH.

Robinson, I., Junqua, G., Van Coillie, R. & Thomas, O. 2007. Trends in the detection of pharmaceutical products, and their impact and mitigation in water and wastewater in North America. *Analytical and Bioanalytical Chemistry,* 387**,** 1143-1151.

Rodgers-Gray, T. P., Jobling, S., Morris, S., Kelly, C., Kirby, S., Janbakhsh, A., Harries, J. E., Waldock, M. J., Sumpter, J. P. & Tyler, C. R. 2000. Long-term temporal effects on fish. *Environ. Sci. Technol.,* 34**,** 1521-1528.

Rodriguez-Narvaez, O. M., Peralta-Hernandez, J. M., Goonetilleke, A. & Bandala, E. R. 2017. Treatment technologies for emerging contaminants in water: A review. *Chemical Engineering Journal,* 323**,** 361-380.

Salimi, M., Esrafili, A., Jonidi Jafari, A., Gholami, M., Sobhi, H. R., Nourbakhsh, M. & Akbari-Adergani, B. 2019. Photocatalytic degradation of cefixime with MIL-125(Ti)-mixed linker decorated by g-C_3N_4 under solar driven light irradiation. *Colloids and Surfaces A: Physicochemical and Engineering Aspects,* 582**,** 123874.

Satyro, S., Saggioro, E. M., Veríssimo, F., Buss, D. F., de Paiva Magalhães, D. & Oliveira, A. 2017. Triclocarban: UV photolysis, wastewater disinfection, and ecotoxicity assessment using molecular biomarkers. *Environmental Science and Pollution Research,* 24**,** 16077-16085.

Sauvé, S. & Desrosiers, M. 2014 A review of what is an emerging contaminant. *Chemistry Central Journal,* 8**,** 1-7.

Sayadi, H., Trivedy, R. K. & Pathak, R. K. 2010. Pollution of Pharmaceuticals in Environment. *Journal of Industrial Pollution Control,* 26 89-94.

Scaria, J., Anupama, K. V. & Nidheesh, P. V. 2021. Tetracyclines in the environment: An overview on the occurrence, fate, toxicity, detection, removal methods, and sludge management. *Science of The Total Environment,* 771**,** 145291.

Sheldrick, W. S. & Wachhold, M. 1997. Solventothermal Synthesis of Solid-State Chalcogenidometalates. *Angewandte Chemie International Edition in English,* 36**,** 206-224.

Shi, T., Yin, W.-J., Al-Jassim, M. & Yan, Y. 2013. Structural, electronic, and optical properties of Cu_3-V-VI_4 compound semiconductors. *Applied Physics Letters,* 103.

Shin, H.-J., Kim, K. K., Benayad, A., Yoon, S.-M., Park, H. K., Jung, I.-S., Jin, M. H., Jeong, H.-K., Kim, J. M., Choi, J.-Y. & Lee, Y. H. 2009. Efficient Reduction of Graphite Oxide by Sodium Borohydride and Its Effect on Electrical Conductance. *Advanced Functional Materials,* 19**,** 1987-1992.

Silva, C. G., Monteiro, J., Marques, R. R., Silva, A. M., Martinez, C., Canle, M. & Faria, J. L. 2013. Photochemical and photocatalytic degradation of trans-resveratrol. *Photochem Photobiol Sci,* 12**,** 638-44.

Smith, A. T., LaChance, A. M., Zeng, S., Liu, B. & Sun, L. 2019. Synthesis, properties, and applications of graphene oxide/reduced graphene oxide and their nanocomposites. *Nano Materials Science,* 1**,** 31-47.

Sophia A, C. & Lima, E. C. 2018. Removal of emerging contaminants from the environment by adsorption. *Ecotoxicology and Environmental Safety,* 150**,** 1-17.

Staudenmaier, L. 1898. Verfahren zur Darstellung der Graphitsäure. *Berichte der deutschen chemischen Gesellschaft,* 31**,** 1481-1487.

Sturala, J., Luxa, J., Pumera, M. & Sofer, Z. 2018. Chemistry of Graphene Derivatives: Synthesis, Applications, and Perspectives. *Chemistry--A European Journal,* 24**,** 5992-6006.

Sun, M., Li, S., Zou, J., Cui, Z., Zhang, Q., Schiettekatte, F., Barba, D., Liu, B. & Wang, Y. 2020. Graphene-Wrapped $ZnMn_2O_4$ Nanoparticles with Enhanced Performance as Lithium-Ion Battery Anode Materials. *Nano,* 15.

Sutherland, D. L. & Ralph, P. J. 2019. Microalgal bioremediation of emerging contaminants - Opportunities and challenges. *Water Research,* 164 114921-114934.

Šutka, A., Järvekülg, M. & Gross, K. A. 2018. Photocatalytic Nanoheterostructures and Chemically Bonded Junctions Made by Solution-Based Approaches. *Critical Reviews in Solid State and Materials Sciences,* 44**,** 239-263.

Tahir, M. & Amin, N. S. 2015. Indium-doped TiO_2 nanoparticles for photocatalytic CO_2 reduction with H_2O vapors to CH_4. *Applied Catalysis B: Environmental,* 162**,** 98-109.

Tetorou, A., Makhatova, A. & Poulopoulos, S. G. 2019. Photochemical mineralization of Ibuprofen medicinal product by means of UV, hydrogen peroxide, titanium dioxide and iron. *Water Sci Technol,* 80**,** 2200-2205.

Torrellas, S. A., Rodríguez, A., Ovejero, G. & García, J., , 2016. Comparative adsorption performance of ibuprofen and tetracycline from aqueous solution by carbonaceous materials. *Chem. Eng. J.* , 283**,** 936-947.

Vadivel, S., Maruthamani, D., Paul, B., Dhar, S. S., Habibi-Yangjeh, A., Balachandran, S., Saravanakumar, B., Selvakumar, A. & Selvam, K. 2016. Biomolecule-assisted solvothermal synthesis of Cu_2SnS_3 flowers/RGO nanocomposites and their visible-light-driven photocatalytic activities. *RSC Advances,* 6**,** 74177-74185.

Valcarcel, Y., Alonso, S. G., Rodriguez-Gil, J. L., Maroto, R. R., Gil, A. & Catala, M. 2011. Analysis of the presence of cardiovascular and analgesic/anti-inflammatory/antipyretic pharmaceuticals in river- and drinking-water of the Madrid Region in Spain. *Chemosphere,* 82**,** 1062-71.

van Embden, J., Chesman, A. S. R. & Jasieniak, J. J. 2015. The Heat-Up Synthesis of Colloidal Nanocrystals. *Chemistry of Materials,* 27**,** 2246-2285.

van Embden, J., Latham, K., Duffy, N. W. & Tachibana, Y. 2013. Near-infrared absorbing $Cu_{12}Sb_4S_{13}$ and Cu_3SbS_4 nanocrystals: synthesis, characterization, and photoelectrochemistry. *J Am Chem Soc,* 135**,** 11562-71.

Venkanna, M. & Chakraborty, A. K. 2014. Synthesis and characterizations of graphene oxide and reduced graphene oxide nanosheets. *AIP Conference Proceedings,* 1591**,** 574-576.

von Sonntag, C. 2008. Advanced oxidation processes: mechanistic aspects. *Water Sci Technol,* 58**,** 1015-21.

Vykoukal, V., Bursik, J., Roupcova, P., Cullen, D. A. & Pinkas, J. 2019. Solvothermal hot injection synthesis of core-shell AgNi nanoparticles. *Journal of Alloys and Compounds,* 770**,** 377-385.

Wang, C. Y., Zhang, X., Song, X. N., Wang, W. K. & Yu, H. Q. 2016. Novel $Bi_{12}O_{15}Cl_6$ Photocatalyst for the Degradation of Bisphenol A under Visible-Light Irradiation. *ACS Appl Mater Interfaces,* 8**,** 5320-6.

Wang, H. & Dai, H. 2013. Strongly coupled inorganic–nano-carbon hybrid materials for energy storage. *Chemical Society Reviews,* 42**,** 3088-3113.

Wang, H., Maiyalagan, T. & Wang, X. 2012. Review on Recent Progress in Nitrogen-Doped Graphene: Synthesis, Characterization, and Its Potential Applications. *ACS Catalysis,* 2**,** 781-794.

Wang, H., Robinson, J. T., Diankov, G. & Dai, H. 2010. Nanocrystal Growth on Graphene with Various Degrees of Oxidation. *Journal of the American Chemical Society,* 132**,** 3270-3271.

Wang, J. & Wang, S. 2016. Removal of pharmaceuticals and personal care products (PPCPs) from wastewater: A review. *J Environ Manage,* 182**,** 620-640.

Wang, Q., Li, J. & Li, J. 2018. Enhanced thermoelectric performance of Cu_3SbS_4 flower-like hierarchical architectures composed of Cl doped nanoflakes via an in situ generated CuS template. *Phys Chem Chem Phys,* 20**,** 1460-1475.

Wang, W., Zhi, G., Liu, J., Hao, L., Yang, L., Zhao, Y. & Hu, Y. 2020. Effect of PVP content on photocatalytic properties of $CuSbS_2$ particles with chemical etching. *Journal of Nanoparticle Research,* 22.

Wang, X., Huang, X., Zuo, C. & Hu, H. 2004. Kinetics of quinoline degradation by O_3/UV in aqueous phase. *Chemosphere,* 55**,** 733-41.

Wang, X., Xing, W., Yu, B., Feng, X., Song, L. & Hu, Y. 2013. A facile and cost-effective approach to the reduction of exfoliated graphite oxide using sodium hypophosphite under acidic conditions. *Journal of Materials Chemistry C,* 1**,** 690-694.

Whittles, T. J., Veal, T. D., Savory, C. N., Yates, P. J., Murgatroyd, P. A. E., Gibbon, J. T., Birkett, M., Potter, R. J., Major, J. D., Durose, K., Scanlon, D. O. & Dhanak, V. R. 2019. Band Alignments, Band Gap, Core Levels, and Valence Band States in Cu_3BiS_3 for Photovoltaics. *ACS Applied Materials & Interfaces,* 11**,** 27033-27047.

Williams, G., Seger, B. & Kamat, P. V. 2008. TiO2-Graphene Nanocomposites. UV-Assisted Photocatalytic Reduction of Graphene Oxide. *ACS Nano,* 2**,** 1487-1491.

Wongso, V., Chung, H. K., Sambudi, N. S., Sufian, S., Abdullah, B., Wirzal, M. D. H. & Ang, W. L. 2020. Silica–carbon quantum dots decorated titanium dioxide as sunlight-driven photocatalyst to diminish acetaminophen from aquatic environment. *Journal of Photochemistry and Photobiology A: Chemistry,* 394**,** 112436.

Wu, Y., Deng, L., Bu, L., Zhu, S., Shi, Z. & Zhou, S. 2019. Degradation of diethyl phthalate (DEP) by vacuum ultraviolet process: influencing factors, oxidation products, and toxicity assessment. *Environmental Science and Pollution Research,* 26**,** 5435-5444.

Xi, L., Zhang, Y. B., Shi, X. Y., Yang, J., Shi, X., Chen, L. D., Zhang, W., Yang, J. & Singh, D. J. 2012. Chemical bonding, conductive network, and thermoelectric performance of the ternary semiconductors Cu^2SnX_3(X=Se, S) from first principles. *Physical Review B,* 86.

Xiao, F. & Pignatello, J. J. 2015. Interactions of triazine herbicides with biochar: steric and electronic effects. *Water Res.,* 80**,** 179-188.

Xu, D., Shen, S., Zhang, Y., Gu, H. & Wang, Q. 2013. Selective synthesis of ternary copper-antimony sulfide nanocrystals. *Inorg Chem,* 52**,** 12958-62.

Xu, T., Zhu, Y., Duan, J., Xia, Y., Tong, T., Zhang, L. & Zhao, D. 2020. Enhanced photocatalytic degradation of perfluorooctanoic acid using carbon-modified bismuth phosphate composite: Effectiveness, material synergy and roles of carbon. *Chemical Engineering Journal,* 395**,** 124991.

Xu, Y., Liu, T. J., Zhang, Y., Ge, F., Steel, R. M. & Sun, L. Y. 2017. Advances in technologies for pharmaceuticals and personal care products removal. *Journal of Materials Chemistry A,* 5**,** 12001-12014.

Yan, M., Wu, Y. L., Yan, Y., Yan, X., Zhu, F. F., Hua, Y. Q. & Shi, W. D. 2016. Synthesis and characterization of novel $BiVO_4/Ag_3VO$ heterojunction with enhanced visible-light-driven photocatalytic degradation of dyes. *ACS Sustainable Chem. Eng.,* 4**,** 757–766.

Yang, B., Wang, L., Han, J., Zhou, Y., Song, H., Chen, S., Zhong, J., Lv, L., Niu, D. & Tang, J. 2014. $CuSbS_2$ as a Promising Earth-Abundant Photovoltaic Absorber Material: A Combined Theoretical and Experimental Study. *Chemistry of Materials,* 26**,** 3135-3143.

Yang, Z.-z., Zheng, Q.-b., Qiu, H.-x., Li, J. & Yang, J.-h. 2015. A simple method for the reduction of graphene oxide by sodium borohydride with $CaCl_2$ as a catalyst. *New Carbon Materials,* 30**,** 41-47.

Ye, L.-H., Liu, B.-G. & Ding-Sheng, W. 2001. Ab initio Molecular Dynamics Study on Small Carbon Nanotubes. *Chinese Physics Letters,* 18**,** 1496.

Ying, G. G., Kookana, R. S. & Ru, Y. J. 2002. Occurrence and fate of hormone steroid in the environment. *Environ. Internat.,* 28 545-551.

Yu, L., Kokenyesi, R. S., Keszler, D. A. & Zunger, A. 2013. Inverse Design of High Absorption Thin-Film Photovoltaic Materials. *Advanced Energy Materials,* 3**,** 43-48.

Yu, P., Lowe, S. E., Simon, G. P. & Zhong, Y. L. 2015. Electrochemical exfoliation of graphite and production of functional graphene. *Current Opinion in Colloid & Interface Science,* 20**,** 329-338.

Zhai, Y.-T., Chen, S., Yang, J.-H., Xiang, H.-J., Gong, X.-G., Walsh, A., Kang, J. & Wei, S.-H. 2011. Structural diversity and electronic properties of Cu_2SnX_3(X=S, Se): A first-principles investigation. *Physical Review B,* 84.

Zhang, S., Li, B., Wang, X., Zhao, G., Hu, B., Lu, Z., Wen, T., Chen, J. & Wang, X. 2020. Recent developments of two-dimensional graphene-based composites in visible-light photocatalysis for eliminating persistent organic pollutants from wastewater. *Chemical Engineering Journal,* 390.

Zhang, Y., Huang, J., Yan, C., Sun, K., Cui, X., Liu, F., Liu, Z., Zhang, X., Liu, X., Stride, J. A., Green, M. A. & Hao, X. 2019. High open-circuit voltage $CuSbS_2$ solar cells achieved through the formation of epitaxial growth of $CdS/CuSbS_2$ hetero-interface by post-annealing treatment. *Progress in Photovoltaics: Research and Applications,* 27**,** 37-43.

Zhao, H., Li, G., Tian, F., Jia, Q., Liu, Y. & Chen, R. 2019. g-C_3N_4 surface-decorated $Bi_2O_2CO_3$ for improved photocatalytic performance: Theoretical calculation and photodegradation of antibiotics in actual water matrix. *Chemical Engineering Journal,* 366**,** 468-479.

Zhu, S., Liu, Y. G., Liu, S. B., Zeng, G. M., Jiang, L. H., Tan, X. F., Zhou, L., Zeng, W., Li, T. T. & Yang, C. P. 2017. Adsorption of emerging contaminant metformin using graphene oxide. *Chemosphere* 179**,** 20-28.

CHAPTER THREE

Temperature controlled pure phase evolution of Cu_9S_5 nanoparticles by solvothermal process

1.0 Introduction

The unique properties of semiconductor nanoparticles have made them a subject of intense research in recent times. These properties are strongly influenced by their morphology, phase and surface characteristics. Their potential application in various fields such as catalysis (Shanmugam *et al.*, 2020), non-linear optics (Chen *et al.*, 2014), photoelectrochemistry (Hao *et al.*, 2020), light emitting diodes (Chen *et al.*, 2020) and biosensing (Yue *et al.*, 2020) is dependent on the ability to manipulate these properties by controlling their size, shape and phases.

Metal nitrides, oxynitrides, oxides and sulphides are among the well explored semiconductors, with oxides and sulphides being the most prominent materials among them. However, most metal oxides are wide band gap semiconductors, due to their valence band comprising of a deep 2p oxygen orbital and the high effective mass of the hole carriers resulting from oxygen's 2p localization state (Shiga *et al.*, 2016, Raebiger *et al.*, 2007, Chandrasekaran *et al.*, 2019). Metal sulphides have therefore inspired great interest as semiconductors because of their suitable band position and electronic band gap. The ability of the sulphides to also exist in a variety of morphologies, crystallinity, and stoichiometries with excellent optical characteristics makes them potential materials in a variety of devices such as thermoelectric devices (Chen *et al.*, 2019), fuel cells, solar cells (Suárez *et al.*, 2017), sensors (Zhao *et al.*, 2020), lithium-ion batteries, non-volatile memory devices (Mazor *et al.*, 2009) and light-emitting diodes (Yoo and Kim, 2009).

Copper sulphides ($Cu_{2-x}S$) are one of the most studied semiconductor metal sulphides due to their wide range of stoichiometric compositions and phases, which influence their optical and electrical properties (Zhang *et al.*, 2019). They are excellent p-type semiconductors, a consequence of the copper vacancies in the crystal lattice and exhibit a stoichiometry dependent bandgap range of 1.2-2.0 eV (Han *et al.*, 2016). Some of the identified stoichiometries with their band gap energies include chalcocite (Cu_2S), 1.2 eV; digentite ($Cu_{1.8}S$ or Cu_9S_5), 1.55 eV; djurleite ($Cu_{1.95}S$), 1.3 eV; anilite ($Cu_{1.75}S$ or Cu_7S_4), 1.70 eV; and covellite (CuS), 2.0 eV (Li *et al.*, 2017, Abdelhady *et al.*, 2011). Cu_9S_5 crystallizes in the hexagonal digentite phase and has been explored in a variety of technologies such as solar cells and in sodium-ion batteries (Jing *et al.*, 2018). It has also showed potential as a material in thermoelectronics (Zhu and Wang, 2019), photoelectrochemicals and sensors (Cheng *et al.*, 2019) .

Development of synthetic routes to copper sulphides is still a rigorously researched area because methods that could offer control over the stoichiometry of the produced materials are still well sought. Some of the methods that have been explored for the synthesis of $Cu_{2-x}S$ include ultrasound (Behboudnia and Khanbabaee, 2007), subcritical and supercritical (Li *et al.*, 2018), mechanochemical (Li *et al.*, 2016), microwave (Zhang *et al.*, 2002), pyrolysis (Jing *et al.*, 2018) and solvothermal (Motaung *et al.*, 2019). Solvothermal synthesis is a widely used route due to the great influence on morphology that it affords by virtue of its moderate temperature requirement. The process also involves the use of environmentally benign solvents (Motaung *et al.*, 2019). The choice of precursors plays an important role on the final stoichiometry and phase of the nanomaterial synthesised. The use of single source precursors in the synthesis of nanoparticles has gained increased attention as it offers monodispersed products via a safe, mild and simple process (Malik *et al.*, 2001). Some of the complexes that have been explored as precursor compounds include dithiocarbamates (Zhu and Wang, 2019), thiadiazole (Cheng *et al.*, 2019), carbamothioyl (Saeed *et al.*, 2013) and thioubuiret (Abdelhady *et al.*, 2011). In the present work, copper(II) bis(*N*-methyl-*N*-phenyl dithiocarbamate) was utilised as single source precursor to prepare pure phase digentite by controlling the temperature of the reaction in the presence of oleylamine (OLA). The aim was to study the role of temperature in the evolution of pure phase of copper sulphide nanoparticles using a dithiocarbamate metal complex.

2.0 Experiment section

2.1 Materials

2.2 Synthesis of ammonium *N*-methyl-*N*-phenyl dithiocarbamate ligand

A previously reported method was used for the synthesis of the ammonium *N*–methyl–*N*–phenyl dithiocarbamate (Onwudiwe and Ajibade, 2010). Briefly, 0.05 mol of carbon disulphide was added into an ice-cold mixture of 0.05 mol *N*-methyl aniline and 15 mL of concentrated aqueous ammonia. The resulting solution was stirred vigorously for 6-7 h, to obtain a yellowish solid product which was filtered by suction and rinsed three times with 75 mL of cold ethanol.

2.3 Synthesis of Cu (II) bis *N*-methyl-*N*-phenyl dithiocarbamate.

Aqueous solutions of the ligand and metal salt in mole ratio of 2:1 were stirred together at ambient temperature for 1 h. The dark brown precipitate formed was filtered and washed severally with water and ethanol. The precipitate was allowed to dry overnight under vacuum and stored for further use.

2.4 Synthesis of Cu_9S_5 nanoparticles.

A specific amount of the precursor complex and 10 ml of oleylamine were introduced into a three-neck flask connected to a reflux and N_2 source. The set-up was then heated to the desired temperature of 200, 220, 240, 260 and 280 °C. The set up was allowed to run for 1 h and then left to cool down. The obtained nanoparticles were rinsed in a mixture of toluene and ethanol by centrifuging to remove excess capping agent and then dispersed in ethanol for characterization. Scheme 1 shows the synthesis steps for obtaining the pure phase Cu_9S_5.

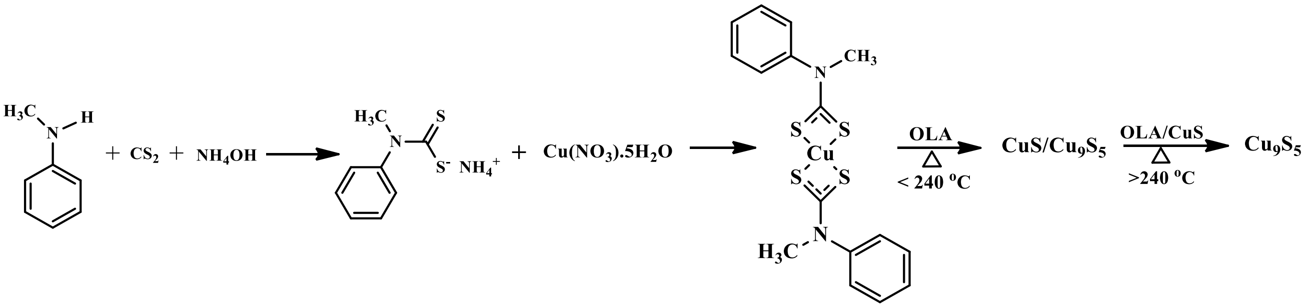

Scheme 1: Synthesis of pure phase Cu_9S_5 from copper(II) bis(*N*-methyl-*N*-phenyl dithiocarbamate) single source precursor.

2.5 Characterization

XRD spectra of the samples was measured with Phillips X'pert diffractometer with a secondary graphite monochromated Cu Kα radiation (λ = 1.546060 Å) at 40 kV/50 mA. PerkinElmer λ20 UV-vis spectrophotometer was used for the UV/visible measurements. The photoluminescence properties were studied using Perkin Elmer LS 45 fluorimeter. Scanning electron microscopy (SEM) and transmission electron microscopy (TEM) were used to study the morphology of the samples using FEI Quanta FEG 250 Environmental Scanning electron microscope (ESEM) and a TECNAI G2 (ACI) equipment (Hillsboro, OR, USA) respectively.

3.0 Results and discussion

3.1 X-ray diffraction studies of the nanoparticles

The XRD patterns of the products obtained after the thermolysis of the copper complex in OLA at different temperatures from 200 -280 °C are shown in Fig. 1. The patterns showed that a gradual evolution of digenite pure phase occurred as the thermolysis temperature was increased. At 200 °C, peaks that could be indexed to both CuS and Cu_9S_5 phases were observed. A reduction in the CuS peaks occurred with concomitant increase in the peak intensity of the Cu_9S_5 phase as the temperature was increased to 220 °C. A further increase in temperature to 240 °C, showed that a pure phase was obtained with peaks indexed to the rhombohedral Cu_9S_5 (JCPDS card No. 47-1748, space group: $R\underline{3}m$ (166), lattice constant: a = b= 3.930 Å, c = 48.140 Å and $\alpha = \beta = 90^{o}$, $\gamma = 120^{o}$) (Wang *et al.*, 2015). Beyond the 240 ºC, the pure phase remained constant, with a slight shift of the 111 peak to high wavelength region which could be attributed to change in crystallite size and lattice strain (Khorsand Zak *et al.*, 2011).

OLA has been reported to possess the ability to play the role not only as capping molecules and solvent in nanoparticle synthesis, but the presence of nitrogen confers on it some electron donating and reducing capabilities. The high affinity of the amine group accounts for OLA's fast interaction and its general tendency to produce large particle size and wide shape variety (Mbewana-Ntshanka *et al.*, 2020). The reducibility of OLA has recently been reported as an important factor in controlling the Cu^{2+}/Cu^{+} kinetics and reactions between $Cu_{2-x}S$ clusters and Cu^{+}, which are important in phase selectivity of $Cu_{2-x}S$ (Fu *et al.*, 2015). In the stoichiometric phase, Cu_2S, Cu^{+} are located at trigonal centres of S^{2-}. The Cu^{+} in this phase is highly mobile even at ambient temperature, generating holes in the valence band and increase in under coordinated S^{-1} (Liu *et al.*, 2019). With increased accumulation of S^{-1}, disulphide bonds are formed and the Cu^{+} are more favoured to occupy tetrahedral centres leading to mobility loss. Among copper sulphide phases, covellite (CuS) possess the highest hole concentration and the lowest Cu:S ratio, accounting for the slow mobility of Cu ion due to their tetrahedral coordination and increased disulphide bond. This disulphide bond could be reduced in the presence of reducing species or cations in lower oxidation states. Studies by Liu *et al.* (2017) and Fu *et al.* (2015) have shown that at low temperatures and with sufficient amount of S, the CuS phase is the most favoured, which accounts for the mixed phases obtained at temperatures below 220 °C in the present study. As the temperature of the system was increased, the reducing ability of OLA got enhanced (Tyagi *et al.*, 2019) and a reduction of the disulphide bond in CuS leads to the conversion of the CuS phase to the Cu_9S_5 phase, which was achieved at 240℃.

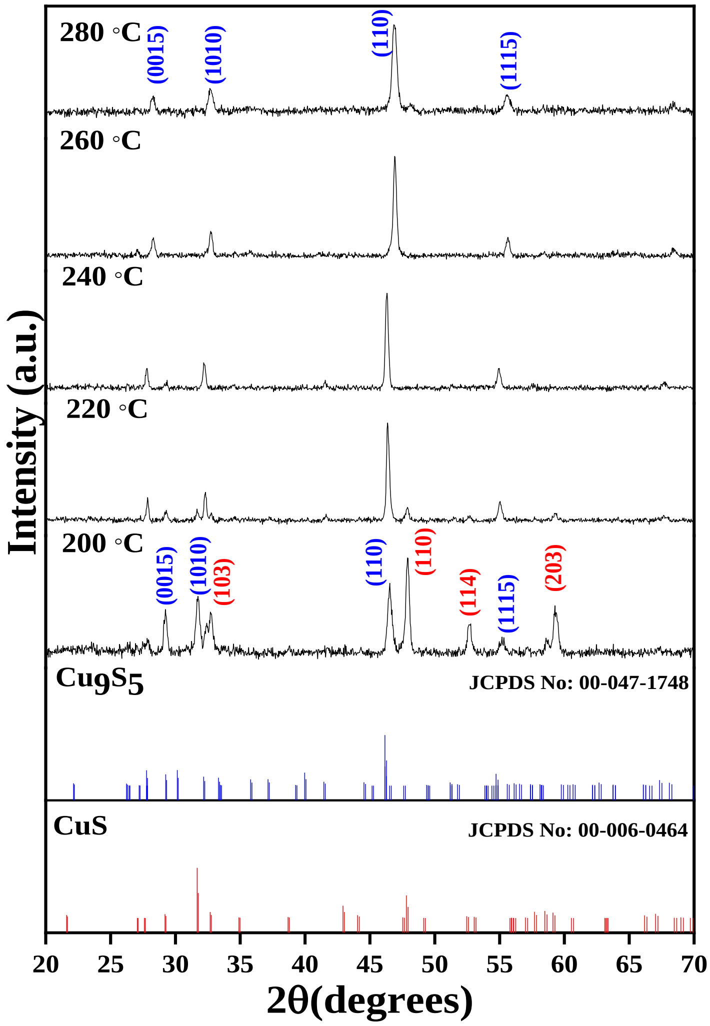

Fig. 1: XRD patterns of the copper sulphide nanoparticles obtained by the thermolysis of Cu(II) bis(*N*-methyl-*N*-phenyl dithiocarbamate) in the temperature range of 200-280℃.

3.2 Morphological studies

The TEM images of the pure phase Cu_9S_5 obtained at 240, 260 and 280℃ are shown in Fig. 2. The nanoparticles were rectangular-shaped at all the temperatures and showed a decrease in size as temperature increases. The length of the nanoparticles was 176 ± 51.9, 111.6 ± 21.1 and 82.1 ± 21. 8 nm. Thus, a narrow size distribution was obtained at higher temperature. Measurement of the width of the cubes also showed a gradual decrease in width with increase in temperature. The obtained values were 34.7 ± 13.3, 12.9 ± 2.3 and 12.1 ± 5.2 nm recorded at 240℃C, 260℃C, and 280℃C respectively. Generally, it has been established that in wet chemical synthesis, nucleation of nanoparticles is enhanced at high temperatures, while particle growth is more favoured at relatively lower temperatures. Thus, particles with larger size are obtained at low temperatures, with a decrease in particle size with temperature (Liu *et al.*, 2020).

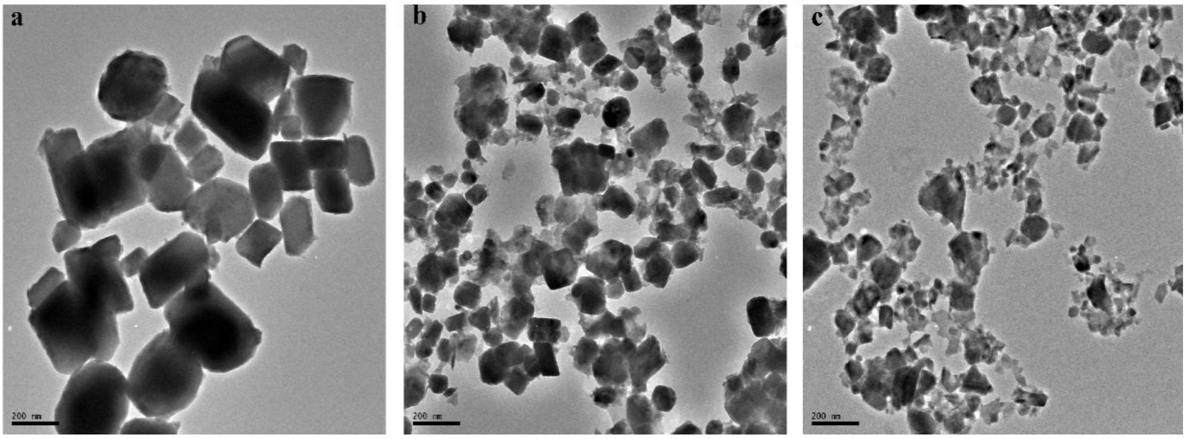

Fig 2: TEM images of pure phase Cu_9S_5 obtained at (a) 240℃ (b) 260℃ and (c) 280℃ using Cu(II) bis(*N*-methyl-*N*-phenyl dithiocarbamate) as single source precursor.

The SEM, elemental mapping image and EDS spectra of the pure Cu_9S_5 obtained at 280 °C are shown in Fig 3. The SEM image showed that the nanoparticles were agglomerated, with the elemental mapping image showing the uniform distribution of Cu and S in the nanoparticle. From the EDS spectra a Cu/S ratio of 1.87:1was obtained for the nanoparticle obtained at 280 °C which was in close agreement with the stoichiometric ratio in the digenite phase of $Cu_{2-x}S$.

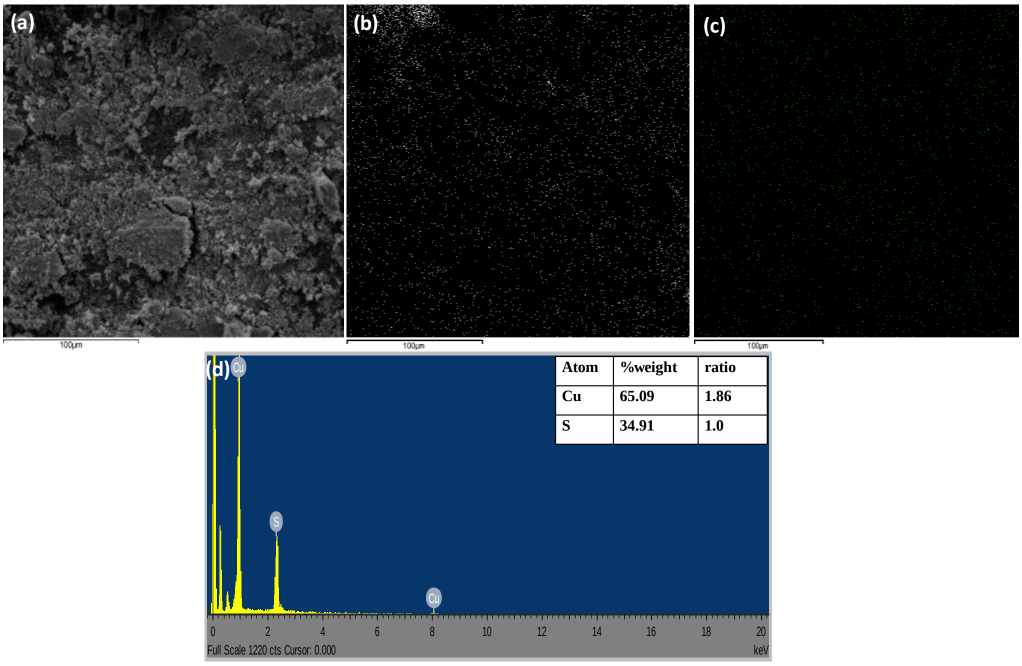

Atom	%weight	ratio
Cu	65.09	1.86
S	34.91	1.0

Fig 3: (a) Elemental mapping of Cu_9S_5 (b) Cu, (c) S elements and the EDX spectra at of 280 °C.

3.3 Optical properties

The optical properties of the synthesized nanoparticles were studied by measuring the absorbance using the UV-vis spectrophotometer and the corresponding Tauc plots were obtained as shown in Fig 3, using the equation (Tauc *et al.*, 1966):

$$\alpha h\nu \propto (h\nu - E_g)^n \tag{1}$$

Where ν is the light frequency, *h* is the Planck's constant, α is the absorption coefficient of the material and E_g represents the band gap. The exponent n indicates the nature of the band-gap and it can take values of 2, ½, 2/3 and 1/3, which corresponds to direct allowed, indirect allowed, forbidden direct and forbidden indirect transitions respectively. The band gap E_g of the nanoparticles was obtained by extrapolating the linear portion of the plots $(\alpha h\nu)^2$ against hν to α = 0. Currently, there is no general consensus on the nature of transitions for most $Cu_{2-x}S$ phases, leading to both direct and indirect transitions being reported for most phases (Pop *et al.*, 2011). A large range of band gap energies has been reported for different $Cu_{2-x}S$ phases, which arises due to the large number of mixed phases and compositions coupled with different crystal size and shapes (Safrani *et al.*, 2013).

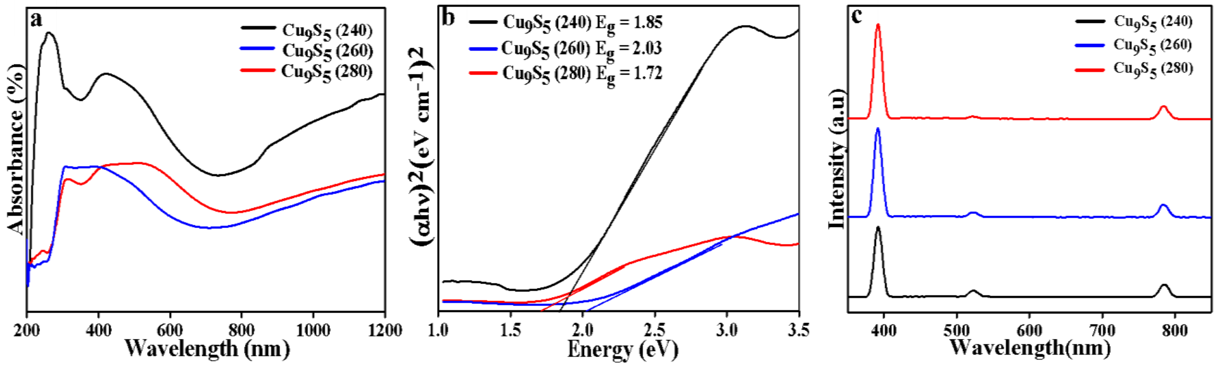

Fig 4: Optical properties of Cu_9S_5 obtained from Cu(II) bis(*N*-methyl-*N*-phenyl dithiocarbamate) as single source precursor: (a) Absorption spectra, (b) Tauc plots and (c) Photoluminescence spectra.

All the samples exhibited broad absorption in the visible region (300 – 500 nm) and tailed into the near infra-red region (Fig. 4a). The absorption onset for the three samples was at ~ 350 nm and the spectra showed an increase in absorbance in the near edge region indicating that the bandgap value will be obtained in the near infra-red region (Adekoya *et al.*, 2019). The increase in absorption at higher wavelengths may be ascribed to free-carrier intra-band absorbance (Zhao *et al.*, 2009). The direct band gap for the three samples obtained from the Tauc plots (Fig. 4b) were 1.85, 2.03 and 1.72 eV for the Cu_9S_5 samples obtained at 240, 260 and 280℃ respectively, which are in agreement with values previously reported in literature (Li *et al.*, 2017, Itzhak *et al.*, 2018, Senthilkumar and Moorthy Babu, 2016).This difference in band gaps for the samples could be attributed to difference in size, stoichiometric variation and the arrangement of the cations and anions in the atomic structure of the compounds.

The emission spectra of the ethanol solution of the Cu_9S_5 samples irradiated at 400 nm is shown in Fig. 4c. The three nanostructures showed similar emission spectra with three peaks observed at 390, 522 and 783 nm which corresponded to energy values of 3.2, 2.3 and 1.57 eV respectively. These observed peaks are in agreement with the absorption spectra of the samples and the peak at 390 nm could be assigned to the near band edge emission. The peaks at 522 and 783 nm both correspond to the band to band transitions in the Cu_9S_5 nanoparticles.

4.0 Conclusion

The synthesis of pure phase Cu_9S_5 using a single source precursor route was explored and the optical and morphological properties of the obtained nanoparticles were studied. The synthetic route was observed to induce a selectivity in the stoichiometric phase by changing the reaction temperature, which also influenced the properties of the OLA employed as solvent and capping agent in the reaction system. The obtained materials showed varying morphological, and optical properties with change in temperature. The band gap energy for the nanoparticles varied between 1.72-2.03 eV in the temperature range studied. While the nanoparticles exhibited the same shape, the dimension the nanoparticles varied with temperature. The length and width of the nanoparticles, decreased with increasing temperature with values in the range of 82-179 nm and 12-34 nm for the length and width respectively. This study has shown possibility of selectively tuning the phase purity of $Cu_{2-x}S$ prepared through the single source precursor route by altering the reaction temperature, which results in the solvent property modification and enhanced phase selectivity.

5.0 Reference

Abdelhady, A. L., Ramasamy, K., Malik, M. A., O'Brien, P., Haigh, S. J. & Raftery, J. 2011. New routes to copper sulfide nanostructures and thin films. *Journal of Materials Chemistry,* 21**,** 17888-17895.

Adekoya, J. A., Khan, M. D. & Revaprasadu, N. 2019. Phase transition in $Cu_{2+x}SnS_{3+y}$ ($0 \leq x \leq 2$; $0 \leq y \leq 1$) ternary systems synthesized from complexes of coumarin derived thiocarbamate motifs: optical and morphological properties. *RSC Advances,* 9**,** 35706-35716.

Behboudnia, M. & Khanbabaee, B. 2007. Investigation of nanocrystalline copper sulfide Cu_7S_4 fabricated by ultrasonic radiation technique. *Journal of Crystal Growth,* 304**,** 158-162.

Chandrasekaran, S., Zhang, P., Peng, F., Bowen, C., Huo, J. & Deng, L. 2019. Tailoring the geometric and electronic structure of tungsten oxide with manganese or vanadium doping toward highly efficient electrochemical and photoelectrochemical water splitting. *Journal of Materials Chemistry A,* 7**,** 6161-6172.

Chen, J. L. T., Nalla, V., Kannaiyan, G., Mamidala, V., Ji, W. & Vittal, J. J. 2014. Synthesis and nonlinear optical switching of Bi_2S_3 nanorods and enhancement in the NLO response of Bi_2S_3@Au nanorod-composites. *New Journal of Chemistry,* 38**,** 985-992.

Chen, W.-C., Shiao, J.-H., Tsai, T.-L., Jiang, D.-H., Chen, L.-C., Chang, C.-H., Lin, B.-H., Lin, J.-H. & Kuo, C.-C. 2020. Multiple Scattering from Electrospun Nanofibers with Embedded Silver

Nanoparticles of Tunable Shape for Random Lasers and White-Light-Emitting Diodes. *ACS Applied Materials & Interfaces,* 12**,** 2783-2792.

Chen, X., Zhang, H., Zhao, Y., Liu, W.-D., Dai, W., Wu, T., Lu, X., Wu, C., Luo, W., Fan, Y., Wang, L., Jiang, W., Chen, Z.-G. & Yang, J. 2019. Carbon-Encapsulated Copper Sulfide Leading to Enhanced Thermoelectric Properties. *ACS Applied Materials & Interfaces,* 11**,** 22457-22463.

Cheng, Y., Deng, S., Sun, F. & Zhou, Y.-H. 2019. Synthesis of luminescent Cu_9S_5 nanoclusters from copper-2,5-dimercapto-1,3,4-thiadiazole coordination polymer as pH sensor. *Journal of Luminescence,* 210**,** 38-46.

Fu, W., Liu, L., Yang, G., Deng, L., Zou, B., Ruan, W. & Zhong, H. 2015. Oleylamine-Assisted Phase-Selective Synthesis of $Cu_{2-x}S$ Nanocrystals and the Mechanism of Phase Control. *Particle & Particle Systems Characterization,* 32**,** 907-914.

Han, S. K., Gu, C., Zhao, S., Xu, S., Gong, M., Li, Z. & Yu, S. H. 2016. Precursor Triggering Synthesis of Self-Coupled Sulfide Polymorphs with Enhanced Photoelectrochemical Properties. *J Am Chem Soc,* 138**,** 12913-12919.

Hao, R., Peng, Z. & Zhang, B. 2020. Single-Molecule Fluorescence Microscopy for Probing the Electrochemical Interface. *ACS Omega,* 5**,** 89-97.

Itzhak, A., Teblum, E., Girshevitz, O., Okashy, S., Turkulets, Y., Burlaka, L., Cohen-Taguri, G., Shawat Avraham, E., Noked, M., Shalish, I. & Nessim, G. D. 2018. Digenite (Cu_9S_5): Layered p-Type Semiconductor Grown by Reactive Annealing of Copper. *Chemistry of Materials,* 30**,** 2379-2388.

Jing, M., Li, F., Chen, M., Zhang, J., Long, F., Jing, L., Lv, X., Ji, X. & Wu, T. 2018. Facile synthetic strategy to uniform Cu_9S_5 embedded into carbon: A novel anode for sodium-ion batteries. *Journal of Alloys and Compounds,* 762**,** 473-479.

Khorsand Zak, A., Abd. Majid, W. H., Abrishami, M. E. & Yousefi, R. 2011. X-ray analysis of ZnO nanoparticles by Williamson–Hall and size–strain plot methods. *Solid State Sciences,* 13**,** 251-256.

Li, S., Cheng, W., Liu, X., Wang, C., Li, W. & Yu, S. 2018. Supercritical methanol synthesis, phase evolution and formation mechanism of $Cu_{1.8}S$ and Cu_9S_5/CuS complex microcrystal. *The Journal of Supercritical Fluids,* 133**,** 429-436.

Li, S., Ge, Z.-H., Zhang, B.-P., Yao, Y., Wang, H.-C., Yang, J., Li, Y., Gao, C. & Lin, Y.-H. 2016. Mechanochemically synthesized sub-5 nm sized CuS quantum dots with high visible-light-driven photocatalytic activity. *Applied Surface Science,* 384**,** 272-278.

Li, S., Zhang, Z., Yan, L., Jiang, S., Zhu, N., Li, J., Li, W. & Yu, S. 2017. Fast synthesis of CuS and Cu_9S_5 microcrystal using subcritical and supercritical methanol and their application in photocatalytic degradation of dye in water. *The Journal of Supercritical Fluids,* 123**,** 11-17.

Liu, H., Zhang, H., Wang, J. & Wei, J. 2020. Effect of temperature on the size of biosynthesized silver nanoparticle: Deep insight into microscopic kinetics analysis. *Arabian Journal of Chemistry,* 13**,** 1011-1019.

Liu, M., Liu, Y., Gu, B., Wei, X., Xu, G., Wang, X., Swihart, M. T. & Yong, K. T. 2019. Recent advances in copper sulphide-based nanoheterostructures. *Chem Soc Rev,* 48**,** 4950-4965.

Liu, Y., Liu, M. & Swihart, M. T. 2017. Reversible Crystal Phase Interconversion between Covellite CuS and High Chalcocite Cu_2S Nanocrystals. *Chemistry of Materials,* 29**,** 4783-4791.

Malik, M. A., Revaprasadu, N. & O'Brien, P. 2001. Air-Stable Single-Source Precursors for the Synthesis of Chalcogenide Semiconductor Nanoparticles. *Chemistry of Materials,* 13**,** 913-920.

Mazor, H., Golodnitsky, D., Burstein, L. & Peled, E. 2009. High Power Copper Sulfide Cathodes for Thin-Film Microbatteries. *Electrochemical and Solid-State Letters,* 12**,** A232.

Mbewana-Ntshanka, N. G., Moloto, M. J. & Mubiayi, P. K. 2020. Role of the amine and phosphine groups in oleylamine and trioctylphosphine in the synthesis of copper chalcogenide nanoparticles. *Heliyon,* 6**,** e05130.

Motaung, M. P., Osuntokun, J. & Onwudiwe, D. C. 2019. The heat-up synthesis of monodispersed Bi_2S_3 and Cu_7S_4 nanoparticles from novel precursor complexes and their characterizations. *Materials Science in Semiconductor Processing,* 99**,** 92-98.

Onwudiwe, D. C. & Ajibade, P. A. 2010. Synthesis and characterization of metal complexes of *N*-alkyl-*N*-phenyl dithiocarbamates. *Polyhedron* 29 1431-1436.

Pop, A., Popescu, V., Danila, M. & Batin, M. 2011. Optical properties of CU_xS NANO-powders. *Chalcogenide Letters,* 8**,** 363-370.

Raebiger, H., Lany, S. & Zunger, A. 2007. Origins of the p-type nature and cation deficiency in Cu_2O and related materials. *Physical Review B,* 76**,** 045209.

Saeed, S., Rashid, N. & Ahmad, K. S. 2013. Aerosol-assisted chemical vapor deposition of copper sulfide nanostructured thin film from newly synthesized single-source precursor. *Turkish Journal of Chemistry,* 37**,** 796-804.

Safrani, T., Jopp, J. & Golan, Y. 2013. A comparative study of the structure and optical properties of copper sulfide thin films chemically deposited on various substrates. *RSC Advances,* 3**,** 23066.

Senthilkumar, M. & Moorthy Babu, S. 2016. Crystal structure controlled synthesis and characterization of copper sulfide nanoparticles. *AIP Conference Proceedings,* 1731**,** 050131.

Shanmugam, M., Sagadevan, A., Charpe, V. P., Pampana, V. K. K. & Hwang, K. C. 2020. Cu_2O Nanocrystals-Catalyzed Photoredox Sonogashira Coupling of Terminal Alkynes and Arylhalides Enhanced by CO_2. *ChemSusChem,* 13**,** 287-292.

Shiga, Y., Umezawa, N., Srinivasan, N., Koyasu, S., Sakai, E. & Miyauchi, M. 2016. A metal sulfide photocatalyst composed of ubiquitous elements for solar hydrogen production. *Chemical Communications,* 52**,** 7470-7473.

Suárez, J. A., Plata, J. J., Márquez, A. M. & Sanz, J. F. 2017. Effects of the capping ligands, linkers and oxide surface on the electron injection mechanism of copper sulfide quantum dot-sensitized solar cells. *Physical Chemistry Chemical Physics,* 19**,** 14580-14587.

Tauc, J., Grigorovici, R. & Vancu, A. 1966. Optical Properties and Electronic Structure of Amorphous Germanium. *physica status solidi (b),* 15**,** 627-637.

Tyagi, A., Kole, G. K., Shah, A. Y., Wadawale, A., Srivastava, A. P., Kumar, M., Kedarnath, G. & Jain, V. K. 2019. Accessing copper-tin-sulfide nanostructures from diorganotin(IV) and copper(I) 2-pyrazinyl thiolates. *Journal of Organometallic Chemistry,* 887**,** 24-31.

Wang, Y., Liu, F., Ji, Y., Yang, M., Liu, W., Wang, W., Sun, Q., Zhang, Z., Zhao, X. & Liu, X. 2015. Controllable synthesis of various kinds of copper sulfides (CuS, Cu_7S_4, Cu_9S_5) for high-performance supercapacitors. *Dalton Trans,* 44**,** 10431-7.

Yoo, S. H. & Kim, C. K. 2009. Nanocomposite Encapsulation of CuS:Eu Light-Emitting Diode Phosphors for the Enhancement of the Stability Against Moisture. *Journal of The Electrochemical Society,* 156**,** J170.

Yue, H. Y., Zhang, H. J., Huang, S., Lu, X. X., Gao, X., Song, S. S., Wang, Z., Wang, W. Q. & Guan, E. H. 2020. Highly sensitive and selective dopamine biosensor using Au nanoparticles-ZnO nanocone arrays/graphene foam electrode. *Materials Science and Engineering: C,* 108**,** 110490.

Zhang, K., Khan, M. W., Zuo, X., Yang, Q., Tang, H., Wu, M. & Li, G. 2019. Controllable synthesis and photoelectric properties of interconnected and self-assembled nanocomposite of porous hollow Cu_7S_4/CuS and nitrogen-doped graphene oxide. *Electrochimica Acta,* 307**,** 64-75.

Zhang, Y., Qiao, Z.-P. & Chen, X.-M. 2002. Microwave-Assisted Elemental-Direct-Reaction Route to Nanocrystalline Copper Sulfides Cu_9S_8 and Cu_7S_4. *Journal of Solid State Chemistry,* 167**,** 249-253.

Zhao, J., Wang, S., Zhang, S., Zhao, P., Wang, J., Yan, M., Ge, S. & Yu, J. 2020. Peptide cleavage-mediated photoelectrochemical signal on-off via CuS electronic extinguisher for PSA detection. *Biosensors and Bioelectronics,* 150**,** 111958.

Zhao, Y., Pan, H., Lou, Y., Qiu, X., Zhu, J. & Burda, C. 2009. Plasmonic $Cu_{2-x}S$ Nanocrystals: Optical and Structural Properties of Copper-Deficient Copper(I) Sulfides. *Journal of the American Chemical Society,* 131**,** 4253-4261.

Zhu, H. & Wang, L. 2019. Smart window based on Cu_7S_4/hydrogel composites with fast photothermal response. *Solar Energy Materials and Solar Cells,* 202**,** 110109.

CHAPTER FOUR

Bismuth sulphide nanorods from the solvothermal process: effect of reaction temperature on microstructural and optical properties

1.0 Introduction

Semiconductor metal chalcogenide nanocrystals have attracted much attention in recent years because of their unique size and shape dependent physical and chemical properties. This has influenced the focus of much research on developing synthetic routes which offer much control over material's morphology (Xiao *et al.*, 2012b). The tunability of the properties of these nanocrystals has made them potential materials for application in different optoelectronic technologies such as light emitting diodes (Song and Yang, 2012, Xiong *et al.*, 2019, Kwon *et al.*, 2015), solar energy conversion (Meyer *et al.*, 2019, Tributsch, 1984) and biological imaging (Joicy and Thangadurai, 2021, Shen and Wang, 2013, Ren *et al.*, 2021). Bismuth sulphide ($B_{i2}S_3$) is an important V-VI semiconductor material, that has gained much attention because of its potential application in solar cells (Liao *et al.*, 2012, Becerra *et al.*, 2011), photocatalysis (Helal *et al.*, 2016, Sharma and Khare, 2017) and bioimaging (Wang *et al.*, 2016, Zhang *et al.*, 2019).

The synthesis of bismuth sulphide majorly proceeded via either solvothermal (Xiao *et al.*, 2012a, Zhou *et al.*, 2015) or hydrothermal processes (Sun *et al.*, 2019), with process parameters such as precursor nature, sulphur source, solvent, reaction temperature and time explored in modulating the properties of the nanoparticles. Recently, other methods such as chemical precipitations and mechanochemical route to Bi_2S_3 have also been reported (Moyseowicz, 2019, Malca *et al.*, 2016). However, the solvothermal techniques remained the most explored route to Bi_2S_3 due to the ease it offers for property modification. Also, the development of novel precursor materials has also increased the interest in solvothermal processes. Recently, the photothermal properties of $B_{i2}S_3$ was reportedly enhanced via the solvothermal synthesis of a defected Bi_2S_3 nanorods (Jiang *et al.*, 2020).

The use of single source precursors in the synthesis of metal sulphide nanoparticles has continued to grow because it offers a simple, mild and safe route to nanoparticle synthesis (Malik *et al.*, 2001). Also, the influence of precursor chemistry on the process is limited as the precursor incorporates all the elements of the nanoparticles in a single metal complex. Different metal complexes have been explored as precursors in nanoparticle synthesis including dithiocarbamate complexes (Onwudiwe and Nkwe, 2020), thiourea (Stavila *et al.*, 2009), xanthate (Koh *et al.*, 2003), dithioate and thiosemicarbaxide (Stavila *et al.*, 2009). In this present study, a bismuth N-methyl N-phenyl dithiocarbamate complex was prepared and thermolyzed via a heat-up process in a mixture of high boiling point organic solvents. The effect of the temperature of synthesis on the microstructural and optical properties of the obtained nanoparticles were studied.

2.0 Experimental

2.1 Chemicals and instruments

Bi(III) nitrate pentahydrate, carbon disulphide (CS_2), oleylamine (OLA), octadecene, dodecanethiol (DDT), methanol, toluene, N-methyl aniline, and ammonium hydroxide (NH_4OH) solution used for this study were all of analytical grade and used as supplied by Sigma-Aldrich. For structural characterization, XRD spectra were recorded on a Phillips X'pert diffractometer with a secondary graphite monochromated Cu K α radiation (I = 1.546060 Å) at 40 kV/50 mA. The optical properties of the nanoparticles were studied using both absorption and emission spectra. UV/Vis-NIR measurement was recorded on a PerkinElmer λ20 UV-vis-NIR spectrophotometer, while the emission spectra were recorded using PerkinElmer LS 45 fluorimeter. Scanning electron microscopy (SEM) and transmission electron microscopy (TEM) measurements were carried out on a FE-SEM FEI 430 Nova NanoSEM system and FEI Tecnai G^2 Twin at 20 kV respectively.

2.2 Synthesis of bismuth(III) tris (*N*-methyl-*N*-phenyl dithiocarbamate)

The dithiocarbamate ligand was prepared by following an earlier reported method (Motaung *et al.*, 2019). In a typical synthesis, equal mole of N-methyl aniline and CS_2 were measured into a round bottom flask and stirred for about 10 min under ice-cooled condition. Afterwards, excess amount of NH_4OH was added and the mixture was left to stir for 4 h. The light-yellow precipitate formed was filtered under vacuum and washed severally with ice-cold methanol. The dried ligand was stored in an airtight container under refrigeration. The bismuth complex was prepared by mixing aqueous solutions of $Bi(NO_3)_3{\cdot}5H_2O$ and the ligand together in a round bottom flask and stirred continuously for 1 h. The bright yellow precipitate obtained was then washed with methanol and water to remove any unreacted metal salt and ligand. The obtained metal complex was dried under vacuum and stored for further use.

2.3 Synthesis of Bi_2S_3 nanoparticles

Bi_2S_3 nanoparticles were prepared by thermolysis of the metal complex in a mixture of high boiling liquids. In a typical synthesis, a weighted amount of the metal complex was measured into a three neck round bottom flask connected to a condenser and a N_2 gas source. The mixture of solvents: 6 mL of octadecene, 2 mL of DDT and 2 mL of OLA were measured into the round bottom flask and then mounted on a digitally controlled heating mantle. The temperature of the heating mantle was set to the target temperature of 120 - 220 °C at a heating rate of 10 ^oC/min, and the reaction was held at these respective target temperatures for 1 h and allowed to cool down naturally. Afterwards, ethanol was used to precipitate the obtained nanoparticles from the mixture and then recovered by centrifugation. The obtained nanoparticles were washed thrice with a mixture of ethanol and toluene. The nanoparticle was then dispersed in ethanol and allowed to dry under vacuum to obtain the Bi_2S_3 nanoparticles.

3.0 Results and discussion

3.1 FTIR spectral studies of the Bi_2S_3

The presence of NRH_2 and SRH group of OLA and DDT on the surface of the nanoparticles was studied using FTIR spectroscopy. The FTIR spectra of Bi_2S_3 synthesized at temperature of 180 – 220 °C is shown in Fig. 1. In all the samples, the antisymmetric and symmetric stretching vibration bands of methyl and methylene groups could be observed at 2832-3000 cm^{-1}, and at around 1475-1430 cm-1 for the deformation vibrations. However, at synthesis conditions between 120-180 °C, the vibration mode of the N-H bond at 3500-3300 cm^{-1} appears significantly enhanced. This could be attributed to a strong interaction between surface of the nanoparticles and the N-H group of OLA (Castellanos-Rubio *et al.*, 2016). This strong interaction seemed to diminish with increase in the reaction temperature and it is relatively constant above 180 °C. The vibrational frequency due to the S-H group of DDT was observed at around 2340-2330 cm^{-1}, with a decrease in broadness as temperature increased (Nyquist, 2001). This could be attributed to a reduction in the interaction between the N-H group of OLA and the S-H group in DDT. This influence of temperature on the activity of the capping agent could influence the microstructural and optical properties of the obtained nanoparticles. In the synthesis solvent mixture, octadecene is a non-coordinating solvent and only served as a solvent in the reaction, while DDT and OLA are coordinating solvents. This is confirmed by the absence of any peak due to octadecene in the spectra. When a mixture of solvents is employed in the synthesis of nanoparticles, properties such as crystallite size, crystallinity and morphology of the nanoparticles can be altered by varying the nature of the solvent. As reported by Bernard *et al.* (2018) changing the volume composition of a mixture of solvents could alter the nature of the reducing power of the solvents, thereby influencing the particle size, crystallinity and surface characteristic of obtained nanoparticles.

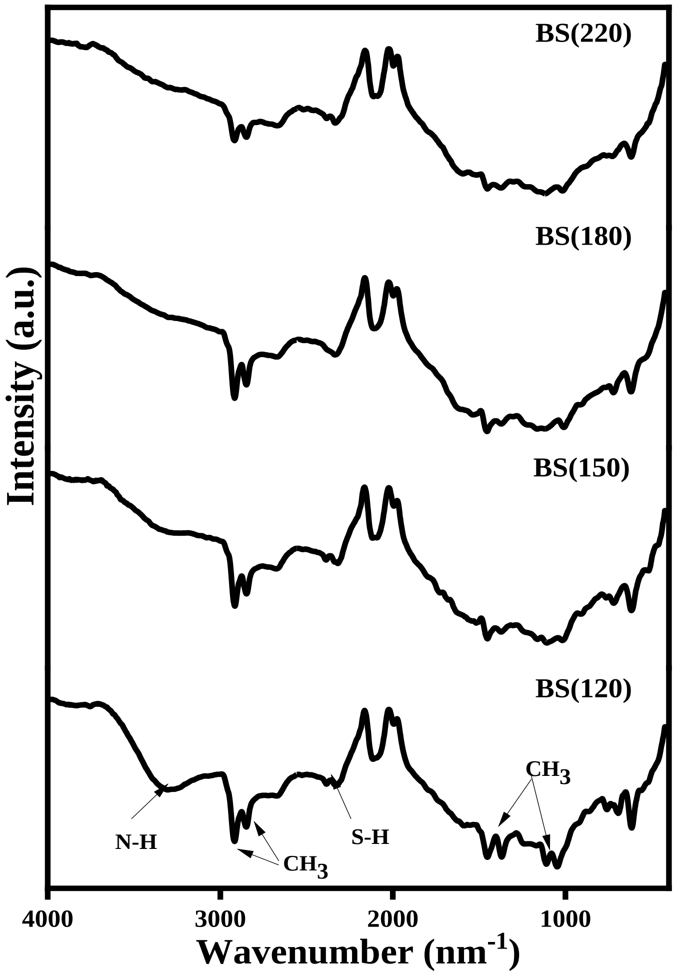

Fig 1: FTIR spectra of Bi_2S_3 obtained at 120, 150, 180 and 220 °C

3.2 Structural properties of Bi_2S_3

Fig. 2(a) shows the XRD spectra of the prepared Bi_2S_3 nanorods obtained in the temperature range of 120-220 °C. All the Bi_2S_3 showed peaks that could be indexed to the orthorhombic phase of Bi_2S_3, with lattice parameters a = 11.319, b = 3.992 and c = 11.17; space group pnma and space group No: 62. The analysis of the XRD spectra, showed that there was a marked variation in the intensity and nature of the peaks with temperature increase (fig. 2b). The intensity of the peaks initially increased upon temperature increase from 120-150 °C, but reduced significantly as the temperature attained 180 °C. As the temperature increased from 180 to 220 °C, a significant increase in the intensity of the peaks was further observed. This further affirms the earlier suggestion from the FTIR spectroscopy, that there was an alteration in the capping properties of OLA and DDT with change in reaction temperature. This could be attributed to the activity of the capping agents, which is significantly influenced by temperature.

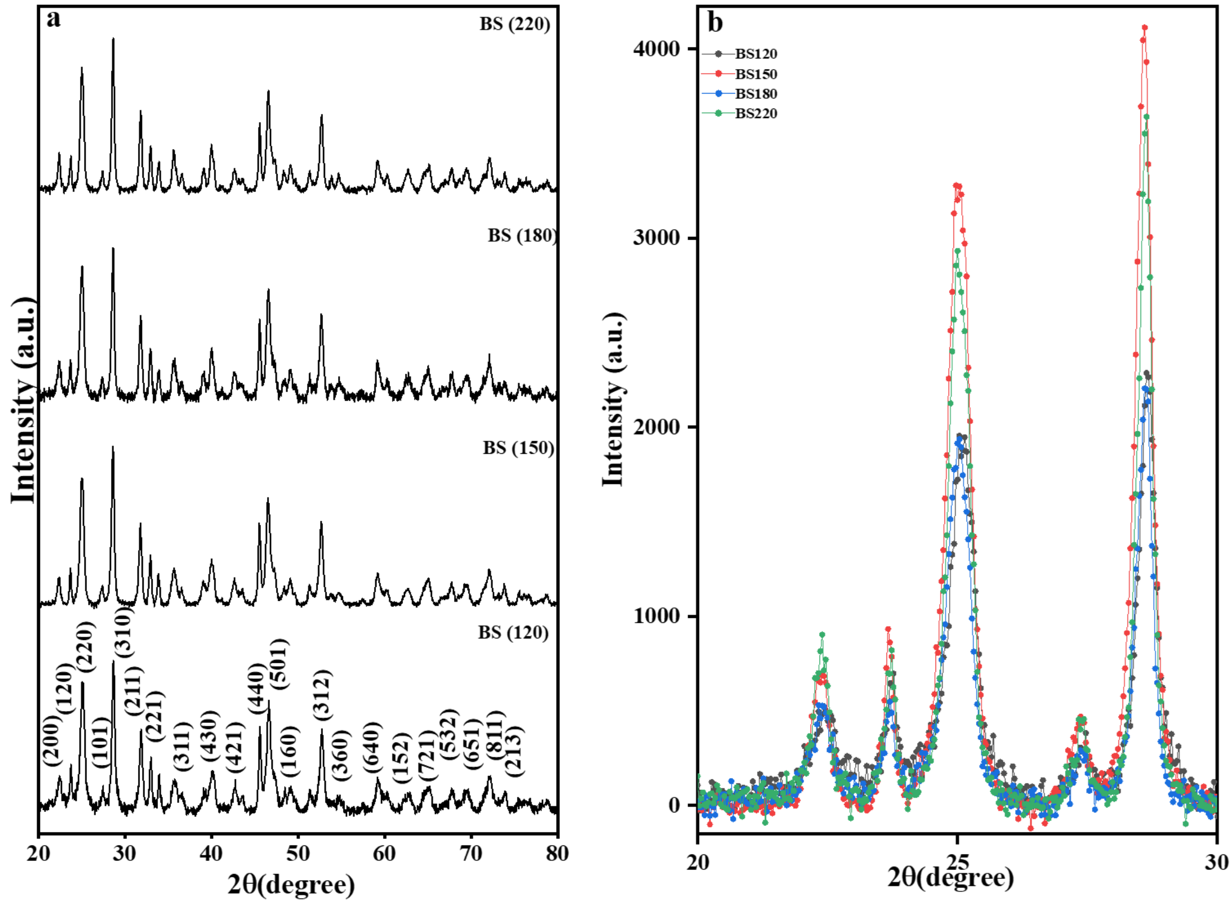

Fig 2: (a)XRD pattern of Bi_2S_3 nanoparticles obtained at 120, 150, 180 and 220 °C; (b) Super-imposed XRD spectra of BS(120), BS(150), BS(180) and BS(220) in the 2θ of 20-30.

3.3 Crystallite size and strain determination

Profile analysis of XRD peaks is a useful and simple technique to determine the peak broadening with crystallite size and strains in lattices due to dislocation. Since the Bragg peak breadth is a combination of factors arising from both sample and instrument effects, accurate determination of size and strain effects due to the sample can only be obtained by accounting for broadening due to the instrument (Gencalp Irizalp and Saklakoglu, 2017). This could be achieved by taking the diffraction patterns of standards such as alumina; and the analysis of the line broadening of the peaks from the standard could be used to evaluate the contribution of instrumental broadening to the pattern of the sample material. The corrected broadening β_{hkl} for the sample can then be calculated using Equation 1,

$$\beta_{hkl} = (\beta_o^2 - \beta_I^2)^{1/2} \qquad (1)$$

where βo and βi are the measured lattice strain dislocation broadening (β_o) and instrumental peak broadening (β_I) respectively.

Using the Debye-Scherrer's equation (Eq. 2), the average crystallite size of the nanocrystals can be evaluated.

$$D = \frac{k\lambda}{\beta cos\theta} \qquad (2)$$

Where D is the crystallite size, K is the shape factor (0.94), λ is the wavelength of CuK_α radiation (1.5406) and β is the corrected total peak broadening. From the obtained crystallite size, the dislocation density (δ), defined as the length of dislocation lines per unit volume of the crystal, which is an indication of the level of defects in the samples, could be estimated using Eq. 3.

$$\delta = \frac{1}{D^2} \qquad (3)$$

Table 1, shows the variation of the microstructural properties of the prepared Bi_2S_3 nanorods with change in reaction temperature. The crystallite size was obtained from the average of the three most prominent peaks. An initial increase in the crystallite size of the nanoparticles was observed with increase in temperature; however, a reduction in the crystallite size was observed above 180 °C. An increase in size with reaction suggested an increase in the rate of crystallite growth compared with nucleation as temperature increased. Above 180 °C, an alteration in the solvent property of the system, which might be due to an increase in interaction between the capping ligands and surface binding sites on the nanoparticles, may account for the reduction of crystal growth relative to nucleation, which resulted in a lower crystallite size (Mozaffari *et al.*, 2017).

The crystallite size of the nanorods was further analyzed using the Williamson-Hall (Fig. 3) and the Rietveld analysis, and the effect of reaction temperature on the strain induced in the nanorods crystal structure was also evaluated. Both analyses gave crystallite sizes that were consistent with the estimated size by Scherrer's equation; however, a slight under estimation of the crystallite size for the nanorods obtained at 180 °C was observed. This suggests a significant alteration in the crystal lattice of the nanorods at this temperature. Also, the variation in the values obtained from the Scherrer's equation, compared to the W-H and Rietveld analyses might be due to the actual measurement of the coherence length of the X-rays, which could be influenced by crystal imperfections that was not taken into consideration by this method. This imperfections in the crystal are usually evaluated through the micro-strain in the crystal by the W-H and Rietveld analyses (Markmann *et al.*, 2008, Wasly *et al.*, 2018).

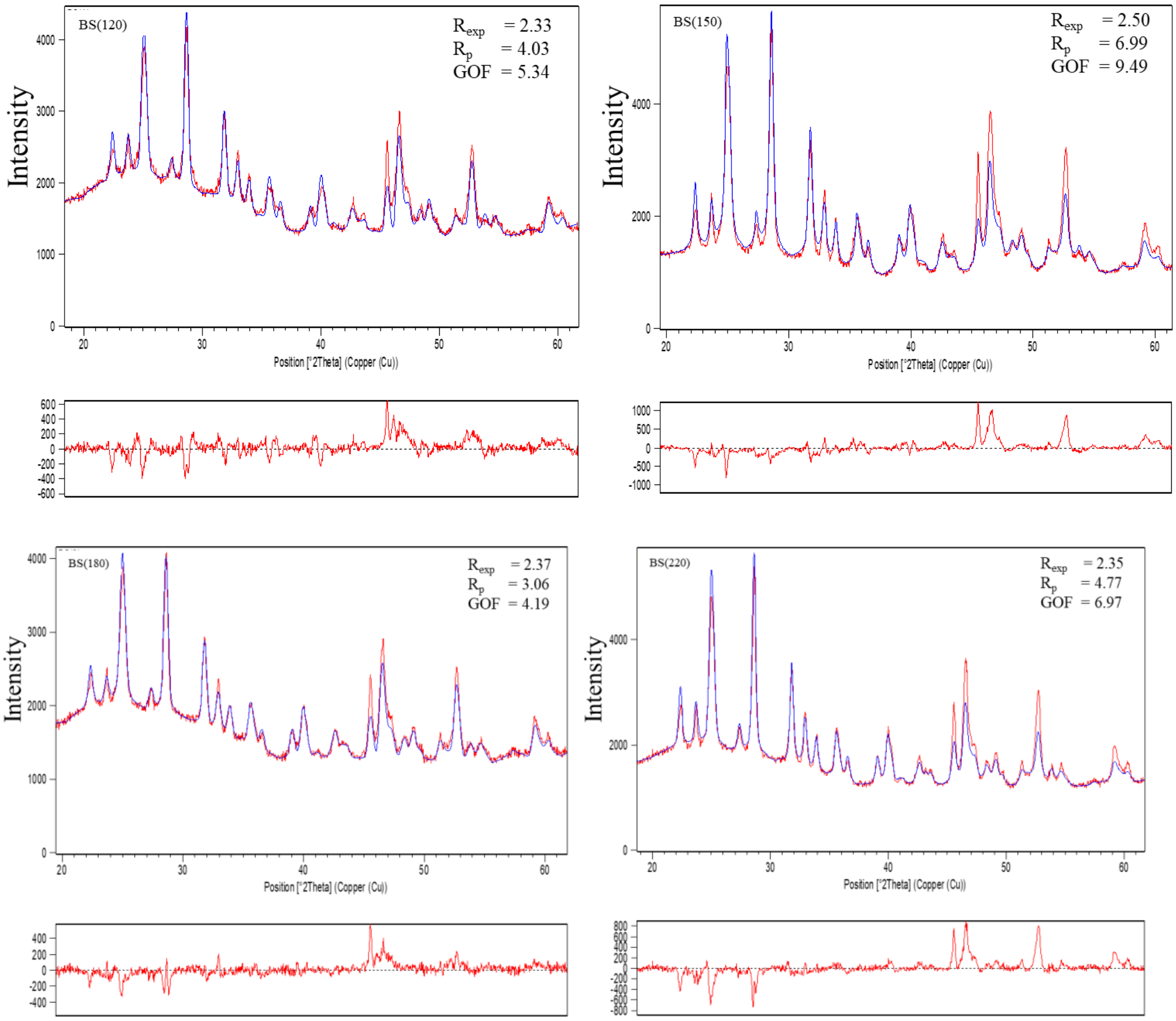

Fig 3: Rietveld analysis plot for BS(120), BS(150), BS(180) and BS(220). The top plot shows the calculated plot (blue line) superimposed on the experimental plot (red line). The bottom plot is the difference plot between the calculated and experimental plot.

Additional properties of the crystals of the nanorods such as strain, density, formula mass and lattice parameters were further estimated using the Rietveld analysis (Fig 3) and are presented in Table 1. It was observed that a reversal in trends in these properties was usually observed at 180 °C, which further supports the earlier suggestion of a significant alteration in the crystal lattice of the nanorods at this temperature. The nature of the strain in the crystal was also observed to be due to contraction as shown by the negative value of the strain obtained from the W-H analysis (fig. 4), except for the sample obtained at 150 °C, that showed a positive strain value. This change in the micro-strain of the samples with temperature, may be attributed to change in microstructure, defects, size and shape of the nanoparticles (Reddy *et al.*, 2011). A gradual reduction in the cell volume of the lattice was observed with increase in reaction temperature, while the cell density and formula mass reached a maximum at reaction temperature of 150 °C, which suggested a variation in the defect/vacancies in the nanorods with temperature.

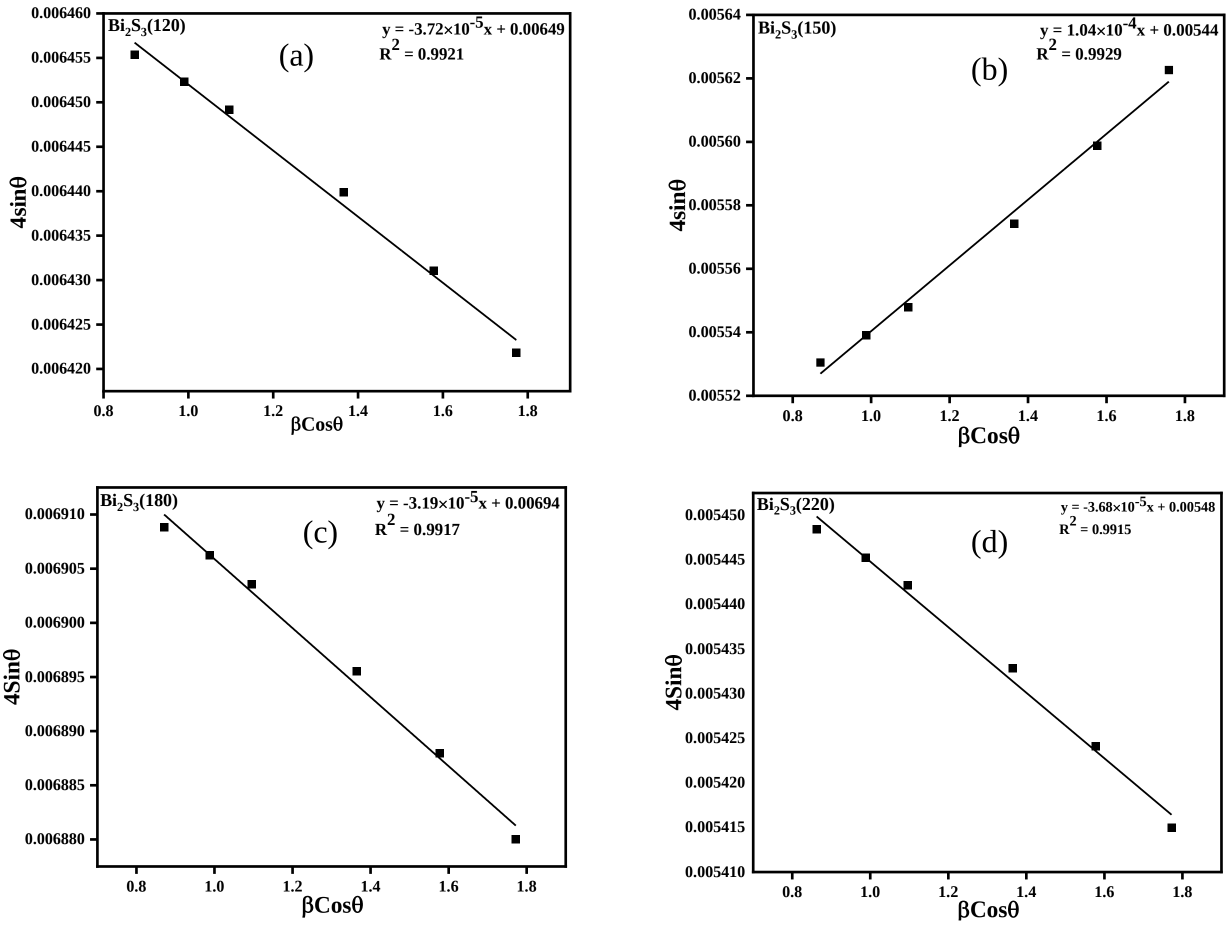

Fig. 4: Williamson-Hall plots for Bi_2S_3 nanorods obtained at (a)120, (b)150, (c)180 and (d) 220 °C

3.4 Morphological properties

The size and shape of the obtained nanorods were analyzed using SEM and TEM. The SEM images (Fig. 5) showed that all the nanorods were agglomerated and the density of the image became lighter with increase in temperature, showing the particles were less densely packed as the reaction temperature increased. The observed rod shape morphology may arise from the inherent chain type structure of Bi_2S_3 as it is well established that it crystallizes with a lamellar structure composed of Bi_2S_3 units that give rise to infinite bands, that are held by weak van der Waals interactions (Wang *et al.*, 2002).

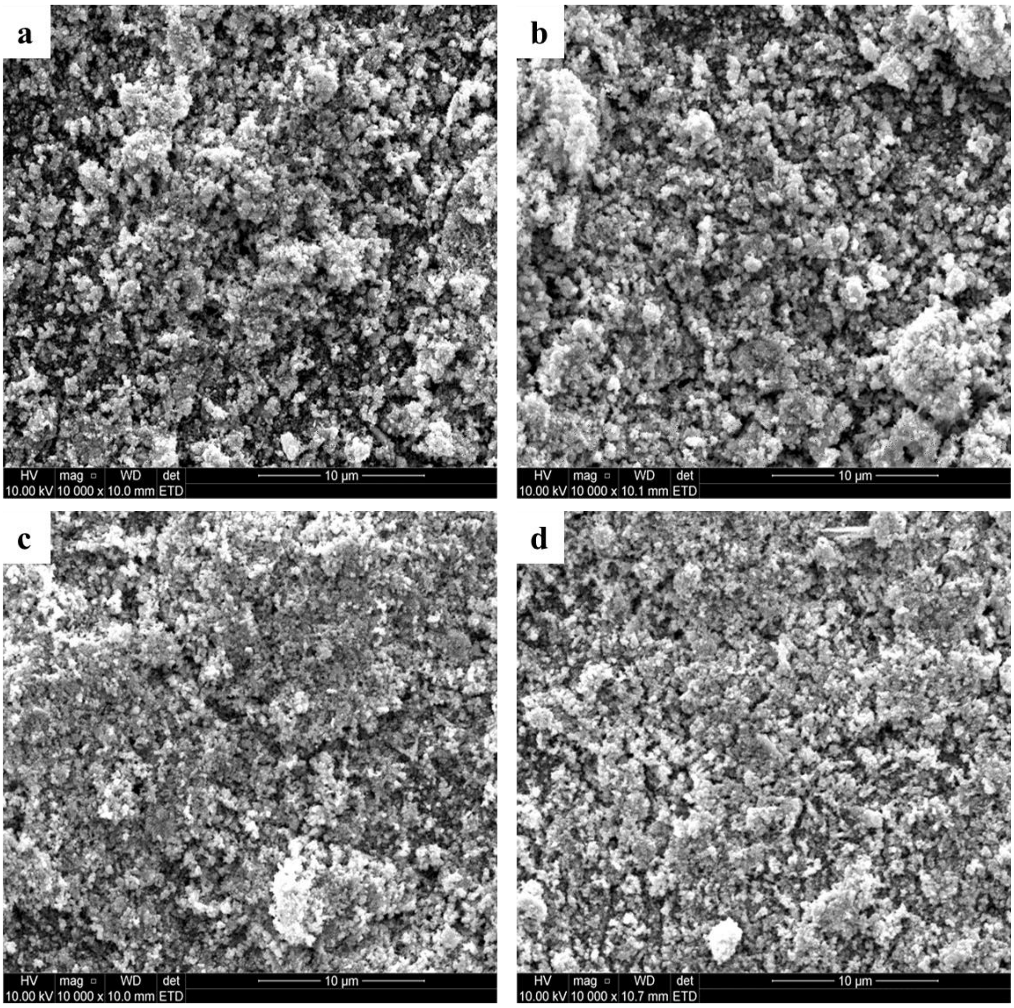

Fig 5: SEM images of Bi_2S_3 obtained at (a) 120, (b)150, (c) 180 and (d) 220 °C

The TEM images (Fig. 6) showed that the Bi_2S_3 were rod-shaped with aspect ratio that varied with temperature. The alteration of the aspect ratio suggested a difference in growth direction in the nanoparticles with temperature, which affirms a change in the capping property of the solvent with temperature change. At reaction temperatures of 120 and 150 °C, longer nanorods were obtained, while at higher temperature, nanorods with shorter lengths were obtained. The average particle size from the TEM images were in close agreement with crystallite size obtained from the Scherrer equation. The rod-shaped morphology of the obtained Bi_2S_3 and the alteration of the aspect ratio of the nanoparticles with reaction temperature are consistent with previous literatures (Wang *et al.*, 2002, Moyseowicz, 2019) Table 2, shows the values of the width and length of the rods, obtained using the image J software, and the calculated aspect ratio.

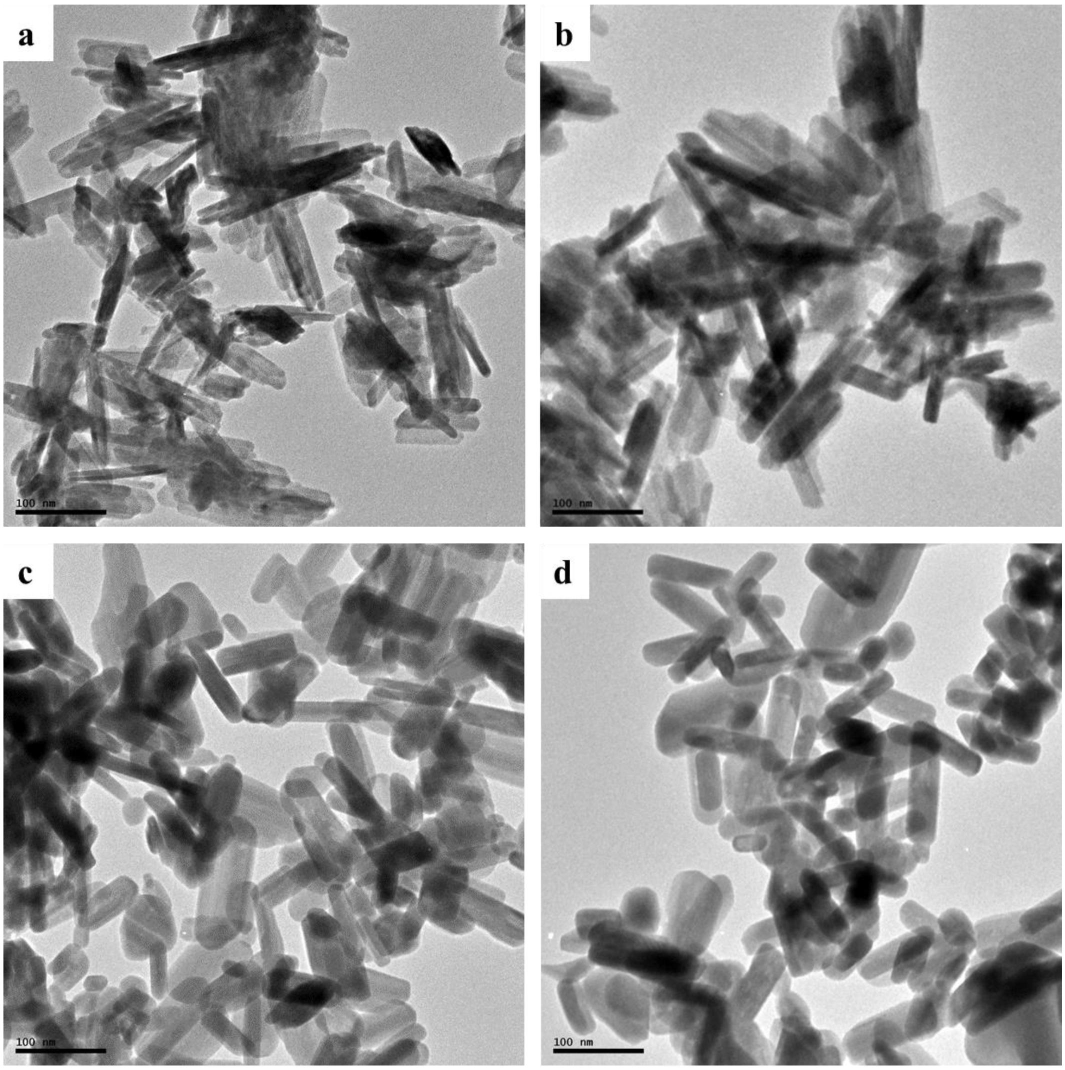

Fig 6: TEM images of Bi_2S_3 obtained at reaction temperatures of (a) 120, (b) 150, (c) 180 and (d) 220 °C.

Table 1: Microstructural properties of Bi_2S_3 obtained at different reaction temperature

	Scherer equation	Williamson-Hall plot		Rietveld analysis		Lattice parameters				Density	Formular weight	Dislocation density
		D	ε (%)	D	ε (%)	a (Å)	b (Å)	c (Å)	Cell volume (Å) × 10^6			
BS(120)	20.1	22.3	-3.72×10^{-5}	24.7	0.008	11.303	3.98	11.147	501.43	6.462	1951	5.0×10^{-2}
BS(150)	30.6	26.6	-1.04×10^{-4}	29.6	0.067	11.290	3.98	11.152	501.19	6.606	1993	3.3×10^{-2}
BS(180)	45.9	20.9	-3.19×10^{-5}	23.0	0.011	11.283	3.98	11.142	501.07	6.577	1980	2.2×10^{-2}
BS(220)	32.1	26.4	-3.68×10^{-5}	29.7	0.014	11.289	3.98	11.145	500.57	6.470	1952	3.1×10^{-2}

Table 2: Size analysis of Bi_2S_3 obtained at reaction temperature of 120,150, 180 and 220 °C

	Width (nm)	Length (nm)	Aspect ratio
BS(120)	20.97± 4.22	111.0 ± 18.1	5.29
BS(150)	26.84± 4.08	148.2 ± 10.9	5.52
BS(180)	41.25± 14.05	79.6 ± 16.9	1.92
BS(220)	24.89 ± 5.53	79.4 ± 5.53	3.19

3.5 Optical properties of the Bi_2S_3 nanorods

Different parameters such as technique of synthesis, process parameters, morphology, doping and influence of environmental interactions could influence the optical properties of materials. Information on the electronic states of a semiconductor could be estimated from the spectral behavior of the absorption coefficient in the high energy region of the optical absorption spectrum, while the low energy region of the spectrum correlates with atomic vibrations (El-Hagary *et al.*, 2012, Hassanien and Akl, 2016). The optical properties of the bismuth sulphide synthesized at different temperatures were studied through absorption and emission spectroscopy. The absorption spectra showed a blue shift to longer wavelength of the absorption edge with increase in reaction temperature (Fig. 7a). This suggested a reduction in the bandgap energy of Bi_2S_3 with increase in the reaction temperature, and could be attributed to the difference in size, strain and the capping ligands present on their surface of the rods. The reaction temperature also influenced the tailing of the absorption spectra of Bi_2S_3 into the near infrared region, with the absorption in the NIR enhanced at higher reaction temperature. This property is significant in the application of Bi_2S_3 as photothermal agent and CT imaging agent (Jiang *et al.*, 2020).

The Tauc plots of the absorption data, obtained by extrapolating the linear portion of the plot of $(\alpha h\nu)^2$ against h*v*, showed a linear decrease in the bandgap of the nanorods from 1.08-0.78 eV with increase in temperature (Fig. 7b). The nanorods showed bandgap energy lower than the reported bandgap energies for polycrystalline Bi_2S_3, which varied between 1.3-1.7 eV (Bernechea *et al.*, 2015). The variation in bandgap energy in Bi_2S_3 has been attributed to quantum confinement effect and stoichiometric variability. Theoretical calculation reports have suggested that in nanocrystals, bandgap variation is usually lower than 0.1 eV for particle size larger than 3 nm, while variation between 0.5-0.8 eV could be achieved for nanocrystals larger than 3 nm (Aresti *et al.*, 2014). However, in this study, a bandgap tuning of ~ 0.3 eV was achieved within the temperature range, suggesting a significant influence of the synthetic process on the band edge potentials of the obtained nanorods. The tailing of the absorption spectra indicated the presence of localized states within the bandgap of the nanorods, which are referred to as tail states. The gradual decrease in the bandgap with increase in reaction temperature, suggested an increase in the width of this tail states (Ikhmayies and Ahmad-Bitar, 2013).

The prepared Bi_2S_3 nanoparticles exhibited similar emission property when excited at 700 nm as shown in Fig 7c. However, a slight variation in the intensity of the emission peak was observed with change in temperature. This change in emission intensity, suggested a difference in the rate of charge carrier recombination in the nanorods, and the difference in nature of charge carrier recombination may be due to the difference in the nature of the tail states in the nanorods (Tai *et al.*, 2015). Also, the difference in the preferential growth orientation could similarly contribute to this difference in emission behaviour (Almeida *et al.*, 2012).

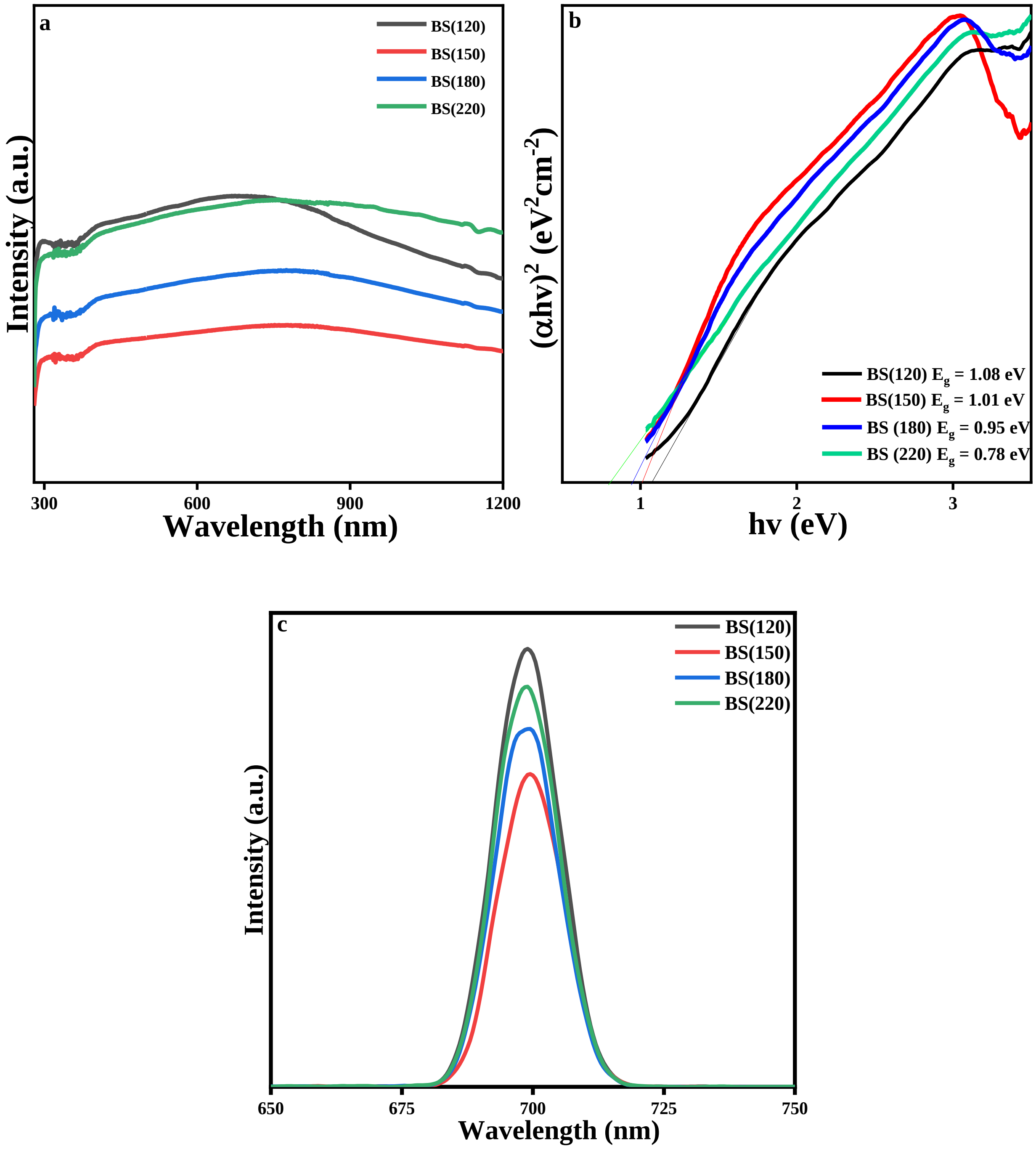

Fig 7: (a) absorption spectra (b) Tauc plot and (c) photoluminescence spectra of BS(120), BS(150), BS(180), BS(200) and BS(220)

.

3.6 Texture coefficient analysis

Since X-ray intensities are a function of atomic structure, deviation in textural coefficient from unity for a particular Miller plane is an indication of a change in atomic densities along that plane. Therefore, a higher/lower value of texture coefficient signifies an increase/decrease in planar density/crystallite orientation along the particular plane compared to ideal crystals. Texture coefficient can be evaluated from hkl plane of the XRD pattern, using Eq. 4:

$$TC_{hkl} = \frac{\frac{I_{(hkl)}}{I_{o(hkl)}}}{\frac{1}{N}\sum\frac{I_{(hkl)}}{I_{o(hkl)}}} \tag{4}$$

Where I is the measured intensity, I_o is the intensity of the standard and N is the number of diffraction peaks employed in the calculation. For the calculation of the texture coefficient of the obtained Bi_2S_3 nanoparticles, the most prominent peaks in the diffraction pattern: 112, 111, 212, 020, 314 and 312 planes were employed in the calculation and the results are presented in Table 3.

Analysis of the texture coefficients of the obtained Bi_2S_3 showed a slight re-orientation of all the crystals along the 111, 020 and 321 plane, with the 321 plane showing the strongest texture coefficient, which indicated a higher planer density compared to 111 and 020 planes. Also, while the textural coefficient of the 111 plane was randomly influenced by the reaction temperature, a gradual decrease in the textural coefficient was observed for the 020 plane as the temperature increased. The 321 plane only showed a significant difference when temperature was increased from 120 to 150 °C, and remained relatively constant at higher reaction temperature. This difference in preferred growth orientation can be ascribed to the change in the solvent properties with increase in temperature and could account for the variation of the bandgap energy and emission characteristics of the nanorods. Tuning the textural properties of nanoparticles has often been achieved by introduction of dopants and also varying the ligand/solvent ratio of the process. In this study, by using a solvent/capping agent mix of oleylamine/octadecene/DDT, tuning of the textural characteristic of the obtained Bi_2S_3 has been achieved. Textural modification has been reported to influence the efficiency of nanoparticles in a field such as gas sensing (Kumar *et al.*, 2015).

Table 3: Texture coefficient of Bi_2S_3 using the 111, 112, 212, 020, 314 and 321 planes

	111	112	212	020	314	321
BiS(120)	1.17	0.69	0.47	1.12	0.87	1.67
BiS(150)	1.09	0.73	0.44	1.10	0.90	1.72
BiS(180)	1.23	0.68	0.44	1.04	0.86	1.72
BiS(220)	1.22	0.75	0.49	0.95	0.88	1.70

4.0 Conclusion

The effect of temperature on the structural and optical properties of Bi_2S_3 prepared using a solvent mixture of oleylamine, dodecanethiol and octadecene has been studied. The interaction between the nanorods and the capping molecules was observed to depend on the temperature of synthesis, with the particle size varying between 20.1-45.9 nm. The nanorods showed temperature dependent aspect ratio that varied between 1.92-5.52 nm, suggesting a variation in preferrential growth direction. The bandgap energy of the nanorods showed significant variation in temperature range of synthesis, which could be due to the presence of defect/tail states. Analysis of the texture coefficient of the nanoparticles showed preferential orientation along the 111, 020 and 321 plane. This study shows that the use of a mixture of solvents and varying temperature can be employed to induce a significant variation in the microsturctural and optical properties of Bi_2S_3

5.0 References

Almeida, M. A. P., Cavalcante, L. S., Morilla-Santos, C., Dalmaschio, C. J., Rajagopal, S., Li, M. S. & Longo, E. 2012. Effect of partial preferential orientation and distortions in octahedral clusters on the photoluminescence properties of $FeWO_4$ nanocrystals. *CrystEngComm,* 14**,** 7127-7132.

Aresti, M., Saba, M., Piras, R., Marongiu, D., Mula, G., Quochi, F., Mura, A., Cannas, C., Mureddu, M., Ardu, A., Ennas, G., Calzia, V., Mattoni, A., Musinu, A. & Bongiovanni, G. 2014. Colloidal Bi_2S_3 Nanocrystals: Quantum Size Effects and Midgap States. *Advanced Functional Materials,* 24**,** 3341-3350.

Becerra, D., Nair, M. & Nair, P. K. 2011. Analysis of a Bismuth Sulfide/Silicon Junction for Building Thin Film Solar Cells. *Journal of The Electrochemical Society,* 158**,** H741.

Bernard, A., Zhang, K., Larson, D., Tabatabaei, K. & Kauzlarich, S. M. 2018. Solvent Effects on Growth, Crystallinity, and Surface Bonding of Ge Nanoparticles. *Inorganic Chemistry,* 57**,** 5299-5306.

Bernechea, M., Cao, Y. & Konstantatos, G. 2015. Size and bandgap tunability in Bi_2S_3 colloidal nanocrystals and its effect in solution processed solar cells. *Journal of Materials Chemistry A,* 3**,** 20642-20648.

Castellanos-Rubio, I., Insausti, M., Gil de Muro, I., Rojo, T. & Lezama, L. 2016. Tuning the Size of Palladium Nanoparticles in Organic and Aqueous Solutions: Influence of Aminated and Thiolated Ligands. *J Nanosci Nanotechnol,* 16**,** 4071-9.

El-Hagary, M., Emam-Ismail, M., Shaaban, E. R. & El-Taher, A. 2012. Effect of γ-irradiation exposure on optical properties of chalcogenide glasses $Se_{70}S_{30-x}Sb_x$ thin films. *Radiation Physics and Chemistry,* 81**,** 1572-1577.

Gencalp Irizalp, S. & Saklakoglu, N. 2017. 1.14 Laser Peening of Metallic Materials. *In:* HASHMI, M. S. J. (ed.) *Comprehensive Materials Finishing.* Oxford: Elsevier.

Hassanien, A. S. & Akl, A. A. 2016. Effect of Se addition on optical and electrical properties of chalcogenide CdSSe thin films. *Superlattices and Microstructures,* 89**,** 153-169.

Helal, A., Harraz, F., Ismail, A., Sami, T. & Ibrahim, I. 2016. Controlled synthesis of bismuth sulfide nanorods by hydrothermal method and their photocatalytic activity. *Materials & Design,* 102.

Ikhmayies, S. & Ahmad-Bitar, R. 2013. A study of the optical bandgap energy and Urbach tail of spray-deposited CdS:In thin films. *Journal of Materials Research and Technology,* 2**,** 221–227.

Jiang, J., Che, X., Qian, Y., Wang, L., Zhang, Y. & Wang, Z. 2020. Bismuth Sulfide Nanorods as Efficient Photothermal Theragnosis Agents for Cancer Treatment. *Frontiers in Materials,* 7.

Joicy, S. & Thangadurai, P. 2021. Metal Sulfide Nanostructures for Bioimaging and Biosensing Applications. *In:* RAJENDRAN, S., NAUSHAD, M., DURGALAKSHMI, D. & LICHTFOUSE, E. (eds.) *Metal, Metal Oxides and Metal Sulphides for Biomedical Applications.* Cham: Springer International Publishing.

Koh, Y. W., Lai, C. S., Du, A. Y., Tiekink, E. R. & Loh, K. P. 2003. Growth of bismuth sulfide nanowire using bismuth trisxanthate single source precursors. *Chemistry of materials,* 15**,** 4544-4554.

Kumar, M., Kumar, A. & Abhyankar, A. C. 2015. Influence of Texture Coefficient on Surface Morphology and Sensing Properties of W-Doped Nanocrystalline Tin Oxide Thin Films. *ACS Applied Materials & Interfaces,* 7**,** 3571-3580.

Kwon, K. C., Kim, C., Le, Q. V., Gim, S., Jeon, J., Ham, J., Lee, J.-L., Jang, H. & Kim, S. 2015. Synthesis of atomically thin transition metal disulfides for charge transport layers in optoelectronic devices. *ACS nano,* 9 4**,** 4146-55.

Liao, H.-C., Wu, M.-C., Jao, M.-H., Chuang, C.-M., Chen, Y.-F. & Su, W.-F. 2012. Synthesis, optical and photovoltaic properties of bismuth sulfide nanorods. *CrystEngComm,* 14**,** 3645-3652.

Malca, M., Bao, H., Kinsella, J. M., Friscic, T. & Moores, A. 2016. Mechanochemical synthesis of bismuth sulfide nanoparticles for their use as contrast probes in computed tomography imaging. *Frontiers in Bioengineering and Biotechnology*.

Malik, M. A., Revaprasadu, N. & O'Brien, P. 2001. Air-stable single-source precursors for the synthesis of chalcogenide semiconductor nanoparticles. *Chemistry of materials,* 13**,** 913-920.

Markmann, J., Yamakov, V. & Weissmüller, J. 2008. Validating grain size analysis from X-ray line broadening: a virtual experiment. *Scripta Materialia,* 59**,** 15-18.

Meyer, E., Bede, A., Zingwe, N. & Taziwa, R. 2019. Metal Sulphides and Their Carbon Supported Composites as Platinum-Free Counter Electrodes in Dye-Sensitized Solar Cells: A Review. *Materials (Basel, Switzerland),* 12**,** 1980.

Motaung, M. P., Osuntokun, J. & Onwudiwe, D. C. 2019. The heat-up synthesis of monodispersed Bi_2S_3 and Cu_7S_4 nanoparticles from novel precursor complexes and their characterizations. *Materials Science in Semiconductor Processing,* 99**,** 92-98.

Moyseowicz, A. 2019. Scalable one-pot synthesis of bismuth sulfide nanorods as an electrode active material for energy storage applications. *Journal of Solid State Electrochemistry,* 23**,** 1191-1199.

Mozaffari, S., Li, W., Thompson, C., Ivanov, S., Seifert, S., Lee, B., Kovarik, L. & Karim, A. M. 2017. Colloidal nanoparticle size control: experimental and kinetic modeling investigation of the ligand-metal binding role in controlling the nucleation and growth kinetics. *Nanoscale,* 9**,** 13772-13785.

Nyquist, R. A. 2001. Chapter 4 - Thiols, Sulfides and Disulfides, Alkanethiols, and Alkanedithiols (S-H stretching). *In:* NYQUIST, R. A. (ed.) *Interpreting Infrared, Raman, and Nuclear Magnetic Resonance Spectra.* San Diego: Academic Press.

Onwudiwe, D. C. & Nkwe, V. M. 2020. Morphological variations in Bi_2S_3 nanoparticles synthesized by using a single source precursor. *Heliyon,* 6**,** e04505.

Reddy, A. J., Kokila, M., Nagabhushana, H., Chakradhar, R., Shivakumara, C., Rao, J. & Nagabhushana, B. 2011. Structural, optical and EPR studies on ZnO: Cu nanopowders prepared via low temperature solution combustion synthesis. *Journal of Alloys and Compounds,* 509**,** 5349-5355.

Ren, Q., Ma, Y., Zhang, S., Ga, L. & Ai, J. 2021. One-Step Synthesis of Water-Soluble Silver Sulfide Quantum Dots and Their Application to Bioimaging. *ACS Omega,* 6**,** 6361-6367.

Sharma, S. & Khare, N. 2017. Synthesis of bismuth sulfide nanostructures for photodegradation of organic dye. *AIP Conference Proceedings,* 1832**,** 050064.

Shen, S. & Wang, Q. 2013. Rational Tuning the Optical Properties of Metal Sulfide Nanocrystals and Their Applications. *Chemistry of Materials,* 25**,** 1166-1178.

Song, W.-S. & Yang, H. 2012. Efficient White-Light-Emitting Diodes Fabricated from Highly Fluorescent Copper Indium Sulfide Core/Shell Quantum Dots. *Chemistry of Materials,* 24**,** 1961–1967.

Stavila, V., Whitmire, K. H. & Rusakova, I. 2009. Synthesis of Bi_2S_3 Nanostructures from Bismuth(III) Thiourea and Thiosemicarbazide Complexes. *Chemistry of Materials,* 21**,** 5456-5465.

Sun, B., Feng, T., Dong, J., Li, X., Liu, X., Wu, J. & Ai, S. 2019. Green synthesis of bismuth sulfide nanostructures with tunable morphologies and robust photoelectrochemical performance. *CrystEngComm,* 21**,** 1474-1481.

Tai, K. F., Gershon, T., Gunawan, O. & Huan, C. H. A. 2015. Examination of electronic structure differences between CIGSSe and CZTSSe by photoluminescence study. *Journal of Applied Physics,* 117**,** 235701.

Tributsch, H. 1984. Metal Sulfides in Photovoltaic, Photoelectrochemical and Solar Biological Energy Conversion. *In:* MÜLLER, A. & KREBS, B. (eds.) *Studies in Inorganic Chemistry.* Elsevier.

Wang, H., Zhu, J.-J., Zhu, J.-M. & Chen, H.-Y. 2002. Sonochemical Method for the Preparation of Bismuth Sulfide Nanorods. *The Journal of Physical Chemistry B,* 106**,** 3848-3854.

Wang, Y., Wu, Y., Liu, Y., Shen, J., Lv, L., Li, L., Yang, L., Zeng, J., Wang, Y., Zhang, L., Li, Z., Gao, M. & Chai, Z. 2016. BSA-Mediated Synthesis of Bismuth Sulfide Nanotheranostic Agents for Tumor Multimodal Imaging and Thermoradiotherapy. *Advanced Functional Materials,* 26.

Wasly, H. S., El-Sadek, M. S. A. & Henini, M. 2018. Influence of reaction time and synthesis temperature on the physical properties of ZnO nanoparticles synthesized by the hydrothermal method. *Applied Physics A,* 124**,** 76.

Xiao, G., Dong, Q., Wang, Y., Sui, Y., Ning, J., Liu, Z., Tian, W., Liu, B., Zou, G. & Zou, B. 2012a. One-step solution synthesis of bismuth sulfide (Bi2S3) with various hierarchical architectures and their photoresponse properties. *RSC Advances,* 2**,** 234-240.

Xiao, G., Dong, Q., Wang, Y., Sui, Y., Ning, J., Liu, Z., Tian, W., Liu, B., Zou, G. & Zou, B. 2012b. One-step solution synthesis of bismuth sulfide (Bi_2S_3) with various hierarchical architectures and their photoresponse properties. *RSC Adv.,* 2**,** 234-240.

Xiong, C., Liu, M., Zhu, X. & Tang, A. 2019. A General One-Pot Approach to Synthesize Binary and Ternary Metal Sulfide Nanocrystals. *Nanoscale Research Letters,* 14**,** 19.

Zhang, L., Chen, Q., Zou, X., Chen, J., Hu, L., Dong, Z., Zhou, J., Chen, Y., Liu, Z. & Cheng, L. 2019. Intelligent protein-coated bismuth sulfide and manganese oxide nanocomposites obtained by biomineralization for multimodal imaging-guided enhanced tumor therapy. *Journal of Materials Chemistry B,* 7**,** 5170-5181.

Zhou, X., Ma, L. & Feng, Z. 2015. Synthesis and Characterization of Bismuth Sulfide Nanorods by Solvothermal Route. *Chemistry Letters,* 44**,** 1113-1115.

CHAPTER FIVE

Lattice strain analysis of solvothermally synthesized antimony sulphide

1.0 Introduction

Antimony sulphide (Sb_2S_3) is a semiconductor material with interesting thermoelectric properties and high photosensitivity, which is being explored in solar cells, photodetectors, photocatalysis, thermoelectric cooling technologies, microwave device, switching devices, television cameras and sodium ion batteries (Choi *et al.*, 2014, Validzic *et al.*, 2016, Bagheriyan, 2013, Ben Naceur *et al.*, 2019). It is a direct band gap semiconductor with band gap range of 1.78-2.5 eV and crystallizes in the orthorhombic crystal structure with space group pbnm (Biswal and Garje, 2013).

Several synthetic routes have been reported for Sb_2S_3, including hydrothermal (Xie *et al.*, 2018), microwave (Davoodi *et al.*, 2016), chemical vapour deposition, surfactant assisted (Zhu *et al.*, 2018a), spray pyrolysis (Rajpure *et al.*, 1997), vacuum evaporation, ionothermal (Ma *et al.*, 2010) and single source precursor routes (Tamilselvan *et al.*, 2019). Different compounds such as xanthates, thiourea, dithiophosphates and dithiocarbamates have been explored as single source precursor for the synthesis of Sb_2S_3(Biswal and Garje, 2013). The single source precursor approach provides a mild, and environmentally friendly route to the synthesis of monodispersed nanomaterials (Malik *et al.*, 2001). The numerous routes to Sb_2S_3 has yielded materials of differing morphologies such as nanowires (Validzic *et al.*, 2016), quantum dots (Zhu *et al.*, 2018b), nanorods (Yang *et al.*, 2000), and nanotubes (Bao *et al.*, 2007).

Size confinements in the lattice of nanocrystals results in intrinsic strain, which is influenced by synthesis factors such as reactant concentration and reaction pH. The analysis of peak broadening in the XRD pattern of a nanocrystal can be effectively used in estimating the crystallite size and strain induced in the lattice of the material. Other important elastic properties such as stress, Young’s modulus, energy density could also be indirectly determined through the strain analysis of the material. Different methods that have been explored in peak broadening analysis include, Williamson-Hall, Warren-Averbach and Balzar methods. Each of these methods explores the characteristic property of the diffraction peaks of a material in lattice strain evaluation (Dey and Das, 2018, Delhez *et al.*, 1982, Mohamed *et al.*, 2005).

Herein, in this study, the structural properties of hexadecylamine-capped Sb_2S_3 nanocrystals were analyzed from its X-ray diffraction data, by employing the Williamson-Hall and size-strain analyses. Three models of the Williamson-Hall models, which include the uniform deformation model, uniform stress deformation model and uniform deformation energy density model were explored for the strain analysis. In the size-strain analysis, the size-strain plot and Halder-Wagner method were explored. The X-ray diffraction data were further subjected to Rietveld refinement for the determination of lattice parameters such as the lattice constants, unit cell volume and bulk density. The study of the strain induced in nanocrystals are important because the presence of strain could influence the nanocrystals' properties (Schneider *et al.*, 2016).

2.0 Experimental

2.1 Materials

Antimony chloride, carbon disulphide, ammonium hydroxide, ethanol, hexadecylamine and toluene were supplied by Sigma Aldrich and Merck Co, and were used without any purification. Powder X-ray diffraction pattern was recorded using a Bruker AXS D_8 Discover diffractometer operated at 40 KV and 40 mA with Cu Kα; source ($\lambda = 154.18$ pm). Scanning electron microscopy (SEM) was performed using FI quanta FEG 250 Environmental scanning electron microscope. Ttansmission electron microscopy (TEM) and high resolution transmission electron microscopy were recorded on a JEOL JEM HRTEM system.

2.2 Synthesis of hexadecylamine capped Sb_2S_3 nanorods

Sb_2S_3 nanorods were synthesized by using antimony(III) tris(*N*–methyl–*N*–phenyl dithiocarbamate) complex, prepared using a previously reported method, as a single source precursor. About 15 mmol of the antimony complex was introduced into a three-necked flask containing 20 mmol hexadecylamine. The mixture was degassed at room temperature for about 25 min, then gradually heated up at the rate of 10 ºC/min to 280 ºC and maintained at this temperature for 1 hr. The heating was then stopped, and the solution was allowed to cool to about 60 ºC. The synthesized nanoparticles were precipitated by adding excess methanol to the obtained solution and centrifuging. Excess capping agent and other reaction by products were removed by redissolving the particles in toluene, reprecipitating with methanol and the washing process was carried out three times. The nanoparticles were recovered by centrifuging at 4000 rpm for 15 min, and then dispersed in toluene for further analysis.

3.0 Results and discussion

3.1 XRD analysis

The XRD pattern of the Sb_2S_3 nanoparticles is shown in Fig 1. The reflections could all be indexed to the orthorhombic phase of pure Sb_2S_3 (JCPDS: 75-1310). No extra reflections were observed in the pattern, which confirmed the formation of a pure Sb_2S_3 phase. The peak intensity of the pattern was sharp and narrow, confirming the high crystallinity and fine grain size of the prepared nanoparticles (Bindu and Thomas, 2014).

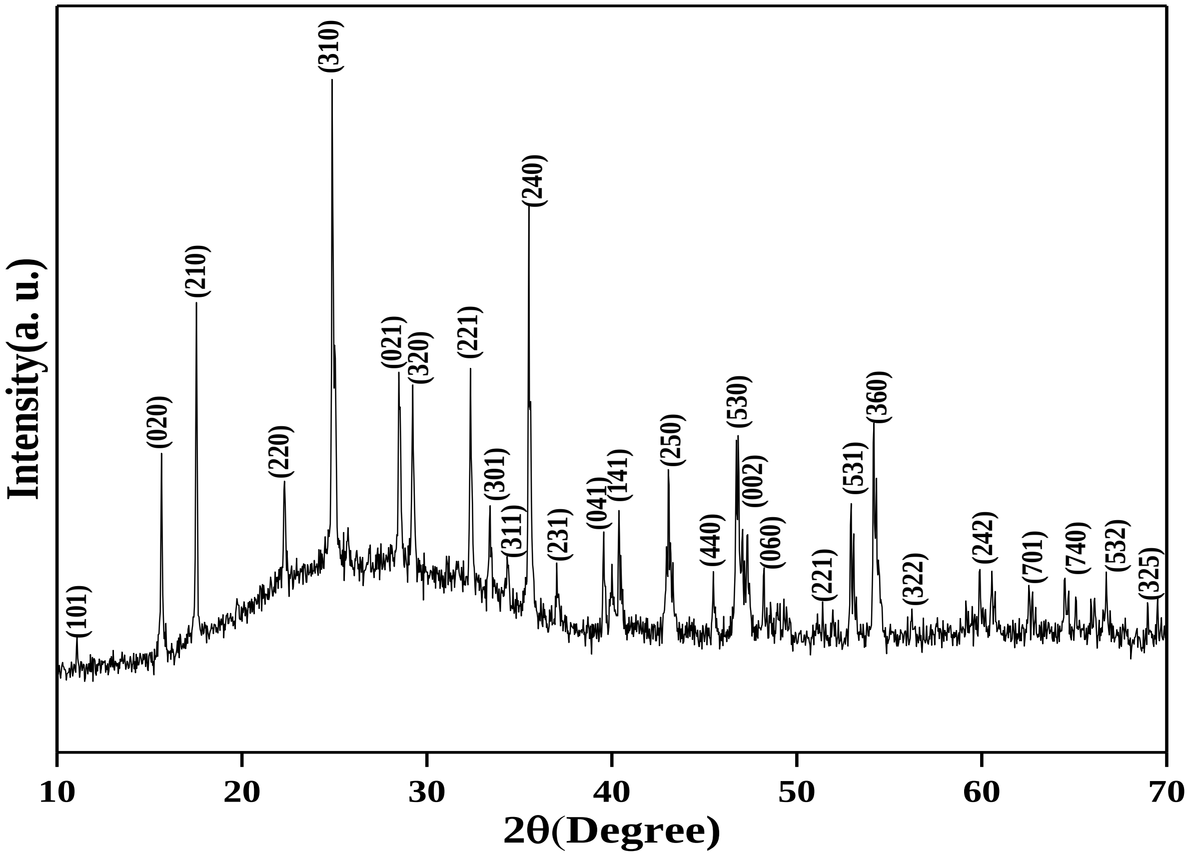

Fig 1: XRD pattern of orthorhombic Sb_2S_3 obtained from the solvothermal decomposition of antimony (III) *N*–methyl–*N*–phenyl dithiocarbamate in hexadecylamine.

3.1.1 Crystallite size and strain analysis

3.1.1.1 Debye-Scherrer's equation

The average crystallite size of the nanocrystals was calculated using the Debye-Scherrer's equation:

$$D = \frac{k\lambda}{\beta cos\theta} \qquad (1)$$

Where D is the crystallite size, K is the shape factor (0.94), λ is the of CuK_α radiation wavelength (1.5406) and β is the corrected total peak broadening. The value of β is a combination of the broadening due to the crystallite (β_D), lattice strain dislocation broadening (β_S) and instrumental peak broadening (β_I). The three peak broadening sources are related by the equations:

$$\beta_o = (\beta_D + \beta_S) \qquad (2)$$

$$\beta = (\beta_o^2 - \beta_I^2)^{1/2} \qquad (3)$$

Equation 1 could be rearranged in terms of θ as:

$$\cos\theta = \frac{k\lambda}{D}\frac{1}{\beta_o} \qquad (4)$$

The Scherrer's plot of the hexadecylamine capped Sb_2S_3 is shown in Fig 2(a). Crystallite size could be evaluated from the plot using slopes from either the linear fit (black line), which gives a crystallite size of 536.3 nm, or from the linear fit to the data through zero (red line), which gives a crystallite size of 111.3 nm as shown in Fig 2(a). When compared to the crystallite size of 106.4 nm, obtained by the direct averaging of the value obtained for the three main peaks, it could be observed that the value obtained from the linear fit showed a wide deviance from the other values. In addition, the y-intercept in the fit is also of no physical significance. A similar trend was observed by Motevalizadeh *et al.* (2014), when the crystallite size of ZnO nanorods were estimated using the Scherrer's plot. The value obtained from the linear fit to the data through zero will be adopted as the Scherrer's plot crystallite size for the synthesized Sb_2S_3.

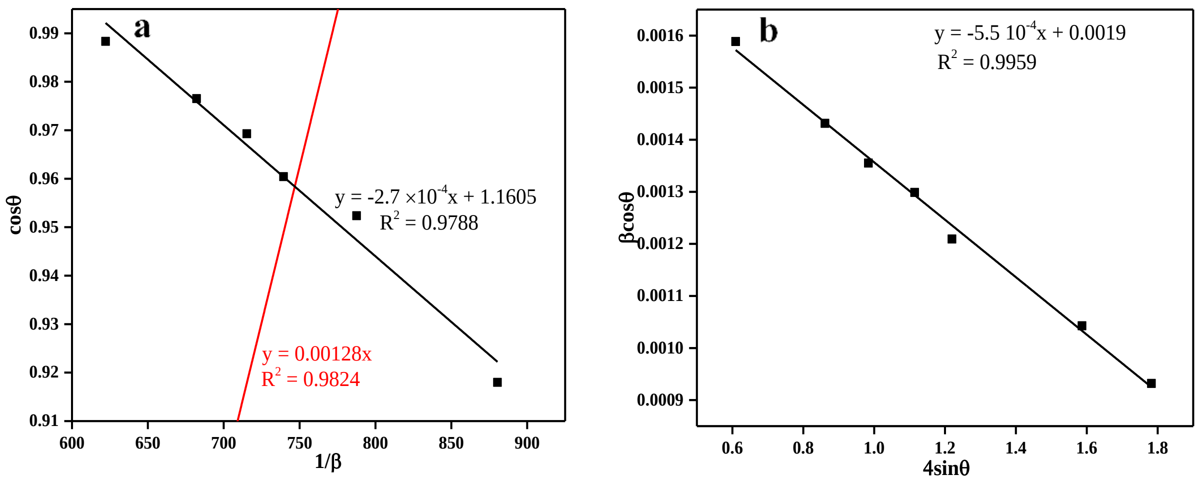

Fig 2: (a) Scherrer plot for hexadecylamine capped Sb_2S_3 (b) UDM plot for hexadecylamine capped Sb_2S_3

3.1.1.2 Williamson-Hall (W-H) analysis

The Scherrer's equation only considers the effect of crystallite size on peak broadening of XRD diffractions, with no consideration given to the strains in the microstructures of the lattice, which may arise in the nanocrystals due to stacking faults, grain boundary, triple junction and point defects (Das and Sarkar, 2015). The strain contribution to the XRD peak broadening in a nanocrystal together with the crystallite size could be estimated from several methods such as the Warren-Averbach, Rietveld refinement, pseudo-Voigt function and Williamson-hall analysis (Rietveld, 1967, Balzar and Ledbetter, 1993, Warren and Averbach, 1950). The Williamson-Hall analysis employs a simplified integral breadth analysis in which size and strain induced broadening are deconvoluted by evaluating the peak width as a function of 2θ (Mote *et al.*, 2012). The total X-ray diffraction peak broadening could then be written as:

$$\beta_{total} = \beta_{size} + \beta_{strain} \tag{5}$$

The crystalline size and lattice strain of the hexadecylamine capped Sb_2S_3 were calculated using three modified W-H analysis, which include the uniform deformation model (UDM), uniform stress deformation model (USDM) and uniform deformation energy density model (UDEDM).

3.1.1.2.1 Uniform deformation model (UDM)

The UDM is based on the assumption that the crystal strain is uniform in all crystallographic directions. The lattice strain is thus considered as an isotropic property that is independent of the direction of measurement (Mote *et al.*, 2012). The physical peak broadening induced by lattice strain is expressed as:

$$\beta_{strain} = 4\varepsilon\tan\theta \tag{6}$$

The observed peak broadening for a peak with hkl (β_{hkl}) value could be taken as the sum of the peak broadening due to crystallite size and strain contributions assuming they are independent of each other and they both possess Cauchy-like profile. By combining equations 1 and 6, the observed line breadth is expressed as:

$$\beta_{hkl} = \frac{K\lambda}{Dcos\theta} + 4\varepsilon tan\theta. \tag{7}$$

Equation 6 can be rearranged to give:

$$\beta_{hkl}\cos\theta = \frac{K\lambda}{D} + 4\varepsilon sin\theta. \tag{8}$$

Equation 8 is the linear plot equation for UDM. A plot of $4\varepsilon\sin\theta$ on the X-axis and $\beta_{hkl}\cos\theta$ on the Y-axis gives a straight line with slope equal to the lattice strain and the crystallite size could be evaluated from the intercept. Fig 2b shows the UDM plot for the hexadecylamine-capped Sb_2S_3 nanoparticles, with crystallite size and lattice strain value of 76.2 nm and 5.5×10^{-4} respectively. The linear fit, showed good correlation coefficient (R^2) of 0.9959. Strains in lattice are majorly induced by either lattice contraction or lattice expansion, caused by the modification of the atomic arrangement that arise from size confinement. Defects in the crystal lattice, which result in lattice strain in the crystal are also a possible consequence of size confinement (Nath *et al.*, 2020). Furthermore, reports have also shown that lattice strain is size and shape dependent (Ouyang *et al.*, 2010, Sarkar and Das, 2018). The negative slope of the UDM plot was an indication that the strain in the nanocrystal of the hexadecylamine-capped Sb_2S_3 was as a result of lattice contraction (Sarkar and Das, 2018).

3.1.1.2.2 Uniform Stress deformation model (USDM)

The assumption of sample homogeneity and isotropic nature on which the UDM model is built is not often justified as real crystals are often anisotropic in nature. Therefore, the W-H requires a modification that will incorporate the anisotropic nature into lattice strain evaluation. The modified model in which lattice deformation stress along all the lattice plane direction with small microstrain is uniformly considered is the uniform stress deformation model (USDM).

The linear relationship between stress (σ) and strain is expressed by Hooke's law, given as:

$$\sigma = \varepsilon \times Y_{hkl}, \tag{9}$$

where Y_{hkl} is the elastic modulus or Young's modulus in the direction perpendicular to the crystal lattice plane. Rearranging equation 9, the strain could be written as:

$$\varepsilon = \frac{\sigma}{Y_{hkl}}\,. \tag{10}$$

Inserting the expression of ε into equation 7, the modified W-H equation that is expressed in terms of the Young's modulus is obtained.

$$\beta_{hkl}\cos\theta = \frac{K\lambda}{D} + \frac{4\sigma sin\theta}{Y_{hkl}} \tag{11}$$

The plot of $\beta_{hkl}\cos\theta$ on the Y-axis and $\frac{4sin\theta}{Y_{hkl}}$ on the X-axis gives a linear plot with slope that is equal to the uniform stress and crystallite size (D), obtained from the intercept. The Young modulus of an orthorhombic crystal is related to its elastic compliances S_{ij} as (Zhang *et al.*, 2008):

$$\frac{1}{Y_{hkl}} = \frac{S_{11}H^4 + S_{22}K_4 + S_{33}L^4 + (2S_{12} + S_{66})H^2K^2 + (2S_{13} + S_{55})H^2L^2 + (2S_{23} + S_{44})K^2L^2}{(H^2 + K^2 + L^2)} \tag{12}$$

S_{11}, S_{22}, S_{33}, S_{44}, S_{55}, S_{66}, S_{12}, S_{13} and S_{23} are the elastic compliances of Sb_2S_3 and their values are 37.4 × 10^{-12}, 104.9 × 10^{-12}, 14 × 10^{-12}, 586.1 × 10^{-12}, 47.3 × 10^{-12}, 101.5 × 10^{-12}, -21.5 × 10^{-12}, -6 × 10^{-12}, and -5.3 × 10^{-12} m^2N^{-1} respectively (de Jong *et al.*, 2015). Using the elastic compliances, the Young's modulus that was calculated for the 201, 301, 302, 212, 402, 610 and 513 peaks were 33.2, 29.8, 37.4, 20.1, 33.2, 27.0, and 27.4 GPa respectively, which averages to 31 GPa. Fig. 3(a) shows the USDM plot for the hexadecylamine capped Sb_2S_3, with the crystallite size and uniform stress evaluated to be 103.4 nm and 7.9 MPa respectively.

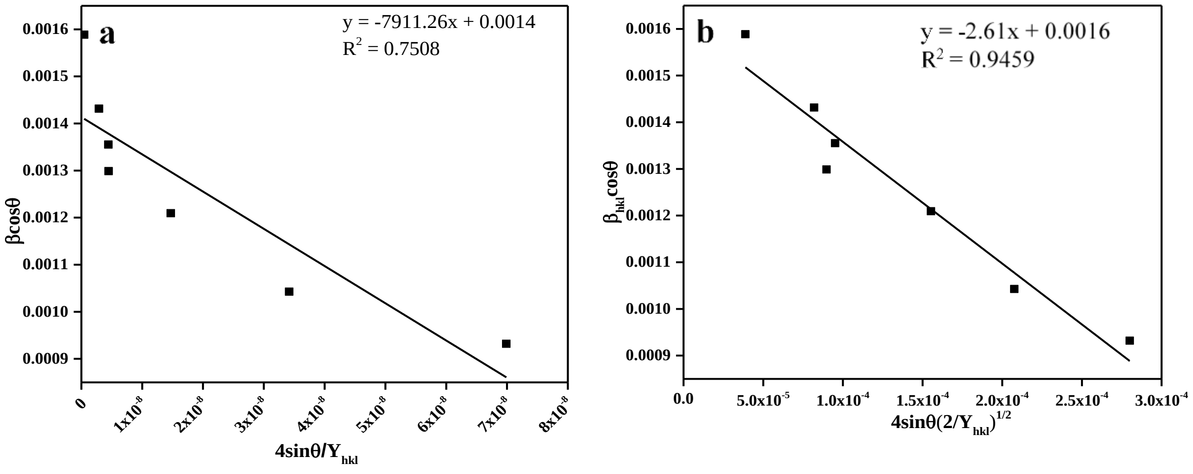

Fig 3: (a) USDM model for hexadecylamine capped Sb_2S_3 (b) UDEDM plot for hexadecylamine capped Sb_2S_3

3.1.1.2.3 Uniform deformation energy density model (UDEDM)

The imperfections created by different dislocations, defects and agglomeration in most crystals implies that the assumptions of crystal isotropy and linear proportionality between stress and strain, on which the UDM and USDM is based, does not hold in real crystals. Furthermore, when the strain energy density (u) is considered, all the proportionality constants associated with the stress-strain relationship are no longer independent (Mote *et al.*, 2012).

The UDEDM considers the density of deformation energy, which is responsible for the anisotropic lattice strain in the crystal (Nath *et al.*, 2020). As stated by Hooke’s law, the energy density u is related to strain by the expression:

$$u = \frac{\varepsilon^2 Y_{hkl}}{2} \tag{13}$$

By rearranging equation 13 in terms of ε and substituting into equation 7, the UDEDM equation is obtained as follows:

$$\beta_{hkl}\cos\theta = \frac{K\lambda}{D} + 4sin\theta\left(\frac{2u}{Y_{hkl}}\right)^{\frac{1}{2}} \tag{14}$$

The size and energy density of the crystal can be evaluated from the intercept and slope of the straight line obtained from the plot of $\beta_{hkl}\cos\theta$ on the Y-axis against $4sin\theta\left(\frac{2}{Y_{hkl}}\right)^{\frac{1}{2}}$ on the X-axis. The UDEDM plot for the hexadecylamine capped Sb_2S_3 is shown in Fig. 3(b). The crystallite size and energy density for the crystal were 90.5 nm and 6.8 KJ/m^3 respectively.

3.1.1.3 Size-strain analysis

3.1.1.3.1 Size-strain plot (SSP)

Size-strain plot is a peak broadening analysis model, which expresses the XRD peak profile as a combination of both Lorentzian and Gaussian functions. The peak analysis is therefore not evaluated as a function of diffraction angle 2θ. This model predominantly uses data in the lower diffraction angles due to the lack of precision and high peak overlap associated with reflecting planes at higher angles (Shunmuga Sundaram *et al.*, 2020). In the SSP model, the profile broadening due to strain is labelled as Gaussian function while the crystallite size contribution to profile broadening is labelled as Lorentz function (Balzar and Ledbetter, 1993). The total SSP peak broadening can then be expressed as the sum of broadening due to Lorentzian (β_L) and Gaussian (β_G) functions:

$$\beta_{hkl} = \beta_L + \beta_G \tag{15}$$

The SSP is evaluated using the equation (Cullity and Stock, 2001):

$$(d_{hkl}\beta_{hkl}cos\theta)^2 = \frac{k\lambda}{D}\left(d_{hkl}^2\beta_{hkl}cos\theta\right) + \frac{\varepsilon^2}{4} \tag{16}$$

The values of d_{hkl} (lattice distance between hkl planes were obtained from the Rietveld analysis date for the 201, 301, 302, 212, 402, 314 and 513 planes, which were 0.5055, 0.3576, 0.3131, 0.2526, 0.1942 and 0.1728 nm respectively. The SSP plot for the hexadecylamine capped Sb_2S_3 is shown in Fig. 4(a) and the crystallite size and lattice strain obtained from the fits were 85.1 and -3.49 x 10^{-4} respectively.

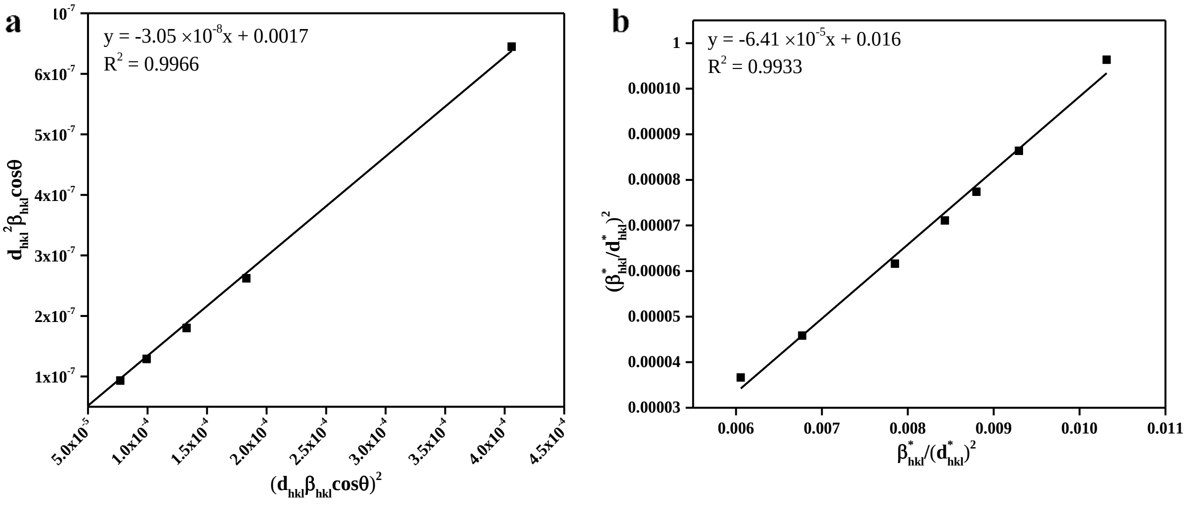

Fig 4: (a) SSP model for hexadecylamine capped Sb_2S_3 (b) Halder-Wagner plot for hexadecylamine capped Sb_2S_3

3.1.1.3.2 Halder-Wagner method

The Halder-Wagner method is based on the assumption that peak profile broadening is a symmetric Voigt function. This method seeks to overcome the difficulty of the SSP method as the XRD peak is neither Gaussian or Lorentzian function. This is because despite the XRD peak region matching the Gaussian function well, the tail regions don't match the Gaussian function because it tails off too rapidly. Thus, matching the Lorentzian function. However, despite the tail region matching the Lorentzian function, the XRD peak region does not match this function (Hepp and Baerlocher, 1988). The Halder-Wagner method, therefore, assumes the symmetric Voigt function which is a convolution of both Lorentzian and Gaussian function (Halder and Wagner, 1966, Motevalizadeh *et al.*, 2014). The integral breadth of a Voigt function according to the Halder and Wagner is expressed as:

$$\beta_{hkl}^2 = \beta_L \beta_{hkl} + \beta_G^2 \qquad (17)$$

Where Lorentzian and Gaussian components of the profile broadening are represented by β_L and β_G. In the Halder-Wagner method the crystallite size and lattice strain are related by the expression:

$$\left(\frac{\beta_{hkl}^*}{d_{hkl}^*}\right)^2 = \frac{1}{D}\frac{\beta_{hkl}^*}{\left(d_{hkl}^*\right)^2} + \left(\frac{\varepsilon}{2}\right)^2 \qquad (18)$$

Where $\beta_{hkl}^* = \beta_{hkl} cos\theta/\lambda$ and $d_{hkl}^* = 2d_{hkl} sin\theta/\lambda$. A plot of $(\beta_{hkl}^*/d_{hkl}^*)^2$ against $\beta_{hkl}^*/(d_{hkl}^*)^2$ gives a straight line with slope equal to 1/D and a y-intercepts which gives the mean value of crystal lattice strain. The Halder-Wagner plot for the hexadecylamine-capped Sb_2S_3 is shown in Fig. 4b. The average crystallite size obtained from the plot was 62.5 nm, while the calculated strain from the plot was 1.6×10^{-2}.

Table 1 shows the summary of the values for crystallite size, lattice strain and other elastic parameters of hexadecylamine-capped Sb_2S_3 obtained from the employed models. It could be observed that the strain estimated from the Halder Wagner model was several multiples of the values obtained from the W-H analysis. This observation could have resulted from the contributions of lower angles in Halder-Wagner model. It could then be suggested that the lattice dislocation may have played a significant role in the broadening of the peak profiles obtained at lower angles compared to those at higher angles (Motevalizadeh *et al.*, 2014).

The crystallite size analysis for the models showed that the USDM gave a similar value to that of Scherrer's plot, while there was no significant difference between the other W-H analysis and the size-strain plots. Among the plots, the most suitable model may be chosen as the one with the best of the experimental data. Comparing the plots for the models shown in Fig, 2, 3 and 4, the best fittings were obtained for the UDM, size-strain plot and the Halder Wagner plots, while the data points were more scattered in the UDSM and UDEDM plots. The difference between the crystallite size obtained from the Scherrer plot and the W-H analysis could be attributed to the difference in averaging the particle size distribution of the material (Mote *et al.*, 2012). Also, the difference in the crystallite size of the W-H analysis showed that the consideration of isotropic and anisotropic contribution to the crystallite size had a slight influence on the estimated size of crystals.

Table 1: Geometric parameters of hexadecylamine capped Sb_2S_3

Scherrer method	Williamson-Hall methods										Size-strain plot		Halder Wagner method	
	UDM		USDM			UDEDM								
Size (nm)	Size (nm)	Strain ($x10^{-4}$)	Size (nm)	Strain ($x10^{-4}$)	Stress (MPa)	Size (nm)	Strain ($x10^{-4}$)	Stress (MPa)	Energy Density (KJ/m^3)		Size (nm)	Strain ($x10^{-4}$)	Size (nm)	Strain ($x10^{-2}$)
111.3	72.6	-5.5	103.4	-2.5	7.9	90.5	-6.6	2.0	6.8		85.1	-3.49	62.5	-1.6

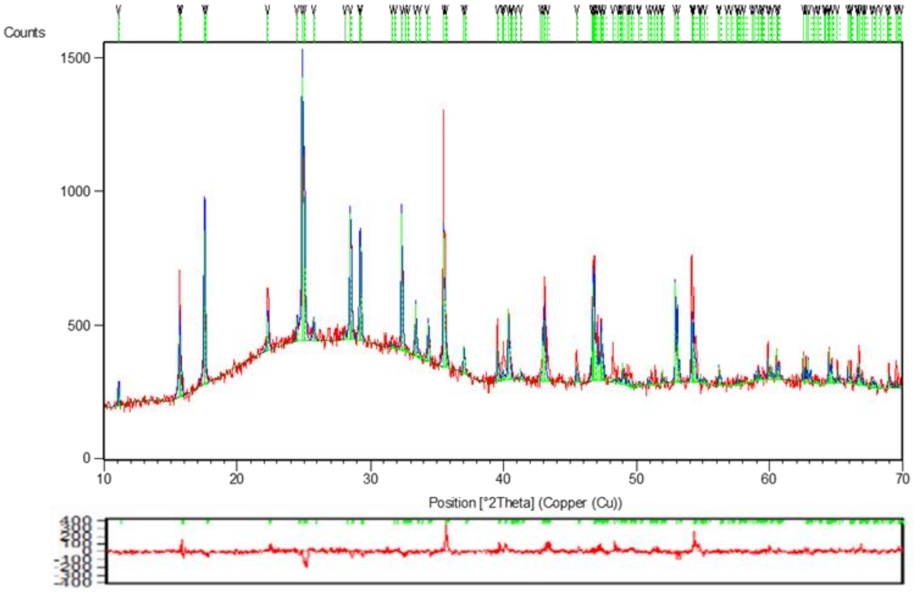

Fig 5: Experimental X-ray powder diffraction pattern (red curve) compared to the Rietveld–refined profile (green curve) for hexadecylamince capped Sb_2S_3. Bottom plot is the difference curve between experimental and simulated curves

3.1.2 Rietveld refinement

Rietveld analysis involves the construction of diffraction patterns, which is calculated in relation to a model employed as crystallographic standard. The analysis uses calculated patterns in simulating profile diffraction and structural parameters of a sample (Oliveira *et al.*, 2020). The Rietveld analysis of the XRD pattern of the hexadecylamine capped Sb_2S_3 was used in determining the crystal properties including lattice parameters, cell volume, bulk density and the stoichiometric composition of the prepared Sb_2S_3. The refinement was done using the X'pert HighScore Plus software and the refined parameters include: scale factor, background, shift lattice constants, profile half-width parameters (u, v, w), and isotropic thermal parameters, which include the lattice parameters and atomic functional positions. The pattern background was used without the application of any correction factor and the peak profile function was modelled using the pseudo-Voigt model.

Fig. 5 shows the Rietveld refinement plot of the hexadecylamine capped Sb_2S_3 for the observed patterns against the calculated patterns of the nanocrystals. The calculated patterns in the analysis were well adjusted to the experimentally observed diffraction profile, and its thus suitable for the calculation of the diffraction profile and structural parameters of the synthesized material. The refinement confirmed that pure crystals were obtained without any secondary phase. The difference plot showed that there were slight differences between the calculated and experimental pattern. However, the obtained fit parameters: R_p, R_{wp}, R_{exp} and GOF, proved the reliability of the refinement data. The data obtained from the Rietveld refinement analysis are shown in Table 2. From the lattice volume, bulk density and molecular weight of the prepared nanomaterials, other empirical parameters such as X-ray density, surface area and porosity were estimated (Kadam *et al.*, 2020). The X-ray intensity of the sample was estimated using the equation:

$$dx = \frac{8M}{N_A V}, \qquad (19)$$

where M, N_A and V are the molecular weight, Avogradro's number and cell volume of the crystals respectively. The percentage porosity of the sample was estimated from the bulk density (d_B) and X-ray density (d_x) from the equation:

$$P = 1 - \frac{d_B}{d_X}\ \%. \qquad (20)$$

The surface area of the material was estimated from the crystallite size and X-ray intensity from the expression:

$$\text{S. A.} = \frac{6}{D \times d_x}. \qquad (21)$$

The estimated values of the X-ray density, porosity and surface area of the hexadecylamine capped Sb_2S_3 are shown in Table 2. The lattice parameters of the material were in agreement with previous reports. The contraction of the crystal lattice of the solvothermally synthesized nanorods suggested by the strain analysis was also confirmed by the Rietveld refinement as unit cell volume of 487.0 x10^6 Pm^3 was obtained compared to 527.4x10^6 Pm^3 reported for bulk Sb_2S_3 (de Jong *et al.*, 2015). A slight reduction in bulk density was also observed in the Sb_2S_3, which suggested that the prepared nanomaterial is porous. The porous nature of the nanomaterial was also supported by the presence Sb vacancies in the crystal as determined by its molecular formula.

Table 2: Empirical parameters for hexadecylamine capped Sb_2S_3 and Rietveld refinement agreement parameters

Lattice parameters (Å)			Bulk density (g/cm^3)	Molecular formula	Volume (10^6) pm^3	Molecular weight	X-ray density (g/cm^3)	Porosity (%)	Surface area (m^2/g)*	R_{exp}	R_{wp}	R_p	GOF
11.3	3.8	11.2	4.2	$Sb_{1.74}S_3$	487.0	307.8	9.2	54.4	7.6	5.5	8.3	6.1	2.2

*Crystallite size obtained from the size-strain plot was used being the best fitted plot.

3.2 Morphological studies

The SEM and TEM images of the synthesized Sb_2S_3 are shown in Fig. 6. The SEM image shows the predominant formation of nanoflakes with small amount of nanorods. Analysis of the TEM image of the rods using the Gutan software showed that the dimensions of the nanorods was 1.055 × 0.348 μm. This value was significantly higher than the values obtained from the crystallite size analysis. Therefore, it indicated that the obtained rods were polycrystalline and might have been formed by the agglomeration of several crystals (Wang *et al.*, 2016). The SEM and TEM images of reactions carried out at longer reaction time (Fig. 6b) showed a reduction in the sizes of the nanoflakes and the presence of larger nanorods. This may suggest that the rods were formed by the dissolution of the nanoflakes as the reaction progressed (Motevalizadeh *et al.*, 2014). Clear lattice fringes are shown in the HRTEM image with d-spacings of 0.271 nm, which corresponds to the (1 0 4) plane.

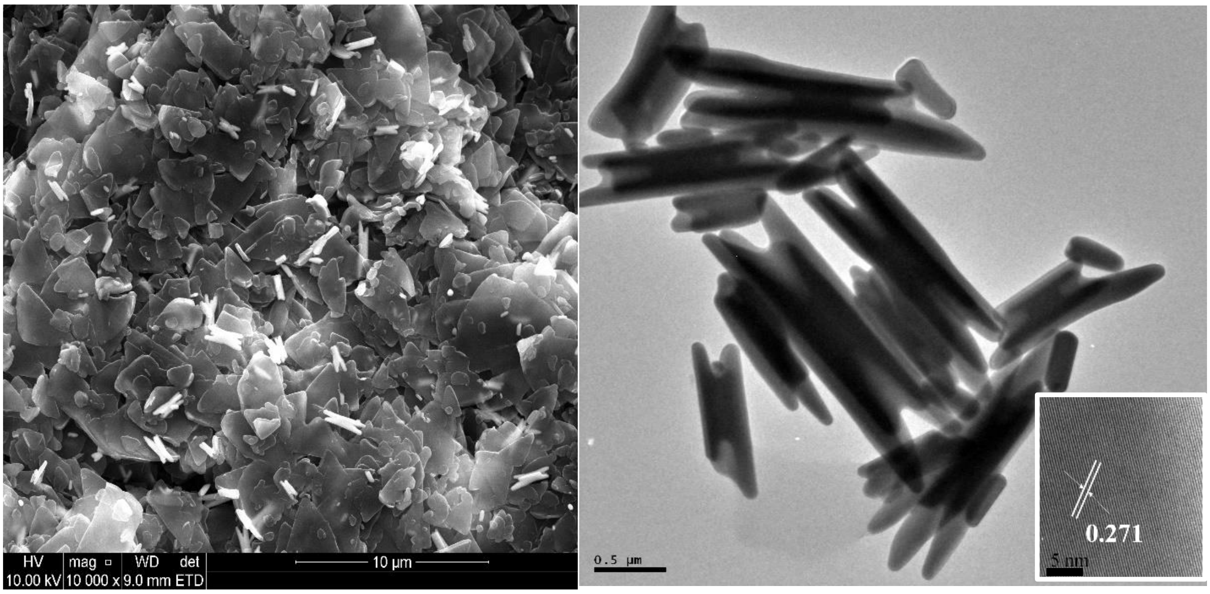

Fig 6: (a) SEM and (b) TEM images (inset: HRTEM) of hexadecylamine capped Sb_2S_3

4.0 Conclusion

Hexadecyamine-capped Sb_2S_3 nanorods were synthesized by the thermolysis of antimony(III) tris(*N*–methyl–*N*–phenyl dithiocarbamate) complex in hexadecylamine and characterized by powder XRD, SEM and TEM. The structural properties of the prepared hexadecylamine-capped Sb_2S_3: crystallite size, microstrain Young's modulus and stress were evaluated using the Scherrer plot, Williamson-Hall models and strain-stress analysis. The models employed in this study showed that the crystallite size and strain were influenced by the assumptions of isotropic and anisotropic nature. The study also confirmed that the strain in the crystal of the material was due to lattice contraction. Further analysis, using Rietveld refinement of the XRD pattern of the prepared Sb_2S_3 nanorods was carried out and crystal properties such as lattice parameters, unit cell volume, bulk density and the composition of the prepared Sb_2S_3 were determined. The lattice parameters obtained were in agreement with literature reports, while a significant reduction in unit cell volume was observed.

5.0 References

Bagheriyan, S. 2013. Sonochemically synthesis of antimonite nanoparticles and its influence on the thermal stability of the ABS terpolymer. *High Temperature Materials and Processes,* 32**,** 339-343.

Balzar, D. & Ledbetter, H. 1993. Voigt-function modeling in Fourier analysis of size- and strain-broadened X-ray diffraction peaks. *Journal of Applied Crystallography,* 26**,** 97-103.

Bao, H., Cui, X., Li, C. M., Song, Q., Lu, Z. & Guo, J. 2007. Synthesis and Electrical Transport Properties of Single-Crystal Antimony Sulfide Nanowires. *The Journal of Physical Chemistry C,* 111**,** 17131-17135.

Ben Naceur, J., Ouertani, R., Chakhari, W. & Chtourou, R. 2019. Photo-electrochemical properties of Sb2S3/TiO2 heterostructures integrally synthesis by hydrothermal method. *Journal of Materials Science-Materials in Electronics,* 30**,** 5631-5639.

Bindu, P. & Thomas, S. 2014. Estimation of lattice strain in ZnO nanoparticles: X-ray peak profile analysis. *Journal of Theoretical and Applied Physics,* 8**,** 123-134.

Biswal, J. B. & Garje, S. S. 2013. Preparation of Antimony Sulfide Nanostructures From Single-Source Antimony Thiosemicarbazone Precursors. *Synthesis and Reactivity in Inorganic Metal-Organic and Nano-Metal Chemistry,* 43**,** 461-465.

Choi, Y. C., Lee, D. U., Noh, J. H., Kim, E. K. & Seok, S. I. 2014. Highly Improved Sb_2S_3 Sensitized-Inorganic–Organic Heterojunction Solar Cells and Quantification of Traps by Deep-Level Transient Spectroscopy. *Advanced Functional Materials,* 24**,** 3587-3592.

Cullity, B. D. & Stock, S. R. 2001. *Elements of X-ray diffraction,* New Jersey, Prentic Hall.

Das, R. & Sarkar, S. J. C. S. 2015. Determination of Intrinsic Strain in Poly(Vinylpyrrolidone)-Capped Silver Nano-Hexapod Using X-Ray Diffraction Technique. 109**,** 775-778.

Davoodi, A., Ahmadi, M. H., Hashemi-karbalaei, M. R., Eskandari, M., Salehi-shahrabi, A. & Fallahian, A. 2016. Microwave synthesis and characterization of Sb_2S_3@NiS nanocomposites and investigation of its solar cell application through the electrophoresis deposition method. *Journal of Materials Science: Materials in Electronics,* 27**,** 13127-13133.

de Jong, M., Chen, W., Angsten, T., Jain, A., Notestine, R., Gamst, A., Sluiter, M., Krishna Ande, C., van der Zwaag, S., Plata, J. J., Toher, C., Curtarolo, S., Ceder, G., Persson, K. A. & Asta, M. 2015. Charting the complete elastic properties of inorganic crystalline compounds. *Scientific Data,* 2**,** 150009.

Delhez, R., de Keijser, T. H. & Mittemeijer, E. J. 1982. Determination of crystallite size and lattice distortions through X-ray diffraction line profile analysis. *Fresenius' Zeitschrift für analytische Chemie,* 312**,** 1-16.

Dey, P. C. & Das, R. 2018. Effect of silver doping on the elastic properties of CdS nanoparticles. *Indian Journal of Physics,* 92**,** 1099-1108.

Halder, N. C. & Wagner, C. N. J. 1966. Separation of particle size and lattice strain in integral breadth measurements. *Acta Crystallographica,* 20**,** 312-313.

Hepp, A. & Baerlocher, C. J. A. J. o. P. 1988. Learned peak shape functions for powder diffraction data. 41**,** 229-236.

Kadam, A. B., Mande, V. K., Kadam, S. B., Kadam, R. H., Shirsath, S. E. & Borade, R. B. 2020. Influence of gadolinium (Gd^{3+}) ion substitution on structural, magnetic and electrical properties of cobalt ferrites. *Journal of Alloys and Compounds,* 840.

Ma, J. M., Duan, X. C., Lian, J. B., Kim, T., Peng, P., Liu, X. D., Liu, Z. F., Li, H. B. & Zheng, W. J. 2010. Sb_2S_3 with Various Nanostructures: Controllable Synthesis, Formation Mechanism, and Electrochemical Performance toward Lithium Storage. *Chemistry-a European Journal,* 16**,** 13210-13217.

Malik, M. A., Revaprasadu, N. & O'Brien, P. 2001. Air-Stable Single-Source Precursors for the Synthesis of Chalcogenide Semiconductor Nanoparticles. *Chemistry of Materials*, 13**,** 913-920.

Mohamed, M. B., Tonti, D., Al-Salman, A., Chemseddine, A. & Chergui, M. 2005. Synthesis of High Quality Zinc Blende CdSe Nanocrystals. *The Journal of Physical Chemistry B,* 109**,** 10533-10537.

Mote, V. D., Purushotham, Y. & Dole, B. N. 2012. Williamson-Hall analysis in estimation of lattice strain in nanometer-sized ZnO particles. *Journal of Theoretical and Applied Physics,* 6**,** 6.

Motevalizadeh, L., Heidary, Z. & Abrishami, M. E. 2014. Facile template free hydrothermal synthesis and microstrain measurement of ZnO nanorods. *Bulletin of Materials Science,* 37**,** 379-405.

Nath, D., Singh, F. & Das, R. 2020. X-ray diffraction analysis by Williamson-Hall, Halder-Wagner and size-strain plot methods of CdSe nanoparticles- a comparative study. *Materials Chemistry and Physics,* 239.

Oliveira, Y. L., Costa, M. J. S., Jucá, A. C. S., Silva, L. K. R., Longo, E., Arul, N. S. & Cavalcante, L. S. 2020. Structural characterization, morphology, optical and colorimetric properties of $NiWO_4$ crystals synthesized by the co-precipitation and polymeric precursor methods. *Journal of Molecular Structure,* 1221**,** 128774.

Ouyang, G., Zhu, W. G., Sun, C. Q., Zhu, Z. M. & Liao, S. Z. 2010. Atomistic origin of lattice strain on stiffness of nanoparticles. *Physical Chemistry Chemical Physics*, 12**,** 1543-1549.

Rajpure, K. Y., Lokhande, C. D. & Bhosale, C. H. 1997. A comparative study of concentration effect of complexing agent on the properties of spray deposited Sb_2S_3 thin films and precipitated powders. *Materials Chemistry and Physics,* 51**,** 252-257.

Rietveld, H. M. 1967. Line profiles of neutron powder-diffraction peaks for structure refinement. *Acta Crystallographica,* 22**,** 151-152.

Sarkar, S. & Das, R. 2018. Shape effect on the elastic properties of Ag nanocrystals. *Micro & Nano Letters,* 13**,** 312-315.

Schneider, R., Weigert, F., Lesnyak, V., Leubner, S., Lorenz, T., Behnke, T., Dubavik, A., Joswig, J. O., Resch-Genger, U., Gaponik, N. & Eychmüller, A. 2016. pH and concentration dependence of the optical properties of thiol-capped CdTe nanocrystals in water and D_2O. *Physical Chemistry Chemical Physics,* 18**,** 19083-19092.

Shunmuga Sundaram, P., Sangeetha, T., Rajakarthihan, S., Vijayalaksmi, R., Elangovan, A. & Arivazhagan, G. 2020. XRD structural studies on cobalt doped zinc oxide nanoparticles synthesized by coprecipitation method: Williamson-Hall and size-strain plot approaches. *Physica B: Condensed Matter,* 595.

Tamilselvan, M., Byregowda, A., Su, C.-Y., Tseng, C.-J. & Bhattacharyya, A. J. 2019. Planar Heterojunction Solar Cell Employing a Single-Source Precursor Solution-Processed Sb_2S_3 Thin Film as the Light Absorber. *ACS Omega,* 4**,** 11380-11387.

Validzic, I. L., Janosevic, V. & Mitric, M. 2016. Characterization and current-voltage characteristics of solar cells based on the composite of synthesized Sb_2S_3 powder with small band gap and natural dye. *Environmental Progress & Sustainable Energy,* 35**,** 512-516.

Wang, H., Odawara, O. & Wada, H. 2016. Facile and Chemically Pure Preparation of $YVO_4:Eu^{3+}$ Colloid with Novel Nanostructure via Laser Ablation in Water. *Scientific Reports,* 6**,** 20507.

Warren, B. E. & Averbach, B. L. 1950. The Effect of Cold-Work Distortion on X-Ray Patterns. *Journal of Applied Physics,* 21**,** 595-599.

Xie, J. J., Liu, L., Xia, J., Zhang, Y., Li, M., Ouyang, Y., Nie, S. & Wang, X. Y. 2018. Template-Free Synthesis of Sb_2S_3 Hollow Microspheres as Anode Materials for Lithium-Ion and Sodium-Ion Batteries. *Nano-Micro Letters,* 10**,** 12.

Yang, J., Zeng, J.-h., Yu, S.-H., Yang, L., Zhang, Y.-H. & Qian, Y.-T. 2000. Pressure-Controlled Fabrication of Stibnite Nanorods by the Solvothermal Decomposition of a Simple Single-Source Precursor. *Chemistry of Materials,* 12**,** 2924-2929.

Zhang, J.-M., Zhang, Y., Xu, K.-W. & Ji, V. 2008. Young's Modulus Surface and Poisson's Ratio Curve for Orthorhombic Crystals. *Journal of Chemical Crystallography,* 38**,** 733-741.

Zhu, J., Yan, X. & Cheng, J. 2018a. Synthesis of water-soluble antimony sulfide quantum dots and their photoelectric properties. *Nanoscale Research Letters,* 13.

Zhu, J., Yan, X. L. & Cheng, J. 2018b. Synthesis of Water-Soluble Antimony Sulfide Quantum Dots and Their Photoelectric Properties. *Nanoscale Research Letters,* 13**,** 6.

CHAPTER SIX

Selective synthesis of kuramite (Cu_2SnS_3) and petrukite (Cu_3SnS_4) phases of copper tin sulphide, and their electrochemical and photocatalytic properties

1.0 Introduction

The search for semiconductor materials with suitable characteristics in terms of cost, toxicity and optical efficiency has continued intensely in the last few decades. The quest is driven by operational limitation, toxicity and cost of currently explored semiconductors such as silicon, CdTe, and GaInAs. Ternary copper sulphides of Cu-Sn-S (CTS) are among the semiconductors that are considered as next-generation compounds for optoelectronic technologies because of their optimum properties for photovoltaic application (Burhanuz Zaman *et al.*, 2019, Dahman and El Mir, 2015, Ghorpade *et al.*, 2016, Giaccherini *et al.*, 2016). Their excellent thermoelectric properties are also being considered for the actualization of nouvelle thermoelectric devices (Tan *et al.*, 2016).

Quite a few numbers of stoichiometric CTS phases have been identified with Cu_2SnS_3, Cu_3SnS_4 and Cu_4SnS_4 as the most studied of the different stoichiometric phases. These compounds exhibit crystal structure dependent energy band gaps with values in the range of 0.9 – 1.7 eV (Robles *et al.*, 2016). The presence of Cu in a multi-valence state allows for high hole density reaching up to ~10^{22} cm^{-3}, which could be influenced by the amount of metal in starting precursor material, temperature and time of reaction, and the reaction rate. CTS have been synthesized through several methods such as mechanochemical process (Maheskumar *et al.*, 2017), microwave-assisted synthesis (Tipcompor *et al.*, 2015), spin coating (Welatta *et al.*, 2018), co-evaporation (Robles *et al.*, 2015) and solvothermal synthesis (Zhao, 2016, Kruszynska *et al.*, 2014). Hydrothermal synthesis of Cu_2SnS_3 with estimated band gap energy of 1.4 eV and particle size of 30 nm was reported by Belaqziz *et al.* (2018). The mechanism of formation was proposed to follow the initial precipitation of Cu_2S, CuS and SnS, which then undergo reaction under hydrothermal condition to giver the ternary compound. Selective synthesis of the zinc blende and wurtzite phase of Cu_2SnS_3 was reported by changing the reaction solvent of the system from octadecylamine to oleylamine. Also, the synthesis of the wurtzite phase was conducted at 190 ºC, compared to 220 ºC for the zinc blende phase (Chang and Waclawik, 2013). Among the different synthetic routes, solvothermal processes offer a facile, reproducible synthetic route, with high control on morphological and structural properties of the prepared nanoparticles. The process also allows for the production of crystalline products at moderate temperature, without the need for any post annealing.

Recently, scanty literature on the use of the single source precursor route involving the co-thermolysis of molecular precursors in high boiling liquids such as oleylamine, ethylene glycol and dodecanethiol has been explored in the synthesis of CTS using ligand systems such as thiourea (Gusain *et al.*, 2015, Tiwari *et al.*, 2013) and dithiocarbamate (Adekoya *et al.*, 2019, Deng *et al.*, 2014) metal complexes. Despite the numerous merits of dithiocarbamte complexes as single source precursors for the synthesis of metal chalcogenides, due to the clean decomposition profile of the compound, there exists only few studies on their use in the synthesis of CTS (Onwudiwe *et al.*, 2021). Therefore, this current study reports the synthesis of Cu(II) bis(*N*-methyl-*N*-phenyl dithiocarbamate) and diphenyltin(II) *N*-methyl-*N*-phenyl dithiocarbamate and their use in the synthesis of CTS. The selective synthesis of two phases Cu_2SnS_3 and Cu_3SnS_4 was achieved by tuning of the reaction parameters such as temperature and solvent. The structural, morphological and optical properties of the prepared nanoparticles were studied, alongside their electrochemical and photocatalytic properties.

2.0 Materials and methods

Cu(II) nitrate pentahydrate, diphenyltin dichloriide, carbon disulphide, N-methyl aniline, oleylamine (OLA), dodecanethiol (DDT), ammonium hydroxide solution, toluene, and methanol used for this study were all of analytical grade and used as supplied by Sigma-Aldrich. For structural characterization, Phillips X’pert diffractometer with a secondary graphite monochromated Cu K α radiation (I = 1.546060 Å) at 40 kV/50 mA was employed for XRD analysis. The optical properties of the nanoparticles were studied using both absorption and emission spectra. PerkinElmer LS 45 fluorimeter was used for recording the emission spectra, while the absorption spectra was recorded using a PerkinElmer λ20 UV-vis-NIR spectrophotometer. Scanning electron microscopy (SEM) and transmission electron microscopy (TEM) measurements were carried out on LYRA 3, TESCAN and JEM—2100 JEOL equipment respectively.

2.1 Synthesis of ammonia salt of *N*-methyl-*N*-phenyl dithiocarbamate ligand

The dithiocarbamate ligand was prepared by following the procedure described by Motaung *et al.* (2019). In brief, equal mole of N-methyl aniline and ammonium hydroxide were mixed together in a round bottom flask that is cooled to ~4℃. The mixture was then allowed to stir for about 10 min after which an equimolar amount of CS_2 was added to the mixture. The reaction was allowed to continue with steady stirring, giving rise to whitish yellow precipitates that was allowed to stir further for another 4 h. The precipitate obtained was filtered with suction and washed with ice-cooled ethanol and the product stored in a refrigerator for further use.

2.2 Synthesis of copper(II) bis(*N*-methyl-*N*-phenyl dithiocarbamate and diphenyl tin(II) bis(*N*-methyl *N*-phenyl dithiocarbamate) complexes

The copper complex of the dithiocarbamate ligand was prepared by mixing aqueous solution of $CuSO_4$ and the obtained dithiocarbamate ligand in 1:2 molar ratio in a round bottom flask which yielded instant formation of dark brown precipitate and was allowed to stir further for 1 h. Afterwards, the precipitate was filtered and washed severally with a mixture of ethanol and water to remove unreacted starting reagents. A similar procedure was employed for the synthesis of organotin(II) bis(*N*-methyl-*N*-phenyl dithiocarbamate) complex. Diphenyl tin dichloride was used as the metal salt and it was dissolved in ethanol instead of water to achieve better solubility. The rest of the synthesis followed the process described for the copper complex.

2.3 Synthesis of Cu_2SnS_3 and Cu_3SnS_4 nanoparticles

The heat-up method, employing the co-thermolysis of precursor complexes, was employed for the synthesis of the nanoparticles. For the Cu_2SnS_3, the copper and tin precursors in ratio 3:1 were mixed together with 15 mL of oleylamine to form a slurry. The set-up was attached to condenser and then purged with N_2 in order to remove oxygen from the system. The set-up was then placed on a digitally controlled heating mantle and heated up to 220℃ (at a heating rate of 10℃/min) and held at this temperature for 1 h. The system was allowed to cool to room temperature and the nanoparticles were precipitated by adding ethanol to the solution. The final product mix was then centrifuged at 5000 rpm to separate the nanoparticles from the solvent and other reaction by products. The nanoparticles were purified by washing with a mixture of ethanol and toluene (3:1) with centrifugation, after which they were dispersed in ethanol and left under vacuum to dry. The dried samples were then stored in air tight sample containers for further use. For the synthesis of Cu_3SnS_4, similar steps as described for Cu_2SnS_4 were employed. However, the solvent in the reaction was changed from oleylamine to a mixture of oleylamine and dodecanethiol (OlA/DDT = 5/1) and the final reaction temperature of the process was set to 180℃.

2.4 Electrochemical measurement

The electrochemical properties of the nanoparticles were determined using a three-electrode electrochemical cell. The cell comprised of modified electrode made up of coated glassy carbon electrode, Ag/AgCl reference electrode, platinum wire as counter electrode and an electrolyte made up of $[Fe(CN)_6]^{4-}[Fe(CN)_6]^{3-}$. The modified electrode was prepared using a dimethylformamide (DMF) solution of the nanoparticles. The measurements were carried out in an Autolab Potentiostate PGSTAT.

The electrochemical impedance spectroscopy (EIS) was measured using Autolab NOVA software. The Bode plot, Nyquist plots and the equivalent circuit were obtained using Nova 2.1.4 software.

2.5 Photocatalytic degradation studies

The photocatalytic activity of the nanoparticles was evaluated against tetracycline as test pollutant. In a typical process, 50 mL of 10 mg/L tetracycline was measured into a 100 mL beaker. Afterwards, 10 mg of the nanoparticle was added and the mixture stirred for 30 min in the dark to achieve adsorption-desorption equilibrium. The 28 W UV LED light was then turned on, and aliquots were taken at intervals. The concentration of tetracycline left in solution was measured using a ONDE spectrophotometer and the percentage degradation was calculated using Eq.1:

$$\%\ \text{degradation} = \frac{C_0 - C_t}{C_o} \times 100. \qquad 1$$

The degradation data was further fitted into the pseudo first order kinetic plot using the linearized equation:

$$-\text{kt} = ln\left(\frac{C_t}{C_o}\right), \qquad 2$$

where Co and Ct represent the initial and concentration at time t of tetracycline, k is the reaction rate constant and t is the reaction time.

3.0 Results and discussion

Two phases of CTS were selectively synthesized by varying the temperature and the solvent in the reaction system. The formation of different phases with the same precursor compound can be explained in terms of the thermodynamics that exist between the precursor and the solvent/capping agent mixture. The two solvents used in this synthesis are well explored high boiling point solvents with unique properties. Oleylamine has been well explored as a capping agent in nanoparticles synthesis because of its great coordinating ability, which enhances the decomposition of metal complexes at lower temperature and also, its ability to induce phase tunability due to its increased reducing ability that increases with temperature (Mourdikoudis and Liz-Marzán, 2013). Meanwhile, dodecanthiol’s (DDT) ability to induce cation exchange in copper chalcogenide by extracting copper from the crystal lattice and also its ability to serve as a sulphur source has been widely explored in the synthesis of different phases and morphology (Chen and Li, 2018). The synthesis of ternary metal sulphides could either follow a path involving cation exchange reaction or solid-state reaction between metal sulphides. In reactions involving single source precursors (SSP), the formation of metal sulphides is considered the most probable pathway to ternary metal sulphides, because the metal complexes decompose into their metal sulphides upon thermolysis in high boiling solvent.

In this study, when [$Cu(DTC)_2$] and [$R_2Sn(DTC)_2$] were co-thermolyzed in oleylamine at 220℃, the kuramite phase (Cu_2SnS_3) was obtained. However, when the reaction system was modified by introducing DDT into the system in a volume ratio of 1:5 (dodecanthiol:oleylamine) and reducing the temperature of the system to 180℃, the petrukite phase (Cu_3SnS_4) was obtained. It is also worthy of note that the stoichiometric ratio of the precursor molecules was maintained at 3:1 for both CTS phase. Efforts to synthesize the Cu_2SnS_3 phase with the stoichiometric amount of precursor molecules yielded mixed phases of copper sulphides and tin sulphides. In a previous study by Liu *et al.* (2017) using preformed CuS template and two tin salts ($SnCl_2$ and $SnCl_4$), it was observed that while the reaction between CuS and $SnCl_2$ yielded Cu_3SnS_4 in oleylamine, Cu_2SnS_3 (mohite phase) was only obtained with $SnCl_4$ in the presence of oleylamine and DDT. The oxidation state of Sn and the copper extracting ability of DDT was observed to play an important role in the successful synthesis of CTS. However, in this study, the synthesis of Cu_3SnS_4 was achieved in the presence of DDT, while Cu_2SnS_3 was obtained with oleylamine as a solvent, suggesting that the reaction must have followed a pathway influenced by the complexing of the Sn ion.

3.1 Structural properties of Cu_2SnS_3 and Cu_3SnS_4

The XRD spectra of the prepared nanocrystals and standard pattern are shown in Fig. 1. All the peaks in the XRD spectra of Fig. 1(a) can be indexed to the tetragonal crystal system of Cu_2SnS_3 with space group 1-42m and lattice parameters a = b = 5.41 and c = 10.52. The diffraction pattern for Cu_3SnS_4 showed peaks that can be indexed to the orthorhombic crystal system, with space group Pmn 2i and lattice parameters a = 6.52; b = 7.52 and c = 37.6 Ǻ (JCPD No: 00-036-0217)

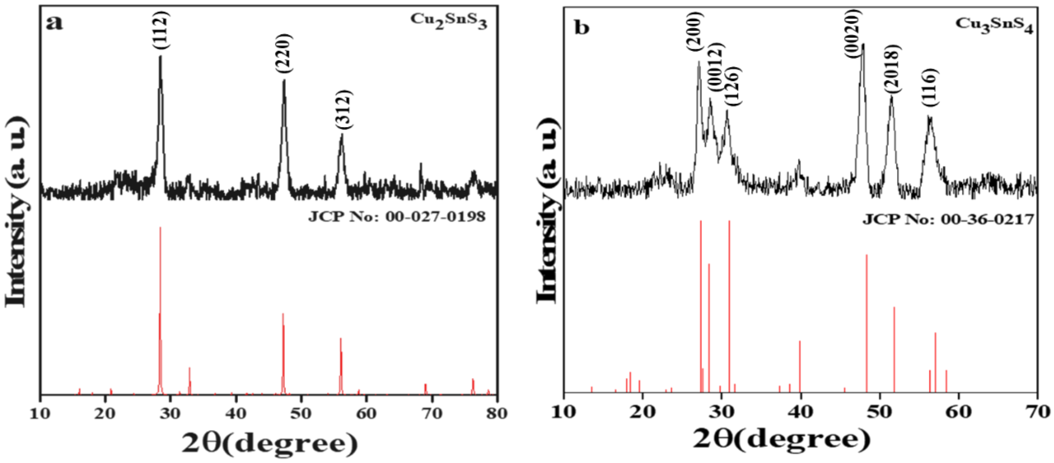

Fig 1: XRD spectra of Cu_2SnS_3 and Cu_3SnS_4 prepared by the co-thermolysis of [$Cu(DTC)_2$] and [$R_2Sn(DTC)]_2$.

To estimate the crystallite size from the XRD patterns, the Scherrer's equation (Eq. 3) was employed.

$$D = \frac{K\lambda}{\beta cos\theta} \qquad 3$$

With parameters D, K, λ, β, and θ representing crystallite size, shape factor (0.90), X-ray wavelength, Bragg angle and the line broadening at half maximum intensity (FWHM) after subtracting instrumental broadening. The average particle size of the nanocrystals obtained from the FWHM of the most prominent peaks of the XRD patterns was 13.1 and 12.3 nm for Cu_2SnS_3 and Cu_3SnS_4 respectively.

3.2 Morphological properties of Cu_2SnS_3 and Cu_3SnS_4

The SEM and TEM images of the CTS nanocrystals are shown in Fig. 2, with the particle size distribution histogram. The SEM images (Fig 2a and b) showed the nanocrystals were slightly agglomerated, with the TEM images (Fig 2c and d) showing the spherical morphology of the particles for both Cu_2SnS_3 and Cu_3SnS_4 respectively. The measured particle size from the TEM images were 13.7 ± 2.4 and 11.3 ± 1.5 nm for the Cu_2SnS_3 and Cu_3SnS_4 respectively, showing the nanocrystals were of narrow particle size distribution. The measured particle sizes were also in good agreement with the crystallite size obtained using the Scherrer's equation.

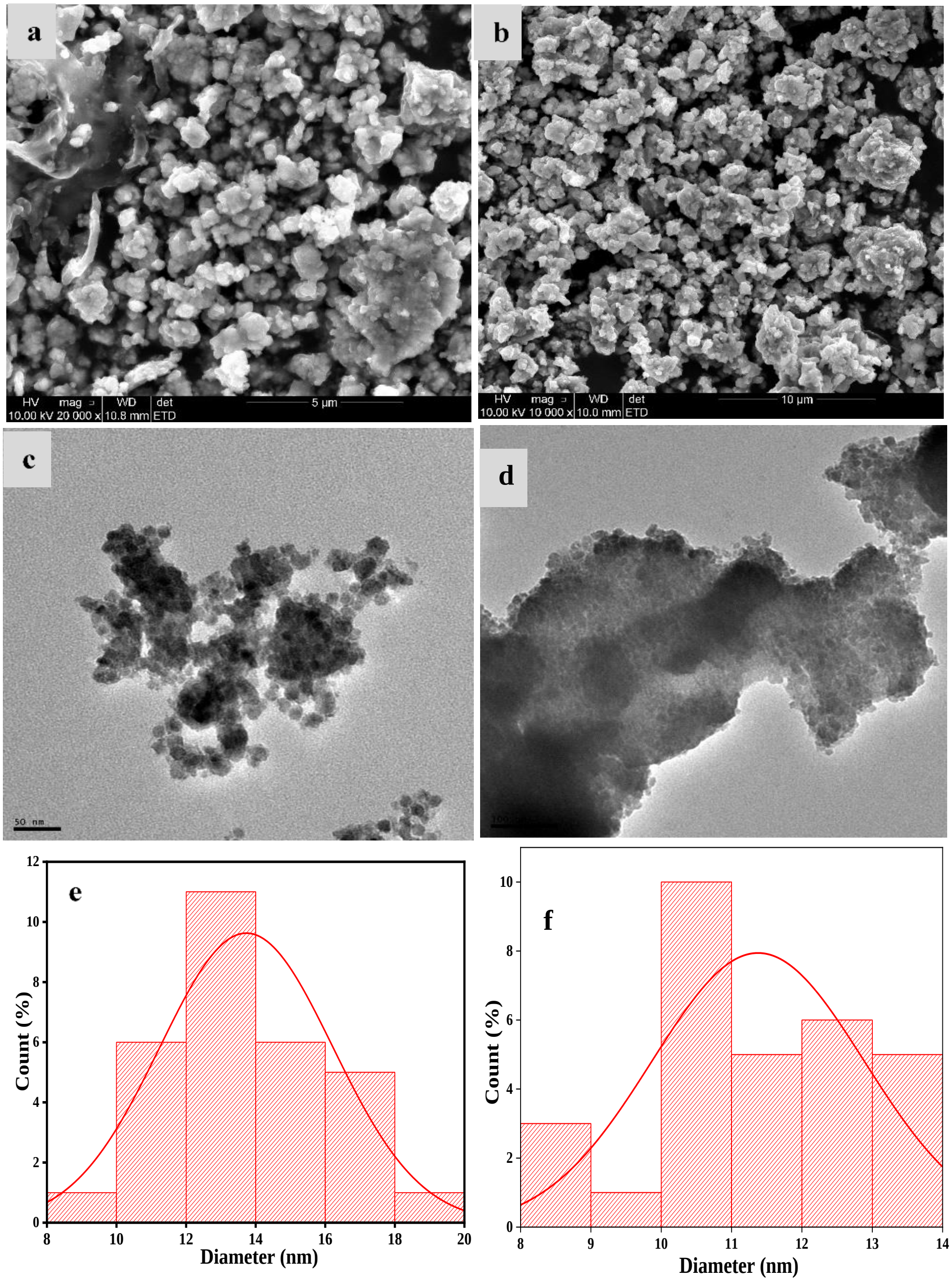

Fig 2: (a, b) SEM images, (c, d) TEM images, and (e, f) size distribution histograms of Cu_2SnS_3 and Cu_3SnS_4 respectively.

3.3 Optical properties of Cu_2SnS_3 and Cu_3SnS_4

The absorption spectra of the Cu_2SnS_3 and Cu_3SnS_4 nanocrystals recorded on a UV-vis-NIR spectrophotometer are shown in Fig. 3 a and b respectively. Both compounds show broad absorption in the UV and NIR regions with absorption onset in the UV-region at about ~400 nm. The Cu_3SnS_4 phase showed higher absorbance in the UV-region and NIR region compared to the Cu_2SnS_3 phase, although the intensity of absorption was slightly reduced in the NIR region. Absorption in the NIR region by CTS compounds has been attributed to localized surface plasmon resonance (LSPR) and the intensity of LSPR has been reported to increase with increase in the Cu/Sn ratio in the crystal. This may account for the higher absorption in the NIR by the Cu_3SnS_4 compared to the Cu_2SnS_3 phase. Also, the stronger NIR absorption is an indication of higher charge carrier density in the Cu_3SnS_4 phase (Li *et al.*, 2015).

The insets of Fig. 3, show the plot of $(\alpha h\nu)^2$ against the light's photon energy (Tauc plot), from which the band gap energy of the nanocrystals was obtained by extrapolating the linear portion of the plot, which is the absorption edge part of the spectrum to the intersection with the x-axis. The band gap energy for the CTS nanocrystal were 1.16 and 1.57 eV for the Cu_2SnS_3 and Cu_3SnS_4 phases respectively, which were in agreement with values reported in literature (Guan *et al.*, 2012). The band gaps were lower than the theoretically calculated values, which may arise due to quantum confinement in the nanosized crystallites.

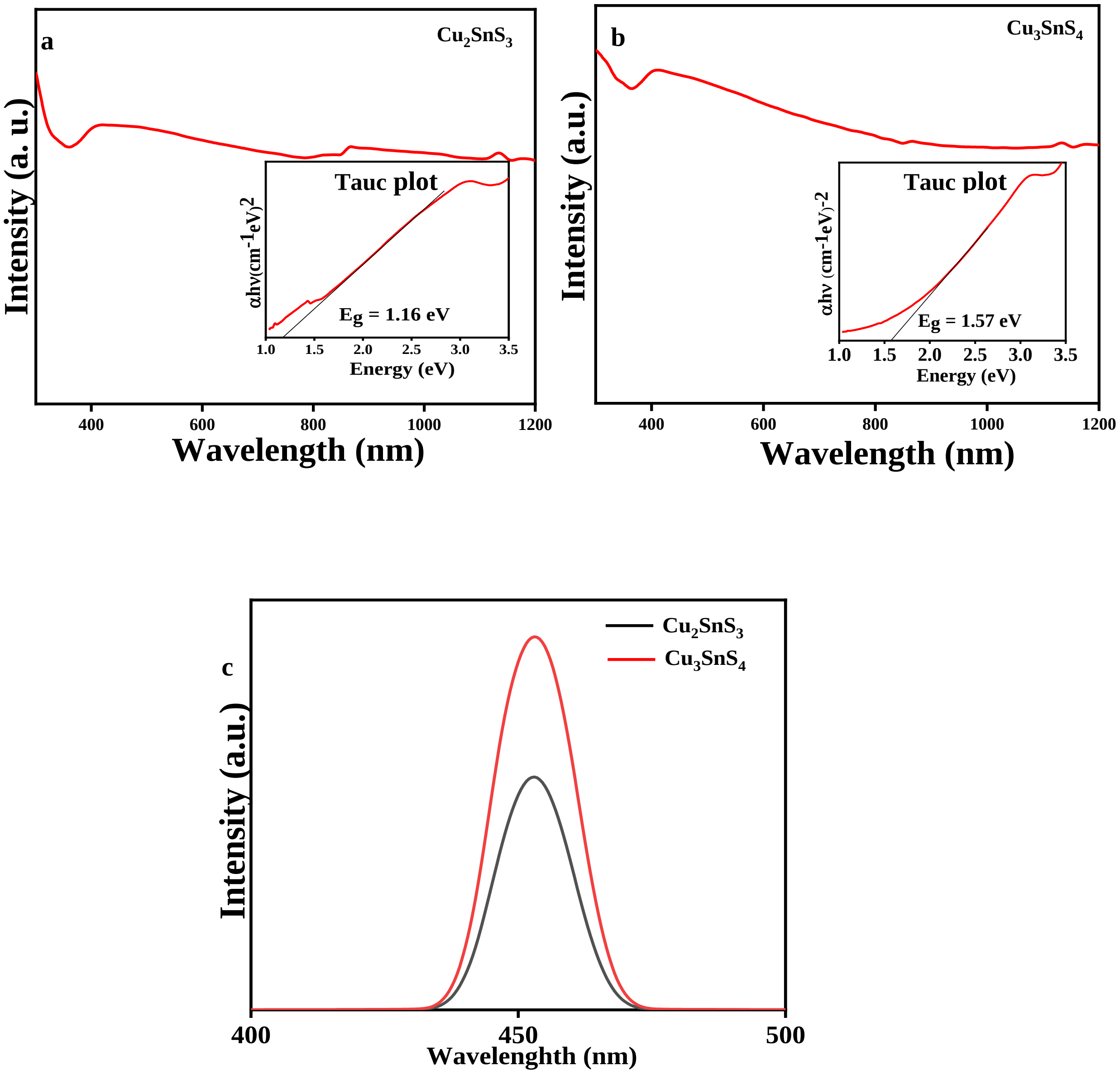

Fig 3: Absorption spectra of (a) Cu_2SnS_3, (b) Cu_3SnS_4 with their respective Tauc plots (inset) and (c) the PL spectra of Cu_2SnS_3 and Cu_3SnS_4 nanocrystals.

The emission spectra of the CTS phases are shown in Fig. 3c. The spectra of the ethanol solution of the nanoparticles excited at 450 nm (2.7 eV), showed intense emission peaks, with higher emission intensity in the spectrum of the Cu_3SnS_4 phase h than that of the Cu_2SnS_3 phase. This emission band can be assigned to band transitions and confirms the presence of mid-band gaps in the electronic structure of the compounds (Adekoya *et al.*, 2019). Also, the difference in the emission properties of the two phases may result from the difference in crystal structure.

3.4 Electrochemical studies

The redox potential of the nanoparticles were determined using cyclic voltammograms of the modified glassy carbon electrodes measured in 5 mM $[Fe(CN)_6]^{4-}[Fe(CN)_6]^{3-}$ redox couple between -0.1 and +0.6 V potential window at a scan rate of 50 mV/s. Fig. 4a shows the cyclic voltammogram of the bare glassy carbon electrode and the electrode modified with Cu_2SnS_3 and Cu_3SnS_4. A pair of redox waves were observed on the three electrodes, which could be ascribed to the $[Fe(CN)_6]^{4-}/[Fe(CN)_6]^{3-}$ redox process. In Fig. 4a, the Cu_2SnS_3 based electrode showed a slightly higher current density compared to the bare electrode, while the Cu_3SnS_4-modified electrode exhibited a slightly lower current density. This suggests a faster redox reaction rate and better electrocatalytic activity for the $[Fe(CN)_6]^{4-}/[Fe(CN)_6]^{3}$ redox couple on Cu_2SnS_3 (Ozel *et al.*, 2016).

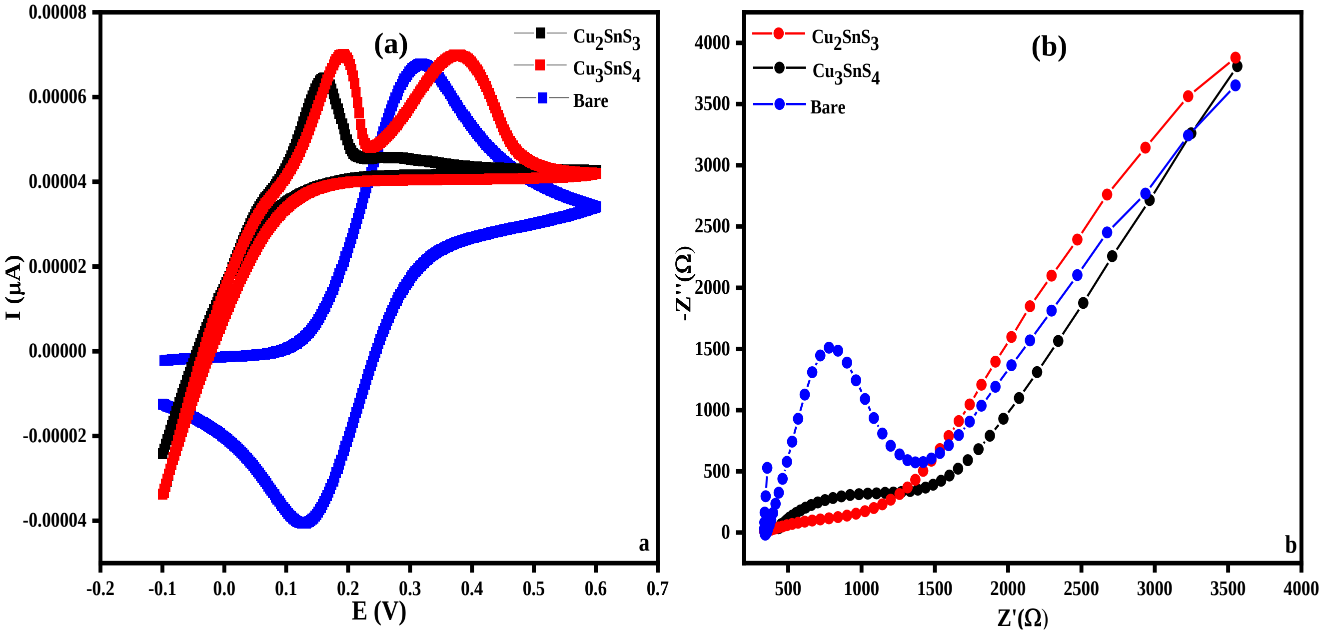

Fig 4: (a) cyclic voltammogram (b) and Nyquist plots of bare electrode, Cu_2SnS_3 and Cu_3SnS_4 modified electrodes.

The electrochemical impedance spectroscopy (EIS) was also measured in order to understand the charge transfer process at the interface between the electrolyte and the counter electrode. EIS could offer information on the ion transport and charge transfer characteristics of the modified electrodes. The EIS spectra of the Cu_2SnS_3 and Cu_3SnS_4 which show the frequency response of the electrode-electrolyte system as a plot of the imaginary component (Z″) against the real component (Z′) is shown in Fig. 4b. The radius of the semicircle of the plots correlates with the charge transfer resistance (R_{ct}) at the nanoparticles/electrolyte interface. The lower the value of R_{ct} the more effective is the charge transfer between the material and the electrolyte. The smaller semicircle arc radius of Cu_2SnS_3 in the EIS spectrum is an indicator of the lower resistance, better charge transport and conducting properties compared to Cu_3SnS_4 (Li *et al.*, 2016). The presence of a semicircle in the high frequency region and a linear portion in the low frequency region is an indication of the capacitive characteristic of the electrode (Liang *et al.*, 2017).

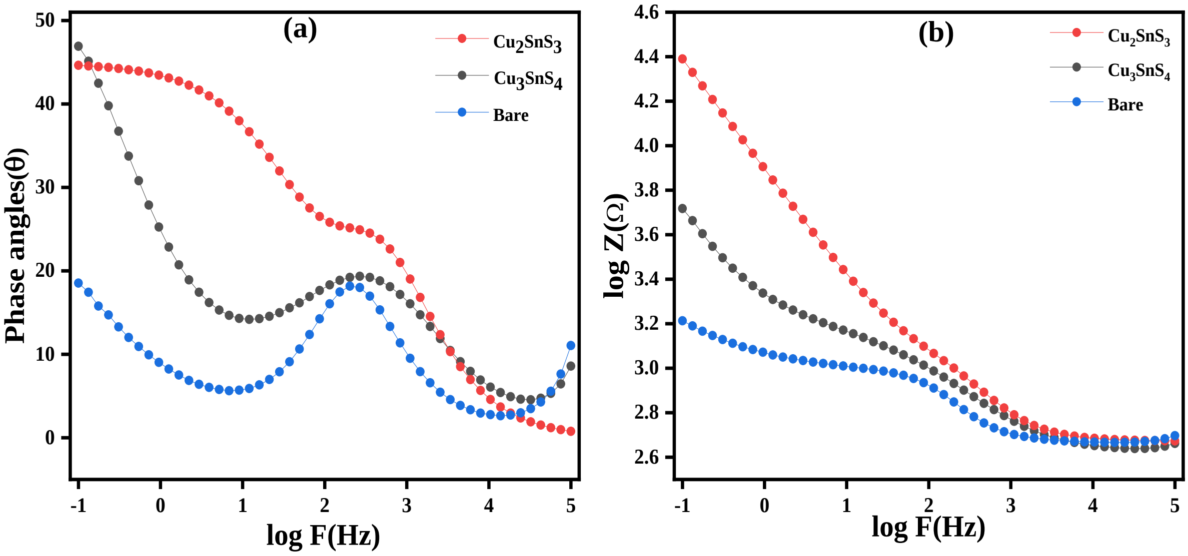

Fig 5: Bode plots of bare electrode and Cu_2SnS_3 and Cu_3SnS_4 modified electrode

The Bode plots fitted for the EIS spectra are shown in Fig. 5a. The plot shows the change in phase angle with respect to applied frequency, which shows the redox diffusion activity in the electrolyte and the charge transfer process taking place at the electrode/electrolyte interface (Motaung *et al.*, 2021). For an ideal capacitor, the phase angle is close to 90° (Yuan *et al.*, 2012). The phase angles for the bare electrode, and modified electrodes were 19, 45 and 47° respectively for the unmodified, Cu_2SnS_3- and Cu_3SnS_4-modified electrodes respectively. This indicates a psuedo-capacitance characteristic of the prepared nanoparticles. Bode plots of impedance spectra, which shows the frequency breakpoint related to the characteristic time constant $\tau = 1/\omega = RsCdl$ of the electrode/electrolyte circuit (Motaung *et al.*, 2021) is shown in Fig. 5b.

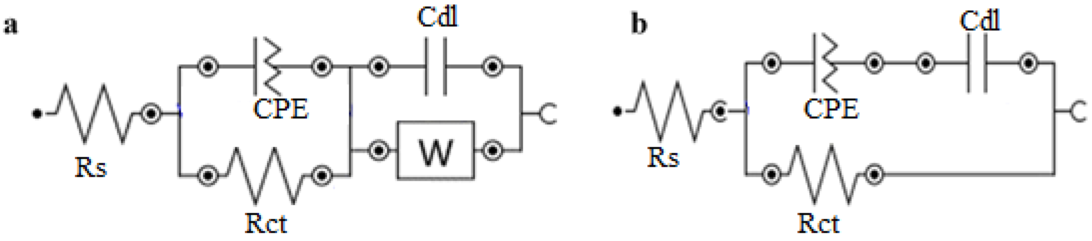

Fig 6: Equivalent circuits for (a) Cu_2SnS_3 and (b) Cu_3SnS_4

The equivalent circuits for Cu_2SnS_3 and Cu_3SnS_4 are shown in Fig. 6. The equivalent circuits showed a difference in the electrochemical properties of the two nanoparticles. While the equivalent circuit of Cu_3SnS_4 comprises of the series resistance (Rs), charge transport resistance (R_{ct}), constant phase element (CPE) and the double layer capacitance, the equivalent circuit of Cu_2SnS_3 contained an additional circuit element, which is the Warburg impedance (W). The non-ideal frequency dependent capacitance at the NP/electrolyte interface, represented by the constant phase element (CPE) was evaluated to be higher in Cu_3SnS_4 compared to Cu_2SnS_3. A higher CPE value correlates to larger surface area of the NP (Fan *et al.*, 2015, Lin *et al.*, 2011).

Table 1: The equivalent circuit components values for Cu_2SnS_3 and Cu_3SnS_4

	R_s(Ω)	R_{ct}(Ω)	CPE	W	C_{dl} (μF)
Cu_2SnS_3	469	698	4.22	51.7	2.41
Cu_3SnS_4	238	32.1*	315	-	212

* unit is in kΩ

3.5 Evaluation of photocatalytic activity

The photocatalytic activity of the CTS NPs was evaluated for the degradation of tetracycline (TCE) under UV-light irradiation. Fig. 7 shows the percentage degradation plot and the kinetics for the degradation process. The percentage degradation of TCE by Cu_2SnS_3 and Cu_3SnS_4 nanoparticles was 94.0 and 73.0% respectively, compared to 14.3% achieved under UV light alone. The photocatalytic activity of Cu_3SnS_4 was comparable to the values reported by Liu *et al.* (2014) for the degradation of bisphenol and rhodamine b dye. The excellent photocatalytic activity of Cu_2SnS_3 for methylene blue degradation was also reported by Tan *et al.* (2012). The higher activity of Cu_2SnS_3 could be attributed to its lower band gap, which resulted in the higher absorption of light and greater generation of charge carriers (Yan *et al.*, 2013, Fatima *et al.*, 2017). Also, its lower photoluminescence band intensity implies that charge carrier recombination is lower in Cu_2SnS_3 compared to Cu_3SnS_4 (Sarma *et al.*, 2016). The pseudo first order kinetic rate constant for the degradation of TCE was 3.5×10^{-2} and 1.1×10^{-2} min^{-1} for Cu_2SnS_3 and Cu_3SnS_4 respectively. The degradation rate by Cu_2SnS_3 was almost 3-fold, the rate of degradation obtained for the Cu_3SnS_4 phase.

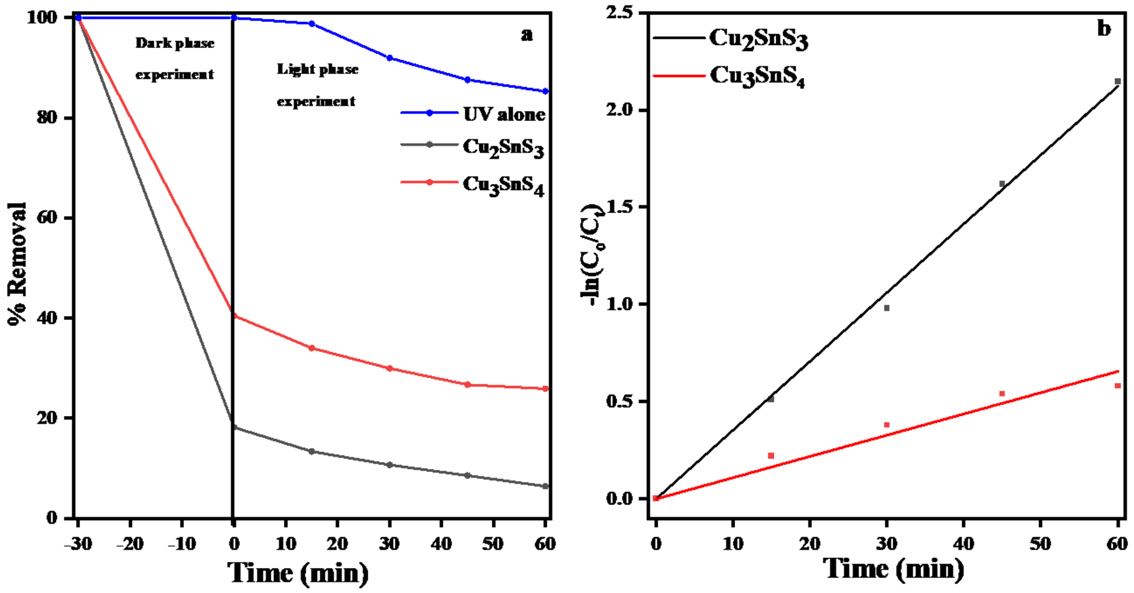

Fig 7: (a) photocatalytic degradation profile of tetracycline under UV light irradiation alone and in the presence of Cu_2SnS_3 and Cu_3SnS_4 (b) Psuedo first order kinetics for the degradation of tetracycline

4.0 Conclusion

In this study, the synthesis of copper tin sulphides from single source precursor of dithiocarbamates complexes and the selective synthesis of two different phases were explored. The study has shown that two stoichiometric phases of copper tin sulphides (CTS), Cu_2SnS_3 and Cu_3SnS_4, could be synthesized by the co-thermolysis of precursor complexes, with phase selectivity achieved by varying the temperature and solvent in the reaction system. The phase purity of the nanoparticles was confirmed by X-ray diffraction, and the particle sizes of the Cu_2SnS_3 and Cu_3SnS_4 were 13.2 and 12.1 nm with optical band gaps of 1.16 and 1.57 eV respectively. The electrochemical and photocatalytic properties of both phases were further evaluated, with the Cu_2SnS_3 phase showing better properties compared to the Cu_3SnS_4 phase. This study further affirmed the suitability of the solvothermal process in achieving phase selectivity of nanoparticles through the manipulation of reaction parameters such as temperature and solvent, and the possibility of a facile route to other less studied stoichiometries of the CTS system.

5.0 References

Adekoya, J. A., Khan, M. D. & Revaprasadu, N. 2019. Phase transition in $Cu_{2+x}SnS_{3+y}$ ($0 \leq x \leq 2$; $0 \leq y \leq 1$) ternary systems synthesized from complexes of coumarin derived thiocarbamate motifs: optical and morphological properties. *RSC Advances,* 9**,** 35706-35716.

Belaqziz, M., Medjnoun, K., Djessas, K., Chehouani, H. & Grillo, S. E. 2018. Structural and optical characterizations of Cu_2SnS_3 (CTS) nanoparticles synthesized by one-step green hydrothermal route. *Materials Research Bulletin,* 99**,** 182-188.

Burhanuz Zaman, M., Chandel, T. & Poolla, R. Solvothermal synthesis of ternary Cu_2SnS_3 (CTS) nanostructures in ethylenediamine: Effect of different oleic acid concentrations on structural, optical and morphological Properties. Materials Today: Proceedings, 2019. 1185-1191.

Chang, J. & Waclawik, E. R. 2013. Controlled synthesis of $CuInS_2$, Cu_2SnS_3 and Cu_2ZnSnS_4 nano-structures: insight into the universal phase-selectivity mechanism. *CrystEngComm,* 15.

Chen, L. & Li, G. 2018. Functions of 1-Dodecanethiol in the Synthesis and Post-Treatment of Copper Sulfide Nanoparticles Relevant to Their Photocatalytic Applications. *ACS Applied Nano Materials,* 1**,** 4587-4593.

Dahman, H. & El Mir, L. 2015. Cu_2SnS_3 thin films deposited by spin coating route: a promise candidate for low cost, safe and flexible solar cells. *Journal of Materials Science: Materials in Electronics,* 26**,** 6032-6039.

Deng, M., Shen, S., Zhang, Y., Xu, H. & Wang, Q. 2014. A generalized strategy for controlled synthesis of ternary metal sulfide nanocrystals. *New J. Chem.,* 38**,** 77-83.

Fan, M.-S., Chen, J.-H., Li, C.-T., Cheng, K.-W. & Ho, K.-C. 2015. Copper zinc tin sulfide as a catalytic material for counter electrodes in dye-sensitized solar cells. *Journal of Materials Chemistry A,* 3**,** 562-569.

Fatima, S., Ali, S. I., Iqbal, M. Z. & Rizwan, S. 2017. The high photocatalytic activity and reduced band gap energy of La and Mn co-doped $BiFeO_3$/graphene nanoplatelet (GNP) nanohybrids. *RSC Advances,* 7**,** 35928-35937.

Ghorpade, U. V., Suryawanshi, M. P., Shin, S. W., Kim, I., Ahn, S. K., Yun, J. H., Jeong, C., Kolekar, S. S. & Kim, J. H. 2016. Colloidal Wurtzite Cu_2SnS_3 (CTS) Nanocrystals and Their Applications in Solar Cells. *Chemistry of Materials,* 28**,** 3308-3317.

Giaccherini, A., Montegrossi, G. & Di Benedetto, F. 2016. Stability of Naturally Relevant Ternary Phases in the Cu–Sn–S System in Contact with an Aqueous Solution. *Minerals,* 6.

Guan, H., Shen, H., Gao, C. & He, X. 2012. Structural and optical properties of Cu_2SnS_3 and Cu_3SnS_4 thin films by successive ionic layer adsorption and reaction. *Journal of Materials Science: Materials in Electronics,* 24**,** 1490-1494.

Gusain, M., Rawat, P. & Nagarajan, R. 2015. Facile synthesis and optical properties of pure and Ni^{2+}, Co^{2+}, Bi^{3+}, Sb^{3+} substituted Cu_3SnS_4. *RSC Advances,* 5**,** 43202-43208.

Kruszynska, M., Parisi, J. & Kolny-Olesiak, J. 2014. Synthesis and Shape Control of Copper Tin Sulphide Nanocrystals and Formation of Gold–Copper Tin Sulphide Hybrid Nanostructures. *Zeitschrift für Naturforschung A,* 69**,** 446-450.

Li, K., Peng, T., Ying, Z., Song, S. & Zhang, J. 2016. Ag-loading on brookite TiO_2 quasi nanocubes with exposed {210} and {001} facets: Activity and selectivity of CO_2 photoreduction to CO/CH_4. *Applied Catalysis B: Environmental,* 180**,** 130-138.

Li, Y., Ling, W., Han, Q., Kim, T. W. & Shi, W. 2015. Localized surface plasmon resonances and its related defects in orthorhombic Cu_3SnS_4 nanocrystals. *Journal of Alloys and Compounds,* 633**,** 347-352.

Liang, K., Wang, C., Xu, X., Leng, J. & Ma, H. 2017. Capacitive and photocatalytic performance of Bi_2S_3 nanostructures synthesized by solvothermal method. *Physics Letters A,* 381**,** 652-657.

Lin, J.-Y., Liao, J.-H. & Chou, S.-W. 2011. Cathodic electrodeposition of highly porous cobalt sulfide counter electrodes for dye-sensitized solar cells. *Electrochimica Acta,* 56**,** 8818-8826.

Liu, H., Chen, Z., Jin, Z., Su, Y. & Wang, Y. 2014. A reduced graphene oxide supported Cu_3SnS_4 composite as an efficient visible-light photocatalyst. *Dalton Trans,* 43**,** 7491-8.

Liu, Y., Liu, M., Yin, D., Wei, W., Prasad, P. N. & Swihart, M. T. 2017. Kuramite Cu_3SnS_4 and Mohite Cu_2SnS_3 Nanoplatelet Synthesis Using Covellite CuS Templates with Sn(II) and Sn(IV) Sources. *Chemistry of Materials,* 29**,** 3555-3562.

Maheskumar, V., Gururajan, B. & Vidhya, B. 2017. Investigations on the structural, optical and visible light photocatalytic activity of Cu_3SnS_4 prepared by mechanical alloying. *Journal of Materials Science: Materials in Electronics,* 28**,** 19081-19089.

Motaung, M. P., Onwudiwe, D. C. & Lei, W. 2021. Microwave-Assisted Synthesis of Bi_2S_3 and Sb_2S_3 Nanoparticles and Their Photoelectrochemical Properties. *ACS Omega,* 6**,** 18975-18987.

Motaung, M. P., Osuntokun, J. & Onwudiwe, D. C. 2019. The heat-up synthesis of monodispersed Bi_2S_3 and Cu_7S_4 nanoparticles from novel precursor complexes and their characterizations. *Materials Science in Semiconductor Processing,* 99**,** 92-98.

Mourdikoudis, S. & Liz-Marzán, L. M. 2013. Oleylamine in Nanoparticle Synthesis. *Chemistry of Materials,* 25**,** 1465-1476.

Onwudiwe, D. C., Olatunde, O. C. & Mathur, S. 2021. Structural studies and morphological properties of antimony sulphide nanorods obtained by solvothermal synthesis. *Physica B: Condensed Matter,* 605**,** 412691.

Ozel, F., Sarilmaz, A., Istanbullu, B., Aljabour, A., Kus, M. & Sonmezoglu, S. 2016. Penternary chalcogenides nanocrystals as catalytic materials for efficient counter electrodes in dye-synthesized solar cells. *Sci Rep,* 6**,** 29207.

Robles, V., Trigo, J. F., Guillén, C. & Herrero, J. 2015. Copper tin sulfide (CTS) absorber thin films obtained by co-evaporation: Influence of the ratio Cu/Sn. *Journal of Alloys and Compounds,* 642**,** 40-44.

Robles, V., Trigo, J. F., Guillén, C. & Herrero, J. 2016. Copper tin sulfide (Cu_xSnS_y) thin films evaporated with x = 3,4 atomic ratios: Influence of the substrate temperature and the subsequent annealing in sulfur. *Materials Research Bulletin,* 83**,** 116-121.

Sarma, B., Deb, S. K. & Sarma, B. K. 2016. Photoluminescence and photocatalytic activities of Ag/ZnO metal-semiconductor heterostructure. *Journal of Physics: Conference Series,* 765**,** 012023.

Tan, Q., Sun, W., Li, Z. & Li, J.-F. 2016. Enhanced thermoelectric properties of earth-abundant Cu_2SnS_3 via In doping effect. *Journal of Alloys and Compounds,* 672**,** 558-563.

Tan, Y., Lin, Z., Ren, W., Long, W., Wang, Y. & Ouyang, X. 2012. Facile solvothermal synthesis of Cu_2SnS_3 architectures and their visible-light-driven photocatalytic properties. *Materials Letters,* 89**,** 240-242.

Tipcompor, N., Thongtem, S. & Thongtem, T. 2015. Effect of microwave radiation on the morphology of tetragonal Cu_3SnS_4 synthesized by refluxing method. *Superlattices and Microstructures,* 85**,** 488-496.

Tiwari, D., Chaudhuri, T. K., Shripathi, T., Deshpande, U. & Rawat, R. 2013. Non-toxic, earth-abundant 2% efficient Cu_2SnS_3 solar cell based on tetragonal films direct-coated from single metal-organic precursor solution. *Solar Energy Materials and Solar Cells,* 113**,** 165-170.

Welatta, F., Kissani, A. E., Aggour, M. & Outzourhit, A. Structural, morphological and optical properties of copper-tin-sulfide thin film synthesized by spin coating technique. IOP Conference Series: Earth and Environmental Science, 2018.

Yan, H., Wang, X., Yao, M. & Yao, X. 2013. Band structure design of semiconductors for enhanced photocatalytic activity: The case of TiO_2. *Progress in Natural Science: Materials International,* 23**,** 402-407.

Yuan, L., Lu, X.-H., Xiao, X., Zhai, T., Dai, J., Zhang, F., Hu, B., Wang, X., Gong, L., Chen, J., Hu, C., Tong, Y., Zhou, J. & Wang, Z. L. 2012. Flexible Solid-State Supercapacitors Based on Carbon Nanoparticles/MnO_2 Nanorods Hybrid Structure. *ACS Nano,* 6**,** 656-661.

Zhao, B. 2016. Synthesis of Cu_3SnS_4 Nanoparticles with a Novel Structure as Low-Cost Counter Electrode in Dye-Sensitized Solar Cell. *International Journal of Electrochemical Science,* 11**,** 6514-6522.

CHAPTER SEVEN

Synthesis of reduced graphene oxide/copper tin sulphide (Cu_2SnS_3) composite for the photocatalytic degradation of tetracycline

1.0 Introduction

Advanced oxidation processes are important, efficient, environmental-friendly and promising techniques used for wastewater treatment (Kumar and Shah, 2021, Tijani *et al.*, 2014, Liu *et al.,* 2020). This technology encompasses a wide variety of processes, including sonochemical, chemical oxidation, photochemical, electrochemical, Fenton and photofenton processes (Tufail *et al.,* 2020). The process is usually driven by the *in-situ* generation of reactive radicals such as $^{\bullet}OH$, $O_2^{\bullet -}$, SO_4^{2-} (Oturan and Aaron, 2014, Deng and Zhao, 2015) that are capable of ultimately degrading pollutants to carbon dioxide and water. They are, thus, destructive methods for dealing with recalcitrant contaminants.

Among the wide range of AOPs, photon-based processes are the most widely explored because of their potential economic feasibility and versatility (Khan *et al.*, 2019). Also, they could be carried out under ambient conditions, in simple reaction systems (Li *et al.*, 2020, Xu *et al.*, 2020b). The recent development in the field of material science have spurred the development of light harvesting materials. In addition, it has shifted the focus of research in photon-based AOPs from basic research to the application of these photocatalytic materials for the degradation of contaminants of different species (Likodimos, 2020). These photocatalytic materials offer high reaction rates, low cost and strong oxidation capability compared to non-photolytic processes (Wang *et al.*, 2014, Kumar *et al.*, 2014).

A wide class of materials such as oxides, sulphides, oxyhalides, nitrides, metal organic frameworks and carbonaceous materials have all been explored for their photocatalytic properties (Khan *et al.*, 2015, Tahir *et al.*, 2020, Hao and Lang, 2019, Sharma *et al.*, 2019, Kim *et al.*, 2021, Wang *et al.*, 2014). Metal sulphides are of specific interest because of their unique optical, electronic, and structural properties, in addition to their ease of synthesis. They are one of the most explored materials (Lai *et al.*, 2012), and offer a diverse group of stoichiometries with unique properties that could be explored in photocatalysis.

Recently, ternary metal sulphides have generated high research interest due to their excellent properties. Copper tin sulphides are a class of ternary copper metal sulphides with a wide array of stoichiometric phases such as Cu_2SnS_3, Cu_3SnS_4, Cu_4SnS_4 and Cu_4SnS_7 (Robles *et al.*, 2016, Lokhande *et al.*, 2019, Nair *et al.*, 2003). Among these phases the Cu_2SnS_3 phase is the most studied. It (CTS) is one of the most promising copper tin sulphide, with phase dependent band gap energy that varies between 0.96 – 1.43 eV. It also exhibits absorption coefficient > 10^5 cm^{-1} in the visible region. Various techniques have been used to synthesize CTS such as solvothermal and wet chemical techniques (Chen and Ma, 2013, Liang *et al.*, 2013, Chang and Waclawik, 2013), spray pyrolysis, sonochemical, spin coating and electrodeposition (Park *et al.*, 2013, Wang *et al.*, 2013, Bouaziz *et al.*, 2009). Due to its facile and ease of exerting control over the properties of nanomaterials, the solvothermal method is the most explored method for CTS synthesis. Lokhande *et al.* (2017) reported the hot-injection method for the synthesis of Cu_2SnS_3 for novel antibacterial application. Also, Kamalanathan *et al.* (2018) reported the solvothermal synthesis of Cu_2SnS_3 and the influence of solvent system on the structural, photoconductive, optical and electrical properties on the synthesized nanoparticles.

The single source precursor route, which involves the incorporation of all required elements into a precursor compound, is one of the well explored solvothermal methods for the synthesis of ternary copper metal sulphides. Despite the advantages of single source precursor routes, there are only few reports on the use of single source precursors for Cu_2SnS_3 synthesis. This approach to nanoparticles synthesis offers advantages such as simplified process, access to unusual or otherwise inaccessible materials and low temperature synthesis, which produces materials with optimal particle size and surface area (Lu *et al.*, 2020).

When composited with photocatalytic nanoparticles, graphene oxide and its derivatives impact important physical and electronic properties on the resulting nanocomposites. Due to its high surface area, strength, electronic properties, GO/rGO-based composites possess enhanced stability, charger carrier characteristics and enhanced optical activity. GO/rGO composites with Cu_2SnS_3 have been explored as anode materials for lithium ion batteries (Tao *et al.*, 2016, Chen *et al.*, 2020), photocatalysis (Han *et al.*, 2018) and electrocatalytic water splitting (Xu *et al.*, 2020a). In this study, the photocatalytic activity of Cu_2SnS_3 nanoparticles synthesized through the single source precursor route and further composited with reduced graphene oxide via a facile *ex-situ* mixing process was evaluated for the degradation of tetracycline under UV light irradiation.

2.0 Materials and methods

Cu(II) sulphate ($CuSO_4$), diphenyl tin dichloride (R_2SnCl_2) carbon disulphide (CS_2), sodium ascorbic acid (ASC), triethanol amine (TEA), tert-butanol (TBA), oleylamine, methanol, toluene, N-methyl aniline, graphite, potassium permanganate, nitric acid, sulfuric acid and ammonium hydroxide solution used were all of analytical grade and used as supplied by Sigma-Aldrich.

2.1 Synthesis of ammonia salt of N-methyl-N-phenyl dithiocarbamate ligand

The dithiocarbamate ligand was prepared by following the synthetic route describe by Motaung *et al.* (2019). In a typical synthesis, N-methyl aniline and excess ammonium hydroxide were mixed together in a round bottom flask that was ice-cooled to ~4℃. The mixture was then stirred for about 10 min, followed by the introduction of an equimolar amount of CS_2 to the mixture. Some faint yellow precipitates appeared after 1 h and the mixture was stirred further for another 4 h. The precipitate obtained was filtered by suction and washed with ice-cooled ethanol. The solid obtained was then stored in an airtight container and placed in a refrigerator for further use.

2.2 Synthesis of copper(II) bis (N-methyl-N-phenyl dithiocarbamate) and diphenyl tin(II) N-methyl N-phenyl dithiocarbamate complexes

The copper dithiocarbamate ($Cu(DTC)_2$) complex was prepared by mixing aqueous solutions of $CuSO_4$ and the obtained dithiocarbamate ligand in a 1:2 stoichiometric mole ratio. The dark brown precipitate that immediately formed upon the addition of copper salt to the ligand solution, was stirred for 1 h. Afterwards, the precipitate was filtered and washed with a mixture of ethanol and water to remove unreacted metal salt and ligand. A similar procedure was employed for the synthesis of diphenyl tin(II) *N*-methyl-***N***-phenyl dithiocarbamate complex ($R_2Sn(DTC)_2$). Diphenyl tin dichloride that was used as the metal salt was dissolved in ethanol instead of water to achieve better solubility. The rest of the synthesis followed the process described for the copper complex.

2.3 Synthesis of Cu_2SnS_3 nanoparticles

Cu_2SnS_3 nanoparticles were prepared by co-thermolysis of the $Cu(DTC)_2$ and $R_2Sn(DTC)_2$ in ratio 3:1 in a heat-up process. The two compounds were mixed together in oleylamine to form a slurry in a three-necked round bottom flask connected to a condenser, N_2 gas source and a temperature probe. The slurry was then heated to 220℃ on a digitally controlled heating mantle and the system was maintained at this temperature for 1 h. Thereafter it was allowed to cool naturally to room temperature. The nanoparticles formed were precipitated by adding ethanol to the reaction mixture from which the product was recovered by centrifugation. The nanoparticles were washed three times with a mixture of toluene and ethanol and afterwards dispersed in ethanol. The ethanol dispersion was left to dry under vacuum for recovery of the Cu_2SnS_3 nanoparticles.

2.4 Synthesis of graphene oxide

Graphene oxide was synthesized by the Tour's method as described by Marcano *et al.* (2010). Graphite flakes and $KMnO_4$ in mass ratio of 1: 6 were mixed together in a 1000 mL beaker. In another 1000 mL conical flask, a mixture containing 340 mL of concentrated H_2SO_4 and 60 mL of H_3PO_4 was prepared. The concentrated acid mixture was then transferred into the graphite flakes/$KMnO_4$ mixture slowly. The mixture was stirred at 50 ℃ for 24 h, yielding a thick greenish-purple paste. After cooling to room temperature, the paste was transferred into another beaker containing 400 mL of ice (to dilute it) and then hydrogen peroxide (30%) was added until the mixture turned bright yellow completely. The mixture was centrifuged at 5000 rpm to separate the GO from the acidic mixture and the product was washed thrice with water, HCl and ethanol. Afterwards, the obtained GO was washed severally with water, until neutral pH was achieved. The GO was then dried at 50 ℃ overnight, to give a black sheet like material, which was grounded and stored for further use.

2.5 Synthesis of rGO-CTS composite

The *ex-situ* mixing of the reactants and simultaneous reduction process was employed in the compositing of GO and CTS. GO dispersion in water was formed by sonicating a weighed amount of GO in water for 1 h. Simultaneously, a weighed amount of CTS was dispersed in ethanol by sonicating the mixture for 1 h. Afterwards, the CTS dispersion was added dropwise to into the GO dispersion and the mixture further sonicated for 1 h. The mixture was then stirred vigorously for 20 h. To reduce GO, an excess amount of ascorbic acid, about 10 times greater than GO was added to the mixture and then heated at 80 ℃ for about 2 h. The obtained rGO-CTS was recovered from the solution by centrifugation and then washed severally with water and ethanol to remove unreacted ascorbic acid. To achieve different percentage ratio of rGO in the composite, the weight of GO in the dispersion was varied between 5-20% relative to the weight of CTS. The prepared composites were labelled rGO-CTS(5%), rGO-CTS(10%) and rGO-CTS(20%) for composites with 5, 10 and 20% composition of rGO respectively.

2.6 Photocatalytic studies

The photocatalytic activity of the prepared materials was evaluated for the degradation of tetracycline using a 28 W UV-LED light irradiation source. The process was carried out in 100 mL beaker placed in a photocatalytic chamber. In a typical process, 20 mg of the photocatalyst and 50 mL of the test solution containing 10 mg/L of TCE were stirred together in the dark for 30 min to achieve adsorption-desorption equilibrium. Afterwards, the light source was turned on and aliquots of the test solution were taken at intervals. The concentration of TCE in the solution was measured at wavelength of 360 nm on a ONDA spectrophotometer. The percentage removal of TCE was obtained using Eq. 4.

$$\% \, removal \ = \frac{C_o - C_f}{C_o} \times 100\%, \tag{4}$$

where C_o and C_f are the initial and final concentrations of TCE respectively. In the study of the effect of initial pH on the degradation process, the initial pH of the solution was brought to the target value by adding 0.1 M HCl or 0.1 M NaOH. The reaction rate for the degradation process was evaluated by fitting the degradation data into the pseudo first order kinetic linear plot according to Eq. 5.

$$-ln\frac{C_f}{C_o} = Kt, \tag{5}$$

Where C_f and C_o are the final and initial concentration of TCE, k is the reaction rate constant and t is the reaction time.

The mechanism of the process was studied through the radical scavenging experiments. Radical scavengers: ascorbic acid (ASC), tert-butanol (TBA) and triethanolamine (TEA) were introduced into the reaction process as super oxide $O_2^{\bullet -}$, hydroxyl radical ($^{\bullet}$OH) and hole (h^+) scavengers respectively. The significance of each radical was evaluated by their influence on the degradation efficiency.

2.7 Characterization of composites

The chemical, structural, optical, morphological properties of the nanoparticles and composites were studied using different characterization techniques. The functional groups present on the nanoparticles and composites were confirmed from the Fourier transform infrared spectroscopy (FTIR). The X-ray diffraction pattern of the samples were recorded on a d8 Advanced X-ray diffractometer with Cu Kα radiation (λ = 154.18 pm). Scanning electron microscopy (SEM) and transmission electron microscopy (TEM) images were recorded on a TECNAI G2 (ACI) equipment (Hillsboro, OR, USA) operating with accelerating voltage of 200 kV. The optical characteristics of the samples were studied through their absorption spectra, which was recorded on a PerkinElmer λ750s UV-vis spectrophotometer, and their emission spectra was recorded on a PerkinElmer LS 45 fluorimeter. For the morphological and optical studies, the samples were dissolved in toluene prior to the analysis. The Zeta potential for the nanoparticles and composites was measured using a Malvern Zetasizer Nano-series (Malvern instruments, United Kingdom).

3.0 Results and discussion

3.1 Characterization of GO, CTS and rGO-CTS composites

The functional group composition of the prepared materials was studied using FTIR spectroscopy. Fig 1 shows the FTIR spectra of graphene oxide, CTS, rGO-CTS(5%), rGO-CTS(10%) and rGO-CTS(20%). The spectrum of GO showed all the characteristic bands of GO, with the vibrational bands of O-H, C=O and C=C observed at 3248, 1726, and 1620 cm^{-1} respectively. The bands at 1220 and 1050 cm^{-1} can be assigned to the vibration of C-O bonds of C-OH and C-O-C[1] respectively. The spectrum of the CTS showed peaks that are consistent with the spectra for oleylamine. The band at 1073 cm^{-1} is due to the stretching vibration of the C-N bond of oleylamine. The broad band at ~3100 cm^{-1} could be assigned to the stretching vibration of N-H bond, while the band at the 1620 cm^{-1} could be attributed to the bending vibration of the N-H bond. This confirms the passivation of the surface of the prepared CTS by oleylamine.

The spectra of the composites showed bands that were consistent with CTS and GO. However, the O-H band of GO at 3248 cm^{-1} completely disappears, in addition to a reduction in the band due to C=O at 1720 cm^{-1}. This confirms the reduction of GO to rGO in the simultaneous compositing and reducing process employed in the synthesis of rGO-CTS. A slight shift in the position and intensity of the C-N band at 1070 cm^{-1} of the CTS was observed in the composite, which suggests that the C-N bond was the point of interaction between CTS and the functional groups on GO.

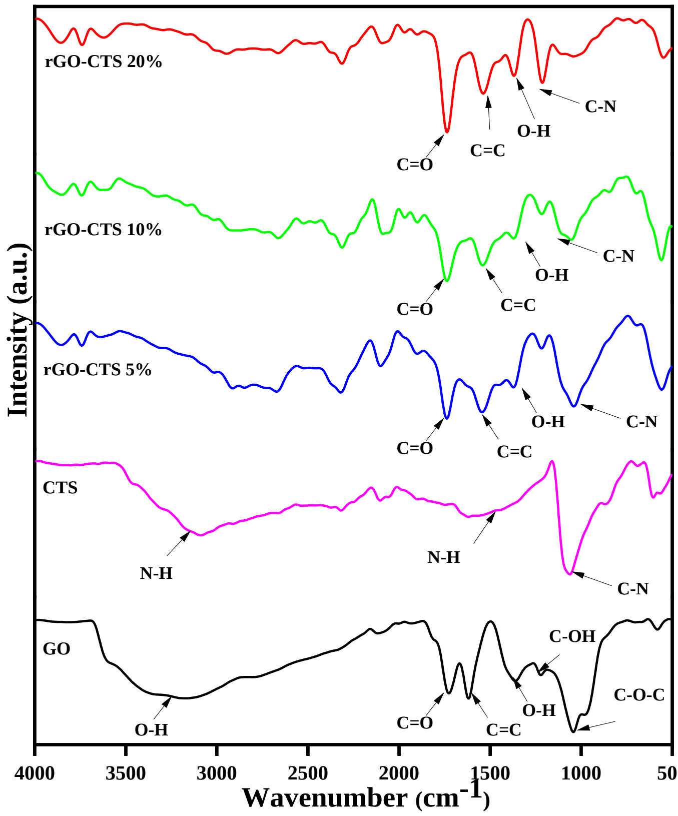

Fig 1: FTIR spectra of GO, CTS and composites rGO-CTS(5%), rGO-CTS(10%) and rGO-CTS(15%).

The XRD spectra of GO, CTS and rGO-CTS composites are shown in Fig. 2. The spectra showed the characteristic peak for GO at 2θ = 10.1, which correlates to the (002) diffraction. The CTS pattern showed peaks that could be indexed to the tetragonal phase of Cu_2SnS_3, space group 1-42 and lattice parameters a = b= 5.41 Å and c = 10.52 Å. The diffraction patterns of the composites were similar to that of the pristine Cu_2SnS_3. The absence of the peaks due to graphene oxide in the spectra of the composites might be as a result of the destruction of the layered structure of GO during the reduction to rGO (Som *et al.,* 2014). The particle size of the CTS nanoparticles was estimated using the Scherrer's equation:

$$D = \frac{K\lambda}{\beta cos\theta}, \quad (1)$$

where D is the average crystallite size, K is the shape factor, λ is the wavelength of the Cu Kα radiation (0.154 nm), β is the FWHM in radians and θ is the Bragg's angle of the peak in radians. The average crystallite size of the CTS nanoparticle was estimated to be 14.3 nm.

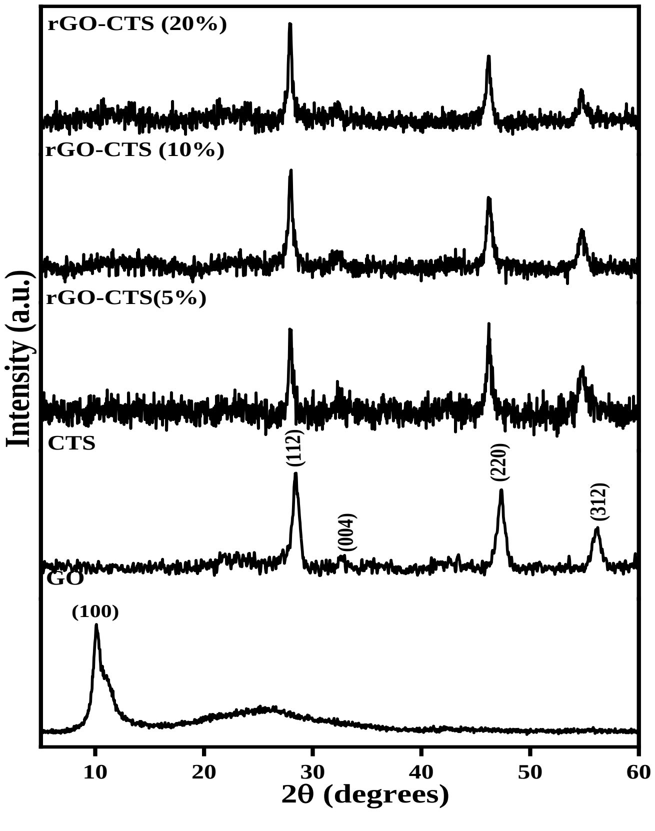

Fig 2: XRD spectra of GO, CTS, rGO-CTS(5%), rGO-CTS(10%) and rGO-CTS(20%).

The SEM and TEM images of the prepared CTS are shown in S1. The SEM images (Fig. S1(a)) of CTS indicated that the particles were aggregated and spherical in shape. The EDX spectrum (S1(b)) showed that the stoichiometric composition of Cu, Sn and S in the material was 1.9:1:3.4, which was in agreement with expected stoichiometric ratio of the compound. Analysis of the TEM images (Fig. S1(c)) showed that the particle size was 16.14 ± 3.05 nm, confirming the narrow size distribution of the nanomaterial as shown in the size distribution histogram (S1(d)).

Fig. 3 shows the SEM (a-c) and TEM (d-f) images of the GO-CTS composites. The SEM images of the composites confirmed that the layered structure of GO was destroyed during the reduction and compositing process, with only slight sheet like structure visible in the background. Also, the agglomeration of the CTS nanoparticles reduced with increase in the amount of rGO and this may be attributed to an increase in the available surface area for interaction between GO and the nanoparticles, thereby improving the surface passivation of the nanoparticles. The TEM images confirmed the attachment of the nanoparticles on the rGO surface, with the irregular spherical shape of the nanoparticles maintained. The sheet like structure of the GO became more conspicuous in the composite with highest amount of GO (rGO-CTS(20%).

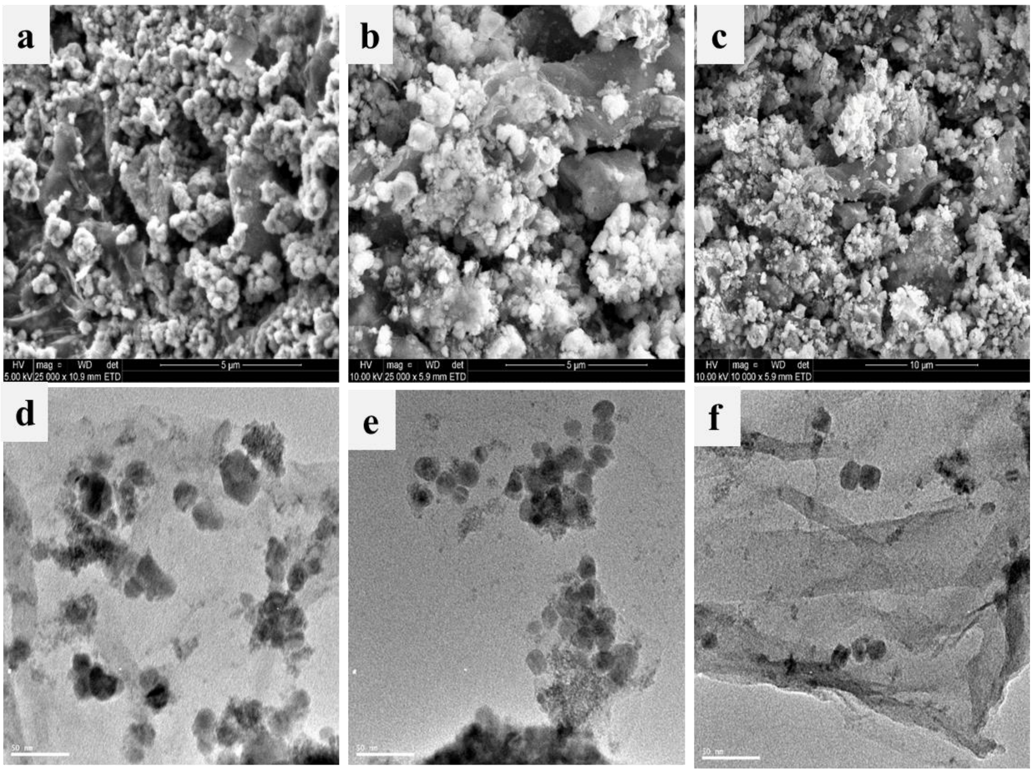

Fig 3: SEM images (a-c) and TEM images (d-f) of rGO-CTS(5%), rGO-CTS(10%) and rGO-CTS(20%).

The distribution of the nanoparticles on rGO was further studied with the aid of elemental mapping. The elemental mapping of rGO-CTS(20%), showing the distribution of carbon (C), oxygen (O), copper (Cu), tin (Sn) and sulpur (S) in the composite are shown in S2. The uniform distribution of each element in the micrographs, confirms the uniform distribution of the nanoparticles on the rGO substrate. The EDX of rGO-CTS(20%), also confirms the presence of these elements in the obtained composites.

The absorption properties of CTS and rGO-CTS composites were studied by UV-vis spectroscopy. Fig 4 shows the absorption spectra and Tauc plots of the absorption data for CTS, rGO-CTS(5%), rGO-

CTS(10%) and rGO-CTS(20%). Absorption spectra of the composites showed marked difference compared to the spectra of pristine CTS. The pristine CTS showed three absorption peaks at 293, 421 and 876 nm, with strong absorption band tailing into the visible region. The band at 876 nm could be assigned to band edge transition, while the bands at 293 and 421 nm could be due to intra-band transitions. In the composites, a red shift in the absorption band at 293 nm to 268 nm was observed in all the composites, while the band at 421 nm red shifted to 359, 384 and 350 nm in rGO-CTS(5%), rGO-CTS(10%) and rGO-CTS(20%) respectively. The intensity of absorption was higher in both the UV and visible region for rGO-CTS(10%) and rGO-CTS(20%) compared to CTS, while rGO-CTS(5%) only showed superior absorption intensity in the visible region. This marked influence of rGO on the absorption properties of CTS, showed the existence of a strong electronic interaction between both materials. The Tauc plots for the materials also showed a gradual decrease in the band gap energies of the materials with increase in the rGO content of the composites. The band gap energy for CTS, rGO-CTS(5%), rGO-CTS(10%), rGO-CTS(15%) and rGO-CTS(20%) was 1.5, 1.40, 1.36, and 1.26 eV respectively. The reduction in band gap energy may result from the formation of sub-band states between the valence band and conduction band of CTS by the incorporation of reduced graphene oxide (Bhargava and Khan, 2018).This shifting of band gap towards lower energy, is important in enhancing the photocatalytic activities of the composites, as it correlates with enhanced photon absorption (Yun *et al.*, 2017, Humayun *et al.*, 2018).

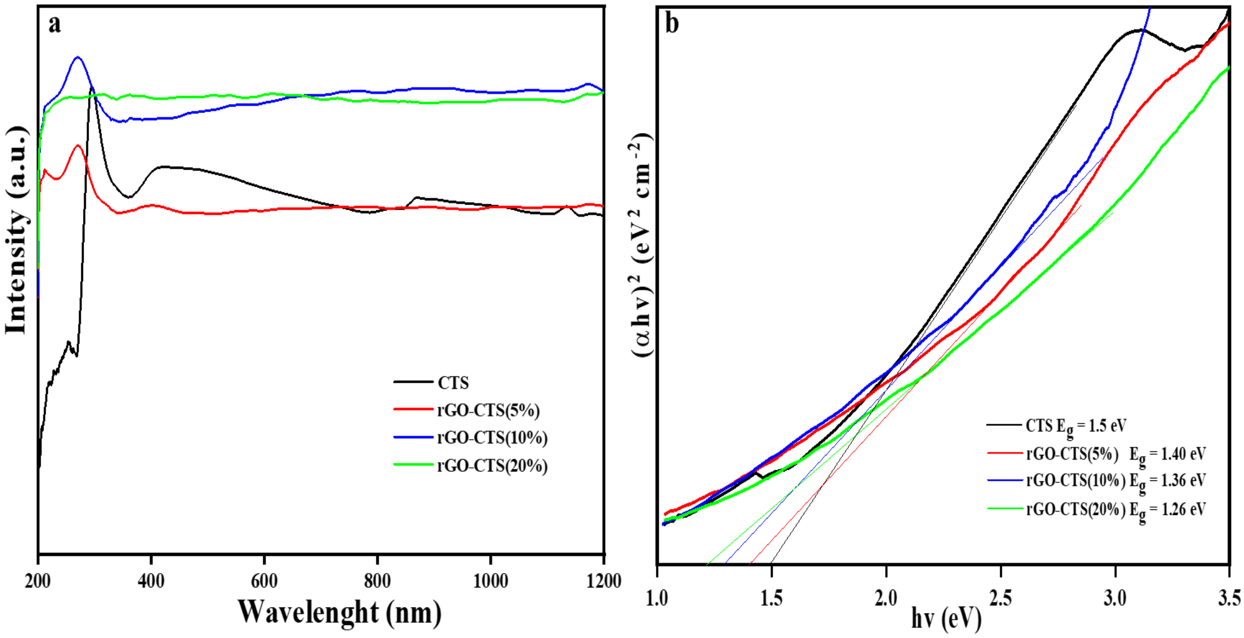

Fig 4: (a) UV-vis spectra and (b) Tauc plots of CTS, rGO-CTS(5%), rGO-CTS(10%) and rGO-CTS(20%).

The band structure is an important factor, which has a strong influence on the photocatalytic activity of a photocatalyst, because it determines the oxidation-reduction ability of the photogenerated charge carriers. The Conduction band (E_{CB}) and valence band (V_{CB}) edge potentials of a catalyst can be calculated from Eq. (2) and (3) (Wu *et al.*, 2018):

$$E_{CB} = \mathrm{X} - E_e - 0.5E_g, \tag{2}$$

$$E_{VB} = E_{CB} + E_g, \tag{3}$$

where X is the absolute electronegativity obtained from the geometric mean of the absolute electronegativity of the constituent element of the semiconductor, E_g is the band gap energy and E_e is the energy of free electrons on the hydrogen scale (4.5 eV). Table 1, shows the value of the band edge potentials for pristine CTS and rGO-CTS composites. Generally, the more negative the conduction band minimum (CBM) is, the stronger the photogenerated electron's reducing power, while the more positive the valence band minimum (VBM), the stronger the oxidizing power of photogenerated holes (Liqiang *et al.*, 2006). The compositing of CTS with rGO resulted in a reduction in the negativity of the E_{CB}, with a simultaneous reduction in the positivity of the E_{VB}.

Table 1: Electronic band structures of CTS and rGO composites

	E_{CB} (eV)	E_{VB} (eV)	Band gap
CTS	-0.03	1.47	1.50
rGO-CTS(5%)	0.02	1.42	1.40
rGO-CTS(10%)	0.04	1.40	1.36
rGO-CTS(20%)	0.09	1.35	1.26

3.2 Photocatalytic studies

The photocatalytic activity of the CTS, rGO-CTS(5%), rGO-CTS(10%) and rGO-CTS(20%) was evaluated under UV-LED irradiation for the degradation of tetracycline. Fig. 5 shows the percentage removal plot of 10 mg TCE by CTS and rGO-CTS composites. The degradation efficiency of TCE for UV, UV/CTS, UV/rGO-CTS(5%), rGO-CTS(10%) and rGO-CTS(20%) was 14.7, 64.0, 65.5, 69.8 and 93.2.0% degradation respectively after 1 h. The photocatalytic activity of the composites increased with increase in the percentage ratio of rGO in the composite. This enhanced activity could be attributed to the increase in surface area of the composite as the percentage composition of rGO in the composites increases and also an increase in the amount of charge carrier generated by light irradiation.

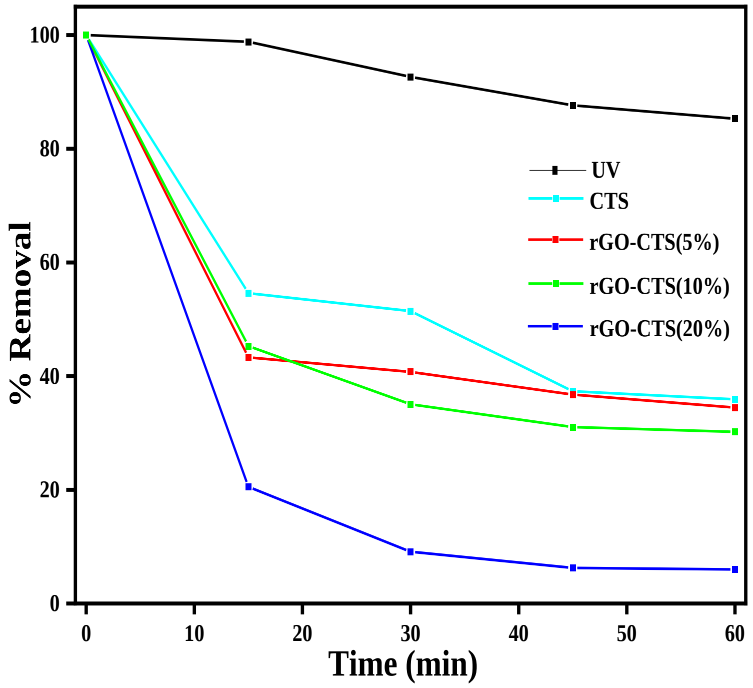

Fig 5: Photocatalytic degradation of TCE by UV, CTS, rGO-CTS(5%), rGO-CTS(10%) and rGO-CTS(20%)(UV-LED = 5W, |TCE|= 10 mg/L, catalyst dose = 20 mg).

Also, an increase in the negativity of the composite's surface was observed as the ratio of rGO increases as shown in S3. The Zeta potential of CTS, rGO-CTS(5%), rGO-CTS(10%) and rGO-CTS(20%) was 6.98, -12.6, -10.4 and -36.3 mV respectively. The increase in the negative surface charge arises from the oxygenated groups on rGO. The significant increase in the surface negative charge of rGO-CTS(20%), could also account for the increase in the adsorption of TCE on the surface of the composite.

3.3 Effect of process parameters on the kinetics of photocatalytic degradation of rGO-CTS(20%)

The effect of percentage ratio of rGO, concentration of TCE, catalyst dosage and initial pH of TCE solution on the catalytic degradation of TCE was explored. Fig. 6 shows the effect of these process parameters on the degradation kinetics of TCE by a plot of -ln(Ct/Co) against reaction time. The effect of rGO level on the kinetics of degradation is shown in Fig. 6(a). The reaction rate constant for 5, 10, 20% rGO level was 2.4×10^{-2}. 2.8×10^{-2} and 9.0×10^{-2} min^{-1} compared to 1.9×10^{-2} min^{-1} for the pristine CTS. Thus, compositing CTS with 20% rGO resulted in increased degradation by approximately 5 times compared to pristine CTS. The effect of TCE concentration on the rate of degradation is shown in Fig 6(b). At TCE concentration of 5, 10, and 20 mg/L, the reaction rate constant was 9.0×10^{-2}, 9.2×10^{-2} and 6.4×10^{-2} min^{-1} respectively. The rate of degradation of TCE using 5 mg/L solution was slightly lower, compared to the rate at 10 mg/L solution. This might be attributed to the low interaction between the composite's surface and pollutant's molecule, due to the low concentration. This interaction was more effective at a higher concentration. The reaction rate reduced from 9.2×10^{-2} min^{-1} at 10 mg/L to 6.4×10^{-2} min^{-1} at 20 mg/L. At high pollutant's concentration, a higher production of radicals is required to effect the degradation of the pollutant. Thus, keeping the catalyst dosage constant at high pollutant concentration, increases the load on the radicals generated by the catalyst, and thus a corresponding reduction in the rate of degradation. Fig 6(c) shows the effect of catalyst dosage on the reaction kinetics of the degradation process. The rate constant for the degradation process at 10, 20 and 30 mg catalyst dose was 6.8×10^{-2}, 9.0×10^{-2} and 8.9×10^{-2} min^{-1} respectively. Increasing the catalyst dosage from 10 to 20 mg, resulted in an increase in the rate constant and this could be attributed to an increase in the amount of radicals generated. It is also as a result of the increase in the adsorption of TCE on the catalyst surface due to an increase in available catalyst particles. At higher catalyst concentration, the rate of degradation reduced, which might be attributed to the increase in turbidity of the solution, leading to a reduction in the penetration of light into the system (Bodzek and Rajca, 2012). Fig. 6(d), shows the effect of pH on the rate constant of the photocatalytic process. At pH values of 4.0, 7.0 and 11, the rate constant for the degradation process was 5.7×10^{-2}, 9.0×10^{-2} and 3.2×10^{-3} min^{-1} respectively. The rate of degradation of TCE was significantly reduced at basic pH.

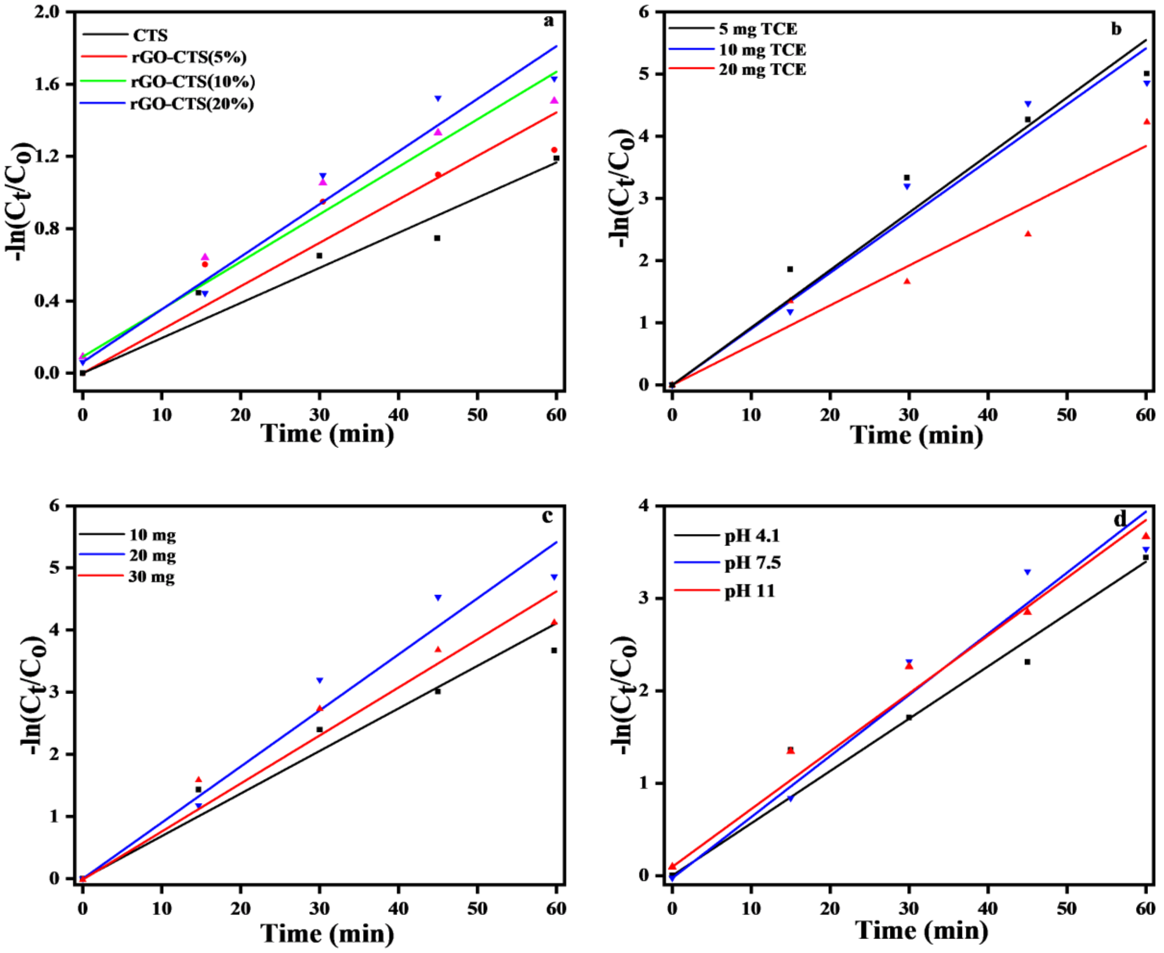

Fig 6: Effect of process parameters (a) percentage ratio of rGO (b) concentration of TCE (c) catalyst dosage and (d) pH on the photocatalytic degradation of TCE.

3.4 Radical scavenging experiments and proposed degradation mechanism

To identify the radical species responsible for the degradation activity of rGO-CTS(20%) and to propose a reaction mechanism for the degradation process, radical scavenging experiments were carried out in the presence of radical scavengers. To evaluate the importance of holes (h^+), hydroxyl radical ($^{\bullet}OH$) and superoxide ($O_2^{\bullet -}$) on the degradation of TCE, the degradation processes were carried out with the addition of 1 mM of TEA, TBA and ASC respectively. Fig. S4(a) shows the effect of each radical scavengers on the reaction rate constant of the degradation process. The rate constant for the degradation process was 7.5×10^{-2}, 5.9×10^{-2}, and 3.3×10^{-2} min^{-1} in the presence of TBA, ASC and TEA respectively compared to 9.0×10^{-2} min^{-1} for the process without scavengers. This showed that the photogenerated holes in the process played a significant role in the degradation of TCE with a 63.3% reduction in the degradation rate, compared to 16 and 34.4 % when $^{\bullet}OH$ and $O_2^{\bullet -}$ were scavenged from the system.

Although, the incorporation of rGO into CTS resulted in a less negative C_{BM}, the positive value, showed the weak reducing ability of the photogenerated electrons and this might be responsible for the low generation of $^{\bullet}OH$ radicals which was suggested by the radical scavenging experiment. However, the positive value of the V_{BM} shows they are capable of directly oxidizing the pollutant molecules.

In order to investigate the charge carrier recombination characteristic of the photocatalyst, the emission spectra of aqueous dispersions of CTS and rGO-CTS(20%) were recorded at an excitation wavelength of 450 nm. Fig. S4(b) shows that the PL spectra of the photocatalyst and the intensity of the PL band was significantly enhanced with the incorporation of rGO into the CTS. Two photophysical processes have been identified to give rise to photoluminescence: band-band PL and excitonic PL. While stronger band-band PL signal indicates higher recombination of photogenerated charge carriers, in excitonic PL spectrum, the PL signal is stronger with higher exciton occurrence (Liqiang *et al.*, 2006). Stronger excitonic PL have been correlated with higher photocatalytic degradation, in contrast to band-band PL. The probability of excitonic PL increase with high surface vacancies, small nanoparticle size and defects in semiconductor. Several studies have confirmed the formation of defects in rGO during reduction process, which may account for the excitonic PL upon the incorporation of CTS and the corresponding increase in the PL intensity. The defects in rGO could act as electron acceptor states, leading to the production of larger local charge density, which enhances charge carrier separation and production of large amount of exciton (Wang *et al.*, 2020b, Zhang and Xi, 2011, Gillespie and Martsinovich, 2019). Also, ternary copper sulphides have been reported to possess a lot of copper and sulfur vacancies; however, the influence of these on excitonic PL have yet to be confirmed. Recent reports have suggested that photocatalytic processes mediated by excitons proceed via the generation of singlet oxygen ($^1O_2$) as a major radical specie. It could therefore be suggested that the significant reduction in degradation of TCE in the presence of ASC as radial scavenger was due to its scavenging ability on $^1O_2$ rather than on $O_2^{\bullet -}$ (Fatima *et al.*, 2016)

Based on the results of the current study and other reports (Wang *et al.*, 2020a, Jaeger *et al.*, 2012), the mechanism of degradation of TCE in the photocatalytic process could be described as follows: upon irradiation of the photocatalyst by the UV lamp, excitation of electrons from the valence band to the conduction band occurred. These electrons then migrate to the surface defects on the rGO. Since these bound states are closer to the valence band of CTS, the columbic interaction between the bound electrons and the holes led to the generation of excitons. The $^1O_2$ was then produced by energy transfer from an exciton to adsorbed O_2 on the surface of the catalyst. The generated holes (h^+) directly reacted with organic pollutants because of their high oxidizing power. The high oxidability of $^1O_2$ and h^+ generated by rGO-CTS(20%) makes it a highly efficient photocatalyst for the degradation of TCE. The proposed mechanism is pictorially represented in S5.

3.5 Evaluation of catalyst's stability

The stability of rGO-CTS(20%) was evaluated by recycling the catalyst for 3 photodegradation cycles. The catalyst showed good stability over the three cycles with only 11% drop in the activity of the catalyst observed over the entire cycles as shown in S6.

4.0 Conclusion

The photocatalytic activity of rGO-CTS prepared by the facile *ex-situ* route and simultaneous reduction process was explored for the degradation of tetracycline (TCE). The activity of the photocatalysts increased under UV light irradiation with the increase in the ratio of rGO in the composite, and aligned with the reduction in the band gap energy of the composite. The enhanced activity of the composite was ascribed to the electronic interaction between rGO and CTS, which enhanced the separation of photogenerated charge carriers and also resulted in improvement in the adsorptive property of the composite. Radical scavenging experiments showed that the photogenerated holes played the most significant role in the degradation process. This study showed that rGO-CTS composites is a promising candidate for the photodegradation of emerging contaminants, especially the pharmaceuticals.

5.0 References

Bhargava, R. & Khan, S. 2018. Enhanced optical properties of Cu_2O anchored on reduced graphene oxide (rGO) sheets. *J Phys Condens Matter,* 30**,** 335703.

Bodzek, M. & Rajca, M. Photocatalysis in the treatment and disinfection of water. Part I. Theoretical backgrounds / Fotokataliza w oczyszczaniu i dezynfekcji wody cz \ i. podstawy teoretyczne. 2012.

Bouaziz, M., Amlouk, M. & Belgacem, S. 2009. Structural and optical properties of Cu_2SnS_3 sprayed thin films. *Thin Solid Films,* 517**,** 2527-2530.

Chang, J. & Waclawik, E. R. 2013. Controlled synthesis of CuInS 2, Cu 2 SnS 3 and Cu 2 ZnSnS 4 nano-structures: insight into the universal phase-selectivity mechanism. *CrystEngComm,* 15**,** 5612-5619.

Chen, Q. & Ma, D. 2013. Preparation of nanostructured Cu_2SnS_3 photocatalysts by solvothermal method. *International Journal of photoenergy,* 2013.

Chen, X., Lin, J., Chen, Y., Zhang, J., Jiang, H., Qiu, F., Chu, R. & Guo, H. 2020. Binder-free and self-supported reduced graphene oxide coated Cu_2SnS_3/Carbon nanofibers for superior lithium storage. *Journal of Alloys and Compounds,* 842**,** 155619.

Deng, Y. & Zhao, R. 2015. Advanced Oxidation Processes (AOPs) in Wastewater Treatment. *Current Pollution Reports,* 1**,** 167-176.

Fatima, K., Masood, N. & Luqman, S. 2016. Quenching of singlet oxygen by natural and synthetic antioxidants and assessment of electronic UV/Visible absorption spectra for alleviating or enhancing the efficacy of photodynamic therapy. *Biomedical Research and Therapy,* 3.

Gillespie, P. N. O. & Martsinovich, N. 2019. Origin of Charge Trapping in TiO_2/Reduced Graphene Oxide Photocatalytic Composites: Insights from Theory. *ACS Applied Materials & Interfaces,* 11**,** 31909-31922.

Han, Y., Yang, Y., Zhao, J., Yin, X. & Que, W. 2018. Facile One-Pot Synthesis of Ternary Copper-Tin-Chalcogenide Quantum Dots on Reduced Graphene Oxide for Enhanced Photocatalytic Activity. *Catalysis Letters,* 148**,** 3112-3118.

Hao, H. & Lang, X. 2019. Metal Sulfide Photocatalysis: Visible-Light-Induced Organic Transformations. *ChemCatChem,* 11**,** 1378-1393.

Humayun, M., Raziq, F., Khan, A. & Luo, W. 2018. Modification strategies of TiO_2 for potential applications in photocatalysis: a critical review. *Green Chemistry Letters and Reviews,* 11**,** 86-102.

Jaeger, H. M., Fischer, S. & Prezhdo, O. V. 2012. The role of surface defects in multi-exciton generation of lead selenide and silicon semiconductor quantum dots. *The Journal of Chemical Physics,* 136**,** 064701.

Kamalanathan, M., Hussain, S., Gopalakrishnan, R. & K, V. 2018. Influence of solvents on solvothermal synthesis of Cu_2SnS_3 nanoparticles with enhanced optical, photoconductive and electrical properties. *Materials Technology,* 33**,** 72-78.

Khan, M. M., Adil, S. F. & Al-Mayouf, A. 2015. Metal oxides as photocatalysts. *Journal of Saudi Chemical Society,* 19**,** 462-464.

Khan, S., Sayed, M., Sohail, M., Shah, L. A. & Raja, M. A. 2019. Chapter 6 - Advanced Oxidation and Reduction Processes. *In:* AHUJA, S. (ed.) *Advances in Water Purification Techniques.* Elsevier.

Kim, H., Jang, D., Choi, S., Kim, J. & Park, S. 2021. Acid-activated carbon nitrides as photocatalysts for degrading organic pollutants under visible light. *Chemosphere,* 273**,** 129731.

Kumar, S., Ahlawat, W., Bhanjana, G., Heydarifard, S., Nazhad, M. & Dilbaghi, N. 2014. Nanotechnology-Based Water Treatment Strategies. *Journal of nanoscience and nanotechnology,* 14**,** 1838-58.

Kumar, V. & Shah, M. 2021. Advanced oxidation processes for complex wastewater treatment. *In:* SHAH, M. P. (ed.) *Advanced oxidation processes for effluent treatment plants.* Elsevier.

Lai, C.-H., Lu, M.-Y. & Chen, L.-J. 2012. Metal sulfide nanostructures: synthesis, properties and applications in energy conversion and storage. *Journal of Materials Chemistry,* 22**,** 19-30.

Li, T., Wang, C., Wang, T. & Zhu, L. 2020. Highly efficient photocatalytic degradation toward perfluorooctanoic acid by bromine doped BiOI with high exposure of (001) facet. *Applied Catalysis B: Environmental,* 268**,** 118442.

Liang, X., Cai, Q., Xiang, W., Chen, Z., Zhong, J., Wang, Y., Shao, M. & Li, Z. 2013. Preparation and characterization of flower-like Cu_2SnS_3 nanostructures by solvothermal route. *Journal of Materials Science & Technology,* 29**,** 231-236.

Likodimos, V. 2020. Advanced Photocatalytic Materials. *Materials (Basel, Switzerland),* 13**,** 821.

Liqiang, J., Yichun, Q., Baiqi, W., Shudan, L., Baojiang, J., Libin, Y., Wei, F., Honggang, F. & Jiazhong, S. 2006. Review of photoluminescence performance of nano-sized semiconductor materials and its relationships with photocatalytic activity. *Solar Energy Materials and Solar Cells,* 90**,** 1773-1787.

Liu, H., Wang, C. & Wang, G. 2020. Photocatalytic Advanced Oxidation Processes for Water Treatment: Recent Advances and Perspective. *Chemistry – An Asian Journal,* 15**,** 3239-3253.

Lokhande, A. C., Babar, P. T., Karade, V. C., Gang, M. G., Lokhande, V. C., Lokhande, C. D. & Kim, J. H. 2019. The versatility of copper tin sulfide. *Journal of Materials Chemistry A,* 7**,** 17118-17182.

Lokhande, A. C., Shelke, A., Babar, P. T., Kim, J., Lee, D. J., Kim, I.-C., Lokhande, C. D. & Kim, J. H. 2017. Novel antibacterial application of photovoltaic Cu_2SnS_3 (CTS) nanoparticles. *RSC Advances,* 7**,** 33737-33744.

Lu, H., Wright, D. S. & Pike, S. D. 2020. The use of mixed-metal single source precursors for the synthesis of complex metal oxides. *Chem Commun (Camb),* 56**,** 854-871.

Marcano, D. C., Kosynkin, D. V., Berlin, J. M., Sinitskii, A., Sun, Z., Slesarev, A., Alemany, L. B., Lu, W. & Tour, J. M. 2010. Improved Synthesis of Graphene Oxide. *ACS Nano,* 4**,** 4806-4814.

Motaung, M. P., Osuntokun, J. & Onwudiwe, D. C. 2019. The heat-up synthesis of monodispersed Bi_2S_3 and Cu_7S_4 nanoparticles from novel precursor complexes and their characterizations. *Materials Science in Semiconductor Processing,* 99**,** 92-98.

Nair, M. T. S., Lop z-Mata, C., GomezDaza, O. & Nair, P. K. 2003. Copper tin sulfide semiconductor thin films produced by heating SnS–CuS layers deposited from chemical bath. *Semiconductor Science and Technology,* 18**,** 755-759.

Oturan, M. A. & Aaron, J.-J. 2014. Advanced Oxidation Processes in Water/Wastewater Treatment: Principles and Applications. A Review. *Critical Reviews in Environmental Science and Technology,* 44**,** 2577-2641.

Park, J., Song, M., Jung, W. M., Lee, W. Y., Kim, H., Kim, Y., Hwang, C. & Shim, I.-W. 2013. Syntheses of Cu_2SnS_3 and Cu_2ZnSnS_4 nanoparticles with tunable Zn/Sn ratios under multibubble sonoluminescence conditions. *Dalton Transactions,* 42**,** 10545-10550.

Robles, V., Trigo, J. F., Guillén, C. & Herrero, J. 2016. Copper tin sulfide (CuxSnSy) thin films evaporated with x=3,4 atomic ratios: Influence of the substrate temperature and the subsequent annealing in sulfur. *Materials Research Bulletin,* 83**,** 116-121.

Sharma, K., Dutta, V., Sharma, S., Raizada, P., Hosseini-Bandegharaei, A., Thakur, P. & Singh, P. 2019. Recent advances in enhanced photocatalytic activity of bismuth oxyhalides for efficient photocatalysis of organic pollutants in water: A review. *Journal of Industrial and Engineering Chemistry,* 78.

Som, T., Troppenz, G. V., Wendt, R. R., Wollgarten, M., Rappich, J., Emmerling, F. & Rademann, K. 2014. Graphene oxide/α-Bi_2O_3 composites for visible-light photocatalysis, chemical catalysis, and solar energy conversion. *ChemSusChem,* 7**,** 854-65.

Tahir, M. B., Rafique, M., Rafique, M. S., Fatima, N. & Israr, Z. 2020. Chapter 6 - Metal oxide- and metal sulfide-based nanomaterials as photocatalysts. *In:* TAHIR, M. B., RAFIQUE, M. & RAFIQUE, M. S. (eds.) *Nanotechnology and Photocatalysis for Environmental Applications.* Elsevier.

Tao, H.-C., Zhu, S.-C., Yang, X.-L., Zhang, L.-L. & Ni, S.-B. 2016. Reduced graphene oxide decorated ternary Cu_2SnS_3 as anode materials for lithium ion batteries. *Journal of Electroanalytical Chemistry,* 760**,** 127-134.

Tijani, J. O., Fatoba, O. O., Madzivire, G. & Petrik, L. F. 2014. A Review of Combined Advanced Oxidation Technologies for the Removal of Organic Pollutants from Water. *Water, Air, & Soil Pollution,* 225**,** 2102.

Tufail, A., Price, W. E. & Hai, F. I. 2020. A critical review on advanced oxidation processes for the removal of trace organic contaminants: A voyage from individual to integrated processes. *Chemosphere,* 260**,** 127460.

Wang, C.-C., Li, J.-R., Lv, X.-L., Zhang, Y.-Q. & Guo, G. 2014. Photocatalytic organic pollutants degradation in metal–organic frameworks. *Energy & Environmental Science,* 7**,** 2831-2867.

Wang, H., Liu, W., He, X., Zhang, P., Zhang, X. & Xie, Y. 2020a. An Excitonic Perspective on Low-Dimensional Semiconductors for Photocatalysis. *J Am Chem Soc,* 142**,** 14007-14022.

Wang, W., Shen, H. & Li, J. 2013. Rapid synthesis of hollow CTS nanoparticles using microwave irradiation. *Materials Letters,* 111**,** 5-8.

Wang, X., Li, K., He, J., Yang, J., Dong, F., Mai, W. & Zhu, M. 2020b. Defect in reduced graphene oxide tailored selectivity of photocatalytic CO_2 reduction on Cs_4PbBr_6 pervoskite hole-in-microdisk structure. *Nano Energy,* 78**,** 105388.

Wu, Q., Zhou, M., Gong, Y., Li, Q., Yang, M., Yang, Q. & Zhang, Z. 2018. Three-dimensional bandgap-tuned Ag_2S quantum dots/reduced graphene oxide composites with enhanced adsorption and photocatalysis under visible light. *Catalysis Science & Technology,* 8**,** 5225-5235.

Xu, J., Wang, R., Chen, X., Zhou, R. & Zhang, J. 2020a. Cu_2SnS_3 nanocrystals decorated rGO nanosheets towards efficient and stable hydrogen evolution reaction in both acid and alkaline solutions. *Materials Today Energy,* 17.

Xu, T., Zhu, Y., Duan, J., Xia, Y., Tong, T., Zhang, L. & Zhao, D. 2020b. Enhanced photocatalytic degradation of perfluorooctanoic acid using carbon-modified bismuth phosphate composite: Effectiveness, material synergy and roles of carbon. *Chemical Engineering Journal,* 395**,** 124991.

Yun, J.-W., Ryu, K. Y., Nguyen, T. K., Ullah, F., Chang Park, Y. & Kim, Y. S. 2017. Tuning optical band gap by electrochemical reduction in TiO_2 nanorods for improving photocatalytic activities. *RSC Advances,* 7**,** 6202-6208.

Zhang, X.-F. & Xi, Q. 2011. A graphene sheet as an efficient electron acceptor and conductor for photoinduced charge separation. *Carbon,* 49**,** 3842-3850.

SUPPLEMENTARY DATA

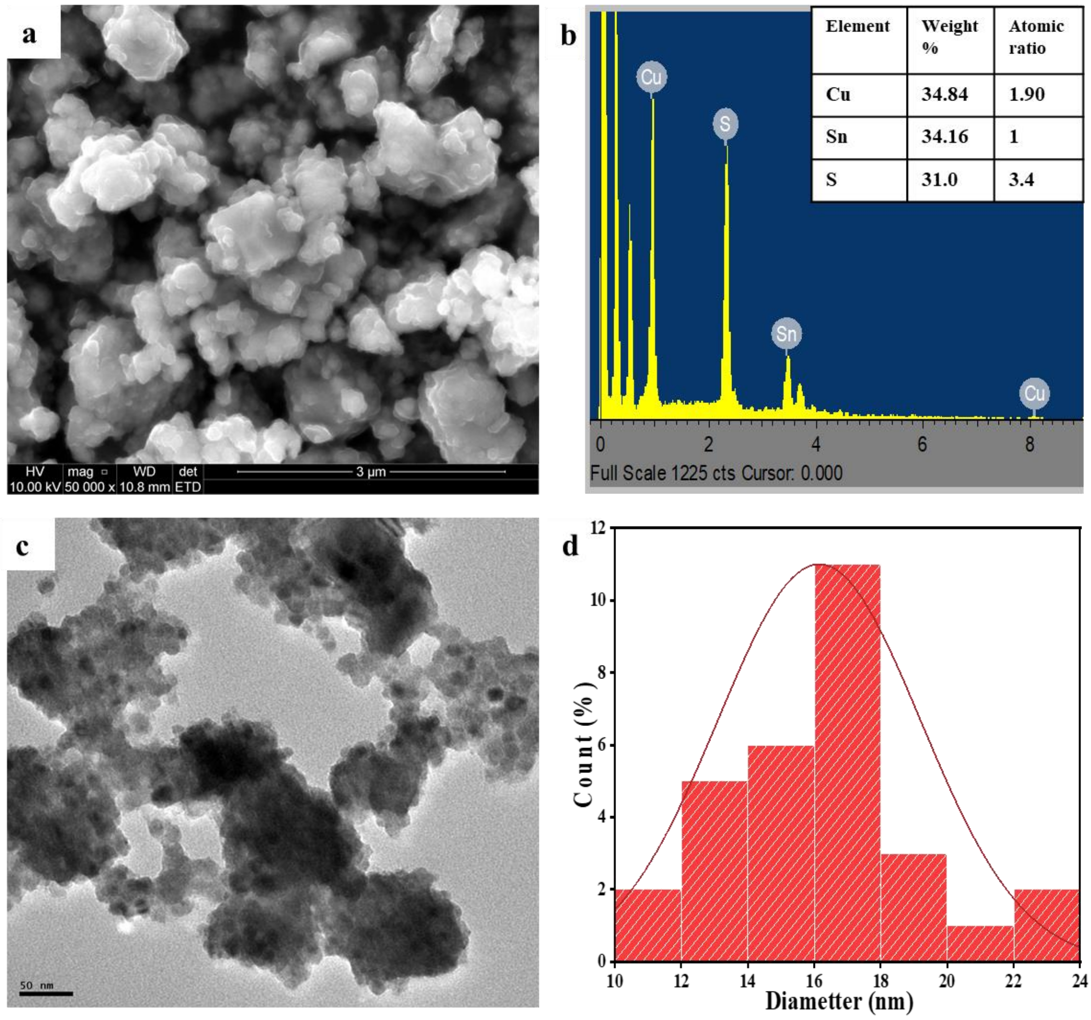

Element	Weight %	Atomic ratio
Cu	34.84	1.90
Sn	34.16	1
S	31.0	3.4

S1: Morphological properties of CTS (a) SEM image (b) EDS spectra (c) TEM image and (d) particle size distribution histogram

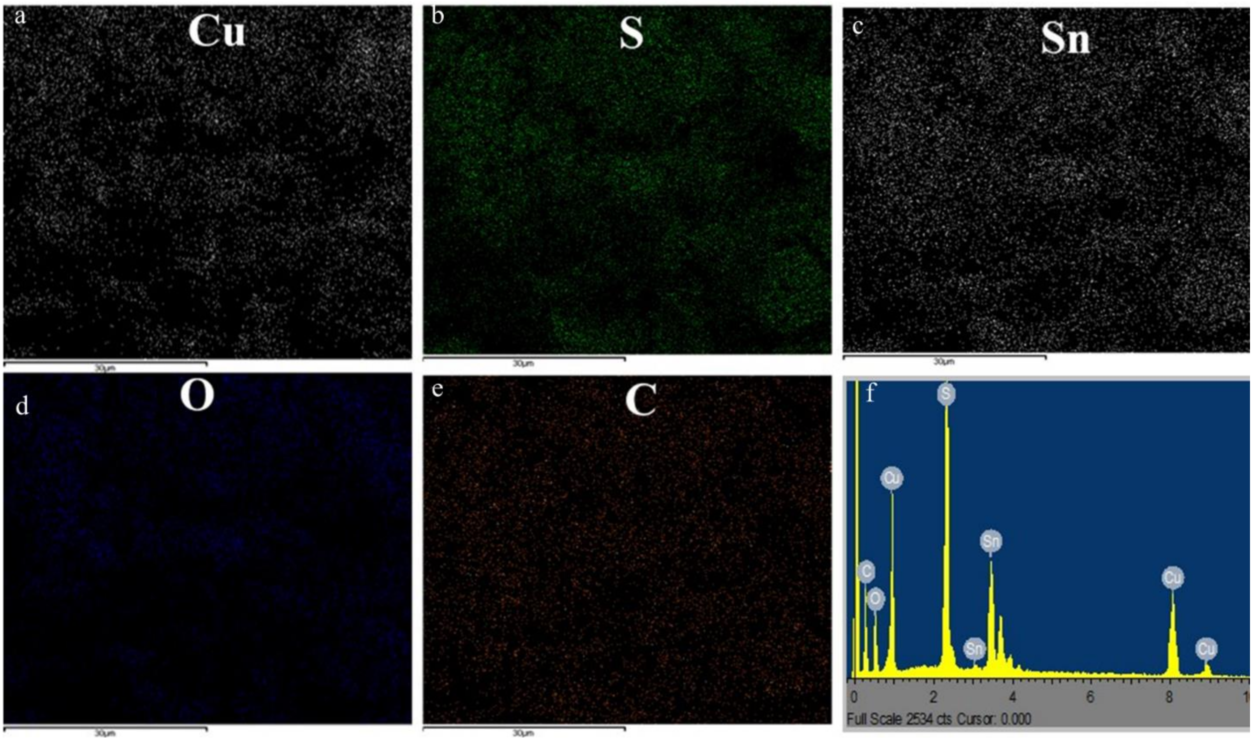

S2: Elemental mapping images of (a) Cu, (b) S, (c) Sn, (d) O, (e) C elements and (f) EDX spectra of rGO-CTS(20%).

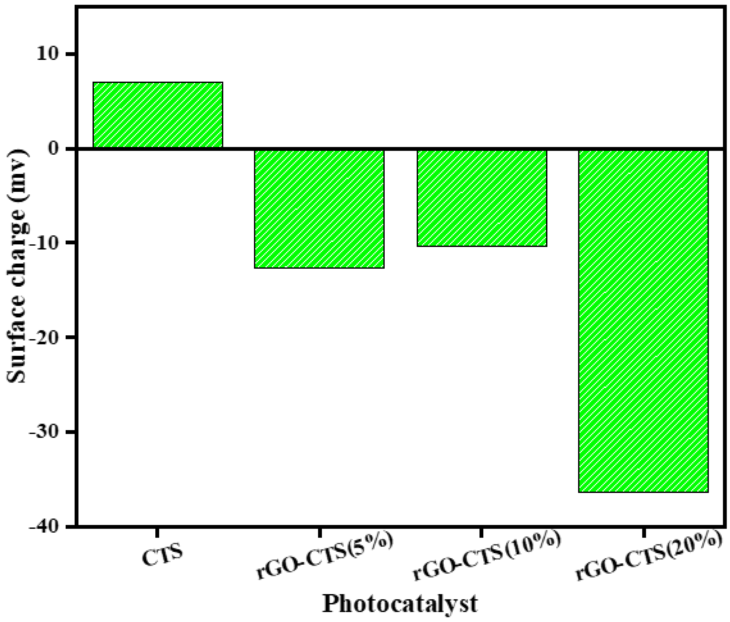

S3: Surface charge of photocatalytic materials

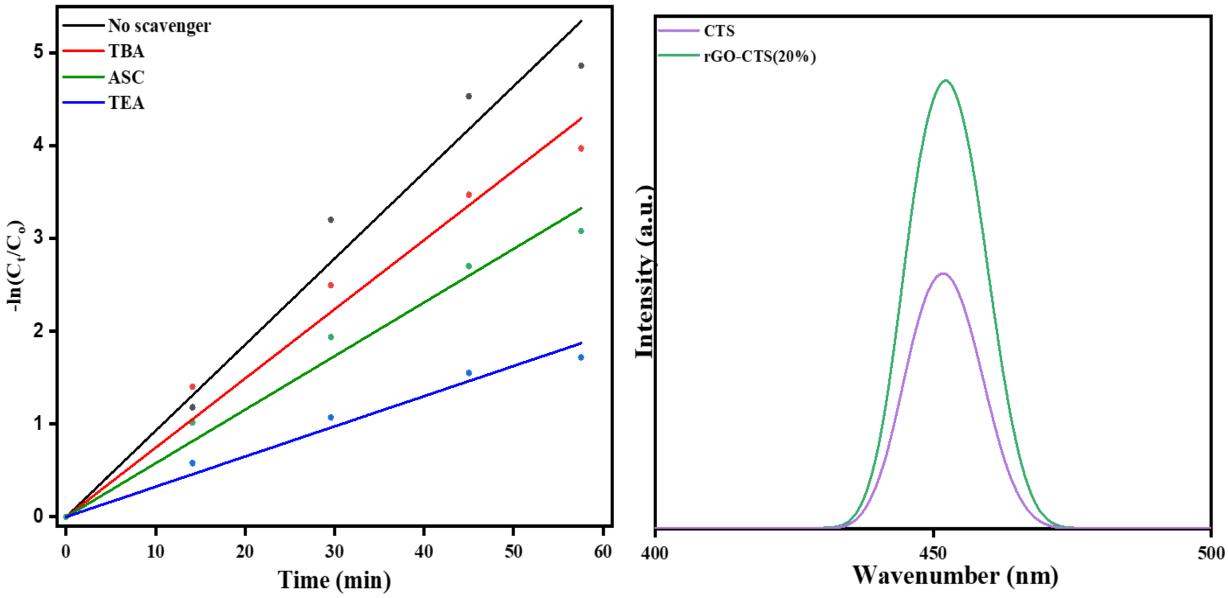

S4: (a) Radical scavenging experiment and (b) Emission spectra of CTS and rGO-CTS(20%)

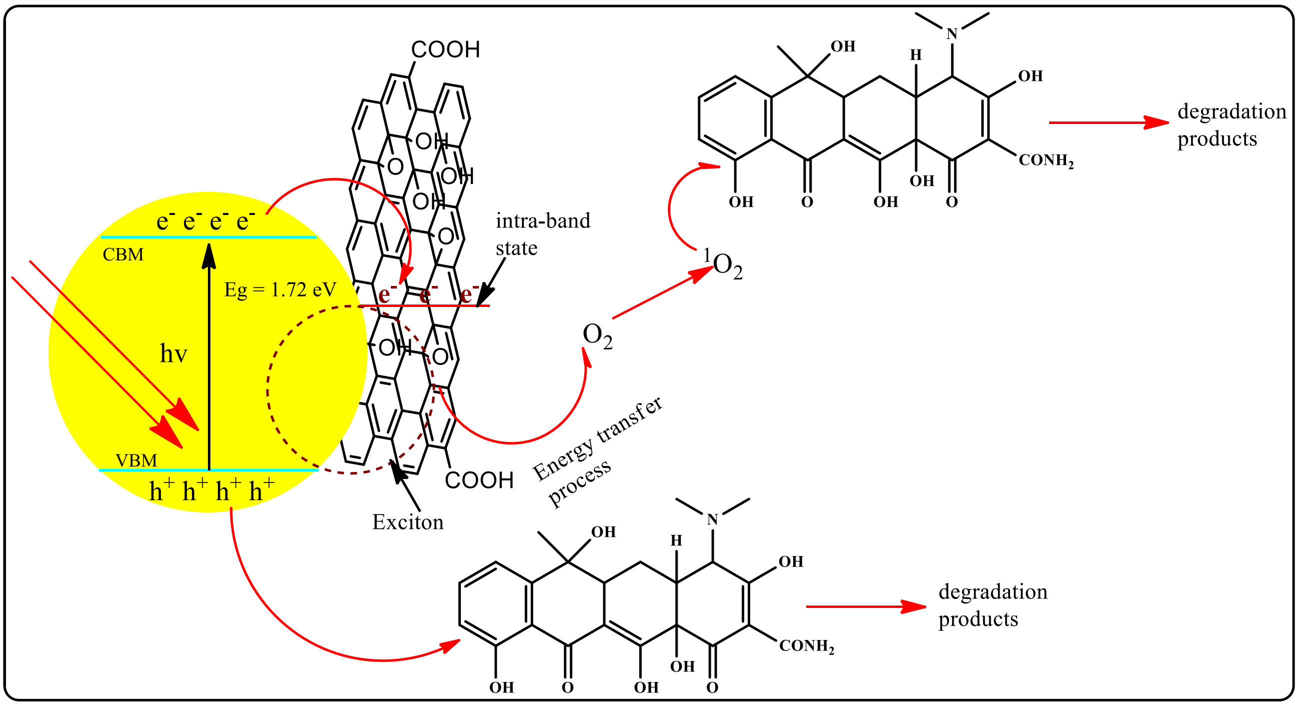

S5: Proposed mechanism for the degradation of tetracycline by rGO-CTS(20%) under UV light irradiation.

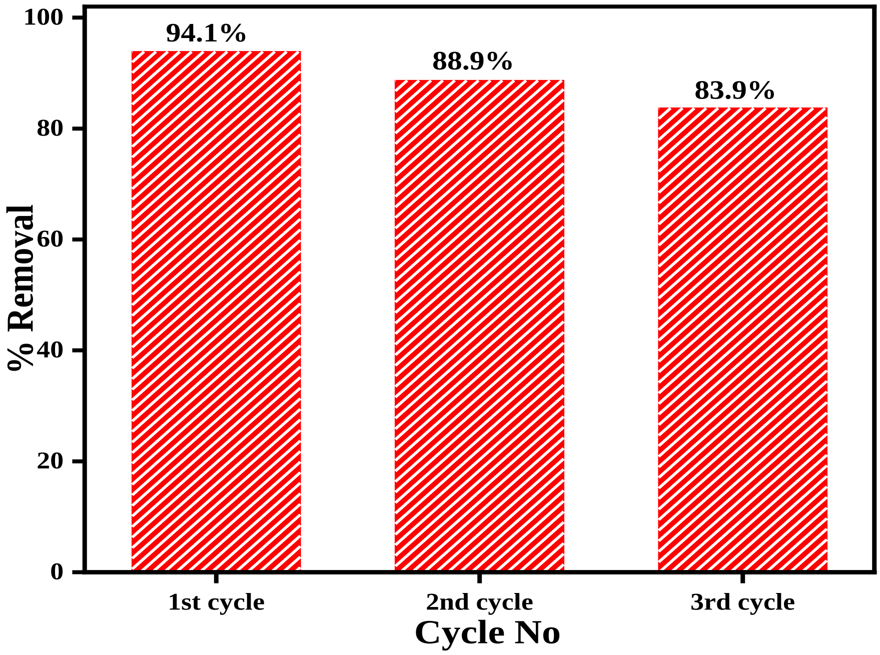

S6: rGO-CTS(20%) stability test after 3 process cycles.

CHAPTER EIGHT

A comparative study of the effect of graphene oxide, graphitic carbon nitride, and their composite on the photocatalytic activity of Cu_3SnS_4

1.0 Introduction

Supporting a catalyst on a suitable material is an important route to the improvement of properties such as adsorption capacity, stability, dispensability, quantum efficiency, electronic band structure and overall reaction kinetics (Olatunde and Onwudiwe, 2021). Several classes of materials such as ceramics, polymers, metals and carbon-based materials have been explored as support materials for the encapsulation of nanoparticles used as catalysts. The incorporation of catalytic materials on carbon-based materials such as graphene and graphitic carbon nitride offer advantages such as improved charge carrier mobility and conductivity, stability and high surface area (Su *et al.*, 2010). Also, carbon-based support materials could establish some interactions between the active phase and support, which significantly influences catalytic activity (Julkapli and Bagheri, 2015). The presence of heteroatoms such as oxygen, nitrogen and sulfur on the surface of the carbon material may confer acid-base and hydrophilic properties on the supported catalysts, which are important in the surface chemical properties of the catalyst.

Graphene is a two-dimensional material, with single-layer network of sp^2 hybridized carbon atoms, arranged in a densely packed honeycomb shape (Cheng *et al.*, 2015). It possesses unique characteristics such as high adsorption capacity, high mechanical strength, ease of functionalization, large surface area and excellent electrical and thermal conductivity, which makes it an ideal support material for catalysts (Radsar *et al.*, 2021, Papageorgiou *et al.*, 2017, Soldano *et al.*, 2010). Graphene supported catalysts have versatile range of applications in technologies such as drug delivery (Fan *et al.*, 2013, Pramanik *et al.*, 2019), fuel cells (Vinothkannan *et al.*, 2018, Xia *et al.*, 2015), biosensors (Dey, 2015, Zhang *et al.*, 2018), lithium ion batteries (Lu *et al.*, 2020, Cong *et al.*, 2021) and water treatment (Tabish *et al.*, 2018, Gandhi *et al.*, 2016). Despite the many advantages of graphene-based catalyst, the chemical inertness of pristine graphene is a major challenge in activating graphene (Sachdeva, 2020). This graphene activation has been achieved by introducing defects or by the introduction of functional groups into graphene (Kong *et al.*, 2014). The most explored functionalization route is the oxidation of graphene to form graphene oxide, which comprises of randomly distributed sp^2 and sp^3 carbon atoms carrying carboxyl, carbonyl, hydroxyl and epoxy functional groups (Georgakilas *et al.*, 2012). This oxygen moieties confer improved hydrophilic property and chemical reactivity on GO and also providing anchor sites for immobilization of different catalytic active species (Zhang, 2020).

Graphitic carbon nitride (g-C_3N_4) is similar to graphene in its layered structure, composed of only C, N, and some H impurity. However, in contrast to graphene, it is a medium band gap semiconductor, with high thermal and chemical stability (Wang *et al.*, 2012). It's layered structure also implies that different inorganic and organic compounds could bind to its matrix, with corresponding improvement in photocatalytic performance (Idris and Devaraj, 2019, Suter *et al.*, 2018). g-C_3N_4 could therefore successfully act as catalyst alone due to the presence of high amount of nitrogen atoms, incompletely condensed amino groups, tertiary and aromatic amines in its matrix which confers Lewis basicity on it and acting as active sites for metal-free catalysis (Shcherban *et al.*, 2018, Sreekanth *et al.*, 2018). Furthermore, the large nitrogen atoms, serve as anchor sites for catalytic nanoparticles, when g-C_3N_4 is explored as catalyst support (Jin *et al.*, 2009).

Although, graphene and g-C_3N_4 share similar microstructural properties, they differ greatly in their physicochemical properties. Also, the two compounds differ significantly in terms of electronic properties. While g-C_3N_4 is a wide-band gap semiconductor, graphite exhibits excellent conductivity. So, these compounds when incorporated with catalytic materials are expected to induce divergent influences on catalytic properties. Therefore, in this study, we have explored graphene oxide, protonated g-C_3N_4 and a composite of both materials as support materials for a ternary copper metal sulphide (Cu_3SnS_4) and their influence on the catalytic activity has been explored in the degradation of tetracycline as a model pollutant of emerging concern.

2.0 Materials and methods

2.1 Materials

Cu(II) sulphate ($CuSO_4$), diphenyl tin dichloride (R_2SnCl_2) carbon disulphide (CS_2), 1-dodecanethiol (DDT), oleylamine, urea, methanol, toluene, N-methyl aniline, graphite, potassium permanganate, nitric acid, sulfuric acid, ammonium hydroxide solution, and hydrochloric acid (HCl), used were all of analytical grade and used as supplied by Sigma-Aldrich.

2.2 Synthesis of protonated-graphitic carbon nitride

The method described by Wee-Jun Onga *et al.* (2015) was employed for the synthesis of protonated-g-C_3N_4,. Firstly, 10 g of urea was weighed into a closed ceramic crucible with lid in order to decrease the sublimation of urea. The urea was then calcined at 550℃ in a furnace for 4 h. The crucible was allowed to cool to room temperature and the obtained yellow product was grounded into powder. The obtained bulk g-C_3N_4 was then exfoliated by treating it (1 g) with 40 mL of 32% HCl and ultrasound for 1 h. The obtained exfoliated g-C_3N_4 was then protonated by further stirring the g-C_3N_4-acid suspension vigorously for 4 h at room temperature. The mixture was filtered and washed repeatedly with deionized water to neutral pH. The obtained PCN was then dried at 50℃ for 24 h.

2.3 Synthesis of graphene oxide (GO)

The Tours method described by Marcano *et al.* (2010) was employed in the synthesis of graphene oxide. In a typical synthesis, concentrated H_2SO_4 and H_3PO_4 were mixed in the ratio 9:1 and the solution was added to a mixture of graphite flakes and $KMnO_4$ (graphite flakes/$KMnO_4$ = 1/6). The mixture was then heated to 50 ºC for 12 h with stirring. The thick greenish-purple paste obtained was allowed to cool to room temperature and then poured into 400 mL of ice. Hydrogen peroxide (30%) was added until the solution completely turns bright yellow. The obtained graphene oxide was then centrifuged and the residue obtained was washed three times with water, HCl and ethanol. The obtained solid material was dried in an oven at 50 ºC for 24 h and the sheet-like black GO obtained was grounded into powder and stored for further use.

2.4 Synthesis of graphene oxide/PCN composites

GO/PCN composite was prepared through the method reported by Hu *et al.* (2016). GO dispersion (0.4 mg/L) was prepared by sonicating 20 mg of GO in water for 1 h. Afterwards an equal amount of PCN was added into the GO dispersion. The mixture was further sonicated for another 1 h, then left to stir for 24 h and the solvent was allowed to evaporate by heating slowly at 70 ℃. The obtained powder was washed thrice with ethanol and water and the GO/PCN powder was recovered after dispersing in ethanol and allowing to dry under vacuum overnight.

2.5 Synthesis of Cu_3SnS_4

Co-thermolysis of single source precursors was used for the synthesis of Cu_3SnS_4. The precursors were initially prepared separately by reacting metal salts of copper ($CuSO_4$) and tin (R_2SnCl_2), with dithiocarbamate ligands, prepared via an earlier reported method (Onwudiwe *et al.*, 2021). Afterwards, the Cu_3SnS_4(CTS) nanoparticles were prepared by mixing stoichiometric amount of $[Cu(DTC)_2]$ and $[Sn(DTC)_2]$ in oleylamine/DDT mixture with volume ratio of 5:1 in a three-necked round bottom flask attached to a condenser and N_2 gas source. The slurry obtained was then heated to 180 ºC and maintained at this temperature for 1 h. Thereafter, the reaction system was allowed to cool down to 65 ºC and the nanoparticles were precipitated with ethanol. The precipitated nanoparticles were washed with a mixture of ethanol and toluene (3:1) three times, after which they were air dried.

2.6 Characterization of prepared nanoparticles

The CTS nanoparticles and the nanocomposites were characterized for their structural, morphological and optical properties. XRD patterns were recorded on a d8 Advanced XR diffractometer with Cu Kα radiation (λ = 154.18 pm) and operating in Bragg-Brentano mode. Morphological studies were carried out with scanning electron microscopy (SEM) and transmission electron microscopy (TEM) recorded on a TECNAI G2 (ACI) equipment (Hillsboro, OR, USA) operating with accelerating voltage of 200 kV. PerkinElmer λ750s UV-vis spectrophotometer and PerkinElmer LS 45 fluorimeter were used to record the absorption and emission spectra of the samples respectively.

2.7 Preparation of GO-CTS, PCN-CTS and GO/PCN-CTS composites

The facile *ex-situ* mixing method was employed in the synthesis of the composites. In a typical synthesis of GO-CTS, CTS was dispersed in ethanol with sonication, while weighted amount of GO (20% w/w) was simultaneously dispersed in water with sonication. After 1 h, the CTS mixture was transferred drop-wisely into the GO solution and the mixture was further sonicated for 1 h. The mixture was allowed to stir overnight and the solvent was slowly evaporated. Afterwards, the obtained powder was washed thrice with ethanol and water and then dried under vacuum. Similar process was followed in the synthesis of PCN-CTS and PCN/GO-CTS.

2.8 Evaluation of photocatalytic activity

The photocatalytic activity of CTS nanoparticles and composites were evaluated for the photocatalytic degradation of tetracycline (TCE) under UV-light irradiation. The process was carried out in a 100 mL glass beaker without controlling the pH of the system. For a typical process, 50 mL of 5 mg/L of TCE solution was stirred with 10 mg of the catalyst in the dark for 30 min in order to establish adsorption-desorption equilibrium. Afterwards the 28 watts UV-LED light was turned on and aliquots were taken at intervals. The concentration of TCE in the system was measured using a ONDA UV spectrometer at λ_{max} of 360 nm. The percentage removal of TCE was evaluated using Eq. 1:

$$\% removal = \frac{C_o - C_f}{C_o} \times 100\%, \tag{1}$$

where C_o and C_f are the initial and final concentrations of TCE respectively. The reaction rate for the degradation process was evaluated by fitting the degradation data into the linear form of the pseudo first order kinetic (Eq. 2)

$$-ln\frac{C_f}{C_o} = Kt, \tag{2}$$

where C_f and C_o are the final and initial concentration of TCE, k is the reaction rate constant and t is the reaction time.

3.0 Results and discussion

3.1 Characterization of GO, PCN, GO-CTS, PCN-CTS and GO/PCN-CTS

The FTIR spectra of GO, PCN, GO-CTS, PCN-CTS and GO/PCN-CTS are shown in Fig 1. The spectra of GO showed characteristic bands due to the vibrational frequencies of O-H, C-O, C=C and C=O at 3248, 1220, 1720, 1620 and 1726 cm^{-1} respectively (Khalili, 2016, Ahmad *et al.*, 2021). The characteristic bands due to N-H, C=N, C-N and heterocyclic CN in PCN were observed at 3190, 1571, 1523 and 809 cm^{-1} respectively (Ben-Refael *et al.*, 2020, Zhu *et al.*, 2020). For the CTS, nanoparticles peaks from functional groups from DDT and OLA were observed in the spectra, thus confirming the presence of both ligands as capping agents for the nanoparticles. The stretching and bending vibrations of N-H in oleylamine were observed at ~3100 and 1620 cm^{-1} respectively, while its C-N stretching vibration was observed at ~1073 cm^{-1}. The vibrational frequency band due to asymmetric and symmetric stretching of methylene group of DDT overlapped with the N-H stretching band of oleylamine, the twisting, rocking and wagging vibrational frequency of the CH_3 group could be seen at around 1600-1200 cm^{-1} (Jayabharathi *et al.*, 2017). Interestingly, the FTIR spectra of the composites revealed the possibility of a difference in the mode of interaction between CTS and the solid supports. The FTIR spectra of GO-CTS, showed peaks that were characteristic of both CTS and GO. However, the asymmetric and symmetric stretching vibrations of DDT, that were masked by the N-H peak of OLA became evident and the N-H peak shifted from around 3100 to 3000 cm^{-1}. This suggests a significant interaction between the N-H group of OLA on the surface CTS and the O-H group on GO. The FTIR spectrum of PCN-CTS composite showed only bands due to PCN. This observation has been reported by other studies on GCN-based composite (Zhu *et al.*, 2017, Zhang *et al.*, 2016) and was attributed to the structure of GCN not being altered by compositing with semiconductor materials (Wang *et al.*, 2020). The suppression of the bands in pristine CTS may also suggest a strong interaction between the main functional groups on it and the PCN. In the spectrum of GO/PCN-CTS, the peaks due to both GO and PCN could be observed, with suppression of peaks due to DDT and OLA. The O-H stretching vibration and the C-O stretching vibrations of GO at 3200 and 1720 cm^{-1} respectively could still be observed, while the C=N stretching frequency of PCN was still evident. Thus, confirming the incorporation of CTS unto the surface of both GO and PCN.

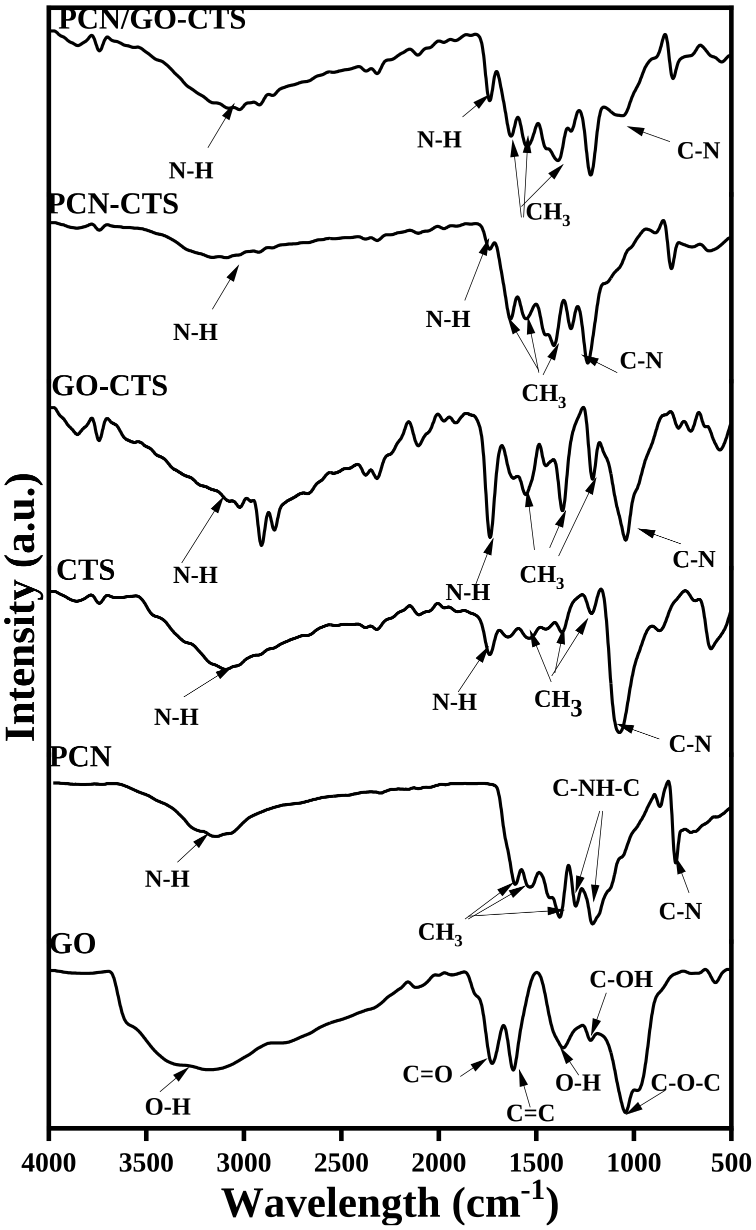

Fig 1: FTIR spectra of GO, PCN, CTS, GO-CTS, PCN-CTS and PCN/GO-CTS

The XRD spectra of GO, PCN, CTS, GO-CTS, PCN-CTS and PCN/GO-CTS are shown in Fig 2. The XRD pattern of CTS, showed peaks that could be indexed to the orthorhombic phase of Cu_3SnS_4, with lattice parameters a = 6.52; b = 7.52 and c = 37.6Å and space group Pmn 2i. The average crystallite size of the nanoparticles was calculated using the Scherrer's equation (Eq. 3)

$$D = \frac{K\lambda}{\beta cos\theta} \tag{3}$$

Where D is the average crystallite size, K is the shape factor (0.90), λ is the X-ray wavelength, β is the line broadening at half the maximum intensity (FWHM) after subtracting instrumental broadening and θ is the

Bragg's angle. The average crystallite size of the CTS was evaluated to be 15.3 nm. The XRD spectra of GO showed the characteristic peak arising from the stacking structure of GO at 2θ of 10.2, which corresponds to a d-spacing value of 0.863 nm. The PCN showed peaks that were typical of GCN (Sridharan *et al.*, 2015). The in-plane structural packing of the tri-s-triazine units with [001] diffraction was observed at 11.8°, while the peak at 27.70°was indexed as the [002] plane (Fina *et al.*, 2015). The indexes corresponded to a d-spacing value of 0.749 and 0.326 nm for the PCN layer respectively. The XRD pattern of the composites showed significant reduction in crystallinity, with PCN having the most influence on the crystallinity of CTS. While the prominent peaks of CTS could still be observed in GO-CTS, although with a significant broadening of the peak around 28°, the CTS peaks were completely masked by the PCN peaks in PCN-CTS. This was similarly observed in the PCN/GO-CTS composite, which further confirms the strong interaction between PCN and CTS nanoparticles.

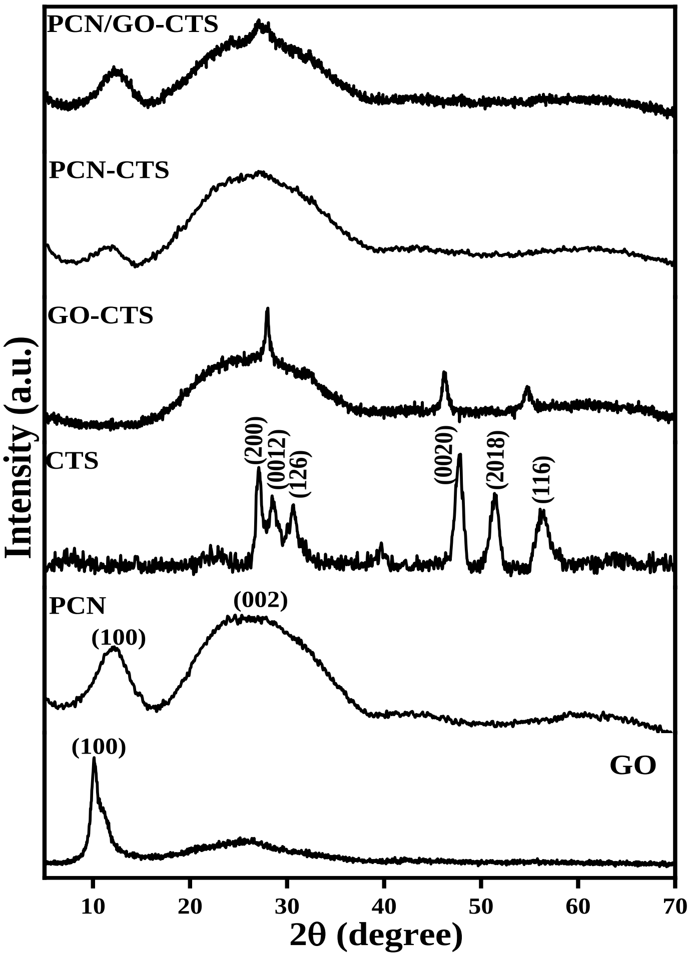

Fig 2: XRD spectra of GO, PCN, CTS, GO-CTS, PCN-CTS and PCN/GO-CTS

Fig 3 shows the SEM, TEM, and EDS spectra of CTS. The SEM image of CTS revealed uniform, agglomerated spherical shaped nanocrystals, which was also supported by the TEM image. The EDS spectra showed the presence of copper (Cu), tin (Sn) and sulfur (S) in the ratio 3.14, 1 and 3.45 respectively, which are in agreement with the expected stoichiometric ratio. The SEM and TEM images of the composites showed that there was a significant difference in the level of agglomeration of CTS in the three composites. Fig 4 shows the SEM, TEM, EDS spectra and elemental mapping images of PCN-CTS. CTS nanoparticles on PCN were more agglomerated compared to the CTS deposited on GO, and the elemental mapping images showed the presence of Cu, Sn, S, C and N, which confirms the incorporation of PCN and CTS. As shown in Fig. 5, The SEM and TEM images of rGO-CTS revealed a lower level of aggregation of CTS particles when incorporated on rGO. The elemental mapping images showed the presence Cu, Sn, S, C and O confirming the incorporation of CTS and rGO and the uniform distribution of the nanoparticles on support materials. For PCN/rGO CTS (Fig. 6), significant improvement in the distribution of CTS on the composite is observed, showing a synergistic effect in the PCN/GO composite on the nanoparticle distribution. The elemental mapping images of PCN/GO-CTS, showed the presence of Cu, Sn, S, C, N and O, which confirms the presence of CTS, PCN and GO in the composite.

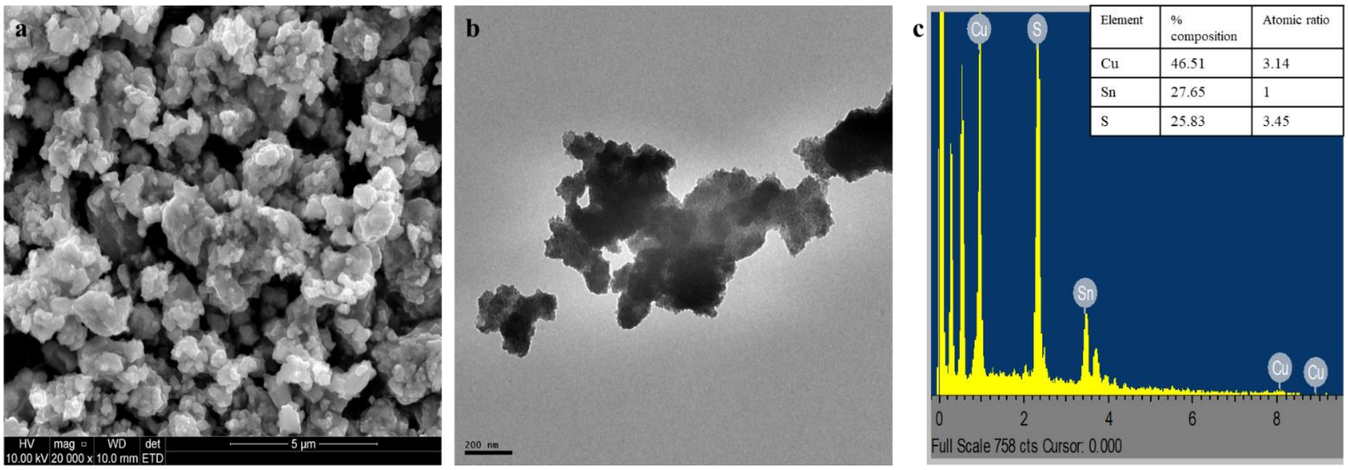

Element	% composition	Atomic ratio
Cu	46.51	3.14
Sn	27.65	1
S	25.83	3.45

Fig 3: (a) SEM image (b) TEM image and (C) EDS spectra of CTS

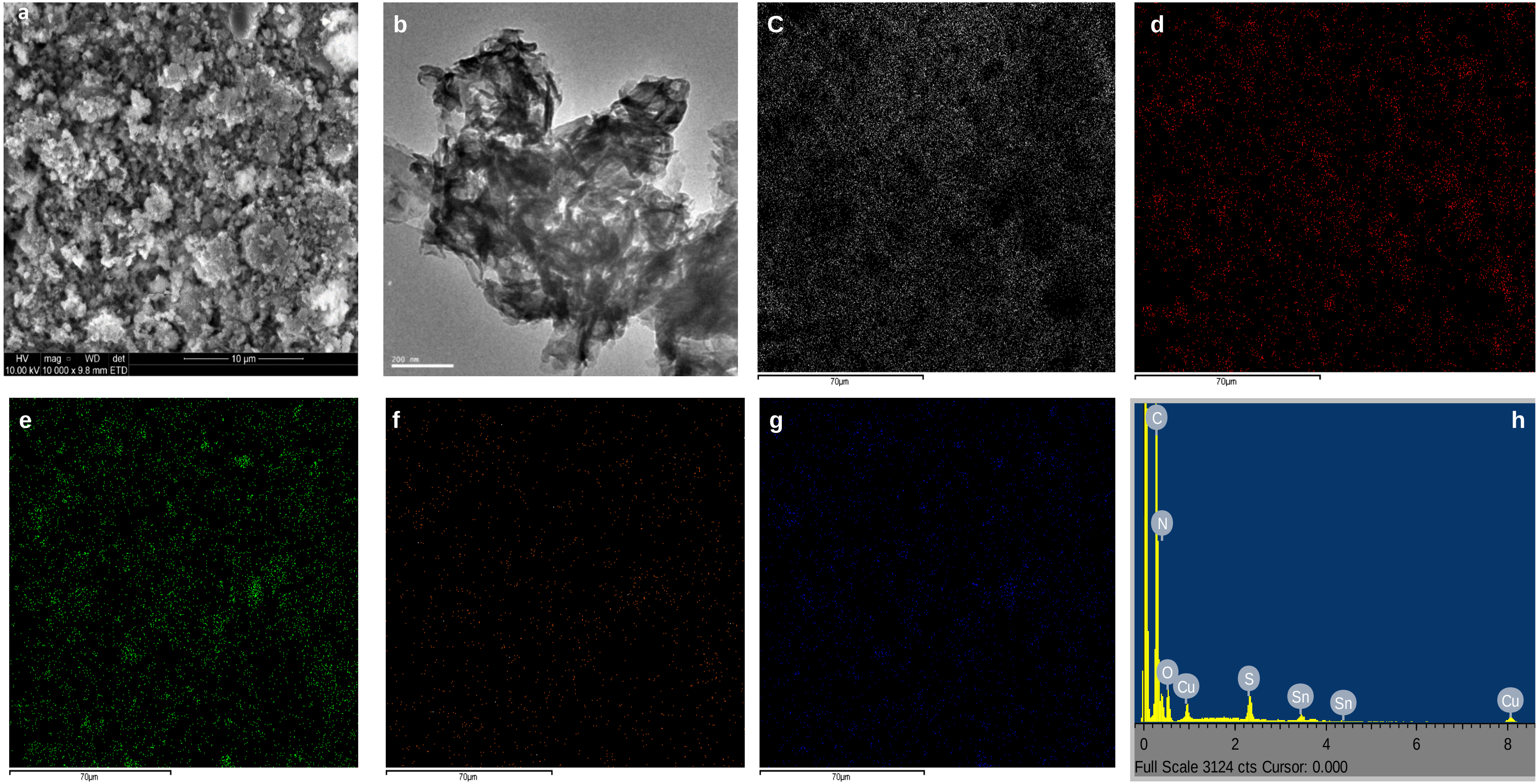

Fig 4: (a) SEM image, (b) TEM image, elemental mapping of (c) carbon (C), (d) nitrogen (N), (e) sulfur (S), (f) Cu (copper) and (g) tin (Sn) and (h) EDS spectra of PCN-CTS

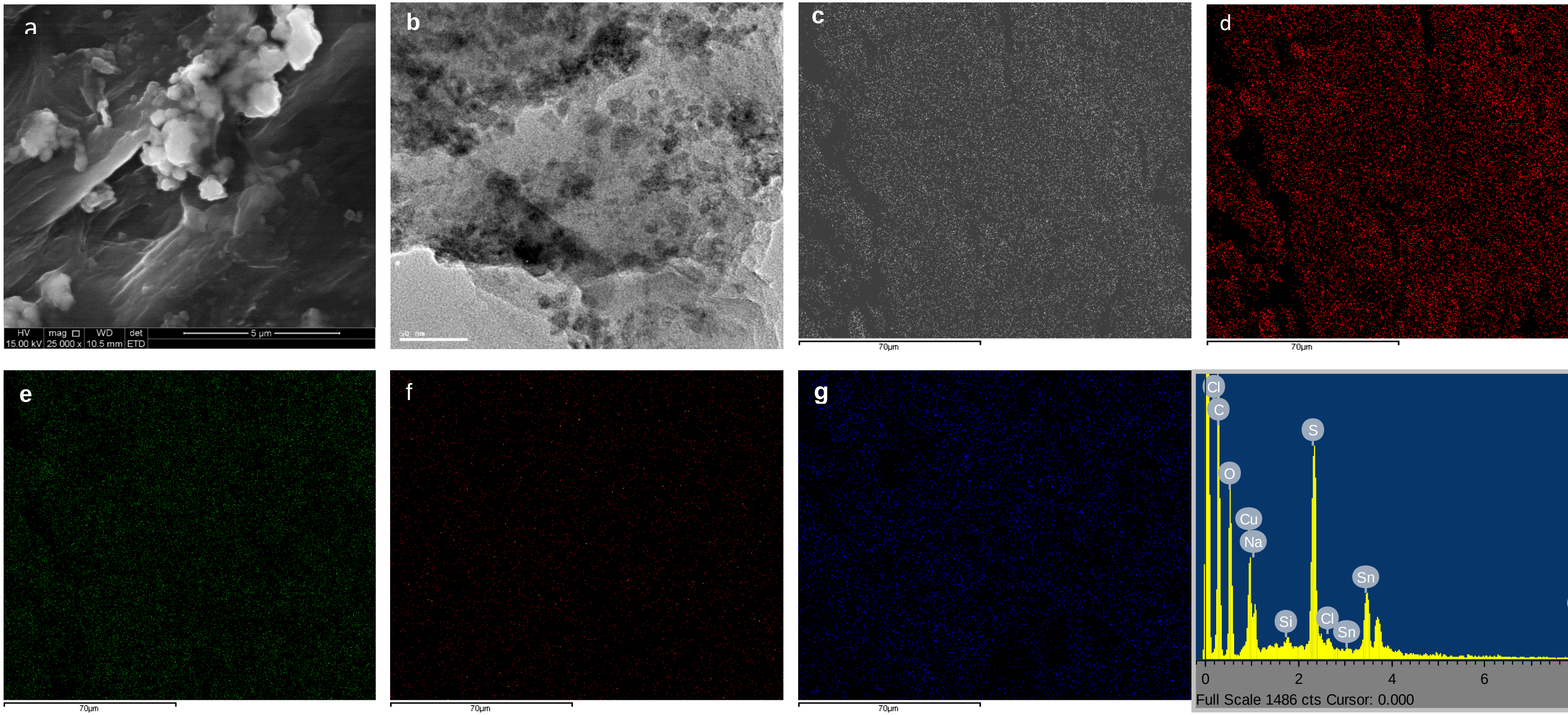

Fig 5: (a) SEM image, (b) TEM image, elemental mapping of (c) carbon (C), (d) nitrogen (N), (e) sulfur (S), (f) Cu (copper) and (g) tin (Sn) and (h) EDS spectra of GO-CTS

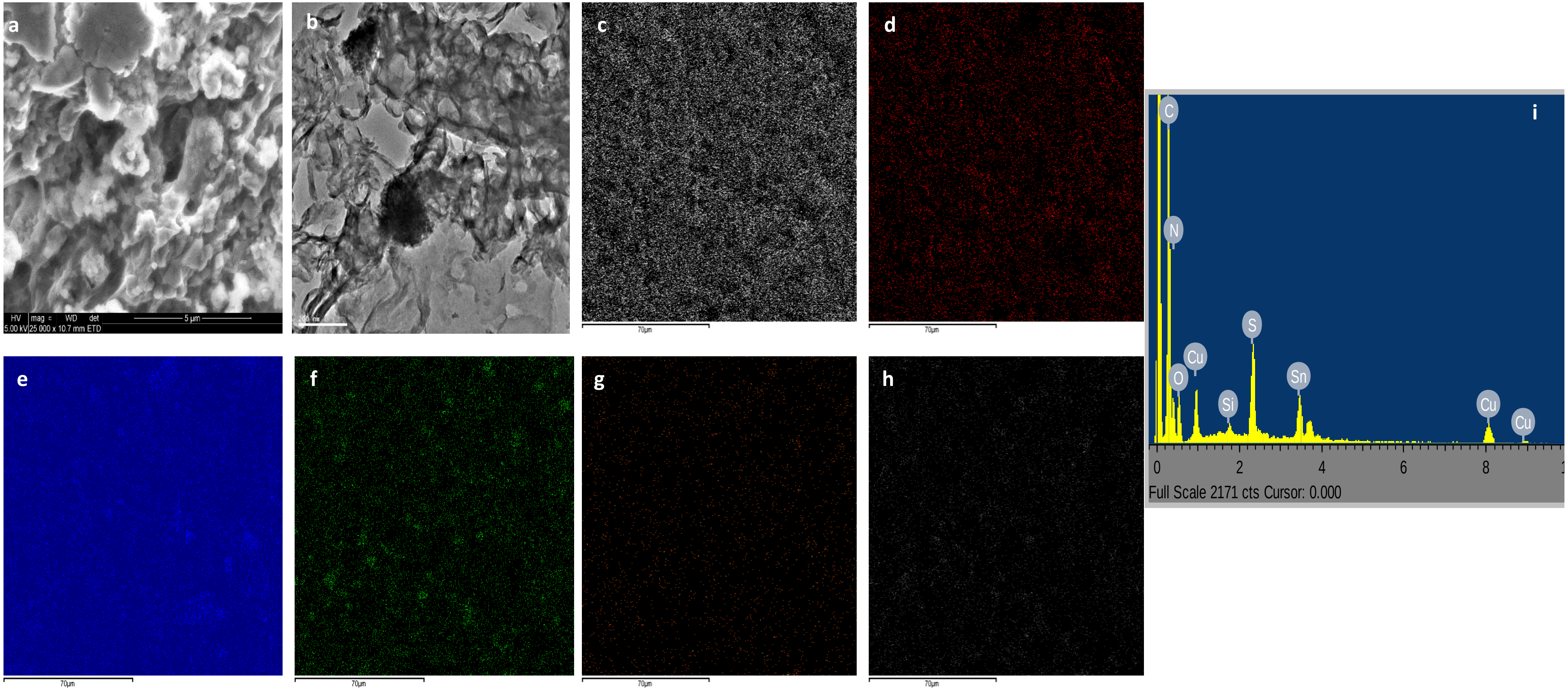

Fig 6: (a) SEM image, (b) TEM image, elemental mapping of (c) carbon (C), (d) nitrogen (N), (e) oxygen (O) (f) sulfur (S), (g) Cu (copper) and (h) tin (Sn) and (i) EDS spectra of PCN/GO-CTS

The absorption spectra and the corresponding Tauc plots (insets) of PCN, GO, CTS, GO-CTS, PCN-CTS and PCN/GO-CTS are shown in Figs. 7 a – f respectively. The spectrum of PCN showed an absorption maximum edge at 302 nm, with the absorption tailing into the visible region. This tailing of the absorption may be attributed to the formation of band tail states, which has been reported to be due to the presence of N-defects in PCN (Xue *et al.*, 2019). The absorption spectrum of GO showed a very sharp absorption edge at about 303 nm, with the absorption falling almost immediately to zero. The calculated band gap for PCN and GO was 2.91 and 2.51 eV respectively, which were in agreement with literature values (Arranz-Mascarós *et al.*, 2020, Xue *et al.*, 2019). CTS showed two significant absorption bands at 312 and 418 nm, with the absorption intensity remaining significantly strong into the visible region. The three composites, showed significant differences in their absorption spectra, indicating a difference in the influence exerted on the electronic structure of CTS by GO, PCN and PCN/GO. In PCN-CTS, a blue shift of the band at 312 nm to 318 nm and broader bands were observed compared to pristine CTS. The absorption tail into the visible region was also reduced compared to CTS. For the GO-CTS, the absorption spectrum was also significantly influenced when compared to CTS. The absorption maximum was observed at 305 nm, which was closer to the value for GO and also very sharp. The absorption also reduced significantly as it tails into the visible region. The absorption spectra of PCN/CTS-GO, showed a broad band at 305 nm, which could be attributed to GO. However, the absorption remained relatively strong into the visible region. Also, a new absorption band was observable at about 950 nm, and this could suggest the possible formation of new intra-band states in PCN/GO-CTS. The evaluated band gap for CTS, PCN-CTS and GO-CTS and PC/GO-CTS was 1.65, 1.46, 1.43 and 1.16 eV respectively. Thus, a red shift to lower energy was observed by the incorporation of PCN and GO into CTS and the red shift was significantly enhanced by the incorporation of both PCN and GO.

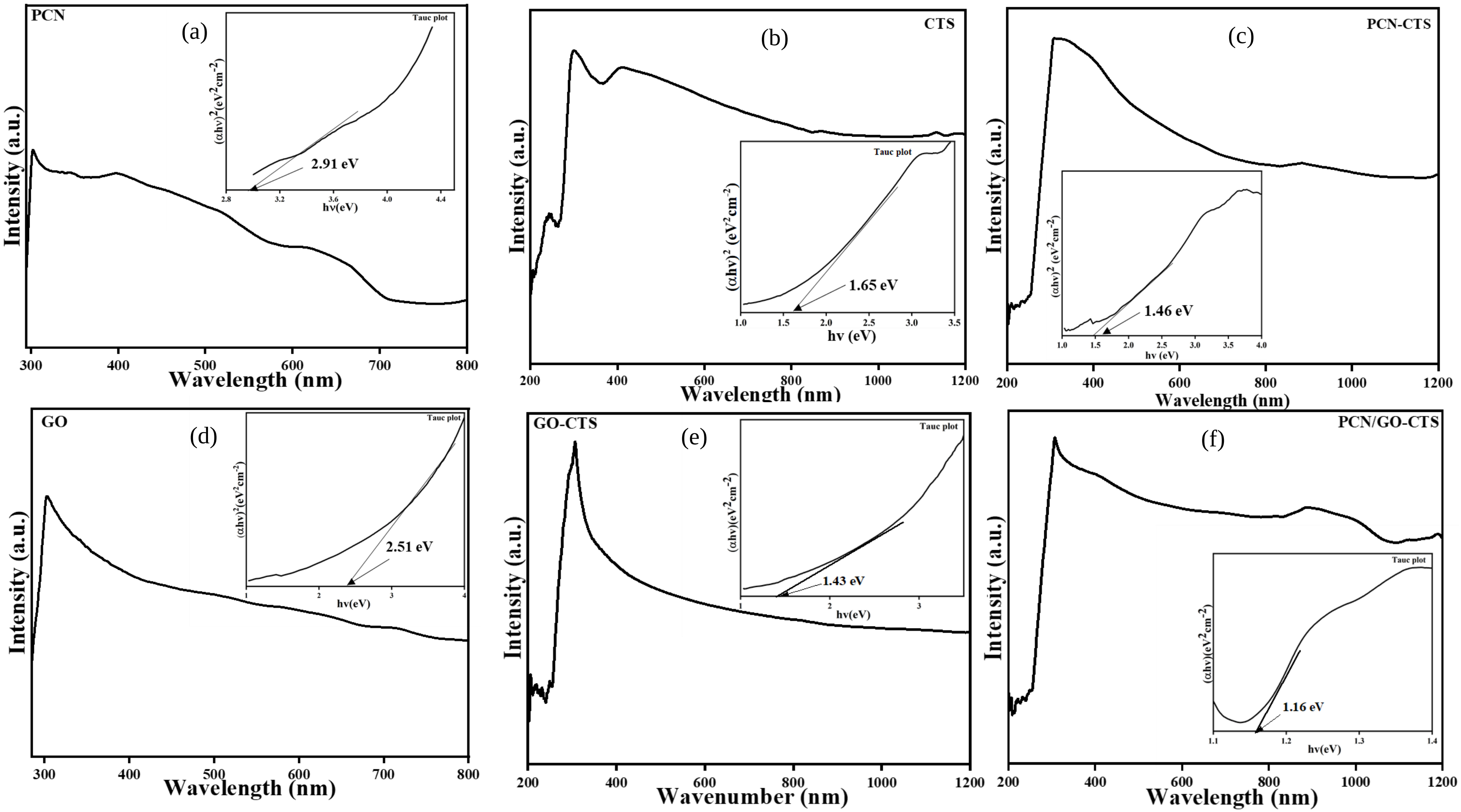

Fig 7: Absorption spectra of (a) PCN, (b) GO, (c) CTS, (d) PCN-CTS, (e) GO-CTS and (f) PCN/GO-CTS; and their respective Tauc plots (inset)

To investigate the characteristics of photogenerated charge carrier recombination in the composites, emission spectra at excitation wavelength of 450 nm were recorded using PL spectroscopy. Fig. 8, shows the PL spectra of CTS, PCN-CTS, GO-CTS and PCN/GO-CTS. Although, no new photoluminescence phenomena was observed in the spectra of all the composites, the intensity of the PL bands was significantly altered. While GO-CTS exhibited a reduction in the band intensity relative to CTS, the PL intensity was significantly increased in PCN-CTS. This suggests a difference in mechanism of charge carrier separation between the two composites. While the charge carrier separation in GO-CTS can be attributed to the transfer of photogenerated electrons from the valence band of CTS to the π-π system of GO, with GO acting as an electron sink (Huang *et al.*, 2017, Yeh *et al.*, 2013), photogenerated electrons are possibly transferred to band-tail states in PCN-CTS (Xue *et al.*, 2019, Yu *et al.*, 2021). These are the consequences of N-defects in PCN, as suggested by the absorption spectra. These defects in PCN are capable of trapping photogenerated electrons and increasing the probability of exciton occurrence, which accounts for the increase in the PL band (Liqiang *et al.*, 2006). Thus, PCN-CTS did not only benefit from the charge separation ability of PCN but also the generation of exciton, which are important for the photocatalytic activity of the composite. In PCN/GO-CTS the PL intensity was also enhanced compared to CTS, but was slightly lower than PCN-CTS. The slight deep might be attributed to the quenching activity of GO. However, it could be observed that despite the equal composition of PCN and GO, the influence of PCN in the photogenerated charge carrier recombination was more significant.

3.2 Evaluation of photocatalytic activity

The photocatalytic activity of CTS, PCN-CTS, GO-CTS and PCN/GO-CTS were evaluated for the degradation of tetracycline under UV light irradiation. The degradation profile of TCE by the photocatalysts and kinetics plots for the degradation are shown in Fig. 9. The degradation efficiency of CTS, PCN-CTS, GO-CTS and PCN/GO-CTS was 74.1, 85.2, 90.9 and 96.5% respectively. Thus, both PCN and GO had a positive effect on the photocatalytic activity of CTS and the combination of PCN and GO resulted in a further enhancement of the degradation efficiency.

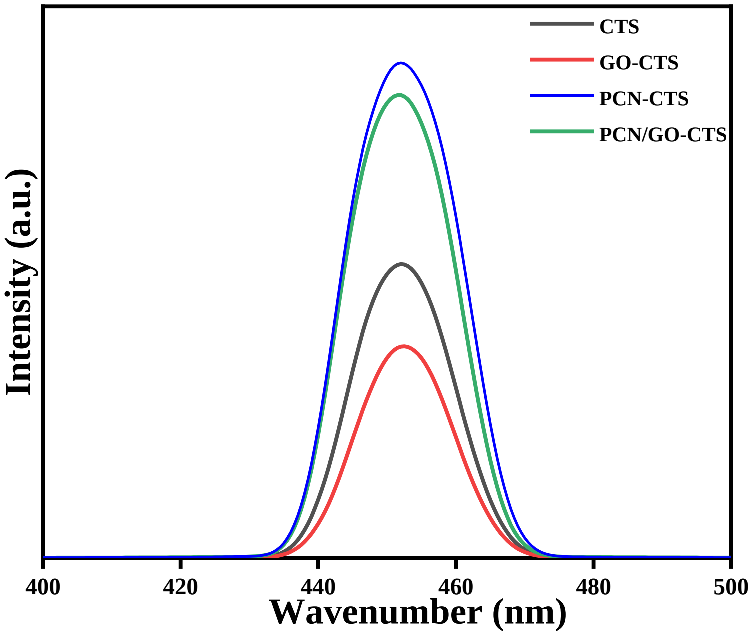

Fig 8: PL spectra of CTS, GO-CTS, PCN-CTS and PCN/GO-CTS

To understand the contribution of PCN and GO to the degradation activity of the composites, the degradation process was carried out using either PCN and GO alone. As shown in Fig. 9, no reduction in the concentration of TCE was observed during the adsorption-desorption equilibrium phase for PCN. However, upon irradiation with the light source, degradation of approximately 5% was observed. This low degradation activity might be as a result of the limited adsorption of TCE to PCN surface due to repulsion. It also suggests that the photogenerated charge carriers by PCN were not sufficient in effecting significant degradation. For GO, approximately 50% of the TCE were absorbed on its surface during the adsorption-desorption equilibrium stage and this might be attributed to the oxygen moieties on its surface. However, during the photocatalytic phase of the process, no significant reduction in the concentration of TCE was observed. This outcome was supported by the increase in adsorption experienced by the composites that contained GO. Although, CTS exhibited high adsorptive property in the adsorption phase of the process, incorporation of GO enhanced the adsorption activity of the composites compared to CTS. The adsorption activity of PCN-CTS was also significantly enhanced, when compared to CTS, and this may be attributed to the improvement of the surface area of PCN-CTS as a result of the lamellar and layered structure of PCN. The rate constants for the degradation were evaluated by a plot of $-\ln(C_t/C_o)$ against time for each of the degradation processes (Fig. 9). The rate constants for TCE degradation under UV light irradiation by CTS, PCN-CTS, GO-CTS and PCN/GO-CTS was 1.45×10^{-2}, 2.57×10^{-2}, 4.43×10^{-2}, 1.55×10^{-1} min^{-1} respectively. This showed that the rate of degradation of TCE by CTS was enhanced by 1.77, 3.05 and 10.7 folds by the incorporation of PCN, GO and PCN/GO respectively.

The photocatalytic activity of CTS, PCN-GO, GO-CTS and PCN/GO-CTS were compared using comparative parameters such as catalytic potential (CP%), electrical energy per order (E_{EO} KW/h) and the time required for the process to achieve 90% degradation ($t_{0.9}$). The values of CP, E_{EO} and $t_{0.9}$ were evaluated using Eq. 3-5.

$$CP(\%) = R_{cat} - (R_{(UV-CTS)} + R_{(UV-GO)} + R_{(UV-PCN)}) \quad (3)$$

$$E_{EO} = \frac{P \times 38.4}{V \times k} \quad (4)$$

$$t_{0.9} = \frac{2.3035}{k} \quad (5).$$

Where R(x) is the eficiency of a process, p is the power rating of light source, v is the colume of the test solution and k is the reaction rate constant. The values of the comparative parameters are shown in table 1.

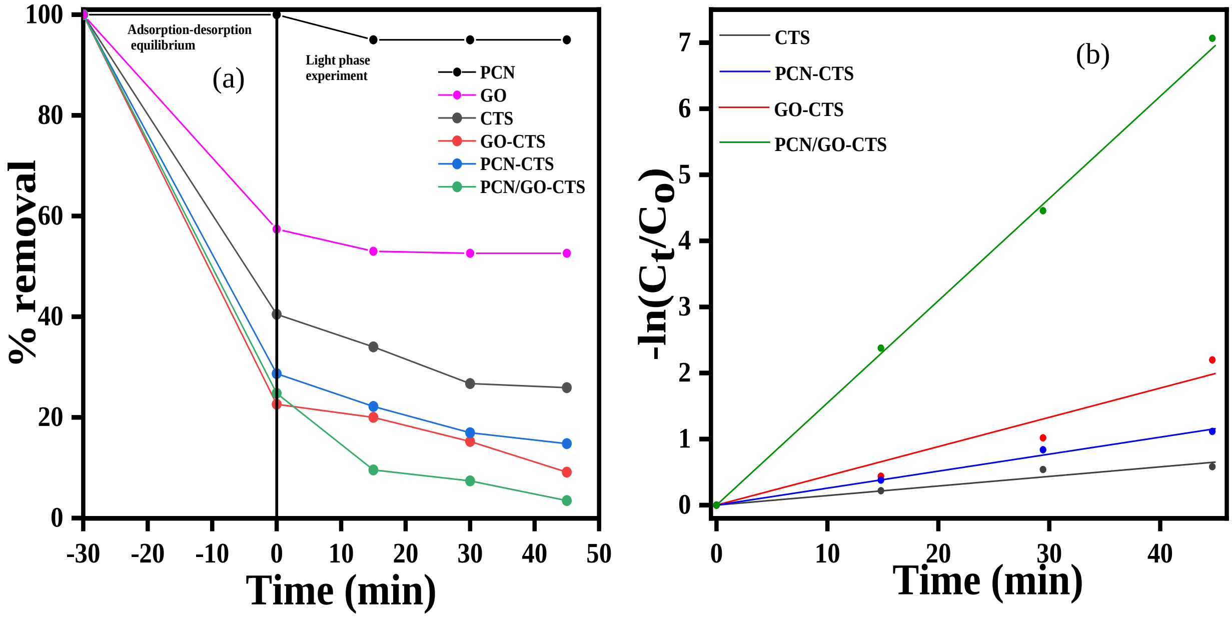

Fig 9: (a) Degradation profile of 5 mg/L of TCE using PCN, GO, CTS, GO-CTS, PCN-CTS and PCN/GO-CTS, and (c) kinetics of degradation TCE by CTS, GO-CTS, PCN-CTS and PCN/GO-CTS.

Table 1: Comparative parameters for the degradation of TCE by CTS, PCN-CTS, GO-CTS and PCN/GO-CTS under UV light irradiation

	CP(%)	E_{EO} (KW/h)	$T_{0.9}$ (min)
CTS	-	22.1	158.9
PCN-CTS	6.1	12.4	89.6
GO-CTS	15.9	7.2	52.0
PCN/GO-CTS	22.4	2.1	14.9

3.3 Proposed mechanism for the degradation process

The adsorption of molecules to the surface of a catalytic material and the generation of radical species are two important factors that significantly influence photocatalytic activity. The influence of adsorption on the photocatalytic activity of CTS and the composites have been discussed in previous section. For the generation of radical species, the efficiency of charge carrier separation and the oxidizing-reducing ability of generated charge carriers are important in the efficiency of the degradation process. A plausible explanation of the charge carrier separation process has been presented using the PL spectrum of the materials. In this section, the nature of radical species generated will be proposed by determining the band edge values of the photocatalysts. The band states of the composites was evaluated using Eq 6-7 (Wu *et al.*, 2018).

$$E_{CB} = \mathrm{X} - E_e - 0.5E_g, \tag{6}$$

$$E_{VB} = E_{CB} + E_g, \tag{7}$$

where X is the absolute electronegativity obtained from the geometric mean of the absolute electronegativity of the constituent element of the semiconductor, E_g is the band gap energy and E_e is the energy of free electrons on the hydrogen scale. The value of X for CTS was determined to be 5.25 eV. The calculated E_{CB} and E_{VB} for the materials are presented in Table 2. This confirmed that a significant alteration in the band state of CTS occurred by the incorporation of PCN and GO.

Table 2: Energy band state values of CTS, PCN-CTS, GO-CTS and PCN-CTS

	CTS	PCN-CTS	GO-CTS	PCN/GO-CTS
E_{CB} (eV)	-0.075	0.02	0.035	0.17
E_{VB} (eV)	1.65	1.48	1.48	1.33

The band states of the materials, support the earlier ascertion that the degradation activity of the materials showed a difference in pathways, due to the difference in their charge carrier recombination properties. The energy band states of the materials showed that the electrons generated in the conduction bands of the photocatalysts had less negative potentials than the $O_2/O_2^{\bullet -}$ (-0.33 eV) and, thus, are incapable of forming $O_2^{\bullet -}$. Also, the holes generated in the valence bands are less positive compared to the $^{\bullet}OH/OH^-$ potential (1.99 eV), limiting the generation of $^{\bullet}OH$ (Abdullah, 2019). However, the holes are capable of directly oxidizing organic molecules because of their high oxidizing power. Studies have shown that the higher the positive value of the E_{VB}, the higher the oxidizing power of the photogenerated holes (Liqiang *et al.*, 2006). Therefore, the photocatalytic activity of CTS can be attributed to the photogenerated holes. The photocatalytic activity of GO-CTS, could also be attributed to the oxidizing ability of photogenerated holes. Although, the holes generated in GO-CTS are expected to have a lower oxidizing ability than the CTS, the large quantity of photogenerated holes due to the smaller band gap in GO-CTS compared to CTS and the improved adsorption of the pollutant could account for its improved activity (Ansari and Cho, 2016). Although the PCN-CTS, posseses similar E_{VB} with GO-CTS, its higher band gap implies that the quantity of photogenerated charge carriers are not as high as will be obtained in GO-CTS; and this coupled with its lower adsorption capacity, could account for its lower activity (Liu *et al.*, 2020). As suggested by the PL spectra, occurrence of excitons could also be significant, in the activity of PCN-CTS. In PCN/GO-CTS, the lower E_{VB}, suggests that the reducing ability of its holes are lower compared to the other photocatalysts, despite the tendency for a larger quantity of charge carriers to be generated. However, the possible formation of excitons as suggested by PL spectra, may account for the its enhanced photocatalytic activity. The lower band gap of PCN/GO-CTS suggests that the intra band states, where electrons from the conduction band are transferred into, are closer to the valence band and enhances the probability of excition formation (Fischer *et al.*, 2011). Excitons have been reported to enhance radical generation in photocatalysis by reacting with O_2 via energy transfer to form singlet oxygen ($^1O_2$) (Yang *et al.*, 2020, Wang *et al.*, 2016).

4.0 Conclusion

The effect of graphene oxide, graphitic carbon nitride and a composite of both materials on the photocatalytic activity of copper tin sulphide (Cu_3SnS_4) have been studied in this work. The morphological, structural, and optical properties of these composites were explored in explaining the factors contributing to the photocatalytic activity of these materials. Significant difference was observed in the absorption and emission spectra of the composites, indicating a notable interaction between the CTS and the support materials at the electronic state. Based on this study, a plausible mechanism was proposed for the degradation activity of the composites, which is suggested to be significantly due to direct oxidative activity of holes in CTS and GO-CTS, while holes and excitons were probable charge carriers responsible for the activities of PCN-CTS and PCN/GO-CTS. This study has therefore shown, the possibility of altering the route of a photocatalytic process, by changing the nature of the support material.

5.0 References

Abdullah, E. A. 2019. Band edge positions as a key parameter to a systematic design of heterogeneous photocatalyst. *European Journal of Chemistry; Vol 10, No 1 (2019): March 2019*.

Ahmad, M. A., Aslam, S., Mustafa, F. & Arshad, U. 2021. Synergistic antibacterial activity of surfactant free Ag–GO nanocomposites. *Scientific Reports,* 11**,** 196.

Ansari, S. A. & Cho, M. H. 2016. Highly Visible Light Responsive, Narrow Band gap TiO_2 Nanoparticles Modified by Elemental Red Phosphorus for Photocatalysis and Photoelectrochemical Applications. *Scientific Reports,* 6**,** 25405.

Arranz-Mascarós, P., Godino-Salido, M. L., López-Garzón, R., García-Gallarín, C., Chamorro-Mena, I., López-Garzón, F. J., Fernández-García, E. & Gutiérrez-Valero, M. D. 2020. Non-covalent Functionalization of Graphene to Tune Its Band Gap and Stabilize Metal Nanoparticles on Its Surface. *ACS Omega,* 5**,** 18849-18861.

Ben-Refael, A., Benisti, I. & Paz, Y. 2020. Transient photoinduced phenomena in graphitic carbon nitride as measured at nanoseconds resolution by step-scan FTIR. *Catalysis Today,* 340**,** 97-105.

Cheng, Y., Fan, Y., Pei, Y. & Qiao, M. 2015. Graphene-supported metal/metal oxide nanohybrids: synthesis and applications in heterogeneous catalysis. *Catalysis Science & Technology,* 5**,** 3903-3916.

Cong, R., Choi, J.-Y., Song, J.-B., Jo, M., Lee, H. & Lee, C.-S. 2021. Characteristics and electrochemical performances of silicon/carbon nanofiber/graphene composite films as anode materials for binder-free lithium-ion batteries. *Scientific Reports,* 11**,** 1283.

Dey, R. S. 2015. Development of Biosensors from Polymer Graphene Composites. *In:* SADASIVUNI, K. K., PONNAMMA, D., KIM, J. & THOMAS, S. (eds.) *Graphene-Based Polymer Nanocomposites in Electronics.* Cham: Springer International Publishing.

Fan, X., Jiao, G., Zhao, W., Jin, P. & Li, X. 2013. Magnetic Fe_3O_4–graphene composites as targeted drug nanocarriers for pH-activated release. *Nanoscale,* 5**,** 1143-1152.

Fina, F., Callear, S., Carins, G. & Irvine, J. 2015. Structural Investigation of Graphitic Carbon Nitride via XRD and Neutron Diffraction. *Chemistry of Materials,* 27**,** 2612-2618.

Fischer, S. A., Isborn, C. M. & Prezhdo, O. V. 2011. Excited states and optical absorption of small semiconducting clusters: Dopants, defects and charging. *Chemical Science,* 2**,** 400-406.

Gandhi, M. R., Vasudevan, S., Shibayama, A. & Yamada, M. 2016. Graphene and Graphene-Based Composites: A Rising Star in Water Purification - A Comprehensive Overview. *ChemistrySelect,* 1**,** 4358-4385.

Georgakilas, V., Otyepka, M., Bourlinos, A. B., Chandra, V., Kim, N., Kemp, K. C., Hobza, P., Zboril, R. & Kim, K. S. 2012. Functionalization of graphene: covalent and non-covalent approaches, derivatives and applications. *Chemical reviews,* 112**,** 6156-6214.

Hu, S., Zhang, W., Bai, J., Lu, G., Zhang, L. & Wu, G. 2016. Construction of a 2D/2D g-C_3N_4/rGO hybrid heterojunction catalyst with outstanding charge separation ability and nitrogen photofixation performance via a surface protonation process. *RSC Advances,* 6**,** 25695-25702.

Huang, J., Fu, K., Deng, X., Yao, N. & Wei, M. 2017. Fabrication of TiO_2 Nanosheet Aarrays/Graphene/Cu_2O Composite Structure for Enhanced Photocatalytic Activities. *Nanoscale Research Letters,* 12**,** 310.

Idris, M. B. & Devaraj, S. 2019. Few-layered mesoporous graphitic carbon nitride: a graphene analogue with high capacitance properties. *New Journal of Chemistry,* 43**,** 11626-11635.

Jayabharathi, J., Sundari, G. A., Thanikachalam, V., Jeeva, P. & Panimozhi, S. 2017. A dodecanethiol-functionalized Ag nanoparticle-modified ITO anode for efficient performance of organic light-emitting devices. *RSC Advances,* 7**,** 38923-38934.

Jin, X., Balasubramanian, V. V., Selvan, S. T., Sawant, D. P., Chari, M. A., Lu, G. Q. & Vinu, A. 2009. Highly Ordered Mesoporous Carbon Nitride Nanoparticles with High Nitrogen Content: A Metal-Free Basic Catalyst. *Angewandte Chemie International Edition,* 48**,** 7884-7887.

Julkapli, N. M. & Bagheri, S. 2015. Graphene supported heterogeneous catalysts: An overview. *International Journal of Hydrogen Energy,* 40**,** 948-979.

Khalili, D. 2016. Graphene oxide: a promising carbocatalyst for the regioselective thiocyanation of aromatic amines, phenols, anisols and enolizable ketones by hydrogen peroxide/KSCN in water. *New Journal of Chemistry,* 40**,** 2547-2553.

Kong, X.-K., Chen, C.-L. & Chen, Q.-W. 2014. Doped graphene for metal-free catalysis. *Chemical Society Reviews,* 43**,** 2841-2857.

Liqiang, J., Yichun, Q., Baiqi, W., Shudan, L., Baojiang, J., Libin, Y., Wei, F., Honggang, F. & Jiazhong, S. 2006. Review of photoluminescence performance of nano-sized semiconductor materials and its relationships with photocatalytic activity. *Solar Energy Materials and Solar Cells,* 90**,** 1773-1787.

Liu, W., He, T., Wang, Y., Ning, G., Xu, Z., Chen, X., Hu, X., Wu, Y. & Zhao, Y. 2020. Synergistic adsorption-photocatalytic degradation effect and norfloxacin mechanism of ZnO/ZnS@BC under UV-light irradiation. *Scientific Reports,* 10**,** 11903.

Lu, Z., Kong, Z., Jing, L., Wang, T., Liu, X., Fu, A., Guo, P., Guo, Y.-G. & Li, H. 2020. Porous SnO_2/Graphene Composites as Anode Materials for Lithium-Ion Batteries: Morphology Control and Performance Improvement. *Energy & Fuels,* 34**,** 13126-13136.

Marcano, D. C., Kosynkin, D. V., Berlin, J. M., Sinitskii, A., Sun, Z., Slesarev, A., Alemany, L. B., Lu, W. & Tour, J. M. 2010. Improved Synthesis of Graphene Oxide. *ACS Nano,* 4**,** 4806-4814.

Olatunde, O. C. & Onwudiwe, D. C. 2021. Graphene-Based Composites as Catalysts for the Degradation of Pharmaceuticals. *Int J Environ Res Public Health,* 18.

Onwudiwe, D. C., Olatunde, O. C. & Mathur, S. 2021. Structural studies and morphological properties of antimony sulphide nanorods obtained by solvothermal synthesis. *Physica B: Condensed Matter,* 605**,** 412691.

Papageorgiou, D. G., Kinloch, I. A. & Young, R. J. 2017. Mechanical properties of graphene and graphene-based nanocomposites. *Progress in Materials Science,* 90**,** 75-127.

Pramanik, N., Ranganathan, S., Rao, S., Suneet, K., Jain, S., Rangarajan, A. & Jhunjhunwala, S. 2019. A Composite of Hyaluronic Acid-Modified Graphene Oxide and Iron Oxide Nanoparticles for Targeted Drug Delivery and Magnetothermal Therapy. *ACS Omega,* 4**,** 9284-9293.

Radsar, T., Khalesi, H. & Ghods, V. 2021. Graphene properties and applications in nanoelectronic. *Optical and Quantum Electronics,* 53**,** 178.

Sachdeva, H. 2020. Recent advances in the catalytic applications of GO/rGO for green organic synthesis. *Green Processing and Synthesis,* 9**,** 515-537.

Shcherban, N. D., Mäki-Arvela, P., Aho, A., Sergiienko, S. A., Yaremov, P. S., Eränen, K. & Murzin, D. Y. 2018. Melamine-derived graphitic carbon nitride as a new effective metal-free catalyst for Knoevenagel condensation of benzaldehyde with ethylcyanoacetate. *Catalysis Science & Technology,* 8**,** 2928-2937.

Soldano, C., Mahmood, A. & Dujardin, E. 2010. Production, properties and potential of graphene. *Carbon,* 48**,** 2127-2150.

Sreekanth, T. V. M., Basivi, P. K., Nagajyothi, P. C., Dillip, G. R., Shim, J., Ko, T. J. & Yoo, K. 2018. Determination of surface properties and Gutmann's Lewis acidity-basicity parameters of thiourea and melamine polymerized graphitic carbon nitride sheets by inverse gas chromatography. *J Chromatogr A,* 1580**,** 134-141.

Sridharan, K., Jang, E., Park, J. H., Kim, J.-H., Lee, J.-H. & Park, T. J. 2015. Silver Quantum Cluster (Ag_9)-Grafted Graphitic Carbon Nitride Nanosheets for Photocatalytic Hydrogen Generation and Dye Degradation. *Chemistry – A European Journal,* 21**,** 9126-9132.

Su, D. S., Zhang, J., Frank, B., Thomas, A., Wang, X., Paraknowitsch, J. & Schlogl, R. 2010. Metal-free heterogeneous catalysis for sustainable chemistry. *ChemSusChem,* 3**,** 169-80.

Suter, T., Brázdová, V., McColl, K., Miller, T. S., Nagashima, H., Salvadori, E., Sella, A., Howard, C. A., Kay, C. W. M., Corà, F. & McMillan, P. F. 2018. Synthesis, Structure and Electronic Properties of Graphitic Carbon Nitride Films. *The Journal of Physical Chemistry C,* 122**,** 25183-25194.

Tabish, T. A., Memon, F. A., Gomez, D. E., Horsell, D. W. & Zhang, S. 2018. A facile synthesis of porous graphene for efficient water and wastewater treatment. *Scientific Reports,* 8**,** 1817.

Vinothkannan, M., Kim, A. R., Gnana kumar, G. & Yoo, D. J. 2018. Sulfonated graphene oxide/Nafion composite membranes for high temperature and low humidity proton exchange membrane fuel cells. *RSC Advances,* 8**,** 7494-7508.

Wang, H., Jiang, S., Chen, S., Li, D., Zhang, X., Shao, W., Sun, X., Xie, J., Zhao, Z., Zhang, Q., Tian, Y. & Xie, Y. 2016. Enhanced Singlet Oxygen Generation in Oxidized Graphitic Carbon Nitride for Organic Synthesis. *Advanced Materials,* 28**,** 6940-6945.

Wang, H., Li, X., Ruan, Q. & Tang, J. 2020. Ru and RuO_x decorated carbon nitride for efficient ammonia photosynthesis. *Nanoscale,* 12**,** 12329-12335.

Wang, X., Blechert, S. & Antonietti, M. 2012. Polymeric Graphitic Carbon Nitride for Heterogeneous Photocatalysis. *ACS Catalysis,* 2**,** 1596-1606.

Wee-Jun Onga, Lling-Lling Tana, Siang-Piao Chaia, Siek-Ting Yonga & Mohamed, A. R. 2015 Surface charge modification via protonation of graphitic carbon nitride (g-C_3N_4) for electrostatic self-assembly construction of 2D/2D reduced graphene oxide (rGO)/g-C_3N_4 nanostructures toward enhanced photocatalytic reduction of carbon dioxide to methane. *Nano Energy,* 13**,** 757-770.

Wu, Q., Zhou, M., Gong, Y., Li, Q., Yang, M., Yang, Q. & Zhang, Z. 2018. Three-dimensional bandgap-tuned Ag_2S quantum dots/reduced graphene oxide composites with enhanced adsorption and photocatalysis under visible light. *Catalysis Science & Technology,* 8**,** 5225-5235.

Xia, Z., Wang, S., Jiang, L., Sun, H., Qi, F., Jin, J. & Sun, G. 2015. Rational design of a highly efficient Pt/graphene–Nafion® composite fuel cell electrode architecture. *Journal of Materials Chemistry A,* 3**,** 1641-1648.

Xue, J., Fujitsuka, M. & Majima, T. 2019. The role of nitrogen defects in graphitic carbon nitride for visible-light-driven hydrogen evolution. *Physical Chemistry Chemical Physics,* 21**,** 2318-2324.

Yang, F., Chu, X., Sun, J., Zhang, Y., Li, Z., Liu, H., Bai, L., Qu, Y. & Jing, L. 2020. Efficient singlet oxygen generation by excitonic energy transfer on ultrathin g-C_3N_4 for selective photocatalytic oxidation of methyl-phenyl-sulfide with O_2. *Chinese Chemical Letters,* 31**,** 2784-2788.

Yeh, T.-F., Cihlář, J., Chang, C.-Y., Cheng, C. & Teng, H. 2013. Roles of graphene oxide in photocatalytic water splitting. *Materials Today,* 16**,** 78-84.

Yu, X., Ng, S.-F., Putri, L. K., Tan, L.-L., Mohamed, A. R. & Ong, W.-J. 2021. Point-Defect Engineering: Leveraging Imperfections in Graphitic Carbon Nitride (g-C_3N_4) Photocatalysts toward Artificial Photosynthesis. *Small,* n/a**,** 2006851.

Zhang, H. 2020. Molecularly imprinted nanoparticles for biomedical applications. *Advanced Materials,* 32**,** 1806328.

Zhang, W., Jia, B. & Furumai, H. 2018. Fabrication of graphene film composite electrochemical biosensor as a pre-screening algal toxin detection tool in the event of water contamination. *Scientific Reports,* 8**,** 10686.

Zhang, W., Zhou, L. & Deng, H. 2016. Ag modified g-C_3N_4 composites with enhanced visible-light photocatalytic activity for diclofenac degradation. *Journal of Molecular Catalysis A: Chemical,* 423**,** 270-276.

Zhu, B., Xia, P., Li, Y., Ho, W. & Yu, J. 2017. Fabrication and photocatalytic activity enhanced mechanism of direct Z-scheme g-C_3N_4/Ag_2WO_4 photocatalyst. *Applied Surface Science,* 391**,** 175-183.

Zhu, G. X., Lu, T. L., Han, L. & Zhan, Y. Z. 2020. Graphitic carbon nitride (g-C_3N_4) as an efficient metal-free Fenton-like catalyst for degrading organic pollutants: the overlooked non-photocatalytic activity. *Water Science and Technology,* 81**,** 518-528.

CHAPTER NINE

Phase selective synthesis of copper antimony sulphides by co-thermolysis of precursor complexes and evaluation of persulphate activation activity

1.0 Introduction

Semiconductor nanocrystals of ternary copper-based chalcogenides continue to attract significant interest due to their potential application in energy harvesting and conversion technologies such as photovoltaics and thermoelectrics (Zou and Jiang, 2014). Ternary Cu-Sb-S (CAS) system is a class of copper-based chalcogenides that has received immense interest because they are sustainable, scalable and cost-efficient photo-absorbers. They possess high absorption coefficients, suitable band gaps and earth abundant elemental composition (Rath *et al.*, 2015). CAS crystallize in four main crystal phases: $CuSbS_2$ (Chalcostibite) (Medina-Montes *et al.*, 2018), Cu_3SbS_3 (skinnerite) (Ikeda *et al.*, 2014), Cu_3SbS_4 (famatinite) (van Embden and Tachibana, 2012) and $Cu_{12}Sb_4S_{13}$ (tetrahedrite) (van Embden *et al.*, 2013), each with its unique optical and electrical properties. $CuSbS_2$ and $Cu_{12}Sb_4S_{12}$ are both considered as prospective solar absorbers due to their high absorption coefficient, which is above 10^5 cm^{-1}, band gap range of 1.4-1.7 eV and p-type electrical conductivity (Yang *et al.*, 2014, Rath *et al.*, 2015). These materials are presently considered as alternatives for commercial solar cell absorbers like CuInGaSe and CdTe in order to avoid the use of toxic and scarce elements such as gallium, cadmium and tellurium (Scheer *et al.*, 2009).

The synthesis of CAS has been achieved by several routes including electrodeposited metal sulphurization, thermal evaporation, sputtering, chemical bath deposition, spray pyrolysis, spin coating, co-evaporation and solvothermal processes (using either metal salts or complexes as precursor compounds) (Welch *et al.*, 2014, Septina *et al.*, 2014, McCarthy *et al.*, 2016, Macías *et al.*, 2017, An *et al.*, 2003, Liang *et al.*, 2016, Colombara *et al.*, 2012). Solvothermal synthesis provides a facile route to control the phase selectivity in CAS synthesis by varying the synthesis parameters such as precursor salts/complex ratio, type of sulphur source, temperature of reaction and type solvent/capping agents used (Chen *et al.*, 2016, Ikeda *et al.*, 2014, van Embden *et al.*, 2013, Ramasamy *et al.*, 2014).

The choice selection of precursor molecules in phase controlled synthesis of CAS is a process that has been explored in different studies. Albuquerque *et al.* (2018) reported the use of $CuCl_2$, $SbCl_3$ and S as precursors (in oleylamine) for the synthesis of Cu_3SbS_4. Cu_2S and Sb_2S_3 dissolved in 2-mercaptoethanol and ethylene diamine mixture were also utilized for the synthesis of $CuSbS_2$. The use of precursor complexes, is a very important and promising approach to achieving the formation of ternary metal sulphides.With precursor complexes, stable, monodispersed colloidal quantum dots with narrow size distribution could be obtained through a simple, safe and mild fabrication process (Malik *et al.*, 2001). There are currently only few reports on the use of precursor complexes for CAS synthesis, with only xanthate (Rath *et al.*, 2015) and dithiocarbamate (Xu *et al.*, 2013) complexes reported so far. The unique characteristics of dithiocarbamate complexes (DTC) such as the ease of functionalization and their ability to undergo clean decomposition make them versatile single source precursors and are often preferred in synthesis (Onwudiwe, 2019).

Solvothermal synthesis could be carried out via two approaches: hot-injection and heat-up methods. The hot-injection method, achieves a burst nucleation upon the introduction of the precursor molecules into a hot capping agent under inert atmosphere. The initiation stage is succeeded by a separate growth stage (Kwon and Hyeon, 2011). This approach (solvothermal), however, suffers from poor scalability and reproducibility (van Embden *et al.*, 2015). On the other hand, the heat-up method involves nucleation and nanocrystal growth achieved via the gradual heating up of precursor complexes in a capping agent. With proper understanding of the chemistry of both precursor complexes and capping agents, the heat-up method is a scalable and reproducible process for preparing nanocrystalline particles with minimum polydispersity (Carey *et al.*, 2015).

The present study, reports the synthesis of three phases of CAS ($CuSbS_2$, Cu_3SbS_4 and $Cu_{12}Sb_4S_{13}$) using copper and antimony complexes of *N*-methyl *N*-phenyl dithiocarbamate. Phase selectivity was achieved by varying the ratio of the capping agent (oleylamine/dodecanethiol) used, precursor concentration and the reaction temperature.

2.0 Experimental

2.1 Materials

All materials were used as received without any further purification. Antimony chloride ($SbCl_3•6H_2O$), copper sulphate ($CuSO_4$), carbon disulphide (CS_2), aqueous ammonia hydroxide (NH_4OH), N-methyl aniline, ethanol, oleylamine, chloroform, 1-dodecanthiol, tert-butanol, silver nitrate and n-hexane were all obtained from Sigma Aldrich chemicals.

2.2 Synthesis of ammonium salt of *N*-methyl *N*-phenyl dithocarbamate ligand.

An earlier reported method was employed for the synthesis of ammonium salt of *N*-methyl *N*-phenyl dithiocarbamate (Motaung *et al.*, 2019). Equal moles of N-methyl aniline and aqueous ammonia were mixed together in a round bottom flask placed in ice bath and left to stir for 20 min. Thereafter, equivalent concentration of carbon disulphide was added to the mixture and left to stir for 4 h. The yellowish white solid product obtained was filtered by suction and washed three times with very cold ethanol. The ligand was kept in the refrigerator for further use.

2.3 Synthesis of antimony(III) tris(*N*-methyl-*N*-phenyldithiocarbamate) ($Sb(DTC)_3$) and copper(II) *N*-methyl *N*-phenyl dithiocarbamate ($Cu(DTC)_2$)

An aqueous solution of the respective metal salts ($SbCl_3•6H_2O$ and $CuSO_4$) was mixed with an aqueous solution of the ammonium *N*-methyl-*N*-phenyldithiocarbamate, in the correct stoichiometric mole ratio. The mixture was stirred for 1 h at room temperature and the precipitates obtained were filtered, rinsed thoroughly with water and ethanol and then allowed to dry overnight under vacuum. The solid was purified by recrystallization in chloroform, to afford pure antimony(III) tris(*N*-methyl-*N*-phenyldithiocarbamate) and copper(II) *N*-methyl *N*-phenyl dithiocarbamate complexes represented as [$Sb(DTC)_3$] and [$Cu(DTC)_2$)] respectively (Onwudiwe *et al.*, 2020, Ekennia *et al.*, 2015) .

2.4 Synthesis of $CuSbS_2$ nanocrystals

The nanocrystal was synthesised under nitrogen atmosphere. Equimolar concentration of [$Sb(DTC)_3$] and [$Cu(DTC)_2$] where added into 20 mmol of oleylamine in a three-necked round bottom flask connected to a reflux. The slurry was heated to 120 ºC on a temperature controlled electric mantle with stirring, and held for 20 min to remove oxygen and water from the system. The temperature of the system was then raised to 280 ºC at a heating rate of 10 ºC/min and held at the temperature for 1 h. After the reaction, the solution was allowed to cool down naturally and the nanoparticles were precipitated by the introduction of excess ethanol. The nanoparticles were separated from the system mix by centrifugation and rinsed three times with ethanol/toluene mixture (3:1 v/v). Each rinsing cycle was completed by centrifugation at 5000 rpm.

2.5 Synthesis of Cu_3SbS_4 nanocrystals

The procedure for the synthesis of Cu_3SbS_4 was similar to that for $CuSbS_2$ nanocrystal, except for a change in the mole ratio of [$Sb(DTC)_3$] to [$Cu(DTC)_2$] 1:1 to 1:3; the final temperature for the reaction was 220 ºC and a mixture of oleylamine and 1-dodecanethiol, in ratio 1:1 was used as the solvent.

2.6 Synthesis of $Cu_{12}Sb_4S_{13}$ nanocrystals

The same procedure used for the synthesis of Cu_3SbS_4 was employed; however, the reaction temperature of the system was increased to 250 ºC. Other synthesis parameters were maintained similar to the conditions for the synthesis of Cu_3SbS_4 .

2.7 Characterization of nanocrystals

Powder X-ray diffraction patterns for the nanocrystals were recorded on a D8 Advanced diffractometer using Cu Kα radiation (λ = 154.18 pm). The morphology of the samples was studied using Field emission scanning electron microscope (FESEM) and TECNAI G2 (ACI) transmission electron microscope with an accelerating voltage of 200 kV. For the TEM analysis, the sample were dissolved in toluene and the solution dropped on the copper grid, which were dried at room temperature before measurement. The sample for the SEM analysis were affixed unto a copper stump using a carbon tape and sputter coated with ultra-thin Au before measurement. PerkinElmer λ750s UV-vis-NIR spectrophotometer was used for the UV/visible-NIR measurements. The photoluminescence properties were studied using Perkinelmer LS 45 fluorimeter.

2.8 Persulfate activation activity

The persulfate activation study of the obtained CAS stoichiometries were evaluated for the degradation of tetracycline (TCE). In a typical process, 10 mg of CAS was measured into a 100 mL beaker containing 50 mL of 10 mg/L TCE at pH 4. Afterwards, 1mM of PS was added into the set up and the system was placed in a dark chamber and stirred. Aliquots of the solution were taken and the concentration of TCE was measured at 360 nm using a ONDE UV-vis spectrophotometer. The percentage degradation of TCE was calculated using eq. 1.

$$\%\, removal \;=\; \frac{C_o - C_f}{C_o} \times 100\%, \qquad (1)$$

where C_o and C_f are the initial and final concentrations of TCE respectively. The reaction rate for the degradation process was evaluated by fitting the degradation data into the linear form of the pseudo first order kinetic (Eq. 2).

$$-ln\frac{C_f}{C_o} = Kt, \qquad (2)$$

where C_f and C_o are the final and initial concentration of TCE, k is the reaction rate constant and t is the reaction time. The effect of pH on the PS activation of CAS was evaluated by adjusting the pH of the test solution with 0.1 M HCl or 0.1 M NaOH. The mechanism of PS activation was studied by adding tert-butanol (TBA) and $AgNO_3$ into the set-up to act as reactive oxygenated specie and electron scavenger respectively.

3.0 Results and discussion

The three phases of CAS nanocrystals were prepared by the co-thermolysis of dithiocarbamate complexes of copper and antimony, as precursor complexes under N_2 atmosphere. Both complexes were co-thermolysed in a heat-up process involving a gradual heating of the precursors in a suitable solvent. During thermolysis process, the two precursor molecules decompose into their respective binary metal sulphides, which then undergo a solid state reaction to produce the ternary materials. The obtained crystalline phase in the solid state reaction was determined by three main factors: (1) the ratio of the precursor complexes, (2) the reaction temperature and (3) the presence of supernumerary sulphur in the reaction system. For the synthesis of $CuSbS_2$, eqimolar ratio of $[Cu(DTC)_2]$ and $[Sb(DTC)_3]$ were thermolysed in 20 mmoles of oleylamine at 280 ºC. The synthesis of Cu_3SbS_4 involved the thermolysis of $[Cu(DTC)_2]$and $[Sb(DTC)_3]$ in 3:1 mole ratio of in 20 mmoles of oleylamine at 240 ºC. The presence of supernumerary sulphur was important in the synthesis of $Cu_{12}Sb_4S_{13}$. This was achieved through the introduction of 1-dodecanethiol into the reaction system. The synthesis of $Cu_{12}Sb_4S_{13}$ was achieved using a 3:1 mole ratio of $[Cu(DTC)_2]$ to $[Sb(DTC)_3]$ and a mixture of oleylamine and 1-dodecanethiol was used as solvent in ratio of 1:1 v/v.

There are only a few reports on the mechanism of phase selectivity in the synthesis of CAS and an important factor is the initial copper sulphide ($Cu_{2-x}S$) phase generated in the reaction system (Liang *et al.*, 2016). Since $Cu_{2-x}S$ can exist in a number of stoichiometric phases, which can be influenced by the reation system, this is often explored in achieving phase selectivity in the synthesis of ternary metal sulphides. Different studies have shown that by varying synthesis parameters such as type of solvent, sulfonating agent, temperature and precursor type, different phases of $Cu_{2-x}S$ could be obtained (Liang *et al.*, 2016, Fu *et al.*, 2015, Wang *et al.*, 2015).

In solvothermal processes involving elemental or metal salt precursors, the reactivity of the metal ion with the sulphur source and/or solvent plays an important role in the pathway, leading to the final stoichiometry of the product in the formation of ternary metal sulphides (Ikeda *et al.*, 2014). The formation of the ternary sulphide could either follow a cation exchange reaction between the initially formed $Cu_{2-x}S$ template and the metal ion in solution or it could follow the solid state reaction between $Cu_{2-x}S$ and metal sulphide formed in the system (Liu *et al.*, 2017). In reactions involving precursor complexes, the effect of the reactivity of the metal salt/ion is nullified as the metal complexes decomposed into $Cu_{2-x}S$ and M-S. Thus, the subsequent solid state reaction is important for the formation of CAS (Fig. 1).

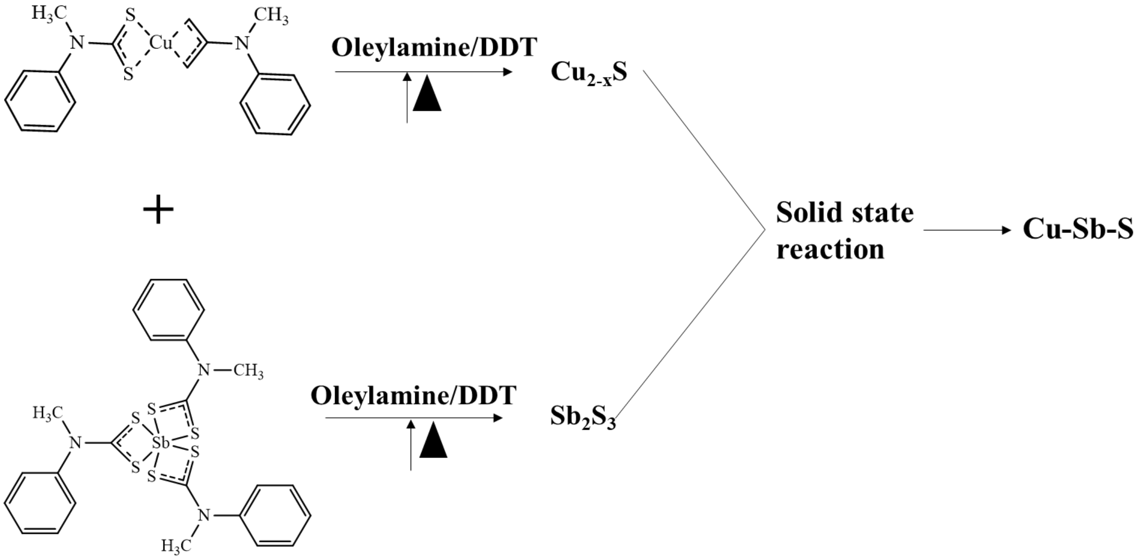

Fig. 1: Schematic representation for the formation of copper antimony suphides from co-thermolysis of [Cu(DTC)$_2$] and [Sb(DTC)$_3$]

3.1 Structural analysis

The phase purity and crystallinity of the three phases of the CAS nanocrystals are shown in Fig. 2. The XRD pattern for $CuSbS_2$ displayed peaks that where indexed to the orthorhombic $CuSbS_2$ (JCPDS No. 44-1417, space group *pbnm* (No. 62), with lattice parameters: a= 6.00 Å, b = 3.78 Å, c = 14.495Å). The diffraction pattern of Cu_3SbS_4, showed all the peaks that could be indexed to the body-centered tetragonal Cu_3SbS_4 (JCPDS No 35-0581, space group 1-42m, lattice parameters: a = b = 5.38 Å, c = 10.76 Å). $Cu_{12}Sb_4S_{13}$ exhibited peaks that were all indexed to the body-centered cubic $Cu_{12}Sb_4S_{13}$ (JCPDs No 00-024-1318 space group 1-43m lattice paramettters: a = b = c = 10.32 Å). The ratio of Cu, Sb and S in the samples were evaluated using the EDX analysis (Fig. S1), which showed that the ratio of Cu:Sb:S for $CuSbS_2$, Cu_3SbS_4 and $Cu_{12}SbS_4S_{13}$ was 0.5:1:0.8, 2.8:1:3.7 and 2.8:1:3.5 respectively. The values obtained for Cu_3SbS_4 and $Cu_{12}Sb_4S_{13}$ were close to theoretical values, while the value of Cu and S atoms in $CuSbS_2$ was under estimated.

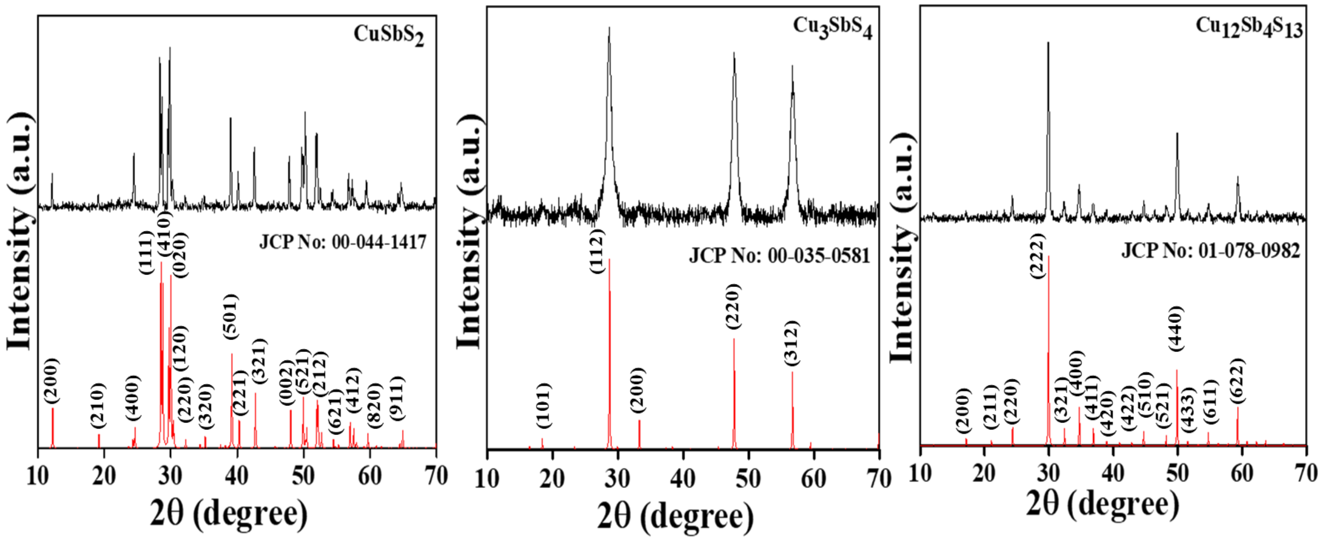

Fig 2: XRD plots of $CuSbS_2$, Cu_3SbS_4 and $Cu_{12}Sb_4S_{13}$ prepared via the thermlysis of copper and bismuth dithiocarbamate complexes

The particle size of the prepared nanoparticles were estimated using the Scherrer equation:

$$D = \frac{K\lambda}{\beta cos\theta} \qquad (1)$$

Where D represents the average particle size, λ is the wavelength of X-ray, θ represents the Bragg angle and β is the line bradening at half the maximum intensity (FWHM) after instrumental braodening was substracted. By employing the FWHM values of the most prominent peaks and using the FWHM of Al_2O_3 for instrumental broadening correction, the average particle size for the $CuSbS_2$, Cu_3SbS_4 and $Cu_{12}Sb_4S_{13}$ phases were estimated as 222.98, 12.0 and 47.8 nm respectively.

The TEM analysis of the nanoparticles showed that the $CuSbS_2$ particles were capsule shaped, while Cu_3SbS_4 and $Cu_{12}SbS_{13}$ were of spherical morphologies with slight agglomeration. From the analysis of the TEM images, the particle size of $CuSbS_2$, Cu_3SbS_4 and $Cu_{12}Sb_4S_{13}$ was 432 ± 52, 12.4 ± 1.7 and 49.5 ± 4.9 nm. While there was good agreement with the crystalline sizes obtained for Cu_3SbS_4 and $Cu_{12}Sb_4S_{13}$ using the Scherrer equation, a significant difference was observed for $CuSbS_2$. This could be attributed to the unsuitability of the Scherrer's equation for anisiotropic nanoparticles and with size larger than 100 nm due to the small size of peak broadening above 100 nm, which has to be separated from strain and instrumental broadening (Londoño-Restrepo *et al.*, 2019).

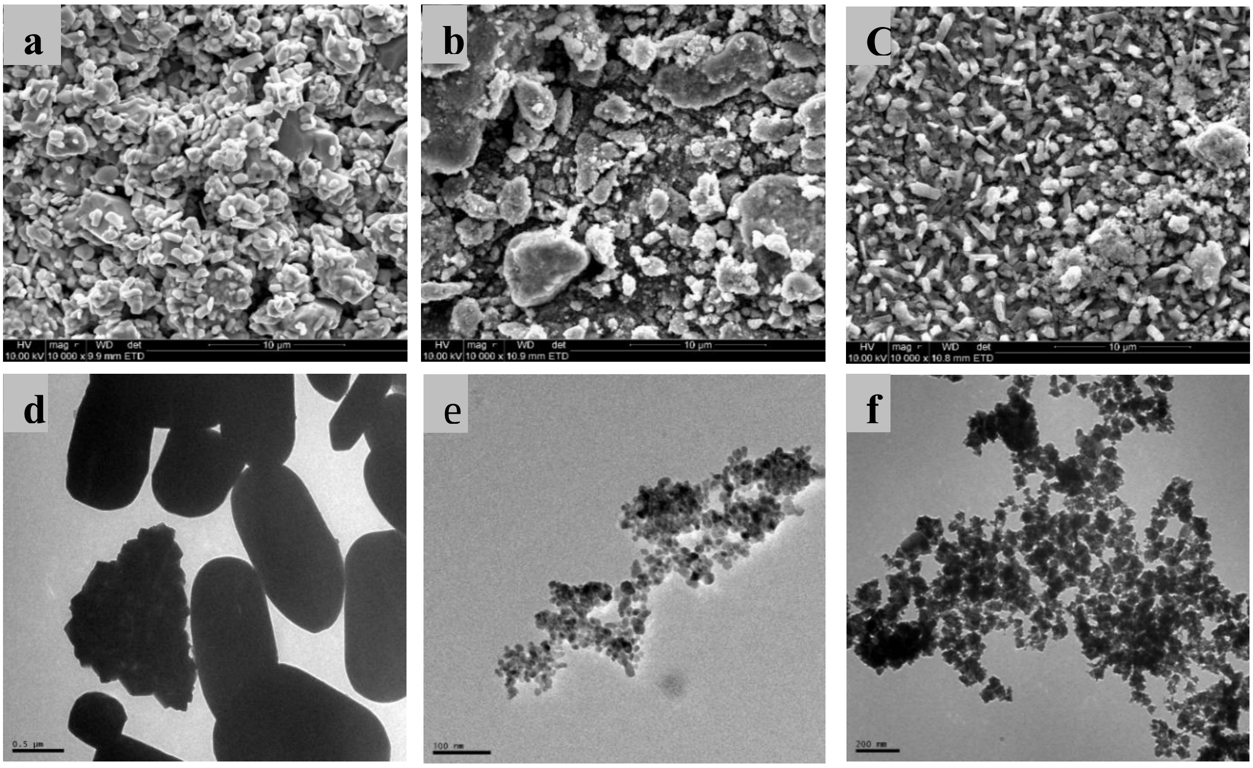

Fig 3: SEM amd TEM images of prepared of $CuSbS_2$ (a & d), Cu_3SbS_4 (b & e), and $Cu_{12}Sb_4S_{13}$ (c & f), prepared via the co-thermal decompostion of copper and antimony dithiocarbamate complexes.

3.2 Optical properties

On the basis of valency of the V-group atoms in CAS, the compounds could be classified as either low valence ($CuSbS_2$ and $Cu_{12}Sb_4S_{13}$) or high valence (Cu_3SbS_4) compounds. The major role played by this difference in oxidation state could be observed in the nature of the electronic state of these compounds. In the high valence compounds the s(V) orbitals of the group V atom contributes largely to the conduction band state than the valence band states, while for the low valence compounds, the p(V) orbitals of the V-group atom contributes more to the conduction band. The contribution of other atoms to the electronic states also hold significant influence on the electronic properties of CAS. While the valence band of the three phases is comprised mainly of Cu-3d and S-3p orbitals, the conduction bands of $CuSbS_2$ is mainly made up of the Sb-p states compared to the Sb-s and S-p states obtained in Cu_3SbS_4 (Di Paola *et al.*, 2020). The absorption properties of the ternary metal sulphides in toluene were measured using a UV-vis- near IR spectroscopy from 200-1200 nm. The compounds all showed broad absorption in both the visible and the NIR region (Fig. 4), with absorption onset at ~400 nm in the visible region. However, while the $CuSbS_2$ showed absorption maximum at ~500 nm, both Cu_3SbS_4 and $Cu_{12}Sb_4S_{13}$ displayed absorption maxima at ~600 nm. The observance of non-zero absorbance in the range of energies studied in the absorption spectrum could either be associated with the presence of localized surface plasmon resonance (LSPR) or the presence of mid-band gap states, with significant oscillator strength (van Embden *et al.*, 2013). The band gap of the samples were calculated using the Tauc plots as shown in Fig 4. The direct band gap energy of the $CuSbS_2$, Cu_3SbS_4 and $Cu_{12}Sb_4S_{13}$ was 1.11, 1.10 and 1.39 eV respectively, which were in aggreement with reported values in previous studies (Pal *et al.*, 2017, Baum *et al.*, 2018, van Embden *et al.*, 2013).

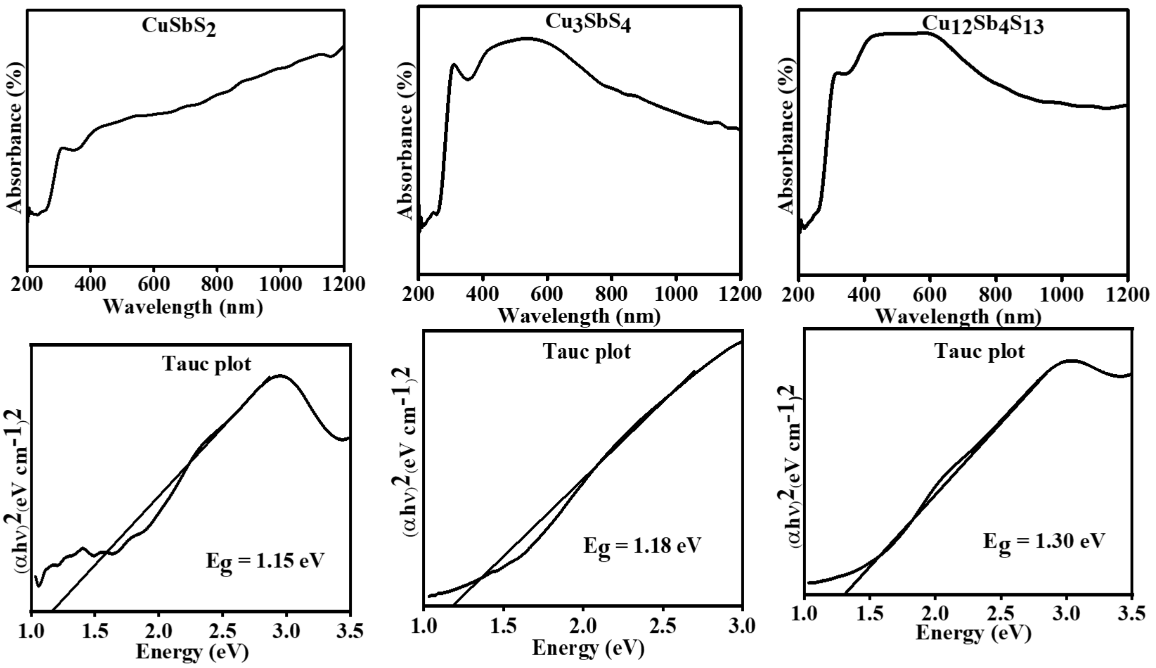

Fig 4: Absorption spectra and respective Tauc plots (directly below) of $CuSbS_2$, Cu_3SbS_4 and $Cu_{12}Sb_4S_{13}$ prepared via the co-thermal decompostion of copper and antimony dithiocarbamate complexes.

The emission spectra of the nanoparticles, studied by exciting the ethanol solution of the samples at 600 nm, are shown in Fig. 5. Emission at this wavelength, which corresponds to energy value of 2.06, could be attributed to band to band transfer, thus confirming the presence of midband gaps in the electronic structure of the compounds as suggested by the absorpion spectrum (Adekoya *et al.*, 2019). The greater increase in the absorbance of the nanoparticles in the infrared region is an indication that the near band edge emission will be observed in the NIR region of the electromagnetic spectrum (Adekoya *et al.*, 2019).

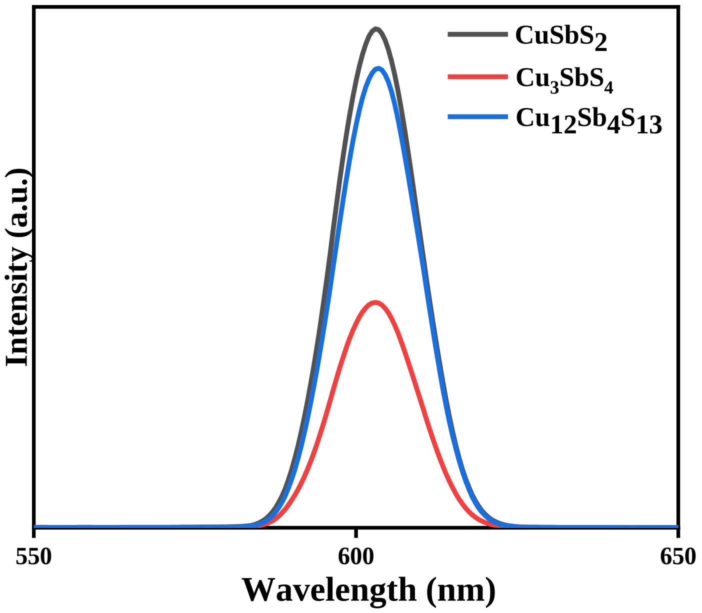

Fig 5: PL Emission spectra of $CuSbS_2$, Cu_3SbS_4 ans $Cu_{12}Sb_4S_{13}$ prepared via the co-thermal decompostion of copper and antimony dithiocarbamate complexes.

3.3 Evaluation of persulphate activation properties of the CAS

The catalytic activity of the three CAS phases was evaluated for the activation of persulphate for tetracycline degradation. Various surface properties such as morphology, surface atom arrangement, multivalence and surface have been correlated to the catalytic activity of heterogenous catalysts (Gao *et al.*, 2019). Fig. 5(a) shows the degradation profile for the degradation process carried out at a pH of 4. The percentage degradation of tetracycline after 120 min was 12% for PS, 26.1% for $CuSbS_2$, 55.6% for Cu_3SbS_4 and 54.6% for $Cu_{12}Sb_4S_{13}$. The reaction rate constant for the process obtained by fitting the degradation data to a psuedo first order kinetics (fig 5b) was evaluated to be 7.1×10^{-4}, 3.0×10^{-4}, 7.5×10^{-3} and 7.2×10^{-3} min^{-1} for PS alone, $CuSbS_2$, Cu_3SbS_4 and $Cu_{12}Sb_4S_{13}$ respectively. The degradation of TCE by the CAS could be observed to take place in two degradation stages: the fast initial stage, which was followed by a the slow second stage (also known as the retardation stage). The first stage could be ascribed to a fast generation of radicals, which was propelled by the initial reaction between CAS and PS. The reaction rate then slows down with the consumption of PS in the system, which leads to a reduction in the generation of radicals in the system. A similar observation was reported for carbamazepine degedration in a Fe(II)-PS activation process (Rao *et al.*, 2014).

Using Cu_3SbS_4 as the catalyst, the PS activation process was further studied under neutral (7) and basic (11) pH as shown in Fig. 5b. The degradation of TCE was observed to be significantly enhanced at neutral pH compared to the acidic and basic conditions. The fast initial degradation stage was observed to be significantly enhanced at neutral pH and this suggests a higher radical generation compared to the reaction at pH of 4 and 11. The percentage degradation of TCE at pH of 4, 7 and 11 was 86.5, 55.4 and 53.0% respectively.

To determine if the degradation process was by the radical or non-radical route, e_{aq}^- and $^{\bullet}OH/SO_4^{\bullet-}$ scavengers were introduced into the degradation system. Nitrate ion was employed as e_{aq}^- scavenger, while TBA was introduced into the system as $^{\bullet}OH/SO_4^{\bullet-}$ scavenger. Fig. 5d shows the influence of introducing these scavengers into the experiment for the degradation of TCE by Cu_3SbS_4 activated PS at pH of 7. The scavenging experiment showed that TCE degradation was by the radical process, with the degradation efficiency being significantly reduced by the introduction TBA. The introduction of nitrate ion, only resulted in a slight reduction in the degradation process. The generation of radicals in the persuphfate activation process is based on the one electron transfer route as shown in Eq.2. The generation of $^{\bullet}OH$ occurs through the reaction of generated sulphate radical with OH^- as shown in Eq. 3 (Xiao *et al.*, 2018, Wang and Wang, 2018).

$$S_2O_8^{2-} + e^- \longrightarrow SO_4^{\bullet -} + SO_4^{2-} \qquad (2)$$

$$SO_4^- + OH^- \longrightarrow SO_4^{2-} + {}^{\bullet}OH \qquad (3)$$

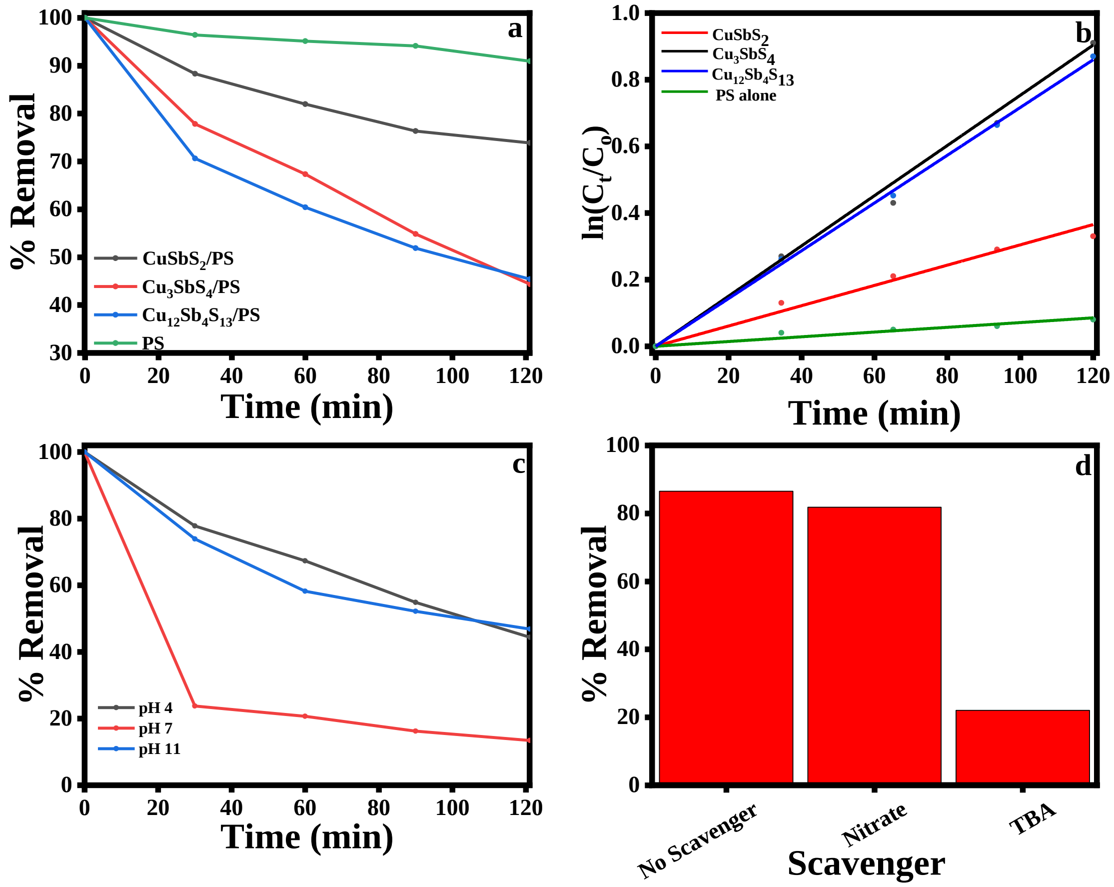

Fig 6: Evaluation of persulphate activation property of CAS (a) degradation profile of tetracycline by persulphate activation using PS alone, $CuSbS_2$, Cu_3SbS_4 and $Cu_{12}Sb_4S_{13}$ (b) kinetic plot of persulphate

activation, (c) Effect of pH on the persulphate activation propertyof Cu_3SbS_4 (d) Evaluation of the effect of radical and non-radical process on the persulfate activation process.

4.0 Conclusion

The selective synthesis of three crystalline phases of copper antimony sulphide have been reported in this study. Through the variation of reaction parameters such as temperature, precursor control and solvent properties, the synthesis of pure phase $CuSbS_2$, Cu_3SbS_4 and $Cu_{12}Sb_4S_{13}$ was achieved. The study of the structural, morphological and optical properties showed phase dependent properties, which can greatly influence the applicability of the obtained nanoparticles. The property of the obtained copper antimony sulphide phases for the activation of persulphate was explored, and the Cu_3SbS_4 phase showed the highest potential in the degradatoin process. Since, the economic and environmental advantages of these compounds implies that they have become well sought after compounds, a facile and environmental friendly synthetic method, employing precursor complexes and enabling the possibility for phase control by the manipulation of the synthesis parameters is a worthwhile study, which advances this research area.

5.0 References

Adekoya, J. A., Khan, M. D. & Revaprasadu, N. 2019. Phase transition in $Cu_{2+x}SnS_{3+y}$ ($0 \leq x \leq 2$; $0 \leq y \leq 1$) ternary systems synthesized from complexes of coumarin derived thiocarbamate motifs: optical and morphological properties. *RSC Advances,* 9**,** 35706-35716.

Albuquerque, G. H., Kim, K.-J., Lopez, J. I., Devaraj, A., Manandhar, S., Liu, Y.-S., Guo, J., Chang, C.-H. & Herman, G. S. 2018. Multimodal characterization of solution-processed Cu_3SbS_4 absorbers for thin film solar cells. *Journal of Materials Chemistry A,* 6**,** 8682-8692.

An, C., Liu, Q., Tang, K., Yang, Q., Chen, X., Liu, J. & Qian, Y. 2003. The influences of surfactant concentration on the quality of chalcostibite nanorods. *J. Cryst. Growth,* 256 128–133.

Baum, F., Pretto, T., Brolo, A. G. & Santos, M. J. L. 2018. Uncovering the Mechanism for the Formation of Copper Thioantimonate (SbV) Nanoparticles and Its Transition to Thioantimonide (SbIII). *Crystal Growth & Design,* 18**,** 6521-6527.

Carey, G. H., Abdelhady, A. L., Ning, Z., Thon, S. M., Bakr, O. M. & Sargent, E. H. 2015. Colloidal Quantum Dot Solar Cells. *Chem Rev.,* 115**,** 12732-12763.

Chen, K., Zhou, J., Chen, W., Chen, Q., Zhou, P. & Liu, Y. 2016. A green synthesis route for the phase and size tunability of copper antimony sulfide nanocrystals with high yield. *Nanoscale,* 8**,** 5146-52.

Colombara, D., Peter, L. M., Rogers, K. D. & Hutchings, K. 2012. Thermochemical and kinetic aspects of the sulfurization of Cu-Sb and Cu-Bi thin films. *J.Solid State Chem.,* 186**,** 36–46.

Di Paola, C., Macheda, F., Laricchia, S., Weber, C. & Bonini, N. 2020. First-principles study of electronic transport and structural properties of $Cu_{12}Sb_4S_{13}$ in its high-temperature phase. *Physical Review Research,* 2.

Ekennia, A. C., Onwudiwe, D. C. & Osowole, A. A. 2015. Spectral, thermal stability and antibacterial studies of copper, nickel and cobalt complexes of N-methyl-N-phenyl dithiocarbamate. *Journal of Sulfur Chemistry,* 36**,** 96-104.

Fu, W., Liu, L., Yang, G., Deng, L., Zou, B., Ruan, W. & Zhong, H. 2015. Oleylamine-Assisted Phase-Selective Synthesis of $Cu_{2-x}S$ Nanocrystals and the Mechanism of Phase Control. *Particle & Particle Systems Characterization,* 32**,** 907-914.

Gao, P., Tian, X., Nie, Y., Yang, C., Zhou, Z. & Wang, Y. 2019. Promoted peroxymonosulfate activation into singlet oxygen over perovskite for ofloxacin degradation by controlling the oxygen defect concentration. *Chemical Engineering Journal,* 359**,** 828-839.

Ikeda, S., Sogawa, S., Tokai, Y., Septina, W., Harada, T. & Matsumura, M. 2014. Selective production of $CuSbS_2$, Cu_3SbS_3, and Cu_3SbS_4 nanoparticles using a hot injection protocol. *RSC Adv.,* 4**,** 40969-40972.

Kwon, S. G. & Hyeon, T. 2011. Formation mechanisms of uniform nanocrystals via hot-injection and heat-up methods. *Small,* 7**,** 2685-2702.

Liang, Q., Huang, K., Ren, X., Zhang, W., Xie, R. & Feng, S. 2016. Synthesis of Cu–Sb–S nanocrystals: insight into the mechanism of composition and crystal phase selection. *CrystEngComm,* 18**,** 3703-3710.

Liu, Y., Liu, M., Yin, D., Wei, W., Prasad, P. N. & Swihart, M. T. 2017. Kuramite Cu_3SnS_4 and Mohite Cu_2SnS_3 Nanoplatelet Synthesis Using Covellite CuS Templates with Sn(II) and Sn(IV) Sources. *Chemistry of Materials,* 29**,** 3555-3562.

Londoño-Restrepo, S. M., Jeronimo-Cruz, R., Millán-Malo, B. M., Rivera-Muñoz, E. M. & Rodriguez-García, M. E. 2019. Effect of the Nano Crystal Size on the X-ray Diffraction Patterns of Biogenic Hydroxyapatite from Human, Bovine, and Porcine Bones. *Scientific reports,* 9**,** 5915-5915.

Macías, C., Lugo, S., Benítez, Á., López, I., Kharissov, B., Vázquez, A. & Pe˜na, Y. 2017. Thin film solar cell based on $CuSbS_2$ absorber prepared by chemical bath deposition (CBD). *Mater. Res. Bull.,* 87 161–166.

Malik, M. A., Revaprasadu, N. & O'Brien, P. 2001. Air-Stable Single-Source Precursors for the Synthesis of Chalcogenide Semiconductor Nanoparticles. *Chemistry of Materials,* 13**,** 913-920.

McCarthy, C. L., Cottingham, P., Abuyen, K., Schueller, E. C., Culver, S. P. & Brutchey, R. L. 2016. Earth abundant $CuSbS_2$ thin films solution processed from thiol–amine mixtures. *Journal of Materials Chemistry C,* 4**,** 6230-6233.

Medina-Montes, M. I., Campos-González, E., Morales-Luna, M., Sánchez, T. G., Becerril-Silva, M., Mayén-Hernández, S. A., de Moure-Flores, F. & Santos-Cruz, J. 2018. Development of phase-pure $CuSbS_2$ thin films by annealing thermally evaporated CuS/Sb_2S_3 stacking layer for solar cell applications. *Materials Science in Semiconductor Processing,* 80**,** 74-84.

Motaung, M. P., Osuntokun, J. & Onwudiwe, D. C. 2019. The heat-up synthesis of monodispersed Bi2S3 and Cu7S4 nanoparticles from novel precursor complexes and their characterizations. *Materials Science in Semiconductor Processing,* 99**,** 92-98.

Onwudiwe, D., Olatunde, O. & Mathur, D. S. 2020. Structural studies and morphological properties of antimony sulphide nanorods obtained by solvothermal synthesis. *Physica B: Condensed Matter,* 605**,** 412691.

Onwudiwe, D. C. 2019. Microwave-assisted synthesis of PbS nanostructures. *Heliyon* 5 e01413.

Pal, M., Torres Luna, Y., Silva González, R., Mathews, N. R., Paraguay-Delgado, F. & Pal, U. 2017. Phase controlled synthesis of $CuSbS_2$ nanostructures: Effect of reaction conditions on phase purity and morphology. *Materials & Design,* 136**,** 165-173.

Ramasamy, K., Sims, H., Butler, W. H. & Gupta, A. 2014. Selective Nanocrystal Synthesis and Calculated Electronic Structure of All Four Phases of Copper–Antimony–Sulfide. *Chemistry of Materials,* 26**,** 2891-2899.

Rao, Y. F., Qu, L., Yang, H. & Chu, W. 2014. Degradation of carbamazepine by Fe(II)-activated persulfate process. *J Hazard Mater,* 268**,** 23-32.

Rath, T., MacLachlan, A. J., Brown, M. D. & Haque, S. A. 2015. Structural, optical and charge generation properties of chalcostibite and tetrahedrite copper antimony sulfide thin films prepared from metal xanthates. *J Mater Chem A Mater,* 3**,** 24155-24162.

Scheer, R., Guillemoles, J. F., Tiwari, A. N., Niki, S., Ferekides, C. S., Abou-Ras, D., Katagiri, H., Jimbo, K., Maw, W. S., Oishi, K., Yamazaki, M., Araki, H. & Takeuchi, A. 2009. Thin Film Chalcogenide Photovoltaic Materials (EMRS, Sumposium L). *Thin Solid Films,* 517**,** 2455−2460.

Septina, W., Ikeda, S., Iga, Y., Harada, T. & Matsumura, M. 2014. Thin film solar cell based on $CuSbS_2$ absorber fabricated from an electrochemically deposited metal stack. *Thin Solid Films,* 550**,** 700-704.

van Embden, J., Chesman, A. S. R. & Jasieniak, J. J. 2015. The Heat-Up Synthesis of Colloidal Nanocrystals. *Chemistry of Materials,* 27**,** 2246-2285.

van Embden, J., Latham, K., Duffy, N. W. & Tachibana, Y. 2013. Near-infrared absorbing $Cu_{12}Sb_4S_{13}$ and Cu_3SbS_4 nanocrystals: synthesis, characterization, and photoelectrochemistry. *J Am Chem Soc,* 135**,** 11562-71.

van Embden, J. & Tachibana, Y. 2012. Synthesis and characterisation of famatinite copper antimony sulfide nanocrystals. *Journal of Materials Chemistry,* 22.

Wang, J. & Wang, S. 2018. Activation of persulfate (PS) and peroxymonosulfate (PMS) and application for the degradation of emerging contaminants. *Chemical Engineering Journal,* 334**,** 1502-1517.

Wang, Y., Liu, F., Ji, Y., Yang, M., Liu, W., Wang, W., Sun, Q., Zhang, Z., Zhao, X. & Liu, X. 2015. Controllable synthesis of various kinds of copper sulfides (CuS, Cu_7S_4, Cu_9S_5) for high-performance supercapacitors. *Dalton Trans,* 44**,** 10431-7.

Welch, A. W., Zawadzki, P. P., Lany, S., Wolden, C. A. & Zakutayev, A. 2014. Self-regulated growth and tunable properties of $CuSbS_2$ solar absorbers. *Sol. Energy Mater. Sol. Cells,* 132 499–506.

Xiao, R., Luo, Z., Wei, Z., Luo, S., Spinney, R., Yang, W. & Dionysiou, D. D. 2018. Activation of peroxymonosulfate/persulfate by nanomaterials for sulfate radical-based advanced oxidation technologies. *Current opinion in chemical engineering,* 19**,** 51-58.

Xu, D., Shen, S., Zhang, Y., Gu, H. & Wang, Q. 2013. Selective synthesis of ternary copper-antimony sulfide nanocrystals. *Inorg Chem,* 52**,** 12958-62.

Yang, B., Wang, L., Han, J., Zhou, Y., Song, H., Chen, S., Zhong, J., Lv, L., Niu, D. & Tang, J. 2014. $CuSbS_2$ as a Promising Earth-Abundant Photovoltaic Absorber Material: A Combined Theoretical and Experimental Study. *Chemistry of Materials,* 26**,** 3135-3143.

Zou, Y. & Jiang, J. 2014. Colloidal synthesis of chalcostibite copper antimony sulfide nanocrystals. *Materials Letters,* 123**,** 66-69.

CHAPTER TEN

Evaluation of the photocatalytic and persulfate activation properties of GO-$CuSbS_2$ composite

1.0 Introduction

Recent studies have shown that ternary metal sulphides are very promising potential alternatives to noble-metals and toxic metal sulphides for various catalytic processes, especially in environmental remediation. This is because of their excellent redox reversibility, electronic properties and low cost (Kulkarni *et al.*, 2017). They also possess attractive structural advantages and the presence of multiple valence cations offer donor-acceptor chemisorption sites, which are important in catalytic processes (Fu and Lee, 2019). Among the ternary metal sulphides, copper-containing sulphides have gained much attention because of their natural abundance, low cost and very good stability (Xu *et al.*, 2020). They also possess excellent functional properties such as small bandgaps, plasmonic properties, low thermal conductivity and high carrier concentrations (Olatunde and Onwudiwe, 2020).

Copper ternary sulphides obtained from main-group metals such as indium (In), tin (Sn), bismuth (Bi) and antimony (Sb) have been widely explored for application in energy storage devices, solar cell absorbers and bioimaging (Ning *et al.*, 2019, Morselli *et al.*, 2021, Ramasamy *et al.*, 2015, Chakraborty *et al.*, 2019, Berg *et al.*, 2012). A wide variety of stoichiometric and non-stoichiometric phases of these ternary copper sulphides can be assessed because of the variable oxidation states of Cu and the main group metals. Also, the possibility of different coordination environment of Cu and the main group elements, in addition to the lower enthalpy of formation of defect pairs in their lattice structures allow for the formation of various stoichiometric phases. Among this large group of compounds, the indium and tin class has been the most explored, with little focus on the Sb and Bi group (Olatunde and Onwudiwe, 2021).

Copper antimony sulphides (CAS) comprise of a group of p-type semiconductor compounds, with absorption coefficients higher than 10^5 cm^{-1} and a band gap in the range of 1.1-1.8 eV (Olatunde and Onwudiwe, 2021). The available four crystalline phases, which are also well studied include: $CuSbS_2$, Cu_3SbS_4, Cu_3SbS_3 and $Cu_{12}Sb_3S_{23}$. Among these phases, $CuSbS_2$ crystallizes in an orthorhombic layered structure, which accounts for its high structural stability, good interfacial property and enhanced characteristic charge transport phenomenon (Krishnan *et al.*, 2015). Despite the optimal optical properties of this compound, reports have shown that it often displays low efficiency when explored as solar absorbers in solar cells, which has been attributed to the low lifetime and mobility of charge carriers. This process limits the diffusion length and photo-generated charge carrier separation (Zhang *et al.*, 2019). Several techniques have, thus, been explored to improve the photovoltaic efficiency of $CuSbS_2$ such as post-annealing treatment (Zhang *et al.*, 2019), chemical etching (Wang *et al.*, 2020b) and thermochemical treatment (de Souza Lucas *et al.*, 2016).

So far, compositing of $CuSbS_2$ with suitable support materials with the potential of improving its optical efficiency has not been well explored. Graphene and its derivatives have been studied in recent years as support materials for semiconductor materials because of their excellent electronic properties and their layered structure, which enhances their ability to improve charge mobility and increase charge separation in semiconductors (Carminati *et al.*, 2021, Singh *et al.*, 2020). These properties have inspired studies involving the application of graphene-based composites in photovoltaic cells, solar absorbers and energy storage batteries (Hu *et al.*, 2021, Mondal *et al.*, 2021, Wang *et al.*, 2020a, Dhinakaran *et al.*, 2021, Iqbal *et al.*, 2021, Solomon *et al.*, 2020). Compositing of nanoparticles with graphene/graphene derivatives can be achieved either via *in-situ* or *ex-situ* processes (Mohan *et al.*, 2018, Huang *et al.*, 2012). The *ex-situ* process affords a facile and easy to control process to the synthesis of graphene-based composites. It involves the mixing of graphene/graphene derivatives with pre-synthesized nanocrystals and, thus, allows for the pre-synthesis of nanocrystals with desired properties (Huang *et al.*, 2012). The nanocrystals are held on the surface of graphene or its derivative via different interactions such as van der Waals forces, coordination bonding, hydrogen bonding, π-π and electrostatic interactions (Jilani *et al.*, 2018).

Currently, there are only a few studies on the photocatalytic application of $CuSbS_2$ for the degradation of organic molecules. Therefore, in this current study, a facile *ex-situ* process was used to synthesize graphene oxide supported $CuSbS_2$ nanoparticles obtained through the co-thermolysis of dithiocarbamate complexes as precursors. The obtained composites were then explored for their photocatalytic and catalytic activation of persulfate in the degradation of tetracycline.

2.0 Experimental

2.1 Materials

Cu (II) nitrate pentahydrate, N-methyl aniline, carbon disulphide, antimony chloride, oleylamine (OLA), dodecanethiol (DDT), ammonium hydroxide solution, methanol, and toluene used for this study were all of analytical grade and used as supplied by Sigma-Aldrich. For structural characterization, Phillips X'pert diffractometer with a secondary graphite monochromated Cu K α radiation (I = 1.546060 Å) at 40 kV/50 mA was employed for XRD analysis. The optical properties of the nanoparticles were studied using PerkinElmer λ20 UV-vis-NIR spectrophotometer for absorption measurement and PerkinElmer LS 45 fluorimeter for the emission spectra. Scanning electron microscopy (SEM) and transmission electron microscopy (TEM) measurements were carried out on LYRA 3, TESCAN and JEM—2100 JEOL equipment respectively.

2.2 Synthesis of ammonia salt of *N*-methyl *N*-phenyl dithiocarbamate ligand

Ammonium *N*-methyl-*N*-phenyl dithiocarbamate was prepared using a previously reported method (Onwudiwe and Ajibade, 2010) . In a typical synthesis, stoichiometric amount of N-methyl aniline and ammonium hydroxide were mixed together at about ~4℃ in a round bottom flask placed in ice. After stirring for 10 min, stoichiometric amount of CS_2 was added to the reaction mixture and stirred. After about 30 min, faint yellow precipitate began to form and the solution was further stirred for 4 h and afterwards recovered by suction aided filtration. The product obtained was washed thrice with ice-cooled ethanol to afford pure ammonium *N*-methyl-*N*-phenyl dithiocarbamate ligand.

2.3 Synthesis of copper(II) bis(*N*-methyl-*N*-phenyl dithiocarbamate) and antimony(III) tris(*N*-methyl-*N*-phenyl dithiocarbamate) complexes

Copper(II) bis(*N*-methyl-*N*-phenyl dithiocarbamate) complex was prepared using aqueous solutions of the ligand and $CuSO_4$. The ligand was reacted with the metal salt in a 2:1 molar ratio, forming a dark brown precipitate which were allowed to stir for 1 h. Afterwards, the precipitates obtained were filtered and washed with water and methanol to remove unreacted materials. Synthesis of antimony(III) tris(*N*-methyl-*N*-phenyl dithiocarbamate) complex followed similar procedure but with a 3:1 molar ratio of ligand to metal salt.

2.4 Synthesis of $CuSbS_2$ nanoparticles

The method involving co-thermolysis of metal complexes was used for the preparation of $CuSbS_2$ nanoparticles. Stoichiometric amounts of the metal complexes were introduced into a three-necked round bottom flask, and 10 mL of oleylamine was added and stirred to form a slurry. The round bottom flask was connected to a condenser and mounted on a heating mantle, under N_2 environment. The slurry was then heated to 280 ºC at a heating rate of 10 ºC/min and then maintained at this temperature for 1 h. The setup was allowed to cool to room temperature, after which ethanol was added to precipitate the $CuSbS_2$ nanoparticles formed. The product was washed thrice with a mixture of ethanol and toluene (3:1 v/v). Powdered nanoparticles were obtained by drying the product under vacuum overnight.

2.5 Synthesis of graphene oxide

The Tour's method described by Marcano *et al.* (2010) was employed for the synthesis of graphene oxide (GO). $KMnO_4$ and graphite flakes (6:1 w/w) were mixed together in a 1000 mL beaker. A concentrated acid mixture containing 340 mL of concentrated H_2SO_4 and 60 mL of H_3PO_4 was prepared in another 1000 mL conical flask. The concentrated acid mixture was then slowly added into the graphite flakes/$KMnO_4$

mixture and was left to stir for 12 h at 50 ºC to form a thickened paste. The paste was allowed to cool to room temperature, and subsequently diluted by transferring it into another 1000 mL beaker containing 400 mL ice. The reaction was terminated by adding hydrogen peroxide (30%) until the solution turned bright yellow. The GO was recovered from the product mix by centrifuging at 5000 rpm and washed thrice with HCl, ethanol and water. The obtained GO was further washed until the pH of the wash solution turned 7. It was then dried at 50 ºC overnight to obtain the dark sheet-like material, which was powdered for further use.

2.6 Synthesis of GO-CAS composite

GO-CAS was synthesized by the two-phase method described by Gao *et al.* (2013). In a typical synthesis, 50 mg of GO was introduced into 50 mL of distilled water and sonicated to obtain even dispersion. Similarly, appropriate weight of CAS was dispersed into 20 mL of toluene. The GO dispersion was transferred into the CAS solution and the mixture was left to stir for 24 h. The GO-CAS composite obtained was washed thoroughly with ethanol and water by centrifugation and dried overnight under vacuum. The weight percentage of CAS in the composite was varied from 5-20% and were labelled as GO-CAS (5%), GO-CAS (10%), GO-CAS (15%), GO-CAS (20%) based on the quantity of CAS.

2.7 Catalytic activity studies of $CuSbS_2$

Catalytic activity was evaluated for TCE degradation in a photocatalytic and persulfate (PS) activation process. In the photocatalytic process, 10 mg of GO-$CuSbS_2$ was weighed into a 100 mL beaker containing 50 mL of 10 mg/L TCE. The mixture was stirred in the dark for 30 min to achieve adsorption-desorption equilibrium. Afterwards, a 28 W UV-LED was turned on and aliquots from the solution were taken at intervals. For the PS activation process, after the adsorption-desorption equilibrium process, PS was added into the reaction system and aliquots taken at intervals. The concentration of TCE was measured at wavelength of 364 nm on a ONDA spectrophotometer. The percentage removal of TCE was obtained using Eq. 1,

$$\%\, removal = \frac{C_o - C_f}{C_o} \times 100\%, \qquad (1)$$

where C_o and C_f are the initial and final concentrations of TCE respectively. The reaction rate for the degradation processes was evaluated by fitting the degradation data into a pseudo first order kinetic linear plot according to Eq. 2.

$$-ln\frac{C_f}{C_o} = Kt, \qquad (2)$$

where C_f and C_o are the final and initial concentration of TCE, K is the reaction rate constant and t is the reaction time.

Radical scavenging experiments were carried out to elucidate the mechanism of degradation for the two processes. Ascorbic acid (ASC), tert-butanol, triethanol amine (TEA) and sodium nitrate were introduced into the reaction solution as super oxide, hydroxyl radical, hole and electron scavengers. The influence of each scavenger on the degradation process was evaluated against the process without scavengers.

3.0 Results and discussion

3.1 Characterization of CAS and GO-CAS composites

To confirm the incorporation of GO and CAS in the composites, XRD and FTIR spectra of CAS and the composites were recorded. The XRD spectra of GO, CAS and GO-CAS composites at different CAS weight percentage of 5, 10, 15 and 20% are shown in Fig. 1. The CAS showed peaks that could all be indexed to orthorhombic $CuSbS_2$, space group pbnm and lattice parameters: a= 6.00 Å, b = 3.78 Å, c = 14.495Å (JCPDS No. 44-1417) (Dekhil *et al.*, 2019). The XRD spectra of GO, showed the characteristic peak due to the planer layer of GO at 2θ value of 10.1° arising from the (001) reflection of graphene oxide. The XRD pattern of the composites all showed peaks that were consistent with the CAS diffraction. However, while the peak due to GO, was visible in composites with 5, 10, and 15% of CAS, the GO peak was completely absent in the pattern for the composite with 20% CAS composition. This could be attributed to the destruction of the regular stacking of GO by the intercalation of CAS at higher percentage level of CAS (Gao *et al.*, 2016). This also correlates with the gradual reduction in the GO peak with increase in the percentage composition of CAS (Zhong and Yun, 2015).

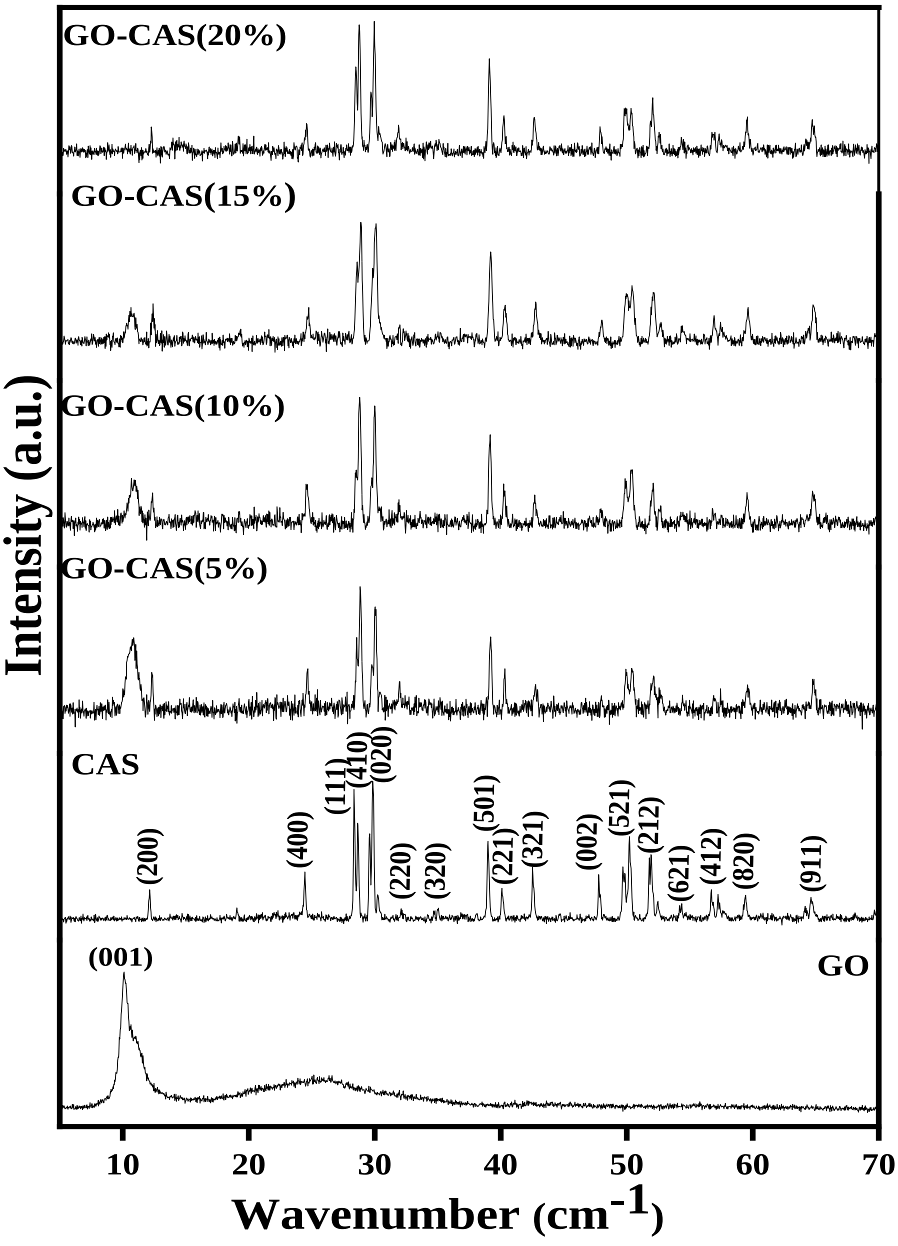

Fig 1: XRD plots of GO, CAS, GO-CAS(5%), GO-CAS(10%), GO-CAS(15%) and GO-CAS(20%) prepared via the thermlysis of copper and antimony dithiocarbamate complexes

The FTIR spectra of GO, CAS, GO-CAS(5%), GO-CAS(10%), GO-CAS(15%) and GO-CAS(20%) are shown in Fig. 2. The spectrum of GO shows the characteristic bands of GO. The bands at 3248 and 1373 cm^{-1} are from the stretching and in-plane bending vibration of the O-H group of GO (Ahmad *et al.*, 2021). The stretching vibrations of the oxygen functional moieties: C=O, C-OH and C-O-C were observed at 1726, 1220 and 1050 cm^{-1} respectively (Xu *et al.*, 2015, Zhu *et al.*, 2010). The spectrum for $CuSbS_2$ showed a broad peak at 1642 cm^{-1} which is due to the vibrational frequency of C=C bond in oleylamine (Shukla *et al.*, 2003), while the peak at 1099 cm^{-1} arises from the stretching vibrations of the C-N bond of olaylamine (Digraskar *et al.*, 2019). The spectra of all the composites showed peaks that were consistent with both GO and $CuSbS_2$. The disappearance of the peak at 1721 cm^{-1} in the composites suggests that the point of interaction between the $CuSbS_2$ and GO was at the C-OH bond.

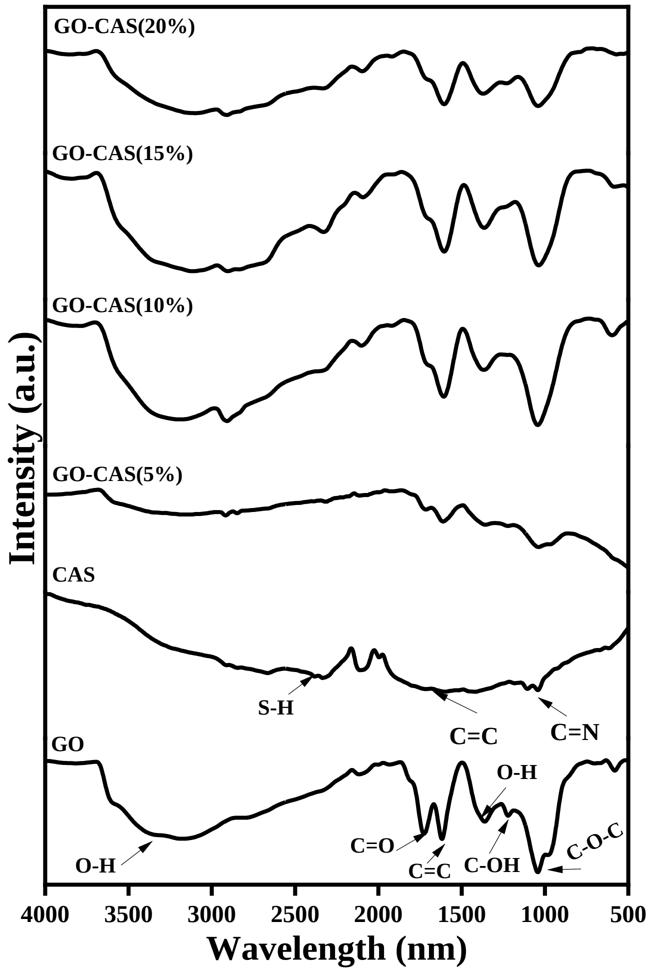

Fig 2: FTIR spectra of GO, CAS, GO-CAS 5%, GO-CAS 10%. GO-CAS 15%, and GO-CAS 20%

3.2 Photoluminescence quenching experiment

To screen the composite GO-CAS at different ratios for the catalytic experiments, the photoluminescence quenching experiment was employed. Fluorescence quenching describes any process that results in a decrease in fluorescence intensity. The process results from a variety of molecular interactions, including molecular rearrangement, collisional quenching, ground-state complex formation, and excited-state reactions (Lakowicz, 2006). PL spectra can reveal some important information such as photo-induced charge carrier separation and recombination processes, surface defects and oxygen vacancies and surface states of a catalytic material (Liqiang *et al.*, 2006). Although, majority of reports have correlated enhanced photocatalytic activity with reduction in intensity of PL signal, few recent reports have however emerged that show that other factors could enhance charge carrier separation with enhanced PL signals. Graphene oxide and other carbon-based materials such as quantum dots have recently gained attention because of their exciting PL quenching ability, which occurs via either electron transfer or foster resonance energy transfer (FRET) (Hamzah *et al.*, 2017, Mei *et al.*, 2019). The compositing of GO with CAS, was observed to induce a reduction in the PL signal of GO, with pristine CAS having the highest PL signal as shown in Fig.3. Thus, the composite with the lowest PL signal, would indicate the composite with the highest charge carrier separation efficiency. On this basis, GO-CAS (10%) was selected for the photocatalytic and persulfate activation process for the degradation of tetracycline.

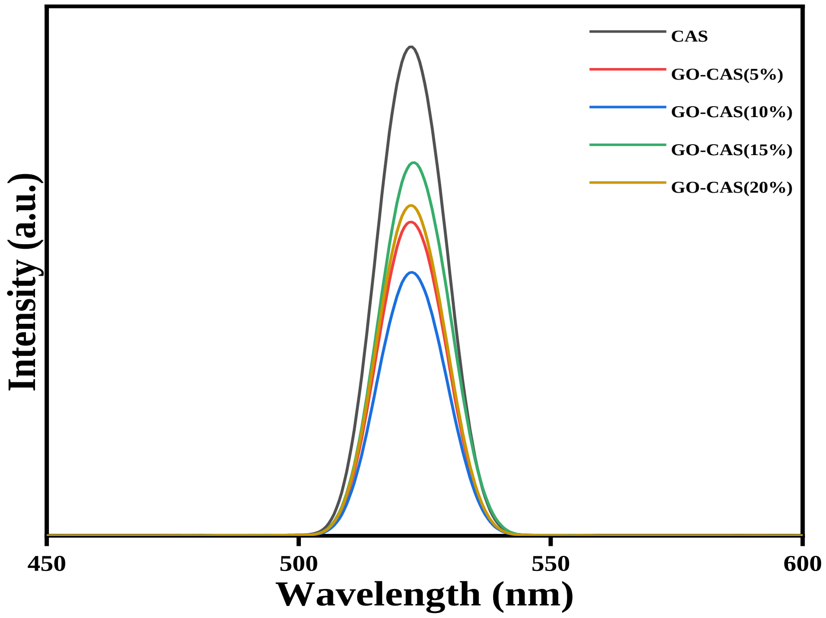

Fig 3: PL quenching effect of GO on the PL spectra of CAS

3.3 Morphological properties of CAS and GO-CAS composites

The SEM, TEM, EDS and size distribution histogram of CAS and composites are shown in Fig. 4. The SEM image showed that CAS nanoparticles were irregularly shaped elongated particles that tend toward rods, and were highly agglomerated. The particle size estimation from the TEM images showed that the average particle size of CAS was 393 ± 98 nm. The size distribution plots also showed a wide particle size distribution, which is due to the particle aggregation. The SEM and TEM images of the composite showed the uniform distribution of CAS on the GO surface. Also, the SEM images showed that the layered structure of GO could still be observed, which corroborates the presence of the GO peak in GO-CAS(10%).

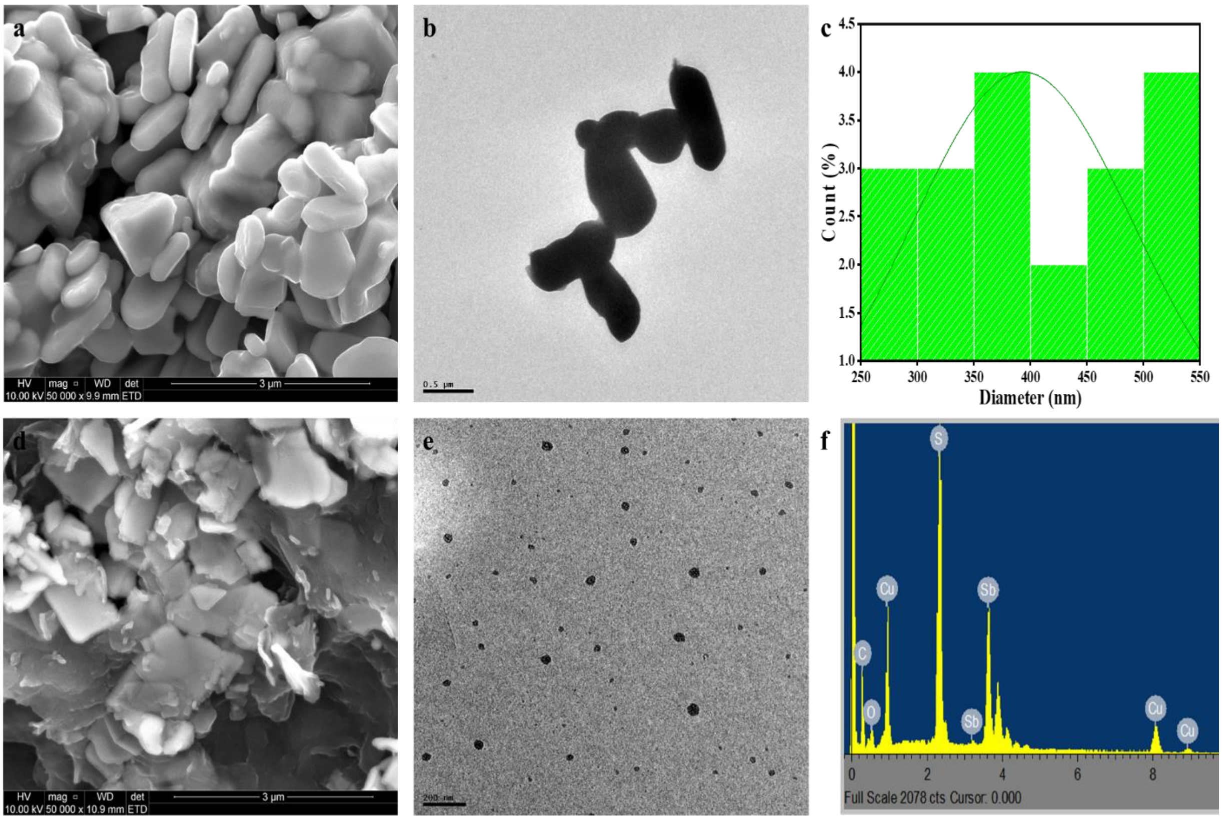

Fig 4: (a-c) SEM, TEM images and particle size distribution histogram for CAS and (d-f) SEM, TEM images and EDS spectra of rGO-CAS(10%)

3.4 Evaluation of catalytic activity of GO-CAS (10%)

The catalytic activity of GO-CAS (10%) was evaluated for its photocatalytic and persulfate activation activity for the degradation of TCE. Fig 5 shows the plot of percentage removal of TCE with time and the kinetic plot for the photocatalytic and persulfate activation processes.

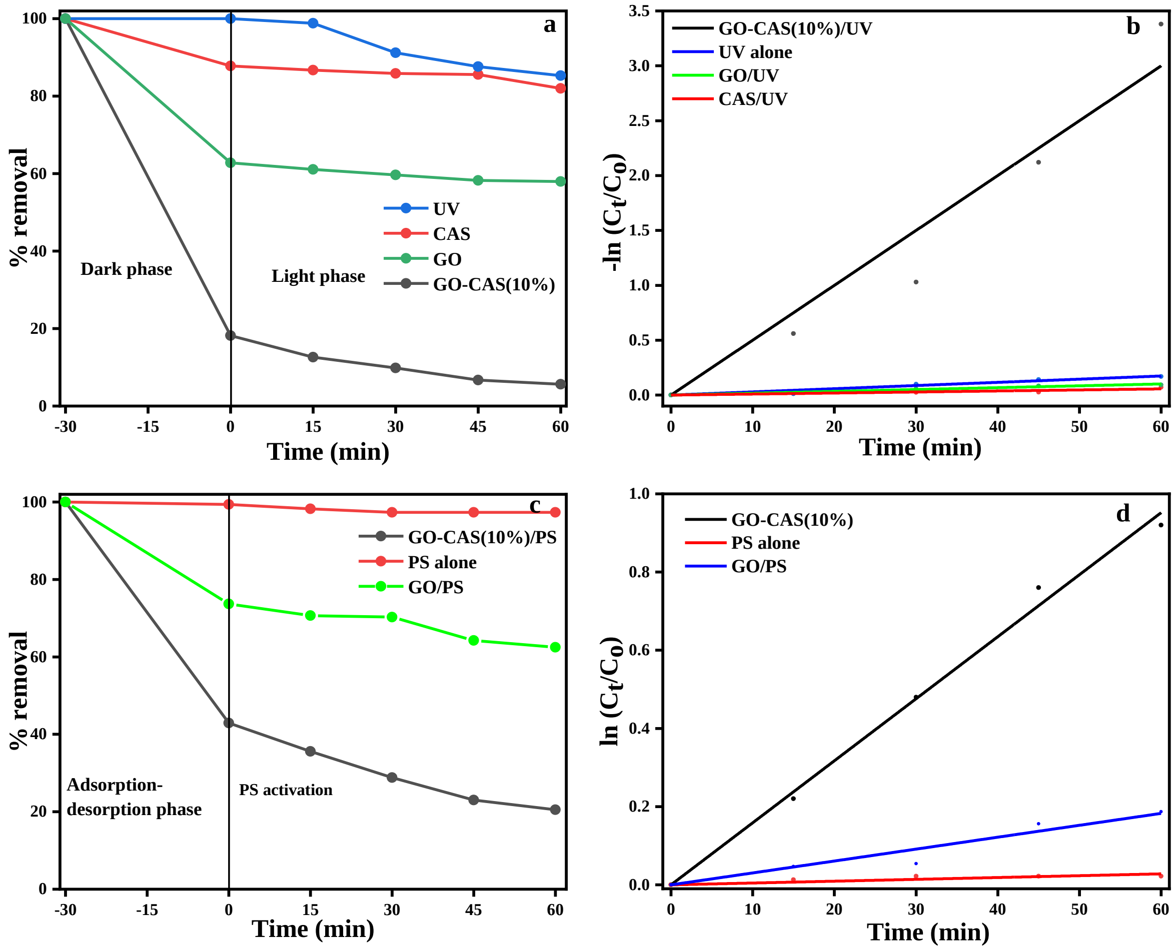

Fig 5: (a & b) TCE removal profile and pseudo first order kinetic plot for photocatalytic process, and (c & d) TCE removal profile and pseudo first order kinetic plot for the persulfate activation process.

The percentage degradation of TCE in the photocatalytic process reached 94% after 60 min, compared to CAS and GO alone which achieved 18.0 and 42.0% removal respectively. The removal activity of GO alone could be attributed solely to the adsorption of TCE as no significant reduction in the concentration of TCE was observed after the adsorption-desorption equilibrium process. Under direct photocatalysis, the degradation of TCE only attained 14.7%. The enhanced removal efficiency of GO-CAS (10%) can be attributed to the improved adsorption capacity that resulted from the compositing of GO and CAS. For the persulfate activation process, the removal efficiency of TCE reached 74% after 60 min. This shows the great capacity of GO-CAS (10%) to enhance the generation of reactive radicals by persulfate activation. The persulfate activation of GO-CAS, was compared to the activity of GO and CAS alone and a great synergy could be observed in the activity of GO-CAS, while PS showed no significant activity towards TCE degradation.

The rate constant for the processes was evaluated by fitting the degradation data into the pseudo-first order kinetic equation. Fig 5c & d show the plot of $-\ln(C_t/C_o)$ against time for the photocatalytic and PS activation processes. The rate constant for UV, CAS, GO and GO-CAS was 2.9×10^{-3}, 9.3×10^{-4}, 1.7×10^{-3} and 5.0×10^{-2} min^{-1} respectively. Thus, the degradation rate of GO-CAS was approximately 17, 53 and 29 times higher than in UV, CAS and GO processes respectively. For the PS activation process, the rate constant for GO-CAS, PS was 1.6×10^{-2} and 4.6×10^{-4} min^{-1} respectively. This showed that GO-CAS acted as a better photocatalyst than PS activator, with a reaction rate of the photocatalytic process approximately 3 times compared to the PS activation process.

The synergistic effect of the incorporation of GO and CAS for the photocatalytic and PS activation processes was evaluated using the R factor calculation according to Eq. 1 and 2 (Moradi *et al.*, 2020). The efficiency of the GO-CAS/UV process was compared with the GO/UV and CAS/UV processes for the photocatalytic process and the efficiency of the GO-CAS/PS process with the GO/PS and CAS/PS processes.

$$R\ factor = \frac{TCE\ removal\ in\ GO{-}CAS\ (10\%)/UV\ system}{Total\ TCE\ removal\ in\ GO/UV\ and\ \ CAS/UV\ systems} \tag{1}$$

$$R\ factor = \frac{TCE\ removal\ in\ GO{-}CAS\ (10\%)/PS\ system}{Total\ TCE\ removal\ in\ GO/PS{,}and\ \ CAS/PS\ systems} \tag{2}$$

The nature of the interaction between two processes can be of three types based on the value of R. For hybrid processes in which R =1, then the interaction between the processes is said to be additive, since the sum of individual effects and the integrated effects are equal. For processes in which R < 1, an antagonist interaction exists between the processes, because the sum of individual processes is higher than the integrated effect. If R > 1, then a synergistic interaction exists between the processes, the integrated effect is higher than the sum of the individual effects. The R factor for the photocatalytic and PS activation process was 1.57 and 1.23 confirming the synergy between GO and CAS in the degradation process.

3.5 Mechanism of photocatalytic degradation process

For the degradation of inorganic pollutants, the effective adsorption of the pollutant molecules and the generation of reactive radicals are two important factors that influence process efficiency. To understand the degradation mechanism, the nature of reactive radicals generated is the sole determining factor. Since, the photoluminescence quenching experiment was employed in screening the composite with most effective charge carrier separation efficiency, the properties of the electronic band energy states, which can be obtained from the energy band gap of the composites can give an insight into the mechanism of the degradation process.

The absorption spectra and Tauc plots of CAS and GO-CAS (Fig. 6), showed that there was a significant difference between the absorption features of CAS and the composite. The spectrum of CAS showed three absorption features with onset at 304, 367 and 830 nm. The absorption peak at 830 nm (1.5 eV) could be attributed to the band edge absorption, while the bands at 304 nm and 367 nm could be attributed to intra-band transition (van Embden *et al.*, 2013). The absorption spectra of CAS increased significantly in the visible region, which indicates that the band gap of the material lies in the visible region. Three absorption features were also observed in the GO-CAS absorption spectra. A very sharp band, which could be attributed to band states from GO was observed at 295 nm. A blue shift in the band at 367 nm in CAS to 373 nm was observed in GO-CAS(10%), while the band at 830 nm was red-shifted to 800 nm. An increase in the intensity of absorption was also observed in the visible region for GO-CAS. The band gap energy for CAS and GO-CAS was evaluated using the Tauc plot and the values were 1.49 and 1.37 eV respectively (Kumar and Persson, 2013, Wada and Maeda, 2017). This showed a red shift in the band gap energy of GO-CAS compared to CAS. The reduction in band gap energy in GO-CAS is important for the enhanced generation of charge carrier, which is important for the generation of reactive radical species necessary for degradation of organic pollutants in photocatalysis.

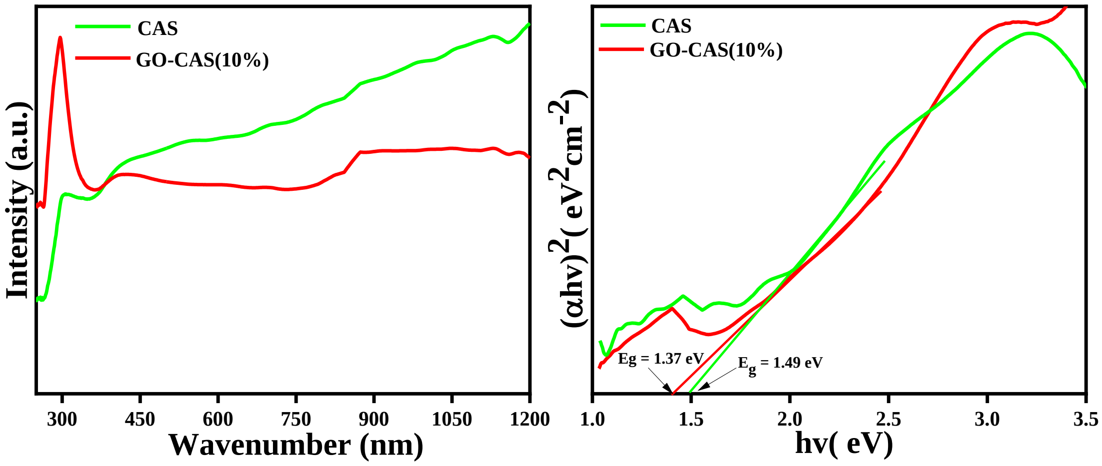

Fig 6: (a) Absorption spectra and (b) Tauc plots of GO-CAS(10%)

From the energy band gaps of the catalytic materials, the nature of generated charge carriers can be evaluated by evaluating the conduction band (E_{CB}) and valence band (E_{VB}) edge potentials of CAS and GO-CAS. The values of E_{CB} and E_{VB} were evaluated using eq. 3 and 4.

$$E_{CB} = \mathrm{X} - E_e - 0.5E_g, \tag{3}$$

$$E_{VB} = E_{CB} + E_g, \tag{4}$$

where X is the absolute electronegativity obtained from the geometric mean of the absolute electronegativity of the constituent elements of the semiconductor, E_g is the band gap energy and E_e is the energy of free electrons on the hydrogen scale (4.5 eV). The values of E_{CB} and E_{VB} for CAS was 0.14 eV and 1.63 eV respectively, while for GO-CAS, the E_{CB} and E_{VB} values were 0.20 and 1.57 eV. The value of E_{CB} and E_{VB} for CAS and GO-CAS were lower compared to 0.85 and 2.45 eV reported for CAS from first principle calculations (Whittles *et al.*, 2017). This showed that the incorporation of CAS into GO resulted in the conduction band being less negatively charged, while the valence band was less positively charged.

The radical scavenging experiment was carried out to determine the influence of radical species on the degradation process (fig. 7). The degradation efficiency of tetracycline in the GO-CAS(10%) was mostly inhibited by the addition of TEA into the process, with about 35% reduction in the degradation process. This suggested that the photogenerated hole was the most significant specie in the degradation process. Addition of TBA, ASC and NO_3^- resulted in 15, 15 and 11% reduction in the degradation efficiency respectively. In the GO-CAS/PS process, introduction of ASC and TBA into the reaction system had no significant influence on the degradation process. The addition of TEA into the reaction system resulted in a 22% reduction in the degradation efficiency of the process. This shows the little contribution of a radical species to the degradation process. The non-radical route to PS activation has been recently confirmed to be predominant in carbon-based catalysts for PS activation (Liu *et al.*, 2020, Nie *et al.*, 2020, Oyekunle *et al.*, 2021, Ren *et al.*, 2019, Tang *et al.*, 2018, Zhu *et al.*, 2020). To affirm the importance of electron transfer to the degradation process, nitrate ion NO_3^- was introduced into the system as an electron acceptor (Pelaez *et al.*, 2016) and a reduction in the degradation efficiency from 74.4 to 57.6% was observed. This confirmed that both radical and non-radical processes contributed to the degradation process, with the non-radical process being the dominant one. This is further affirmed by the increase in the degradation efficiency recorded in the addition of ASC into the process, since ASC could serve as the scavenger for oxygenated species in the system, which could have competed for the photogenerated electrons in the system.

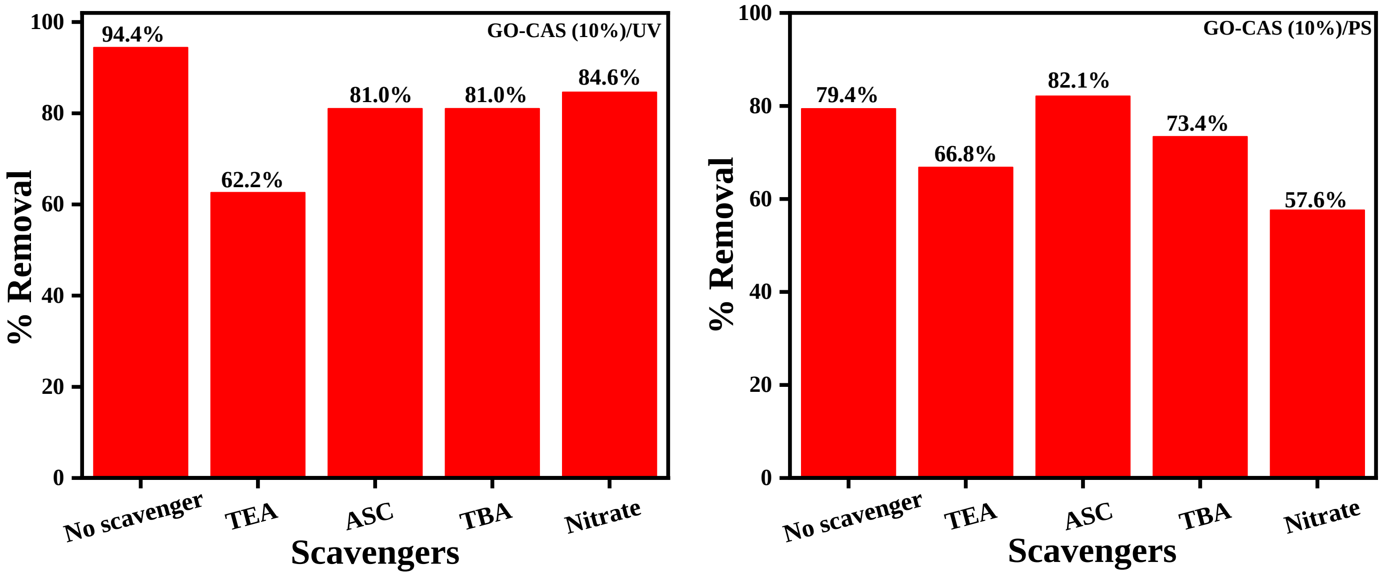

Fig 7: Radical scavenging experiment for the photocatalytic process (left) and the persulfate activation process (right)

4.0 Conclusion

The composite of graphene oxide and copper antimony sulphide ($CuSbS_2$) were successfully prepared by the *ex-situ* precursor mixing technique and their photocatalytic and persulfate activation activity was explored for the degradation of tetracycline. The composite showed higher photocatalytic activity compared to the persulfate activation activity, with degradation efficiency of 94 and 74% respectively. The enhanced photocatalytic activity of GO-CAS could be attributed to the red shift in the band gap energy and the improved charge carrier recombination process upon the incorporation of CAS into GO. Radical scavenging experiments showed that in the photocatalytic process photogenerated holes played the most significant role in TCE degradation, while in the persulfate activation process, the degradation process was most significantly inhibited by the presence of nitrate ions which suggested that electron transfer between the catalyst and PS was significant in the process. Thus, this study has affirmed the potential for improving the photocatalytic and persulfate activation activity of $CuSbS_2$ by supporting it on graphene oxide.

5.0 References

Lakowicz, J. R. 2006. Quenching of Fluorescence. *In:* LAKOWICZ, J. R. (ed.) *Principles of Fluorescence Spectroscopy.* Boston, MA: Springer US.

Ahmad, M. A., Aslam, S., Mustafa, F. & Arshad, U. 2021. Synergistic antibacterial activity of surfactant free Ag-GO nanocomposites. *Sci Rep,* 11**,** 196.

Berg, D., Djemour, R., Gütay, L., Zoppi, G., Siebentritt, S. & Dale, P. 2012. Thin film solar cells based on the ternary compound Cu_2SnS_3. *Thin Solid Films,* 520**,** 6291-6294.

Carminati, S. A., Rodríguez-Gutiérrez, I., de Morais, A., da Silva, B. L., Melo, M. A., Souza, F. L. & Nogueira, A. F. 2021. Challenges and prospects about the graphene role in the design of photoelectrodes for sunlight-driven water splitting. *RSC Advances,* 11**,** 14374-14398.

Chakraborty, M., Thangavel, R., Komninou, P., Zhou, Z. & Gupta, A. 2019. Nanospheres and nanoflowers of copper bismuth sulphide (Cu_3BiS_3): Colloidal synthesis, structural, optical and electrical characterization. *Journal of Alloys and Compounds,* 776**,** 142-148.

de Souza Lucas, F. W., Welch, A. W., Baranowski, L. L., Dippo, P. C., Hempel, H., Unold, T., Eichberger, R., Blank, B., Rau, U., Mascaro, L. H. & Zakutayev, A. 2016. Effects of Thermochemical Treatment on $CuSbS_2$ Photovoltaic Absorber Quality and Solar Cell Reproducibility. *The Journal of Physical Chemistry C,* 120**,** 18377-18385.

Dekhil, S., Dahman, H., Ghribi, F., Mortada, H., Yaacoub, N. & El Mir, L. 2019. Study of $CuSbS_2$ thin films nanofibers prepared by spin coating technique using ultra pure water as a solvent. *Materials Research Express,* 6**,** 086450.

Dhinakaran, V., Stalin, B., Sai, M. S., Vairamuthu, J. & Marichamy, S. 2021. Recent developments of graphene composites for energy storage devices. *Materials Today: Proceedings,* 45**,** 1779-1782.

Digraskar, R. V., Sapner, V. S., Ghule, A. V. & Sathe, B. R. 2019. Enhanced Overall Water-Splitting Performance: Oleylamine-Functionalized GO/Cu_2ZnSnS_4 Composite as a Nobel Metal-Free and NonPrecious Electrocatalyst. *ACS Omega,* 4**,** 18969-18977.

Fu, G. & Lee, J.-M. 2019. Ternary metal sulfides for electrocatalytic energy conversion. *Journal of Materials Chemistry A,* 7**,** 9386-9405.

Gao, P., Liu, J., Sun, D. D. & Ng, W. 2013. Graphene oxide-CdS composite with high photocatalytic degradation and disinfection activities under visible light irradiation. *J Hazard Mater,* 250-251**,** 412-20.

Gao, T., Chen, L., Li, Z., Yu, L., Wu, Z. & Zhang, Z. 2016. Preparation of zinc hydroxystannate-decorated graphene oxide nanohybrids and their synergistic reinforcement on reducing fire hazards of flexible poly (vinyl chloride). *Nanoscale Research Letters,* 11**,** 192.

Hamzah, M., Khenfouch, M. & Srinivasu, V. V. 2017. The quenching of silver nanoparticles photoluminescence by graphene oxide: spectroscopic and morphological investigations. *Journal of Materials Science: Materials in Electronics,* 28**,** 1804-1811.

Hu, Y., Zhou, C., Wang, H., Chen, M., Zeng, G., Liu, Z., Liu, Y., Wang, W., Wu, T., Shao, B. & Liang, Q. 2021. Recent advance of graphene/semiconductor composite nanocatalysts: Synthesis, mechanism, applications and perspectives. *Chemical Engineering Journal,* 414**,** 128795.

Huang, X., Qi, X., Boey, F. & Zhang, H. 2012. Graphene-based composites. *Chemical Society Reviews,* 41**,** 666-686.

Iqbal, S. M. Z., Qadir, K. W., Abdullah, H. Y., Dastgheib, A. M. & Bashir, M. M. 2021. Characterization of Solar Absorber Coated by Reduced Graphene Oxide Polymer Composite on Metal Sheets. *International Journal of Thermophysics,* 42**,** 33.

Jilani, A., Othman, M., Ansari, M., Hussain, S. Z., Ismail, A., Khan, I. & Inamuddin 2018. Graphene and its derivatives: synthesis, modifications, and applications in wastewater treatment. *Environmental Chemistry Letters,* 16.

Krishnan, B., Shaji, S. & Ornelas, R. E. 2015. Progress in development of copper antimony sulfide thin films as an alternative material for solar energy harvesting. *Journal of Materials Science: Materials in Electronics,* 26**,** 4770-4781.

Kulkarni, P., Nataraj, S. K., Balakrishna, R. G., Nagaraju, D. H. & Reddy, M. V. 2017. Nanostructured binary and ternary metal sulfides: synthesis methods and their application in energy conversion and storage devices. *Journal of Materials Chemistry A,* 5**,** 22040-22094.

Kumar, M. & Persson, C. 2013. CuSbS2 and CuBiS2 as potential absorber materials for thin-film solar cells. *Journal of Renewable and Sustainable Energy,* 5**,** 031616.

Liqiang, J., Yichun, Q., Baiqi, W., Shudan, L., Baojiang, J., Libin, Y., Wei, F., Honggang, F. & Jiazhong, S. 2006. Review of photoluminescence performance of nano-sized semiconductor materials and its relationships with photocatalytic activity. *Solar Energy Materials and Solar Cells,* 90**,** 1773-1787.

Liu, Y., Luo, J., Tang, L., Feng, C., Wang, J., Deng, Y., Liu, H., Yu, J., Feng, H. & Wang, J. 2020. Origin of the Enhanced Reusability and Electron Transfer of the Carbon-Coated Mn_3O_4 Nanocube for Persulfate Activation. *ACS Catalysis,* 10**,** 14857-14870.

Marcano, D. C., Kosynkin, D. V., Berlin, J. M., Sinitskii, A., Sun, Z., Slesarev, A., Alemany, L. B., Lu, W. & Tour, J. M. 2010. Improved Synthesis of Graphene Oxide. *ACS Nano,* 4**,** 4806-4814.

Mei, Q., Liu, B., Han, G., Liu, R., Han, M.-Y. & Zhang, Z. 2019. Graphene Oxide: From Tunable Structures to Diverse Luminescence Behaviors. *Advanced Science,* 6**,** 1900855.

Mohan, V. B., Lau, K.-t., Hui, D. & Bhattacharyya, D. 2018. Graphene-based materials and their composites: A review on production, applications and product limitations. *Composites Part B: Engineering,* 142**,** 200-220.

Mondal, A., Prabhakaran, A., Gupta, S. & Subramanian, V. R. 2021. Boosting Photocatalytic Activity Using Reduced Graphene Oxide (RGO)/Semiconductor Nanocomposites: Issues and Future Scope. *ACS omega,* 6**,** 8734-8743.

Moradi, S., Sobhgol, S. A., Hayati, F., Isari, A. A., Kakavandi, B., Bashardoust, P. & Anvaripour, B. 2020. Performance and reaction mechanism of MgO/ZnO/Graphene ternary nanocomposite in coupling with LED and ultrasound waves for the degradation of sulfamethoxazole and pharmaceutical wastewater. *Separation and Purification Technology,* 251.

Morselli, G., Villa, M., Fermi, A., Critchley, K. & Ceroni, P. 2021. Luminescent copper indium sulfide (CIS) quantum dots for bioimaging applications. *Nanoscale Horizons*.

Nie, C., Dai, Z., Liu, W., Duan, X., Wang, C., Lai, B., Ao, Z., Wang, S. & An, T. 2020. Criteria of active sites in nonradical persulfate activation process from integrated experimental and theoretical investigations: boron–nitrogen-co-doped nanocarbon-mediated peroxydisulfate activation as an example. *Environmental Science: Nano,* 7**,** 1899-1911.

Ning, J., Kershaw, S. V. & Rogach, A. L. 2019. Shape-Controlled Synthesis of Copper Indium Sulfide Nanostructures: Flowers, Platelets and Spheres. *Nanomaterials (Basel, Switzerland),* 9**,** 1779.

Olatunde, O. C. & Onwudiwe, D. C. 2020. Copper-based ternary metal sulfide nanocrystals embedded in graphene oxide as photocatalyst in water treatment. *Nanotechnology in the Beverage Industry.*

Olatunde, O. C. & Onwudiwe, D. C. 2021. Stoichiometric phases and mechanism of crystal phase selectivity of copper-based ternary sulphides. *Materials Science in Semiconductor Processing,* 125**,** 105627.

Onwudiwe, D. C. & Ajibade, P. A. 2010. Synthesis and characterization of metal complexes of N-alkyl-N-phenyl dithiocarbamates. *Polyhedron,* 29**,** 1431-1436.

Oyekunle, D. T., Zhou, X., Shahzad, A. & Chen, Z. 2021. Review on carbonaceous materials as persulfate activators: structure–performance relationship, mechanism and future perspectives on water treatment. *Journal of Materials Chemistry A,* 9**,** 8012-8050.

Pelaez, M., Falaras, P., Likodimos, V., O'Shea, K., de la Cruz, A. A., Dunlop, P. S. M., Byrne, J. A. & Dionysiou, D. D. 2016. Use of Selected Scavengers for the Determination of NF-TiO_2 Reactive Oxygen Species during the Degradation of Microcystin-LR under Visible Light Irradiation. *Journal of molecular catalysis. A, Chemical,* 425**,** 183-189.

Ramasamy, K., Gupta, R. K., Sims, H., Palchoudhury, S., Ivanov, S. & Gupta, A. 2015. Layered ternary sulfide CuSbS2 nanoplates for flexible solid-state supercapacitors. *Journal of Materials Chemistry A,* 3**,** 13263-13274.

Ren, W., Xiong, L., Yuan, X., Yu, Z., Zhang, H., Duan, X. & Wang, S. 2019. Activation of Peroxydisulfate on Carbon Nanotubes: Electron-Transfer Mechanism. *Environ Sci Technol,* 53**,** 14595-14603.

Shukla, N., Liu, C., Jones, P. M. & Weller, D. 2003. FTIR study of surfactant bonding to FePt nanoparticles. *Journal of Magnetism and Magnetic Materials,* 266**,** 178-184.

Singh, S., Faraz, M. & Khare, N. 2020. Recent Advances in Semiconductor-Graphene and Semiconductor-Ferroelectric/Ferromagnetic Nanoheterostructures for Efficient Hydrogen Generation and Environmental Remediation. *ACS omega,* 5**,** 11874-11882.

Solomon, G., Kohan, M. G., Landström, A., Vomiero, A. & Concina, I. 2020. Semiconducting metal oxides empowered by graphene and its derivatives: Progresses and critical perspective on selected functional applications. *Journal of Applied Physics,* 128.

Tang, L., Liu, Y., Wang, J., Zeng, G., Deng, Y., Dong, H., Feng, H., Wang, J. & Peng, B. 2018. Enhanced activation process of persulfate by mesoporous carbon for degradation of aqueous organic pollutants: Electron transfer mechanism. *Applied Catalysis B: Environmental,* 231**,** 1-10.

van Embden, J., Latham, K., Duffy, N. W. & Tachibana, Y. 2013. Near-Infrared Absorbing Cu12Sb4S13 and Cu3SbS4 Nanocrystals: Synthesis, Characterization, and Photoelectrochemistry. *Journal of the American Chemical Society,* 135**,** 11562-11571.

Wada, T. & Maeda, T. 2017. Optical properties and electronic structures of $CuSbS_2$, $CuSbSe_2$, and $CuSb(S_{1-x}Se_x)_2$ solid solution. *physica status solidi c,* 14**,** 1600196.

Wang, B., Ruan, T., Chen, Y., Jin, F., Peng, L., Zhou, Y., Wang, D. & Dou, S. 2020a. Graphene-based composites for electrochemical energy storage. *Energy Storage Materials,* 24**,** 22-51.

Wang, W., Zhi, G., Liu, J., Hao, L., Yang, L., Zhao, Y. & Hu, Y. 2020b. Effect of PVP content on photocatalytic properties of $CuSbS_2$ particles with chemical etching. *Journal of Nanoparticle Research,* 22.

Whittles, T. J., Veal, T. D., Savory, C. N., Welch, A. W., de Souza Lucas, F. W., Gibbon, J. T., Birkett, M., Potter, R. J., Scanlon, D. O., Zakutayev, A. & Dhanak, V. R. 2017. Core Levels, Band Alignments, and Valence-Band States in $CuSbS_2$ for Solar Cell Applications. *ACS Appl Mater Interfaces,* 9**,** 41916-41926.

Xu, C., Shi, X., Ji, A., Shi, L., Zhou, C. & Cui, Y. 2015. Fabrication and Characteristics of Reduced Graphene Oxide Produced with Different Green Reductants. *PloS one,* 10**,** e0144842-e0144842.

Xu, J.-M., Wang, X.-C. & Cheng, J.-P. 2020. Supercapacitive Performances of Ternary $CuCo_2S_4$ Sulfides. *ACS Omega,* 5**,** 1305-1311.

Zhang, Y., Huang, J., Yan, C., Sun, K., Cui, X., Liu, F., Liu, Z., Zhang, X., Liu, X., Stride, J. A., Green, M. A. & Hao, X. 2019. High open-circuit voltage $CuSbS_2$

solar cells achieved through the formation of epitaxial growth of $CdS/CuSbS_2$

hetero-interface by post-annealing treatment. *Progress in Photovoltaics: Research and Applications,* 27**,** 37-43.

Zhong, L. & Yun, K. 2015. Graphene oxide-modified ZnO particles: synthesis, characterization, and antibacterial properties. *Int J Nanomedicine,* 10 Spec Iss**,** 79-92.

Zhu, C., Guo, S., Fang, Y. & Dong, S. 2010. Reducing sugar: new functional molecules for the green synthesis of graphene nanosheets. *ACS Nano,* 4**,** 2429-37.

Zhu, S., Jin, C., Duan, X., Wang, S. & Ho, S.-H. 2020. Nonradical oxidation in persulfate activation by graphene-like nanosheets (GNS): Differentiating the contributions of singlet oxygen (1O2) and sorption-dependent electron transfer. *Chemical Engineering Journal,* 393.

CHAPTER ELEVEN

UV-light assisted activation of persulfate by rGO-Cu_3BiS_3 for the degradation of diclofenac

1.0 Introduction

The presence of contaminants in water continues to be a serious global threat and one of the major causes of illness, accounting for approximately 14,000 deaths daily. With the continuous increase in the rate of waste discharge into water bodies, occasioned by the increase in industrial and agricultural activities, the future of clean water availability continues to grow bleak on a daily basis. Also, of new concern are the release of highly recalcitrant substances, which are often termed emerging contaminants into the environment. These contaminants of emerging concern find their ways into the environment from domestic activities and industries involved in the production of products such as pharmaceuticals, household substances, and paper and pulp (Olatunde *et al.*, 2020).

The presence of pharmaceuticals in water is one of the most studied emerging environmental contaminants of concern because of the recent discovery of their presence in rather high levels than expected in the environment (Xu *et al.*, 2017, Valcárcel *et al.*, 2011, Mompelat *et al.*, 2009). This can be attributed to two main factors: (1) the increase in consumption of pharmaceuticals because of their therapeutic function and (2) the inability of current wastewater treatment plants to effectively remove or degrade them from wastewater streams (Oluwole *et al.*, 2020, Patel *et al.*, 2019). This implies that, the level of pharmaceuticals in the environment, especially water bodies are expected to continue to increase, and the potential of wastewater reuse via recycling continues to reduce, because of the recalcitrant nature of these compounds, thereby further leading to a strain in water availability. The emergence of studies on the chronic and acute effects of pharmaceutical on the ecosystem and living organism, especially on human metabolism and development of drug resistance in microorganisms is another major concern occasioned by the presence of pharmaceuticals in the environment. (Quinn *et al.*, 2008, Küster and Adler, 2014).

Different techniques have been explored for the remediation of the environment from pharmaceuticals. Some of them include chemical oxidation, adsorption, and membrane technology. The chemical oxidation processes are the most explored of these techniques because they offer the potential for complete degradation of pharmaceuticals into simple, non-toxic, inorganic compounds through the actions of highly reactive radicals such as $^{\bullet}OH$, $SO_4^{\bullet -}$ and $O_2^{\bullet -}$ (Xia *et al.*, 2020, O'Shea and Dionysiou, 2012). These radical species are generated *in-situ* by the activation of chemical oxidants, some of which could be introduced into the system such as H_2O_2, $Na_2S_2O_8$ or process components such as H_2O or O_2. Radical generation could also be initiated by compounds, referred to as photocatalysts, which are able to generate energetic charge carriers by absorption of light energy.

There are several studies on the combination of catalytic processes with activation of chemical oxidants such as persulfate (PS) (Jiang *et al.*, 2020, Pulicharla *et al.*, 2018). The catalytic activation of PS via light-assisted processes have also been explored (Wang *et al.*, 2020, Wang *et al.*, 2017b). These hybrid processes have been found to show enhanced degradation activity due to the synergy between the two processes. Activation of PS could be achieved via basic pH conditions, UV irradiation, sonochemical, transition metal oxides and electrochemical processes (Furman *et al.*, 2010, Jiang *et al.*, 2020). Recently, the use of carbonaceous materials such as biochar, graphitic carbon nitride, and graphene oxides/reduced graphene oxide (GO/rGO) have been found to be effective in PS activation (Hasija *et al.*, 2021, Wang *et al.*, 2019, Sun *et al.*, 2020). Because of the surface defects on GO/rGO, synergistic electronic interaction can be established with catalytic nanomaterials in order to produce composites with enhanced catalytic functionalities (Mondal *et al.*, 2021).

While most studies have focused on the use of transition and transition metal oxides as catalysts for persulfate activation, there are only few studies that have explored the use of metal sulphides (Peng *et al.*, 2018). In this study, a ternary metal sulphide (Cu_3BiS_3) supported with reduced graphene oxide has been explored in a UV-light assisted process for the catalytic degradation of diclofenac. The influence of process parameters such as pH, concentration of catalyst and concentration of PS have also been studied, and a mechanism of degradation process has been proposed based on the radical scavenging experiment results.

2.0 Experimental

2.1 Chemicals and instruments

Bi(III) nitrate pentahydrate, Cu(II) sulfate, carbon disulphide, sodium persulfate (PS), ascorbic acid, triethanol amine, tert-butanol, oleylamine, methanol, toluene, N-methyl aniline, graphite, potassium permanganate, nitric acid, sulfuric acid and ammonium hydroxide solution used were all of analytical grade and used as supplied by Sigma-Aldrich. For structural characterization, XRD patterns were recorded using a d8 Advanced X-ray diffractometer with Cu Kα radiation ($\lambda = 154.18$ pm). Optical properties of composite were studied by absorption and emission spectroscopies recorded on a PerkinElmer λ20 UV-vis spectrophotometer and Perkin Elmer LS 45 fluorimeter respectively. Scanning electron microscopy (SEM) and transmission electron microscopy (TEM) images used in studying the morphology of the samples were carried out on a TECNAI G2 (ACI) equipment (Hillsboro, OR, USA) operating with accelerating voltage of 200 kV

2.2 Synthesis of bismuth(III) tris(*N*-methyl-*N*-phenyldithiocarbamate) [Bi(DTC)$_3$], and copper(II) bis(*N*-methyl *N*-phenyl dithiocarbamate) [Cu(DTC)$_2$]

Bismuth complex of the dithiocarbamate was prepared by mixing aqueous solutions of bismuth nitrate with an aqueous solution of the ammonium *N*-methyl-*N*-phenyldithiocarbamate (Onwudiwe and Ajibade, 2011) in 1:3 stoichiometric ratio and stirred for 1 h. . The bright yellow precipitates obtained were filtered, rinsed thoroughly with water and ethanol, and then vacuum dried overnight. The complex was further recrystallized in chloroform in order to obtain a pure sample The same procedure was employed for the synthesis of [Cu(DTC)$_2$], but 1:2 ratio of the metal salts to ligand was used.

2.3 Synthesis of Cu$_3$BiS$_3$ nanocrystals

The Cu$_3$BiS$_3$ nanocrystal was synthesised under nitrogen atmosphere. In a typical synthesis (Chakraborty *et al.*, 2018), stoichiometric amount of [Bi(DTC)$_3$] and [Cu(DTC)$_2$] (0.15mmol) where added into 20 mmol of oleylamine in a three-necked round bottom flask connected to a condenser. The slurry formed after stirring was heated up to 120 ˚C and held for 20 min in order to remove oxygen and water from the system. The temperature of the system was then increased to 280 ºC at a heating rate of 10 ºC/min and held at this temperature for 1 h. The system was allowed to cool down naturally and the nanoparticles were precipitated by adding excess ethanol. Separation of the nanoparticles from the solution was by centrifugation at 5000 rpm.and washing three times with n-hexane/ethanol mixture (3:1 v/v).

2.4 Synthesis of graphene oxide (GO)

The Tours method described by Marcano *et al.* (2010) was employed for the synthesis of graphene oxide. Concentrated H_2SO_4 and H_3PO_4 were mixed in ratio 9:1 and then added to a mixture of graphite flakes and $KMnO_4$ (graphite flakes/$KMnO_4$ = 1/6). The mixture was heated at 50 ºC for 12 h with stirring. The thick greenish-purple paste obtained was allowed to cool to room temperature and then poured into 400 mL of ice. Hydrogen peroxide (30%) was added until the solution turned bright yellow. The obtained graphene oxide was centrifuged and the residue that resulted washed three times with water, HCl and ethanol. The obtained GO was washed severally with water until neutral pH was attained. Finally, it was oven dried at 50 ºC and stored for further use.

2.5 Synthesis of rGO-CBS

The solvothermal treatment method was used for the synthesis of rGO-CBS. A known weight of GO was dispersed in ethylene glycol via sonication for 1 h, after which the nanoparticles dispersed in ethanol were mixed with the GO dispersion. The mixture was then transferred into a 100 mL autoclave and heated at 150 ºC for 20 h. The obtained black precipitate, was washed repeatedly with water and finally with ethanol. The composite was dried overnight in an oven at 50 ºC. The percent weight of the nanoparticle in the composite was varied between 5-20%, to afford composites denoted as rGO-Cu_3BiS_3(5%), rGO-Cu_3BiS_3(10%), rGO-Cu_3BiS_3(15%), and rGO-Cu_3BiS_3(20%).

2.6 Photocatalytic studies

The photocatalytic activity of the composites was evaluated for the decomposition of diclofenac in a UV/rGO-CBS and UV/PS/rGO-CBS process. The process was carried out in a 250 mL glass beaker. In a typical process, 50 mL of 10 mg/L diclofenac solution was stirred with 50 mg of the catalyst in the dark for 30 min in order to establish adsorption-desorption equilibrium. Afterwards, PS was introduced into the system for the UV/PS/rGO-CBS process and a 28 watts UV-LED light was turned on. Aliquots of the solution were taken at intervals. The UV/rGO-CBS process was carried out following same procedure but without the introduction of PS. The concentration of DCF in the system was measured using a UV spectrometer at λ_{max} of 275 nm. The percentage removal of DCF was evaluated using the Eq. 1:

$$\%\, removal = \frac{C_o - C_f}{C_o} \times 100\%, \qquad (1)$$

where C_o and C_f are the initial and final concentrations of DCF respectively. For the study of effect of pH on the degradation process, the initial pH of the solution was adjusted with 0.1M HCl and 0.1 NaOH. Radical scavenging experiments were carried out to elucidate the mechanism of degradation of DCF. This was done by introducing ascorbic acid (ASC), tert-butanol (TBA) and triethanol amine as super oxide, hydroxyl radical and hole scavengers into the reaction system, and the influence of each radical on the photocatalytic process was measured by its influence on the degradation efficiency. The reaction rate for the degradation process was evaluated by fitting the degradation data into the linear form of the pseudo first order kinetics (Eq. 2):

$$-ln\frac{C_f}{C_o} = Kt, \qquad (2)$$

where C_f and C_o are the final and initial concentration of DCF, k is the reaction rate constant and t is the reaction time.

3.0 Results and discussion

3.1 Characterization of rGO-Cu_3BiS_3 nanocomposite

The nanocomposite of Cu_3BiS_3 with reduced graphene oxide (rGO) was prepared by the *ex-situ* incorporation of Cu_3BiS_3 into GO under solvothermal conditions with the simultaneous reduction of GO to rGO. The functional groups present, structural, morphological and optical properties of the prepared nanocomposites containing 5, 10, 15 and 20% weight ratios of Cu_3BiS_3 were studied. The functional groups present in GO, Cu_3BiS_3 and rGO-Cu_3BiS_3 were identified using the Fourier transform infrared spectroscopy as shown in Fig. 1. The characteristic bands of the infrared spectra for GO were observed in the IR spectrum. The stretching vibration and in-plane bending vibration of the O-H group were observed at 3248 and 1373 cm^{-1} respectively (Mokhtar Mohamed *et al.*, 2018). Stretching vibration from the C=O of carbonyl group is observed at 1726 cm^{-1} and at 1620 cm^{-1}, the stretching vibration for C=C group was observed (Ostwal *et al.*, 2018). The C–O vibration of C–OH and C-O-C groups accounts for the bands observed at 1220 and 1050 cm^{-1} respectively (Fan *et al.*, 2020). The spectrum of Cu_3BiS_3 showed a broad peak at about 1642 cm^{-1}, which could be ascribed to the vibrational frequency of C=C of oleylamine, with the peak at 1099 cm^{-1} arising from the bending modes of the amine group of oleylamine (Soosaimanickam *et al.*, 2015). The presence of DDT on the surface of the nanoparticles can be confirmed from the peak at 2682 cm^{-1}, which could be attributed to the S-H group of DDT. The spectra of the composites showed peaks that were due to both Cu_3BiS_3 and GO; however, it could be observed that the peaks associated with the oxygenated groups (O-H, C-O-C and C-O) were significantly reduced, confirming the reduction of GO to rGO in the solvothermal process. There was a complete disappearance of the O-H peaks at 3248 and 1373 cm^{-1}, with the C-O peak also not visible in the composites. However, the intensity of the C-O-C peak remained relatively unchanged in the composite, which agrees with the finding by Luo *et al.* (2011) that suggests the inability of high temperature treatment to remove C-O-C group. Furthermore, a significant shift in the wavelength position from 1050 cm^{-1} to 1215 $cm^{-1}$was observed in the composite, which may suggest that the point of interaction between the nanoparticles and the reduced graphene oxide was at C-O-C functional group.

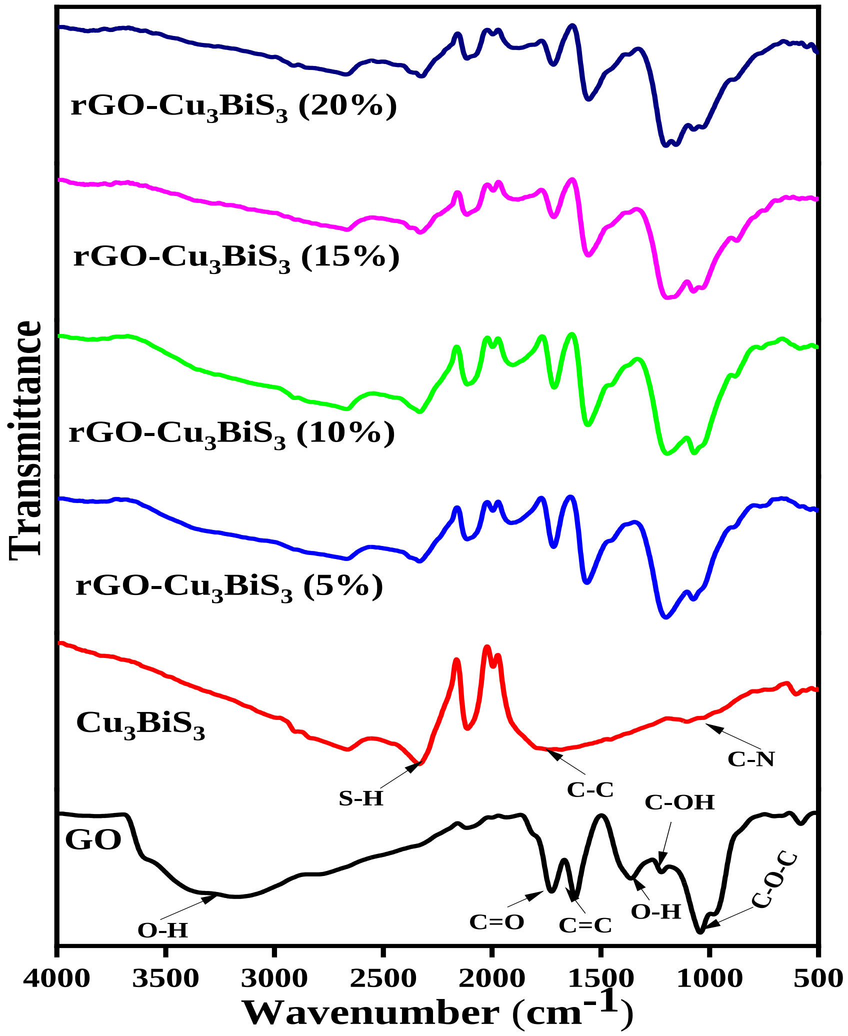

Fig 1: FTIR spectra of graphene oxide, Cu$_3$BiS$_3$, and composites of rGO-Cu$_3$BiS$_3$ containg 5, 10, 15, and 20% of Cu$_3$BiS$_3$.

The XRD pattern of the prepared GO, Cu$_3$BiS$_3$, and rGO-Cu$_3$BiS$_3$ composites are shown in Fig. 2. The characteristic peak of GO is observed at 2θ = 10.2°, which corresponds to a d -spacing value (Equ. 1) (Sheng *et al.*, 2013) of 0.865 nm between each GO sheet.

$$\lambda = 2dsin(\theta) \qquad (3)$$

All the peaks of the pristine Cu$_3$BiS$_3$ can be indexed to the orthorombic phase of wittichenite. The crystallite size of Cu$_3$BiS$_3$ was evaluated using the Scherrer equation (Eq.2).

$$D = \frac{k\lambda}{\beta cos\theta}, \qquad (4)$$

where k, λ, β and θ represents the shape factor (0.90), X-ray wavelength of the Cu α radiation (0.154 nm), line broadening at FWHM in radians and Bragg’s angles in degrees respectively.The average crystallite size for Cu$_3$BiS$_3$ was calculated to be 60.1 nm.

All the rGO-Cu$_3$BiS$_3$ composites show diffraction patterns similar to the pristine Cu$_3$BiS$_3$, with the GO peaks not observed. This can be attributed to the destruction of the stacking structure of GO during the solvothermal process of incorporating the nanoparticles with GO, which simultaneously resulted in the reduction of GO (Liu *et al.*, 2014, Gao *et al.*, 2013).

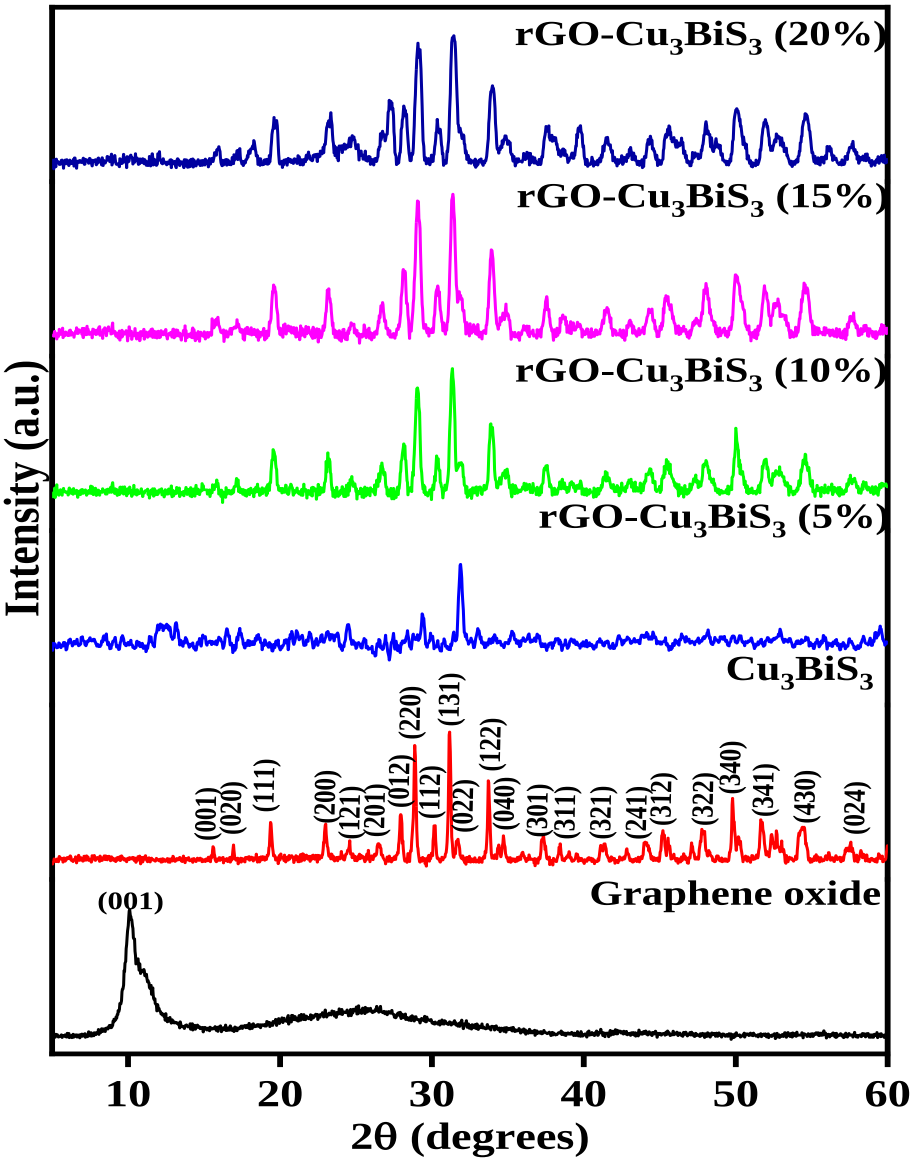

Fig 2: XRD patterns of graphene oxide, Cu_3BiS_3 and rGO-Cu_3BiS_3 composites with 5, 10, 15, 20% Cu_3BiS_3 weight percentage compoisition.

3.2 Photoluminescence quenching study

The photoluminescence (PL) quenching and fluorophore ability of graphitic systems is a well established and explored property (Srivastava *et al.*, 2018, Wen *et al.*, 2010, Bi *et al.*, 2012). The strong quenching activity of GO/rGO has been suggested to be due to the residual graphitic domains in the basal plane that have escaped the chemical oxidation process (Kim *et al.*, 2010). The PL quenching activity could either be through charge transfer from the excited states of a fluorophore to their π system or the Forster resonance energy transfer (FRET) processes due to its 2D planer structure and super electrical conductivity (Zheng and Wu, 2017). While the charge transfer process is a short-range energy transfer process, requiring the donor and acceptor to be within 10 Ǻ of each other, the FRET process is a long range energy transfer mechanism, with effectiveness up to a distance of ~6nm (Foster distance) (Zheng and Wu, 2017). Thus, the nature of interaction between GO/rGO and nanoparticles is important in determining the mechanism of PL quenching. Reports comparing the quenching ability of the graphitic systems shows that rGO exhibits higher quenching efficiency compared to graphite and GO, which results from the efficient π-π stacking and enhanced surface area in rGO (Srivastava *et al.*, 2018, Kim *et al.*, 2010). Steady-state PL is widely employed in exploring the charge carrier transfer and trapping efficiency, and to understand electron-hole pair behaviours in nanoparticles (Bajjou *et al.*, 2015). Since PL is a measure of photon emission and electron-hole recombinantion, strong PL quenching is a strong indication of the lower efficiency of radiative recombination of electrons and holes (Aawani *et al.*, 2019). Reducing the electron-hole recombination in a photocatalytic material is significant in enhancing the efficiency of the photocatalytic process. Hence, the PL quenching efficiency of compositing Cu_3BiS_3 with rGO was employed in screeing between rGO-Cu_3BiS_3(5%), rGO-Cu_3BiS_3(10%), rGO-Cu_3BiS_3(15%), and rGO-Cu_3BiS_3(20%). The photoluminescent spectra of ethanol solutions of the composites are shown in Fig. 3. All the composites, showed PL spectra similar to the pristine Cu_3BiS_3; however, the intensity of the peaks were significantly reduced. A gradual increase in the PL quenching efficiency was observed from the composites with 5-10% Cu_3BiS_3; however, beyound 15% weight composition of Cu_3BiS_3, the quenching efficiency was reduced. The reduction in PL quenching efficiency at higher composition of Cu_3BiS_3 may be attributed to increase in aggregation of the nanoparticles on the surface of rGO as PL enhancement is usually observed on rough surfaces or large nanoparticle sizes compared to smoother surfaces or smaller nanoparticles (Ruiz Peralta Mde *et al.*, 2012).

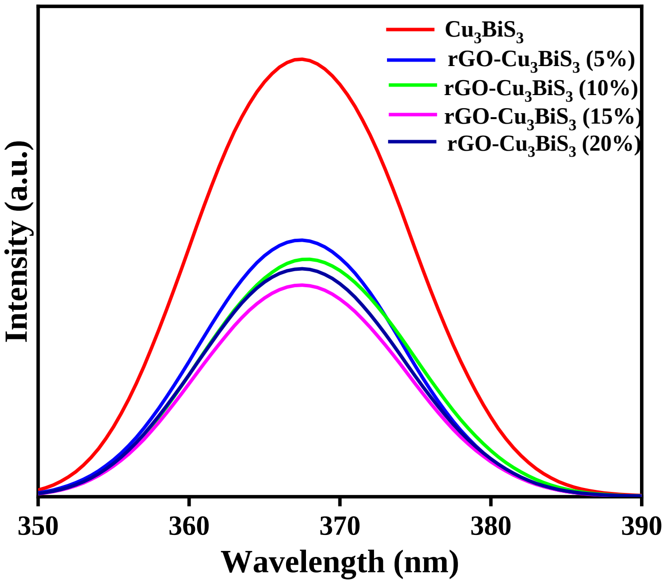

Fig. 3: PL spectra of Cu_3BiS_3, rGO-Cu_3BiS_3 (5%), rGO-Cu_3BiS_3 (10%), rGO-Cu_3BiS_3 (15%) and rGO-Cu_3BiS_3 (20%).

3.3 Morphological and optical properties of rGO-Cu_3BiS_3

The morphological and optical properties of Cu_3BiS_3, GO, and rGO-Cu_3BiS_3 are shown in Fig. 4. From Fig. 4(a&b), the Cu_3BiS_3 nanoparticles could be observed to be agglomerated and oval in shape. The SEM micrograph of GO shows the two-dimensional sheet-like and multiple lamellar layer of GO. The image also shows the possibility of distinquishing the edges of each GO sheet. The GO sheets are also observed to be thicker at the edges, which is due to the presence of large amounts of oxygen containing funtional moieties at the edges (Alam *et al.*, 2017). The thickness of the graphene oxide was 0.034-0.097 µm, which is much higher than the thickness of single layer graphene (0.335) (Ni *et al.*, 2007). This is due to the incorporation of oxygen moities into the graphene layer. The SEM image also shows that graphene sheets with width of up to 4.0 µm was obtained alongside with other smaller sheets. Fig 4c & d show the SEM and TEM images of rGO-Cu_3BiS_3 respectively, with a modification in the morphology of the GO sheets observed. The thickness of the sheets were thinner and the layer by layer arrangement of the sheet was destroyed. This could be attributed to the removal of oxygen-containing functionalities from the GO sheets to form rGO. The TEM image confirmed the attachement of Cu_3BiS_3 nanoparticles on the rGO surface.

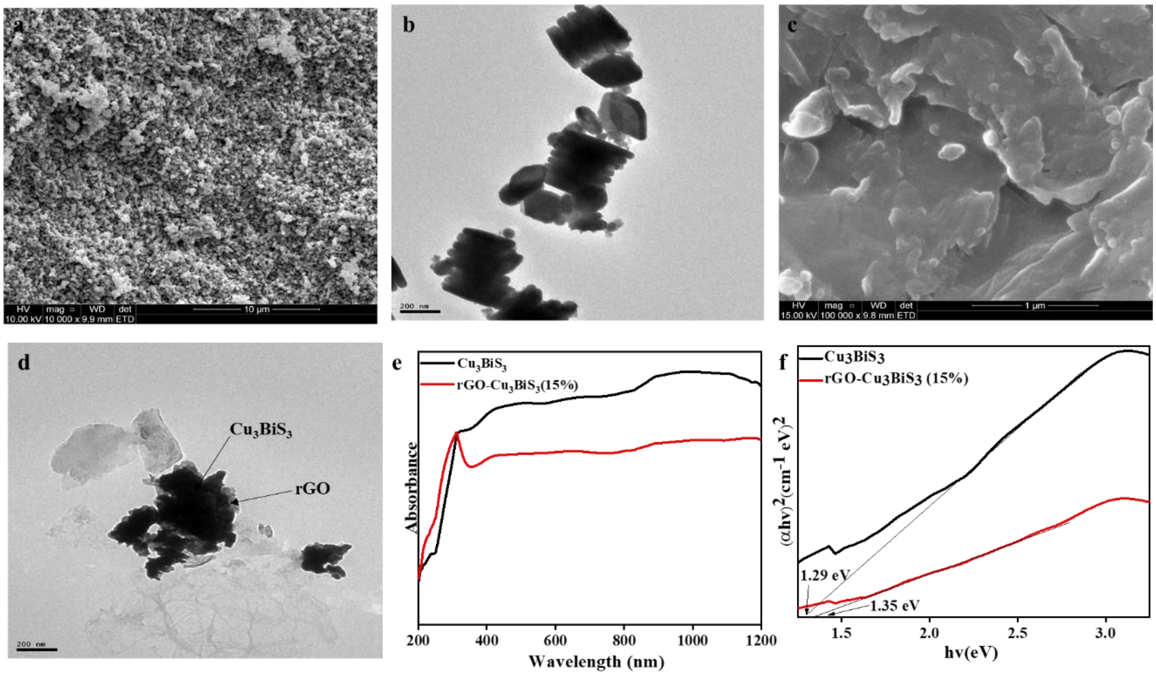

Fig 4: (a) SEM image of Cu_3BiS_3 (b)TEM image of CBS, (c) TEM image of graphene oxide(d) TEM image of rGO-CBS (15%) (e) absorbance spectra of CBS and rGO-CBS (15%) (e) Tauc plt for CBS and rGO-CBS (15%)

The absorption spectra of the pristine Cu_3BiS_3 and rGO-Cu_3BiS_3(15%) composite is shown in Fig. 4e. The pure Cu_3BiS_3 showed a higher absorption intensity, with higher absorption observed in the near IR region. However for the composite, an absorption maxima was observed at 310 nm, with a lower absortpion in the NIR region compared to the pristine nanoparticles. The observed reduction in absorption is consistent with reports for graphene-based composites in which the graphitic system is the major component (Gao *et al.*, 2012, Ni *et al.*, 2007). This was attributed to the formation of chemical bonds between the nanoparticles and rGO, and the delocalization of charges from the electronic interactions between the two compounds (Khan *et al.*, 2012).

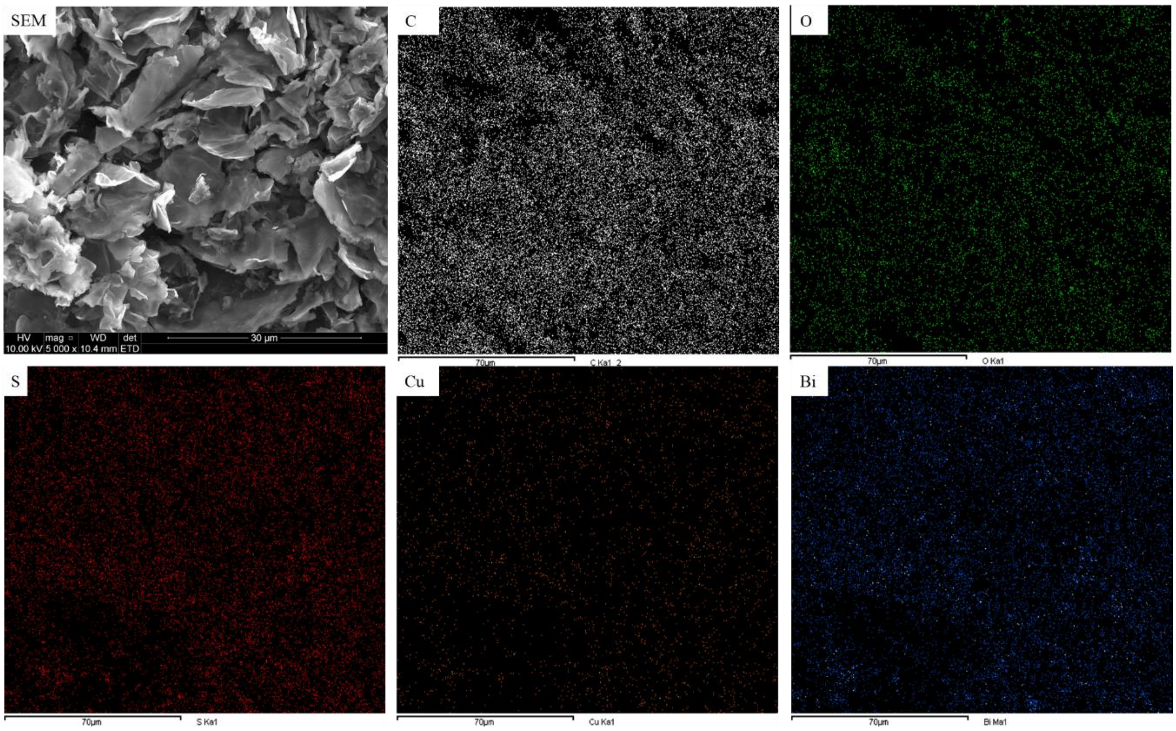

Fig 5: SEM image of rGO-CBS (15%) and elemental mapping images of carbon (C), Oxygen (O), sulphur (S), Copper (Cu) and Bismuth (Bi).

3.4 Photocatalytic activity of rGO-Cu_3BiS_3 (15%)

The photocatalytic activity of the composite was explored under UV-LED irradiation for the degradation of diclofenac. The composite was explored in a direct photocatalytic process and in a persulfate activation photocatalytic process. Fig. 6 shows the degradation activity at different catalyst dosage of 10-50 mg/L (0.2-1.0 g/L). For the direct photocatalytic process (Fig. 6a), the highest degradation efficiency of 78% was achieved after 270 min using a catalyst dose of 30 mg. Above this dosage, the efficiency reduced slightly to 72% with no further change at higher dosage. In the persulfate activated process (Fig. 6b), a similar trend in the effect of catalyst dosage on the catalytic efficiency was observed. At the catalyst dosage of 30 mg, degradation of diclofenac reached 81% after 60 min. Beyond this catalyst dosage, a reduction in degradation efficiency was observed. Studies have shown that, although high catalyst dosage leads to increase in adsorption sites, it often results in an increase in the turbidity of the solutions, which reduces the exent of light penetration and a consequent reduction in radical generation in the process (Olatunde and Onwudiwe, 2021, Sayadi *et al.*, 2019).

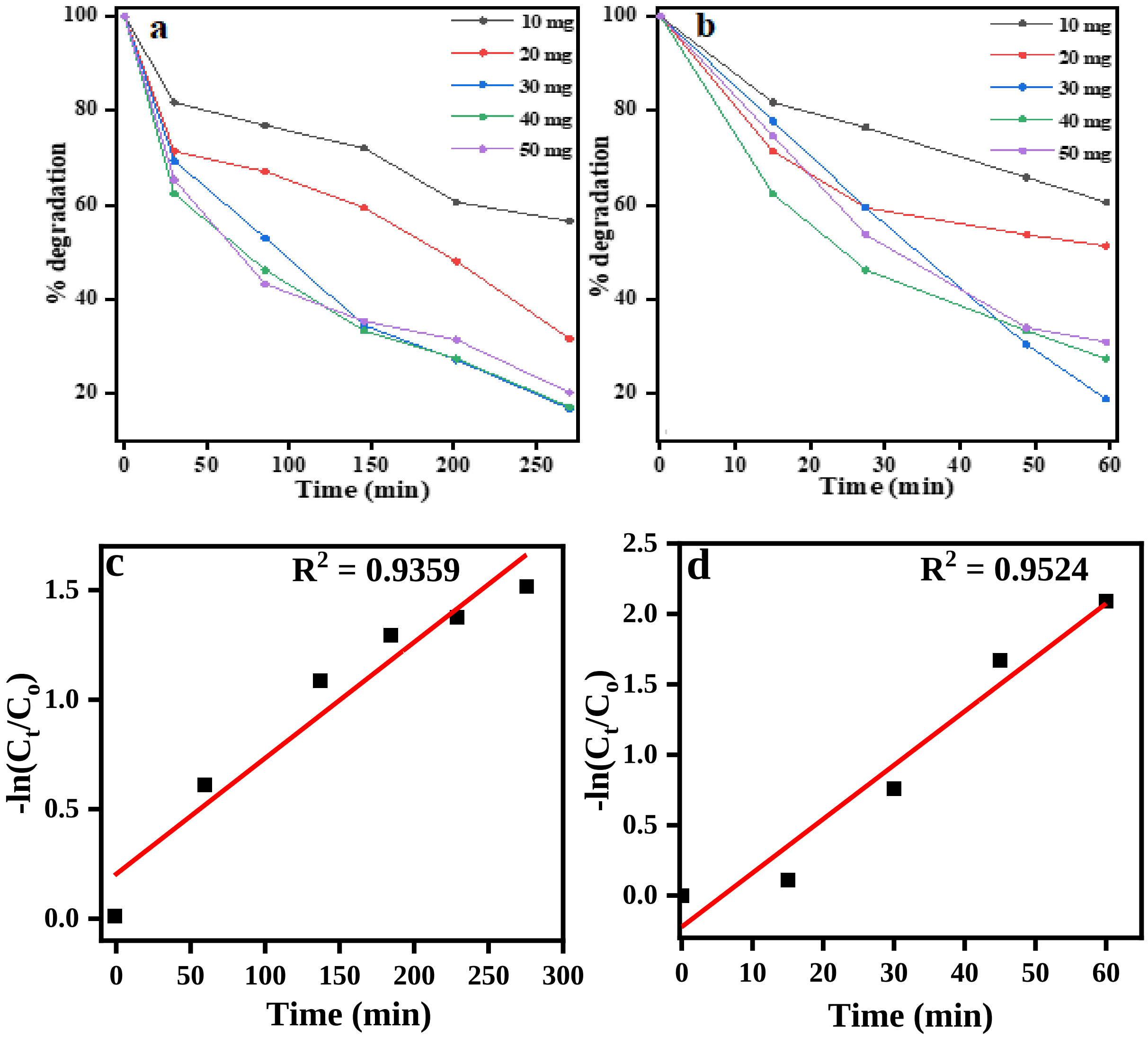

Fig 6: Catalytic degradation of diclofenac (a) direct photocatalytic process, (b) UV-assisted persulfate activation process process (UV LED light = 15 W; diclofenac concentration =10 mg/L; catalyst concentration = 10-50 mg), (c & d)kinetic plots for direct photocatalytic and UV-assisted persulfate activation process

The pseudo first order kinetics was fitted for the the degradation process as shown in Fig. 6(c&d). The rate constants k for both direct photocatalytic and persulfate activation process were 5.2×10^{-3} and 3.8×10^{-2} min^{-1} respectively. The rate of the UV/PS/rGO-CBS(15%) process was about 7.23 times greater than the UV-rGO-CBS(15%) process.

3.5 Effect of process parameters on photocatalytic activity of rGO-Cu_3BiS_3

The effect of process variables: persulfate concentration, pH and diclofenac concentration on the efficiency of the persulfate activation process was also explored. Fig. 7(a-c), shows the effect of these process parameters on the rate of degradation of diclofenac in the process. The effect of persulfate concentration was explored at three levels of 1, 3 and 5 mM. The efficiency of the process was observed to increase with the amount of persulfate, achieving degradation efficiencies of 57%, 64% and 85% at persulfate concentrations of 1, 3 and 5 mM respectively, with reaction rate constants of 1.6×10^{-2}, 2.1×10^{-2} and 3.8×10^{-2} min respectively. High concentrations of persulfate has been reported to reduce the efficiency of a catalytic process, due to its ability to scavenge generated free radicals (Ma *et al.*, 2021). However, within the concentration range 1-5 mM, the photocatalytic degradation process was enhanced. This suggests an increase in radical generaton with the increase in the concentration of $S_2O_8^{2-}$.

The effect of pH on the persulfate activation process was evaluated under acidic, basic and the neutral pH conditions of the test solution. The reaction rate constants for the degradation process were 2.3×10^{-2}, 2.6×10^{-2} and 8.6×10^{-3} at pH of 3, 7 and 11 respectively. The degradation rate was higher under acidic and neutral conditions compared to the basic conditions. This observation suggests that the degradation of diclofenac was mainly by the non-radical mechanism and follows a similar trend reported by Hu *et al.* (2021). This is further supported by the increase in reaction rate constant with increase in PS concentration, since high PS concentration results in scavenging of radical species. Recent studies have suggested that in acidic and neutral conditions, singlet oxidation process by singlet oxygen ($^1O_2$) is enhanced through the catalyzation of persulfate self-decay by carbonaceous materials and metal-driven nanomaterials (Cheng *et al.*, 2017, Wang *et al.*, 2017a, Tian *et al.*, 2017, Liang *et al.*, 2017, Gao *et al.*, 2019). The enhanced activity of rGO-CBS (15%) for persulfate activation under acidic and neutral conditions could be attributed to the carbonyl groups on the rGO, which are important for PS decay (Zhou *et al.*, 2017). Also, the reduction at high pH may be attributed to the repulsion between the surface of rGO-CBS(15%) and the ionic form of PS, which is $S_2O_8^{2-}$ at pH range of 2-14 due to its low pKa. This repulsion inhibits electron transfer from the CB of rGO-CBS(15%) to PS, which reduces the generation of $SO_4^{\bullet-}$. This leads to a reduction in the generation of $^{\bullet}$OH, which is responsible for the degradation activity of PS at high pH (Guan *et al.*, 2011). The effect of catalyst dosage on the reaction rate of the degradation process is shown in Fig. 5d, with increase in degradation rate from 1.4×10^{-2} to 3.4×10^{-2} observed when the catalyst dosage was increased from 20 mg to 30 mg. However, increasing the catalyst dosage to 40 mg resulted in a decrease in reaction rate to 2.5×10^{-2}. This could be attributed to a reduction in light penetration into the system, caused by the increase in tubidity

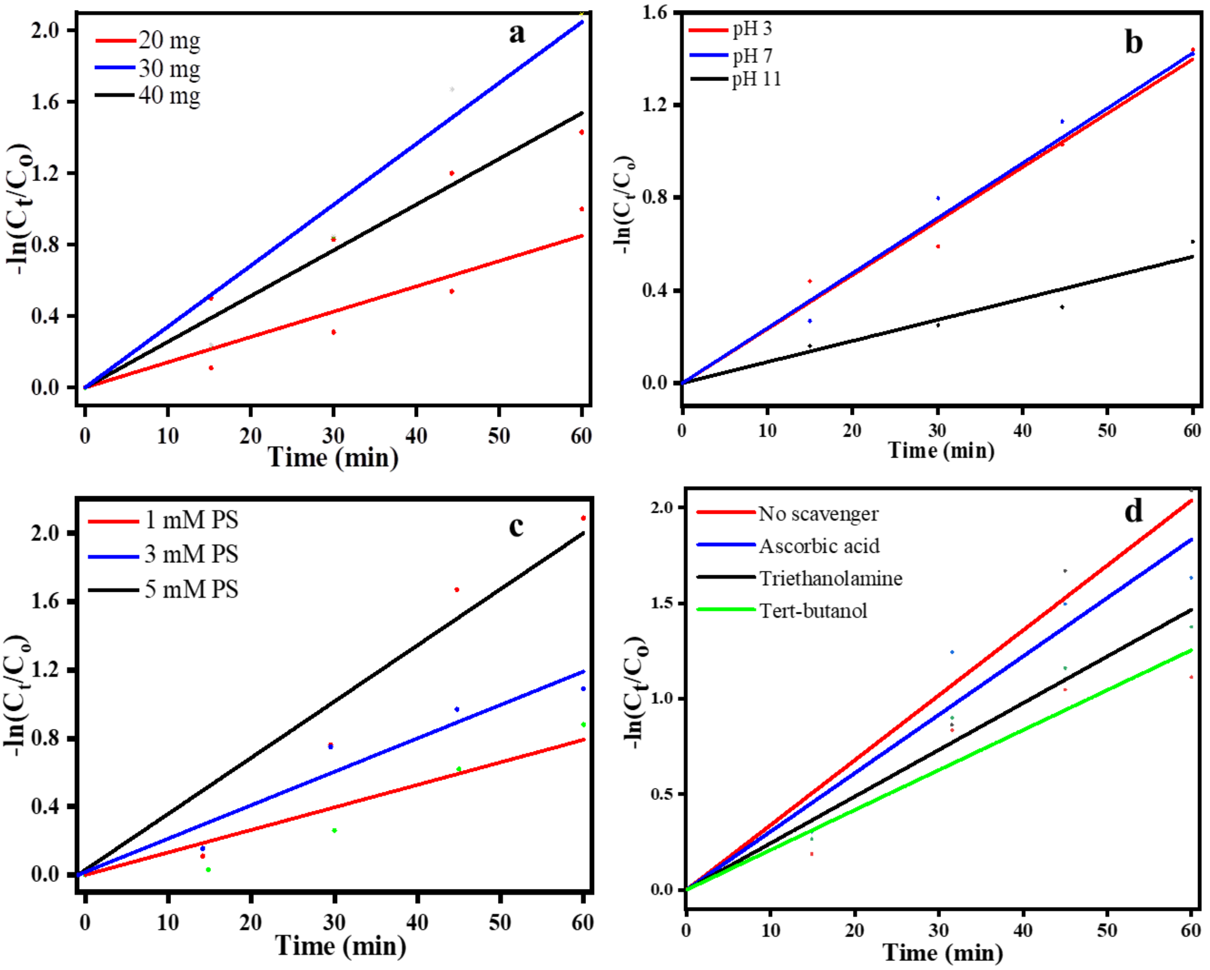

Fig 7: Effect of process parameters (a) catalyst dosage (b) pH, (c) concentration of PS and (d) presence of radical scavengers on the degradation process.

3.6 Radical scavenging experiments and proposed mechanism

To identify the radical species responsible for the degradation of diclofenac in the process, degradation experiments were carried out in the presence of radical scavengers: ascorbic acid, triethanolamine, and tert-butanol to act as hole, superoxide radical and hydroxyl radical scavengers respectively. Fig. 6 shows the effect of the radical scavengers on the rate of diclofenac degradation. The rates of degradation in the presence of TEA, TBA and Asc were 2.5×10^{-2}, 2.1×10^{-2} and 3.0×10^{-2} min^{-1}, compared to the degradation rate of 3.8×10^{-2} recorded in the absence of the radical scavengers. This corresponds to 34, 45 and 21% reduction in reaction rate in the presence of TEA, TBA and ASC respectively. The little effects of these scavengers on the degradation rates affirms that holes and $^{\bullet}$OH species only played slight roles in the degradation process and agrees with degradation processes in which $^1O_2$ is the dominant radical specie (Liang *et al.*, 2017). This supported the earlier assertion that $^1O_2$ played a significant role in the degradation process. The order of contribution of each specie to the degradation of DCF is given as $^1O_2$ > $^{\bullet}$OH > h^+.

3.7 Efficiency of degradation for other pollutants, stability test and comparative study

The degradation efficiency of the UV/rGO-CBS(15%)/PS process was also evaluated for the degradation of other organic pollutants. The photodegradation potency of the composite was further explored on two pharmaceuticals: bisphenol and tetracycline, and two organic dyes: methyl orange and methylene blue. As shown in Fig 8(a), the process showed high efficiency for the degradation of all the organic pollutants with 100% degradation recorded for tetracyline, methyl orange, and methylene blue, while the degradation efficiency for bisphenol was 81%. This showed the suitability of this composite for the degradation of a wide range of organic pollutants. The stability of the catalyst was evaluated by reusing the catalyst for three process cycles. Fig 8(b), shows the degradation efficiency of the process for the three cycles. The catalyst efficiency of the process only dropped by 16% after the third cycle, showing the stability of the catalyst for the UV/rGO-CBS(15%)/PS process.

The UV/rGO-CBS(15%)/PS process was further compared to other reported processes employed in the degradation of DCF. The processes were compared in terms of their electrical energy per order (E_{EO}), reaction rate (k) and the time required to achieve 90% degradation. The E_{EO} is the electrical energy in KW/h required for the degradation of 90% of the contaminant in 1 m^3 stream. The E_{EO} can be obtained from the following equations (Olatunde *et al.*, 2020):

$$E_{EO} = \frac{P \times t \times 1000}{V \times 60 \times log\frac{C_i}{C_f}} \quad , \qquad (5)$$

$$\ln{(C_i/C_t)} = kt \quad , \qquad (6)$$

where P is the rated power of the process in KW/h, V is the volume in L, t is the irradiation time in min, C_i and C_f are the intial and final concentrations of the pollutants and k is the pseudo first order rate constant in min^{-1}. By combining Eqs 4 and 5, EEO can be expressed as:

$$E_{EO} = \frac{P \times 38.4}{V \times k} , \qquad (7)$$

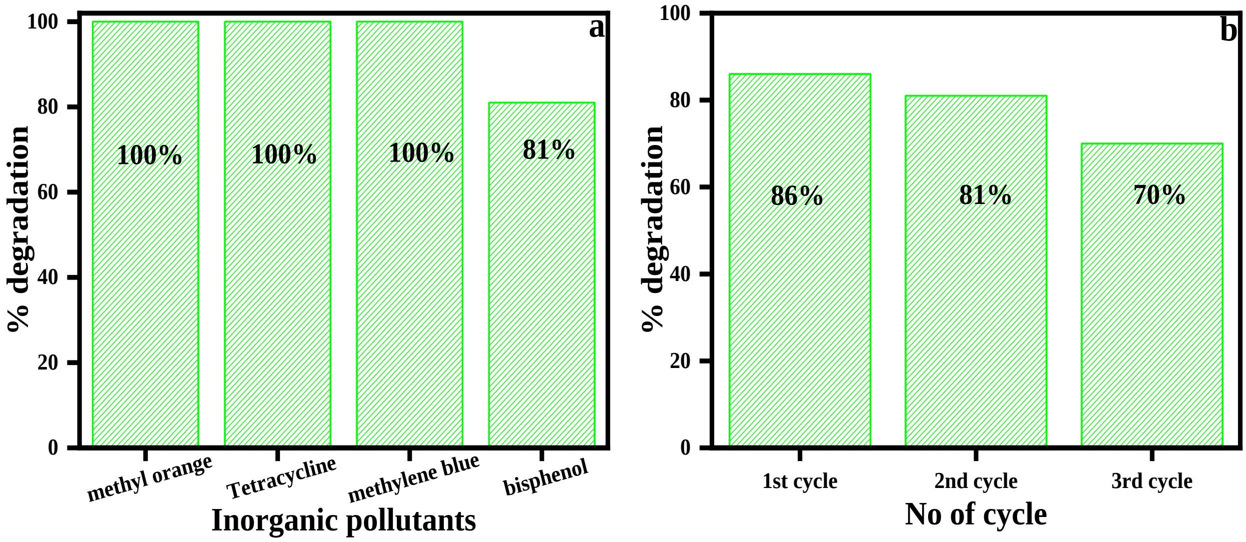

Fig 8: (a) Evaluation of the suitability of the UV/PS/rGO-CBS(15%) process for other pollutants (b) Evaluation of the stability of rGO-CBS(15%) for the UV/PS/rGO-15%) process.

The time required for 90% degradation ($t_{0.9}$) to be achieved in the process was determined from Eq. 7 (Olatunde and Onwudiwe, 2021).

$$t_{0.9} = \frac{2.3035}{k} \quad 8.$$

Table 1. shows the result of the degradation process for DCF obtained in this work and the comparison with other reported processes.

Table 1: Comparative study of the UV/rGO-CBS(15%)/PS process with other reported processes

Process	Rate constant (k) (min^{-1})	$t_{0.9}$ (min)	E_{EO} (KW/h)	Ref
UV/rGO-CBS(15%)/PS	3.8×10^{-2}	60.6	5.02	This study
UV/BiOCl-GO	3.7×10^{-3}	622.5	166.5	(Rashid *et al.*, 2020)
Vis/ZnIn2S4-CD	4.5×10^{-1}	5.06	8.4	(Yang *et al.*, 2020)
Vis/CQD/g-C3N4	7.4×10^{-2}	31.1	51.9	(Liu *et al.*, 2019)
Vis/Fe-GCN/S(IV)	8.2×10^{-2}	28.1	46.8	(Zhao *et al.*, 2021)

4.0 Conclusion

The activity of Cu_3BiS_3 (CBS) nanoparticles supported on reduced graphene oxide for a UV-light activated persulfate process has been studied for the degradation of diclofenac. The rGO-Cu_3BiS_3 with 15% CBS nanoparticles exhibited enhanced diclofenac degradation compared to PS, CBS and UV-light alone. The high catalytic activity of rGO-Cu_3BiS_3(15%) compared to other composites (rGO-Cu_3BiS_3(5%), rGO-Cu_3BiS_3(10%), and rGO-Cu_3BiS_3(20%) is attributed to the improved charge carrier transfer, which resulted in reduced recombination of photogenerated charge carriers. From the radical scavenging experiment, the process was observed to proceed via a non-radical process, with no significant influence on the degradation process observed with the introduction of scavengers. The process also demonstrated great potential for the degradation of a wide range of organic pollutants. This study, therefore, showed the improved catalytic potential of Cu_3BiS_3 for a UV-assisted persulfate activation process when supported on reduced graphene oxide.

5.0 References

Aawani, E., Memarian, N. & Dizaji, H. R. 2019. Synthesis and characterization of reduced graphene oxide–V_2O_5 nanocomposite for enhanced photocatalytic activity under different types of irradiation. *Journal of Physics and Chemistry of Solids,* 125**,** 8-15.

Alam, S. N., Sharma, N. & Kumar, L. 2017. Synthesis of Graphene Oxide (GO) by Modified Hummers Method and Its Thermal Reduction to Obtain Reduced Graphene Oxide (rGO). *Graphene,* 06**,** 1-18.

Bajjou, O., Mongwaketsi, P. N., Khenfouch, M., Bakour, A., Baïtoul, M., Maaza, M. & Venturini, J. W. 2015. Photoluminescence Quenching and Structure of Nanocomposite Based on Graphene Oxide Layers Decorated with Nanostructured Porphyrin. *Nanomaterials and Nanotechnology,* 5.

Bi, S., Zhao, T. & Luo, B. 2012. A graphene oxide platform for the assay of biomolecules based on chemiluminescence resonance energy transfer. *Chem Commun (Camb),* 48**,** 106-8.

Chakraborty, M., Thangavel, D. R., Komninou, P., Zhou, Z. & Gupta, A. 2018. Nanospheres and nanoflowers of copper bismuth sulphide (Cu_3BiS_3): Colloidal synthesis, structural, optical and electrical characterization. *Journal of Alloys and Compounds,* 776.

Cheng, X., Guo, H., Zhang, Y., Wu, X. & Liu, Y. 2017. Non-photochemical production of singlet oxygen via activation of persulfate by carbon nanotubes. *Water Research,* 113**,** 80-88.

Fan, X., Cai, C., Gao, J., Han, X. & Li, J. 2020. Hydrothermal reduced graphene oxide membranes for dyes removing. *Separation and Purification Technology,* 241.

Furman, O. S., Teel, A. L. & Watts, R. J. 2010. Mechanism of Base Activation of Persulfate. *Environmental Science & Technology,* 44**,** 6423-6428.

Gao, P., Liu, J., Lee, S., Zhang, T. & Sun, D. D. 2012. High quality graphene oxide–CdS–Pt nanocomposites for efficient photocatalytic hydrogen evolution. *J. Mater. Chem.,* 22**,** 2292-2298.

Gao, P., Liu, J., Sun, D. D. & Ng, W. 2013. Graphene oxide-CdS composite with high photocatalytic degradation and disinfection activities under visible light irradiation. *J Hazard Mater,* 250-251**,** 412-20.

Gao, P., Tian, X., Nie, Y., Yang, C., Zhou, Z. & Wang, Y. 2019. Promoted peroxymonosulfate activation into singlet oxygen over perovskite for ofloxacin degradation by controlling the oxygen defect concentration. *Chemical Engineering Journal,* 359**,** 828-839.

Guan, Y.-H., Ma, J., Li, X.-C., Fang, J.-Y. & Chen, L.-W. 2011. Influence of pH on the Formation of Sulfate and Hydroxyl Radicals in the UV/Peroxymonosulfate System. *Environmental Science & Technology,* 45**,** 9308-9314.

Hasija, V., Nguyen, V.-H., Kumar, A., Raizada, P., Krishnan, V., Khan, A. A. P., Singh, P., Lichtfouse, E., Wang, C. & Thi Huong, P. 2021. Advanced activation of persulfate by polymeric g-C_3N_4 based photocatalysts for environmental remediation: A review. *Journal of Hazardous Materials,* 413**,** 125324.

Hu, F., Luo, W., Liu, C., Dai, H., Xu, X., Yue, Q., Xu, L., Xu, G., Jian, Y. & Peng, X. 2021. Fabrication of graphitic carbon nitride functionalized P-$CoFe_2O_4$ for the removal of tetracycline under visible light: Optimization, degradation pathways and mechanism evaluation. *Chemosphere,* 274**,** 129783.

Jiang, L., Xu, X., Yuan, J., Zuo, Y., Tao, Y., Yao, D., He, G. & Chen, H. 2020. Heterogeneous activation of persulfate for the degradation of bisphenol A with Ni_2SnO_4–RGO. *New Journal of Chemistry,* 44**,** 6355-6361.

Khan, Z., Chetia, T. R., Vardhaman, A. K., Barpuzary, D., Sastri, C. V. & Qureshi, M. 2012. Visible light assisted photocatalytic hydrogen generation and organic dye degradation by CdS–metal oxide hybrids in presence of graphene oxide. *RSC Advances,* 2.

Kim, J., Cote, L. J., Kim, F. & Huang, J. 2010. Visualizing Graphene Based Sheets by Fluorescence Quenching Microscopy. *Journal of the American Chemical Society,* 132**,** 260-267.

Küster, A. & Adler, N. 2014. Pharmaceuticals in the environment: scientific evidence of risks and its regulation. *Philosophical transactions of the Royal Society of London. Series B, Biological sciences,* 369**,** 20130587.

Liang, P., Zhang, C., Duan, X., Sun, H., Liu, S., Tade, M. O. & Wang, S. 2017. An insight into metal organic framework derived N-doped graphene for the oxidative degradation of persistent contaminants: formation mechanism and generation of singlet oxygen from peroxymonosulfate. *Environmental Science: Nano,* 4**,** 315-324.

Liu, H., Chen, Z., Jin, Z., Su, Y. & Wang, Y. 2014. A reduced graphene oxide supported Cu_3SnS_4 composite as an efficient visible-light photocatalyst. *Dalton Trans,* 43**,** 7491-8.

Liu, W., Li, Y., Liu, F., Jiang, W., Zhang, D. & Liang, J. 2019. Visible-light-driven photocatalytic degradation of diclofenac by carbon quantum dots modified porous g-C_3N_4: Mechanisms, degradation pathway and DFT calculation. *Water Res,* 151**,** 8-19.

Luo, D., Zhang, G., Liu, J. & Sun, X. 2011. Evaluation Criteria for Reduced Graphene Oxide. *The Journal of Physical Chemistry C,* 115**,** 11327-11335.

Ma, Z., Cao, H., Lv, F., Yang, Y., Chen, C., Yang, T., Zheng, H. & Wu, D. 2021. Preparation of nZVI embedded modified mesoporous carbon for catalytic persulfate to degradation of reactive black 5. *Frontiers of Environmental Science & Engineering,* 15.

Marcano, D. C., Kosynkin, D. V., Berlin, J. M., Sinitskii, A., Sun, Z., Slesarev, A., Alemany, L. B., Lu, W. & Tour, J. M. 2010. Improved Synthesis of Graphene Oxide. *ACS Nano,* 4**,** 4806-4814.

Mokhtar Mohamed, M., Mousa, M. A., Khairy, M. & Amer, A. A. 2018. Nitrogen Graphene: A New and Exciting Generation of Visible Light Driven Photocatalyst and Energy Storage Application. *ACS Omega,* 3**,** 1801-1814.

Mompelat, S., Le Bot, B. & Thomas, O. 2009. Occurrence and fate of pharmaceutical products and by-products, from resource to drinking water. *Environment International,* 35**,** 803-814.

Mondal, A., Prabhakaran, A., Gupta, S. & Subramanian, V. R. 2021. Boosting Photocatalytic Activity Using Reduced Graphene Oxide (RGO)/Semiconductor Nanocomposites: Issues and Future Scope. *ACS omega,* 6**,** 8734-8743.

Ni, Z. H., Wang, H. M., Kasim, J., Fan, H. M., Yu, T., Wu, Y. H., Feng, Y. P. & Shen, Z. X. 2007. Graphene thickness determination using reflection and contrast spectroscopy. *Nano Lett,* 7**,** 2758-63.

O'Shea, K. E. & Dionysiou, D. D. 2012. Advanced Oxidation Processes for Water Treatment. *The Journal of Physical Chemistry Letters,* 3**,** 2112-2113.

Olatunde, O. C., Kuvarega, A. T. & Onwudiwe, D. C. 2020. Photo enhanced degradation of contaminants of emerging concern in waste water. *Emerging Contaminants,* 6**,** 283-302.

Olatunde, O. C. & Onwudiwe, D. C. 2021. Graphene-Based Composites as Catalysts for the Degradation of Pharmaceuticals. *Int J Environ Res Public Health,* 18.

Oluwole, A. O., Omotola, E. O. & Olatunji, O. S. 2020. Pharmaceuticals and personal care products in water and wastewater: a review of treatment processes and use of photocatalyst immobilized on functionalized carbon in AOP degradation. *BMC Chemistry,* 14**,** 62.

Onwudiwe, D. C. & Ajibade, P. A. 2011. Synthesis, Characterization and Thermal Studies of Zn(II), Cd(II) and Hg(II) Complexes of N-Methyl-N-Phenyldithiocarbamate: The Single Crystal Structure of $[(C_6H_5)(CH_3)NCS_2]4Hg_2$. *International Journal of Molecular Sciences,* 12.

Ostwal, M., Shinde, D. B., Wang, X., Gadwal, I. & Lai, Z. 2018. Graphene oxide – molybdenum disulfide hybrid membranes for hydrogen separation. *Journal of Membrane Science,* 550**,** 145-154.

Patel, M., Kumar, R., Kishor, K., Mlsna, T., Pittman, C. U. & Mohan, D. 2019. Pharmaceuticals of Emerging Concern in Aquatic Systems: Chemistry, Occurrence, Effects, and Removal Methods. *Chemical Reviews,* 119**,** 3510-3673.

Peng, J., Lu, X., Jiang, X., Zhang, Y., Chen, Q., Lai, B. & Yao, G. 2018. Degradation of atrazine by persulfate activation with copper sulfide (CuS): Kinetics study, degradation pathways and mechanism. *Chemical Engineering Journal,* 354**,** 740-752.

Pulicharla, R., Drouinaud, R., Brar, S. K., Drogui, P., Proulx, F., Verma, M. & Surampalli, R. Y. 2018. Activation of persulfate by homogeneous and heterogeneous iron catalyst to degrade chlortetracycline in aqueous solution. *Chemosphere,* 207**,** 543-551.

Quinn, B., Gagné, F. & Blaise, C. 2008. An investigation into the acute and chronic toxicity of eleven pharmaceuticals (and their solvents) found in wastewater effluent on the cnidarian, Hydra attenuata. *Sci Total Environ,* 389**,** 306-14.

Rashid, J., Karim, S., Kumar, R., Barakat, M. A., Akram, B., Hussain, N., Bin, H. B. & Xu, M. 2020. A facile synthesis of bismuth oxychloride-graphene oxide composite for visible light photocatalysis of aqueous diclofenac sodium. *Sci Rep,* 10**,** 14191.

Ruiz Peralta Mde, L., Pal, U. & Zeferino, R. S. 2012. Photoluminescence (PL) quenching and enhanced photocatalytic activity of Au-decorated ZnO nanorods fabricated through microwave-assisted chemical synthesis. *ACS Appl Mater Interfaces,* 4**,** 4807-16.

Sayadi, M. H., Sobhani, S. & Shekari, H. 2019. Photocatalytic degradation of azithromycin using GO@Fe_3O_4/ ZnO/ SnO_2 nanocomposites. *Journal of Cleaner Production,* 232**,** 127-136.

Sheng, Y., Tang, X., Peng, E. & Xue, J. 2013. Graphene oxide based fluorescent nanocomposites for cellular imaging. *J Mater Chem B,* 1**,** 512-521.

Soosaimanickam, A., Jeyagopal, R., Hayakawa, Y. & Sridharan, M. B. 2015. Synthesis of oleylamine-capped $Cu_2ZnSn(S,Se)_4$ nanoparticles using 1-dodecanethiol as sulfur source. *Japanese Journal of Applied Physics,* 54**,** 08KA10.

Srivastava, S., Senguttuvan, T. D. & Gupta, B. K. 2018. Highly efficient fluorescence quenching with chemically exfoliated reduced graphene oxide. *Journal of Vacuum Science & Technology B,* 36.

Sun, C., Chen, T., Huang, Q., Zhan, M., Li, X. & Yan, J. 2020. Activation of persulfate by CO_2-activated biochar for improved phenolic pollutant degradation: Performance and mechanism. *Chemical Engineering Journal,* 380**,** 122519.

Tian, X., Gao, P., Nie, Y., Yang, C., Zhou, Z., Li, Y. & Wang, Y. 2017. A novel singlet oxygen involved peroxymonosulfate activation mechanism for degradation of ofloxacin and phenol in water. *Chem Commun (Camb),* 53**,** 6589-6592.

Valcárcel, Y., Alonso, S. G., Rodríguez-Gil, J. L., Maroto, R. R., Gil, A. & Catalá, M. 2011. Analysis of the presence of cardiovascular and analgesic/anti-inflammatory/antipyretic pharmaceuticals in river- and drinking-water of the Madrid Region in Spain. *Chemosphere,* 82**,** 1062-1071.

Wang, B., Fu, T., An, B. & Liu, Y. 2020. UV light-assisted persulfate activation by CuO-Cu_2O for the degradation of sulfamerazine. *Separation and Purification Technology,* 251.

Wang, Q., Li, L., Luo, L., Yang, Y., Yang, Z., Li, H. & Zhou, Y. 2019. Activation of persulfate with dual-doped reduced graphene oxide for degradation of alkylphenols. *Chemical Engineering Journal,* 376**,** 120891.

Wang, Y., Cao, D., Liu, M. & Zhao, X. 2017a. Insights into heterogeneous catalytic activation of peroxymonosulfate by Pd/g-C_3N_4: The role of superoxide radical and singlet oxygen. *Catalysis Communications,* 102**,** 85-88.

Wang, Y., Zhao, X., Cao, D., Wang, Y. & Zhu, Y. 2017b. Peroxymonosulfate enhanced visible light photocatalytic degradation bisphenol A by single-atom dispersed Ag mesoporous g-C_3N_4 hybrid. *Applied Catalysis B: Environmental,* 211**,** 79-88.

Wen, Y., Xing, F., He, S., Song, S., Wang, L., Long, Y., Li, D. & Fan, C. 2010. A graphene-based fluorescent nanoprobe for silver(I) ions detection by using graphene oxide and a silver-specific oligonucleotide. *Chem Commun (Camb),* 46**,** 2596-8.

Xia, X., Zhu, F., Li, J., Yang, H., Wei, L., Li, Q., Jiang, J., Zhang, G. & Zhao, Q. 2020. A Review Study on Sulfate-Radical-Based Advanced Oxidation Processes for Domestic/Industrial Wastewater Treatment: Degradation, Efficiency, and Mechanism. *Frontiers in Chemistry,* 8.

Xu, Y., Liu, T., Zhang, Y., Ge, F., Steel, R. M. & Sun, L. 2017. Advances in technologies for pharmaceuticals and personal care products removal. *Journal of Materials Chemistry A,* 5**,** 12001-12014.

Yang, D., Liang, J., Luo, L., Deng, R., Li, G., He, Q. & Chen, Y. 2020. Facile defect engineering in $ZnIn_2S_4$ coupled with carbon dots for rapid diclofenac degradation. *Chinese Chemical Letters*.

Zhao, Z., Zhang, W., Liu, W., Li, Y., Ye, J., Liang, J. & Tong, M. 2021. Activation of sulfite by single-atom Fe deposited graphitic carbon nitride for diclofenac removal: The synergetic effect of transition metal and photocatalysis. *Chemical Engineering Journal,* 407.

Zheng, P. & Wu, N. 2017. Fluorescence and Sensing Applications of Graphene Oxide and Graphene Quantum Dots: A Review. *Chem Asian J,* 12**,** 2343-2353.

Zhou, Y., Jiang, J., Gao, Y., Pang, S. Y., Yang, Y., Ma, J., Gu, J., Li, J., Wang, Z., Wang, L. H., Yuan, L. P. & Yang, Y. 2017. Activation of peroxymonosulfate by phenols: Important role of quinone intermediates and involvement of singlet oxygen. *Water Res,* 125**,** 209-218.

CHAPTER TWELVE

Conclusion and recommendation

1.0 Conclusion

The photocatalytic activity of supported copper-based ternary sulphides prepared through the single source precursor route in a solvothermal heat-up process is reported in this thesis. The effect of reaction parameters such as temperature, solvent properties and precursor ratios on the stoichiometric phase selectivity of the compounds was studied within the different chapters. Furthermore, the influence of process parameters such as catalyst dosage, pH, and contaminant concentration were also presented, with radical scavenging experiments for understanding the degradation process.

In chapters 3-5, the suitability of the metal complexes as single source precursors was evaluated by studying their capability to generate metal sulphides when thermolyzed in high boiling liquids. The studies confirmed the formation of Bi_2S_3, Sb_2S_3 and the potential for generating different phases of Cu_xS by the synthesized dithiocarbamate metal complexes.

In Chapter six, selective synthesis of two phases of copper tin sulphides (Cu_2SnS_3 and Cu_3SnS_4) was achieved by varying the solvent, reaction temperature and precursor concentration using copper(II) dithiocarbamate and diphenyl tin dichloride as single source precursors and OLA and DDT as capping agents. The electrochemical properties and photocatalytic studies of the two phases showed that the Cu_2SnS_3 phase possessed better electrocatalytic and photocatalytic properties. The Cu_2SnS_3 exhibited a higher charge transport and conducting property and achieved a better photocatalytic activity towards the degradation of tetracycline. The varying properties of the optical and electrochemical properties of these two phases indicates the possibility of obtaining semiconductor materials with excellent properties by exploring the possibility of accessing several stoichiometric phases from this class of compound.

Chapter seven focused on the influence of incorporating reduced graphene oxide (rGO) with Cu_2SnS_3 on the photocatalytic activity was studied. The *ex-situ* precursor mixture process was employed in the composite synthesis and the mass ratio of rGO in the composite varied. The activity of the composite was observed to increase with increase in GO content and this could be attributed to a red shift in the band gap energy of the composite to 1.26 eV, increased in adsorptive property, enhanced surface negative charge and reduced charge carrier recombination. The synergy between Cu_2SnS_3 and GO showed that the semiconductor material's properties could be significantly enhanced by supporting it on a suitable material.

In chapter eight, the effect of support material on the photocatalytic activity of Cu_3SnS_4 was studied. Three support materials: graphene oxide (GO), protonated graphitic carbon nitride (PCN) and GO/PCN were explored as support for the nanoparticles. The study showed that the electronic properties of the nanoparticles was significantly influenced by the nature of the support material. Also, the mechanism of contaminant degradation differed for the supported nanoparticles. While photogenerated holes were the most probable reactive radical in GO/CTS, the enhanced degradation activity of GO/PCN suggests the possible generation of excitons. The difference in mechanism of action was further confirmed by the photoluminescence spectroscopy of the composites.

In chapter nine, the selective synthesis of three phases of copper antimony sulphide ($CuSbS_2$, Cu_3SbS_4 and $Cu_{12}Sb_4S_{13}$) was presented alongside with evaluation of their persulfate activation properties. By varying reaction parameters such as solvent, precursor ratio and reaction temperature and employing Cu(II) dithiocarbamate and Sb(III) dithiocarbamate complexes as single source precursors, the different stoichiometric phases were obtained. The study of the persulfate activation activity of the phases showed that the Cu_3SbS_4 and $Cu_{12}Sb_4S_{13}$ phases exhibited better efficiency compared to $CuSbS_2$ at pH 4. Further study of the influence of pH on the degradation process showed that the degradation process was more efficient at neutral pH compared to acidic and basic condition. The radical scavenging study showed that the process of persulfate activation was by the radical process rather than the non-radical process.

The focus of Chapter ten, was on evaluation of the potential of graphene oxide to improve on the catalytic activity of $CuSbS_2$. Synthesized $CuSbS_2$ was incorporated into graphene oxide via a facile *ex-situ* process. The obtained GO-$CuSbS_2$ was evaluated as a catalyst for persulfate activation and photocatalytic degradation of tetracycline. The study revealed the higher photocatalytic activity of the composite compared to persulfate activation. Radical scavenging experiments confirmed the importance of photogenerated holes in the photocatalytic process, while the radical process was significant in the persulfate activation process.

Finally in chapter eleven, the UV-assisted persulfate activation process using reduced graphene oxide supported copper bismuth sulphide (rGO-Cu_3BiS_3) as catalyst for the degradation of diclofenac was reported. While the composite showed a slow degradation rate when explored as photocatalyst, incorporation of UV light assisted persulfate activation, and significantly enhanced the degradation process. The process not only showed great energy consumption profile but also showed potential for the degradation of a wide range of pollutants.

In summary, selective synthesis of copper-based ternary sulphides was achieved by tuning of reaction process parameters. The semiconductor materials were further composited with graphene oxide/reduced graphene oxide. The catalytic properties of the obtained composites were explored for the degradation of emerging contaminants, with the effect of process parameters studied. Attempts at understanding the mechanism of action of the catalysts were explored using radical scavenging experiment, alongside studies on the stability of the obtained composites.

2.0 Future work

Despite the significant progress made in this study, there are several questions that still needs to be addressed to further understand the potential of copper-based ternary metal sulphides as catalysts for pollutant degradation. Some of these include:

1. Further study on the influence of process parameters on the morphology and optical properties of the ternary metal sulphides and on the photocatalytic activity of the semiconductors

2. Deeper understanding of the mechanism of degradation, enhanced spectroscopic techniques for identification of reactive radical species need to be explored

3. Degradation products identification using spectroscopic methods should be explored further

4. Evaluation of the toxicity of the degradation products should be studied further.